

Physical modeling of soil spatial variability: application to shallow foundation



Lina Ximena Garzón Avila
Faculty of Engineering
Department of Civil Engineering

A document presented for the
Doctoral Dissertation
Bogotá Colombia
January 2019

To my mon, dad, sister, brother and to me.

ACKNOWLEDGMENT

I am because you are: Ubuntu.

It has been a long way since I began my doctorate studies. I innocently undertook this enterprise, maybe I threw myself into the void without the necessary tools to fly, and sometimes I fell, sometimes I got hurt, but if I am here writing these acknowledgments it means that I achieved it! Doing this Ph.D. meant leaving my comfort zone, often in a violent manner, but I am convinced that facing new challenges are those that allow us to grow intellectually and emotionally. I am because you are, says the African philosophy Ubuntu, this is why I want to thank all the people who helped me and made it possible for me to carry out this Ph.D.

Professor Bernardo Caicedo Hormaza, I do not have words to thank everything you have taught me; thank you for your patience, for your pandering, for trusting and believing in me, without your help this would not have been possible.

Professor Mauricio Sánchez-Silva and Professor Kok-Kwang Phoon, thank you for the time that you gave me and for helping me do my internship in Singapore.

Juliet Monroy, the engineer of the geotechnical model laboratory of the Universidad de los Andes and José Naranjo, technician at the soil laboratory, thank you for your patience and your full collaboration I received throughout these years. To the other laboratory technicians, thank you for your help, you were always there when I needed you.

Loveable doctoral friends who listened to me and helped me in times of crisis, your “bullying” made my trip more enjoyable, your friendship is the greatest gift this Ph.D. leaves me with.

ABSTRACT

The spatial variability of soil properties is a critical factor that brings inevitable uncertainty on the design and analysis of geotechnical structures. In particular, the effects of soil heterogeneity on the bearing capacity of a shallow foundation has been widely studied numerical using random field theory to model the heterogeneity, and finite elements to compute the bearing capacity response, in conjunction with Monte Carlo Simulation approach (Fenton & Griffiths, 2002; Fenton & Griffiths, 2003; Popescu et al., 2005; Griffiths et al. 2006; Al-Bittar & Soubra, 2012; Griffiths et al. 2009; Hicks & Spencer, 2010; Kasama & Zen, 2011; Fenton & Griffiths, 2002; Huber et al., 2010 and Haldar & Babu, 2008). On the other hand, in geotechnical engineering, physical modeling methods such as full-scale field tests and centrifuge model tests are frequently used for modeling prototypes, investigation of new phenomena, and validation of numerical models (Randolph & House, 2001; Yang et al., 2008; Chen & Yu, 2011; Rajesh & Viswanadham, 2012; Chakraborty & Popescu, 2012). This document presents a new methodology to validate the effect of the variability of soil properties on the behavior of shallow foundation experimentally. The approach is developed in two parts: the first relates to the preparation of reduced scale soils models with controlled spatial variability, and the second refers to the performing of in-flight bearing capacity tests of a single rigid strip footing resting on a spatial varying soft soil. The method proposed in this document offers new possibilities to study the effect of soil variability on the behavior of geotechnical structures.

KEYWORDS: Soil spatial variability, Random field, Geotechnical centrifuge, Bearing capacity test.

CONTENT

1	INTRODUCTION	12
1.1	Research objectives.....	14
1.2	Structure of the document	14
2	Uncertainty in geotechnical engineering	15
2.1	Sources and types of uncertainty	15
2.2	Random field model for inherent soil variability	16
2.3	Values of the statistical parameters of index laboratory properties.....	17
2.3.1	Coefficient of variation of index parameters.....	17
2.3.2	Scale of fluctuation of index parameters.....	18
2.4	Conclusion	19
3	EFFECTS OF SOIL VARIABILITY ON BEARING CAPACITY OF SHALLOW FOUNDATION.....	20
3.1	Literate review	20
3.2	Conclusion	24
4	CENTRIFUGE MODELING	25
4.1	Principles of centrifuge modeling	25
4.2	Basic scaling laws	25
4.3	Soil samples materials.....	26
4.4	Preparation of soil.....	26
4.4.1	One dimensional compression or oedometric consolidation.....	27
4.4.2	Centrifuge consolidation technique.....	27
4.4.3	Seepage consolidation technique	27
4.5	Mini geotechnical centrifuge of Universidad de los Andes	28
4.5.1	Mini geotechnical centrifuge	28
4.5.2	Pneumatic consolidometer	28
4.1	Conclusion	29
5	PHYSICAL MODELING OF SOIL VARIABILITY	30
5.1	Introduction	30
5.2	Random field generation	30
5.3	Parameters of the random field.....	32
5.4	Properties analysis of homogenous mixed soils	33
5.4.1	Basic properties of mixed soils.....	33
5.4.2	Compressibility behavior of mixed soils	36
5.4.3	Undrained shear strength behavior of mixed soil	39
5.5	Development of the random soil construction technique: two-layers	46
5.5.1	Heterogeneous soil construction technique.....	47
5.5.2	Consolidation process	48
5.5.3	Computerized Axial Tomography (CAT Scan)	50
5.5.4	Resistance (Electrical Needle Probe)	51
5.5.5	Undrained shear strength measurements.....	54
5.6	Development of the random soil construction technique: one-layer	62

5.6.1	Modification of random soil construction technique	63
5.6.2	Undrained shear strength measurements	63
5.7	Conclusions	86
6	PHYSICAL MODELING of shallow foundation.....	88
6.1	Bearing capacity test characteristic	88
6.2	Micro-loading system.....	92
6.2.1	General description.....	92
6.2.2	Driving motor part.....	92
6.2.3	Moving platform part.....	93
6.2.4	Software development	94
6.3	Step by step of the bearing capacity test.....	94
6.4	Bearing capacity test results: models built in two-layers procedure	95
6.5	Bearing capacity test results: models built in one-layer procedure	98
6.5.1	Analysis of the failure mechanism	98
6.5.2	Ultimate bearing capacity strength criteria	107
6.5.3	Ultimate bearing capacity serviceability criteria	109
6.5.4	Undrained shear strength measurements	116
6.6	Conclusions	117
7	GENERAL CONCLUSIONS AND RECOMMENDATIONS.....	119

LIST OF FIGURES

Figure 2.1 Sources and types of uncertainty (Adapted Phoon and Kulhawy, (1999a)).	15
Figure 2.2 Inherent soil variability (Adapted Phoon and Kulhawy, (1999)).	17
Figure 3.1 Estimated mean bearing capacity factor, mN_c , as a function of undrained shear strength statistics, COV and θ . (Taken from Griffiths & Fenton (2001)).	21
Figure 3.2 Typical deformed meshes and a corresponding plot of displacement vectors for two realizations (rough footing). (Taken from Griffiths & Fenton (2002)).	21
Figure 3.3 Monte Carlo simulation results involving 100 sample functions for the case COV = 40%, $L_x = 5$ m: a) normalized bearing pressures vs. settlements, b) normalized bearing pressures vs. footing rotations. (Taken from Popescu et al. (2005)).	23
Figure 3.4 Deformed mesh corresponding to a realization of the random soil (Taken from Soubra et al. (2008)).	23
Figure 4.1 Mini geotechnical centrifuge of Universidad de los Andes.	28
Figure 4.2 Graphical method of settlement prediction (Adapted Asaoka (1978)).	29
Figure 4.3 Mini-pneumatic consolidometer of Universidad de los Andes.	29
Figure 5.1 Example of a random field generation.	33
Figure 5.2 Basic relationship of homogeneous soils: (a) liquid limit and bentonite fraction (b) plasticity index and bentonite fraction (c) plasticity chart of the clay mixtures.	35
Figure 5.3 Basic relationships of soil properties: (a) relationship between liquid limit and plastic limit, (b) relationship between liquid limit and specific gravity.	35
Figure 5.4 Oedometric test results: compression curves.	36
Figure 5.5 Oedometric test results: relationship between liquid limit and compression index.	37
Figure 5.6 Intrinsic compression curves of the eight homogeneous soil mixtures.	38
Figure 5.7 Relationship between e_L and the intrinsic compression parameter C_c^* .	39
Figure 5.8 Relationship between e_L and the intrinsic compression parameter e_{100}^* .	39
Figure 5.9 Triaxial compression tests result at 100 kPa confining stress.	40
Figure 5.10 Triaxial compression tests result at 200 kPa confining stress.	41
Figure 5.11 Triaxial compression tests result at 300 kPa confining stress.	41
Figure 5.12 Triaxial CU results: (a) relationship between liquid limit and the critical line value, (b) relationship between liquid limit and the friction angle.	42
Figure 5.13 Relationship between shear strength of clay and consistency index: (a) soils S1 to S4 and (b) soils S5 to S8	44
Figure 5.14 τ_{mob}/C_u versus shear strain, γ .	46
Figure 5.15 τ_{mob}/C_u versus Predicted τ_{mob}/C_u .	46
Figure 5.16 Construction of the heterogeneous model: (a) container box and acrylic extensions, (b) container box and caulking guns, (c) container box with the porous stone and the grid, (d) process of placing the strings of slurries into the container.	48
Figure 5.17 Construction of the heterogeneous model: (a) container box and caulking guns, (b) acrylic extensions of the container box, (c) container box with the porous stone and the grid, (d) process of placing the strings of slurries into the container.	49

Figure 5.18 Consolidation process: (a) one-dimensional consolidation, (b) centrifuge consolidation.....	49
Figure 5.19 Three isotropic heterogeneous models: (a) Model 1, (b) Model 2, (c) Model 3.	50
Figure 5.20 Computerized Axial Tomography of a preliminary model.	51
Figure 5.21 Computerized Axial Tomography: (a) Model 1, (b) Model 2.....	51
Figure 5.22 Measurement made by the electrical needle probe: (a) locations of the point measurements in the model, (b) electrical needle position.....	52
Figure 5.23 Three profiles of the heterogeneous model measurement by the electrical needle probe.	52
Figure 5.24 Resistance profiles of homogeneous models: (a) traditional technique left position, (b) traditional technique centre position, (c)) traditional technique right position, (d) random technique left position, (e) random technique centre position and (f) random technique right position.....	53
Figure 5.25 Resistance profiles of heterogeneous models: (a) left position, (b) centre position and (c) right position.	54
Figure 5.26 Sampling process of the 112 elements of the mode.....	55
Figure 5.27 2D Random effective normal stress values and histogram in kPa: (a) Model 1, (b) Model 2, (c) Model 3.....	56
Figure 5.28 2D Random effective normal stress values in kPa: (a) Model 1, (b) Model 2, (c) Model 3.	58
Figure 5.29 Map of the effective normal stress values in kPa for the three models.	59
Figure 5.30 Variation with depth of the vertical stress for the three models: mean value and mean plus minus one standard deviation.....	60
Figure 5.31 Map of the undrained shear strength values in kPa for the three models.	61
Figure 5.32 Variation with depth of the undrained shear strength for the three models: mean value and mean plus minus one standard deviation.	62
Figure 5.33 Models one-layer stage: (a) homogeneous model soil S3, (b) heterogenous models	62
Figure 5.34 Construction of the models: (a) traditional technique, (b) random technique.	63
Figure 5.35 Construction of the heterogeneous model: (a) container box with vertical extensions, (b) caulking guns, (c) process of placing the strings of slurries into the container.	63
Figure 5.36 Water content measurement: (a) process of sampling with the syringe, (b) soil samples.	64
Figure 5.37 Undrained shear strength indirect measurements in kPa for homogeneous models traditional technique: (a) Cam clay theory, (b) Leroueil et al., (1983) and (c) Hong et al., (2003)..	67
Figure 5.38 Undrained shear strength indirect measurements in kPa for homogeneous models random technique: (a) Cam clay theory, (b) Leroueil et al., (1983) and (c) Hong et al., (2003).	68
Figure 5.39 Undrained shear strength indirect measurements in kPa for homogeneous models Equation 5.17: (a) traditional technique, (b) random technique.	69
Figure 5.40 Undrained shear strength indirect measurements in kPa of heterogeneous models: (a) Cam clay theory, (b) Leroueil et al., (1983) and (c) Hong et al., (2003).	71

Figure 5.41 Undrained shear strength indirect measurements in kPa of heterogeneous models Equations 5.17 and 5.18.....	72
Figure 5.42 Direct measurements tools: (a) mini vane and (b) mini ball penetrometer.	73
Figure 5.43 Undrained shear strength direct measurements: (a) mini vane and (b) mini ball penetrometer.....	74
Figure 5.44 Undrained shear strength direct measurements in kPa of homogenous traditional technique models: (a) mini ball penetrometer and (b) mini vane.	76
Figure 5.45 Undrained shear strength direct measurements in kPa of homogenous random technique models: (a) mini ball penetrometer and (b) mini vane.	77
Figure 5.46 Undrained shear strength direct measurements in kPa of heterogeneous models: (a) mini ball penetrometer, (b) mini vane and (c) mini vane Bjerrum correction.....	79
Figure 5.47 Average undrained shear strength direct measurements in kPa of heterogeneous models: (a) mini ball penetrometer, (b) mini vane and (c) mini vane Bjerrum's correction.	81
Figure 5.48 Relationship between liquid limit and direct measurements of undrained shear strength: (a) mini ball penetrometer, (b) mini vane and (c) mini vane Bjerrum's correction.....	82
Figure 5.49 Relationship between water content and direct measurements of undrained shear strength: (a) mini ball penetrometer, (b) mini vane and (c) mini vane Bjerrum's correction.....	83
Figure 5.50 Relationship between liquidity index and direct measurements of undrained shear strength: (a) mini ball penetrometer, (b) mini vane and (c) mini vane Bjerrum's correction.....	84
Figure 5.51 Relationship between normalized water content, w^* and direct measurements of undrained shear strength: (a) mini ball penetrometer, (b) mini vane and (c) mini vane Bjerrum's correction.	85
Figure 6.1 Random fields: (a) horizontal scale of fluctuation of 30m, (b) horizontal scale of fluctuation of 60m.	90
Figure 6.2 Random fields: (a) horizontal scale of fluctuation of 6m, (b) horizontal scale of fluctuation of 15m.	91
Figure 6.3 Micro-loading system: (a) scheme, (b) constructed model.....	92
Figure 6.4 Schema of the driving motor part.	93
Figure 6.5 Schema of the moving platform: (a) front view, (b) lateral view.	93
Figure 6.6 Painted grid model: (a) heterogeneous model, (b) homogeneous model.....	94
Figure 6.7 Micro-loading system installed in the mini centrifuge.	95
Figure 6.8 Initial and final images and settlement-load curves: homogenous model S2	96
Figure 6.9 Initial and final images and settlement-load curves: models M1-1.5m and M2-1.5m	96
Figure 6.10 Initial and final images and settlement-load curves: models M1-6m and M2-6m...	97
Figure 6.11 Initial and final images and settlement-load curves: models M1-6m and M2-6m...	97
Figure 6.12 Effect of the horizontal scale of fluctuation.	98
Figure 6.13 Evolution of the failure mechanism of homogeneous model Homo 3.	101
Figure 6.14 Evolution of the failure mechanism of heterogeneous model COV_{WL} 13%.	102
Figure 6.15 Evolution of the failure mechanism of heterogeneous model COV_{WL} 30%.	103
Figure 6.16 Evolution of the failure mechanism of heterogenous model COV_{WL} 51%.	104
Figure 6.17 Evolution of the failure mechanism of heterogenous model $\delta_h=6m$	105

Figure 6.18 Evolution of the failure mechanism of heterogenous model $\delta_h=15m$	106
Figure 6.19 Mean of the undrained shear strength in kPa estimated by Equations 5.17 and 5.18: (a) homogeneous model, (b) isotropic heterogeneous model.	108
Figure 6.20 Mean of unit soil weight in kN/m^3 (a) homogeneous model, (b) isotropic heterogeneous model.....	108
Figure 6.21 Comparison between the ultimate bearing capacity estimated by Equations 6.2 and the calculated by the in-flight test: (a) homogeneous model, (b) isotropic heterogeneous model.	109
Figure 6.22 Load intensity- settlement curves homogenous models	110
Figure 6.23 Load intensity- settlement curves heterogeneous models $COV_{WL}13\%$	111
Figure 6.24 Load intensity- settlement curves heterogeneous models $COV_{WL}30\%$	111
Figure 6.25 Load intensity- settlement curves heterogeneous models $COV_{WL}51\%$	112
Figure 6.26 Effect of the variation of the COV_{WL} on the bearing capacity.	112
Figure 6.27 COV_{WL} versus the normalized bearing capacity $\frac{\mu_{q_s}}{\mu_{q_{Homo}}}$	113
Figure 6.28 Load intensity- settlement curves heterogeneous models $\delta_h=1.5m$	114
Figure 6.29 Load intensity- settlement curves heterogeneous models $\delta_h=6m$	114
Figure 6.30 Load intensity- settlement curves heterogeneous models $\delta_h=15m$	115
Figure 6.31 Effect of the horizontal scale of fluctuation, δ_{hWL} on the bearing capacity.....	115
Figure 6.32 δ_{hWL} versus the normalized bearing capacity $\frac{\mu_{q_s}}{\mu_{q_{Homo}}}$	116
Figure 6.33 Range of values of coefficient of variation of the undrained shear strength, COV_{Cu} for various tests (Adapted Popescu et al. (2005)).	117

LIST OF TABLES

Table 2.1 Values of the coefficient of variation of index parameters.	18
Table 2.2 Summary of the scale of fluctuation of some index parameter.	19
Table 4.1 Some common scaling laws for centrifuge test.	26
Table 5.1 Inherent variability of liquid limit W_L	32
Table 5.2 Vertical scale of fluctuation values of liquid limit W_L	32
Table 5.3 Composition and Specific Gravity of the colorants.	33
Table 5.4 Homogeneous soils properties.	42
Table 5.5 Data used to define the relationship between undrained shear strength and the consistency index.	43
Table 5.6 Indirect values of undrained shear strength for homogeneous models.	66
Table 5.7 Indirect values of undrained shear strength for heterogeneous models.	70
Table 5.8 Direct values of undrained shear strength for homogeneous models.	75
Table 5.9 Direct values of undrained shear strength for heterogeneous models.	78
Table 6.1 Bearing capacity tests plan.	89
Table 6.2 Undrained shear strength and unit soil weight of the homogeneous and heterogeneous models.	108
Table 6.3 Mean of q_f , q_{test} and q_u in kPa for homogeneous and heterogeneous models.	109
Table 6.4 Effect of the variation of the COV_{WL} on the bearing capacity.	113
Table 6.5 Effect of the horizontal scale of fluctuation, δ_h on the bearing capacity.	116
Table 6.6 Statistical parameters of the undrained shear strength.	117

1 INTRODUCTION

Soil is a complex material whose properties result from a combination of geological, environmental, and physical-chemical processes, which permanently modify its mechanical properties. The variability of the soil properties due to these natural processes lead to substantial uncertainties in geotechnical engineering analysis and design. For example, it influences the bearing capacity, foundation settlement and slope stability of geotechnical structures. In the last decade, several authors had studied the effects of soil variability on the mechanical behavior of various geotechnical problems. The methodologies used in most of these studies involve a combination of Random Field Theory with the Finite Element Method applied in a Monte Carlo Simulation.

Griffiths & Fenton (2001), Fenton & Griffiths (2003), Popescu et al. (2005), Griffiths et al. (2006), Soubra et al. (2008), Cho & Park (2010), Al-Bittar & Soubra (2012), and Honjo & Otake, (2013) studied the bearing capacity of shallow foundations. The major conclusion of these studies is that the inherent spatial variability of soil properties can modify the basic form of the failure mechanisms; as a result, the value of the ultimate bearing capacity is reduced substantially compared to the corresponding value obtained for a homogeneous soil. Furthermore, differential settlements appear in the spatially varying soil leading to the rotation of the footing.

Li et al. (2016) studied slope stability and reliability in 3D using conditional random fields. Zhu et al. (2015) investigated the failure mechanisms and the probability of failure of slopes in random undrained soil over a wide range of slope angles. Li et al., (2015) carried out a series of analyses on slope reliability, compared the performance of the random finite element model (RFEM) with Vanmarcke's analytical model. Griffiths et al. (2009), Hicks & Spencer (2010), Kasama & Zen (2011), Hong & Helin (2011) studied slope stability. They concluded that the spatial variability of soil properties reduces the slope stability factor in comparison to a conventional calculation based on mean soil parameters. They also point out that traditional analysis based on mean strengths is inappropriate for heterogeneous soil, due to the tendency for failure to be attracted to weaker zones. Furthermore, the effect of soil variability in foundation settlements have been studied by Fenton & Griffiths (2002); differential settlement due to tunneling by Huber et al. (2010); and the response of laterally loaded pile in undrained clay by Haldar & Babu (2008). Furthermore, taking soil spatial variability into account will lead to a rational and economical design of foundations and geotechnical structures (Salgado and Kim 2014; Fan et al. 2014).

The results obtained from analytical stochastic geotechnical models, such as those mentioned above, are difficult to verify experimentally, mainly due to the excessive time and cost that is required to build full-scale field tests. However, centrifuge modeling has shown to be a powerful tool to validate numerical models. In geotechnical centrifuge modeling, the soil characteristics and the boundary conditions can be controlled; and the structural performance well monitored (Kimura et al. 1984; Taylor, 1995; Mitchell, 1998; Andersen et al. 2005).

One crucial numerical observation is that the geotechnical capacity is lower in a spatially heterogeneous medium compared to a spatially homogeneous medium having the average strength of the spatially heterogeneous medium. In short, averaging soil properties to simplify the analysis will produce an unconservative outcome. Ching and co-workers (Ching and Phoon 2013a, 2013b; Ching et al. 2014a) showed that the mobilized shear strength is not the spatial average along any prescribed curve but the spatial average along the critical slip curve. The main difference is that the critical slip curve is not a specified curve but an emergent curve that depends on the random field realizations. More recently, Ching et al. (2016a) showed that the mobilized shear strength could not be adequately represented by any spatial average unless the critical slip curve is constrained by boundary effects. Studies have been extended to a 3D setting (Ching et al. 2016b) and other soil properties beyond shear strength (Ching et al. 2016c).

The previous studies indicate that a geotechnical structure (e.g., foundations, slopes, retaining structures) interacts with a spatially heterogeneous medium in a fairly sophisticated way. This complex interaction results in practically essential design outcomes that cannot be reproduced by an equivalent homogeneous medium. Despite the practical importance of these numerical observations to geotechnical design, no physical tests have been conducted for validation to the knowledge of the authors. One reason is that it is difficult to prepare physical soil samples following a prescribed spatially heterogeneous distribution of soil properties. Conventional experiments are based on homogeneous or layered soil samples. Nonetheless, it is necessary to validate the growing volume of numerical results physically.

This thesis aims to validate experimentally the ultimate bearing capacity of a rigid strip footing resting on a spatially varying soil. This document presents the methodology proposed in this research, which is developed in two parts: (i) preparation of reduced scale soils models with controlled spatial variability, and (ii) perform bearing capacity tests of a single rigid strip foundation. Reduced scale heterogeneous soils are fabricated by reproducing the variability in mineralogy, i.e., liquid limit and reproducing the history of field stresses by using an oedometer and geotechnical centrifuge. In-flight bearing capacity tests are performed in the small geochemical centrifuge of Universidad de los Andes. A micro loading device was designed and constructed for that purpose; this device can carry out bearing capacity test at a constant rate of strain allowing a reliable recording of the bearing capacity. Likewise, the device can measure vertical and horizontal forces as well as moments.

1.1 Research objectives

This project aims to validate the effect of the variability of soil properties on the behavior of shallow foundation experimentally. More precisely the objectives are:

- ✓ Development of a new technique to build up soils with controlled variability in reduced scale models using a geotechnical centrifuge.
- ✓ Development a micro loading device for small geotechnical centrifuge and perform bearing capacity test.
- ✓ Study the failure mechanisms in the physical models.

1.2 Structure of the document

The document is organized as follows: Chapter 2 presents the basis of geotechnical uncertainties and also provides a summary of the most common index parameters values of the coefficients of variation, COV and the scale of fluctuation, δ_v . Chapter 3 presents a review of the effects of soil spatial variability on bearing capacity of shallow foundation; likewise, the principles of the centrifuge modeling are described in Chapter 4. Then, in Chapter 5, the new technique to prepare scaled soil models with controlled variability is presented. Chapter 6 makes a description of the micro-loading device, and present the results of the in-flight bearing capacity tests. Finally, Chapter 7 present the general conclusions and recommendations.

2 UNCERTAINTY IN GEOTECHNICAL ENGINEERING

In this section, first, a brief of the different sources of uncertainties is presented. Then, the soil spatial variability is explained in some detail. Finally, a summary of the standard index parameters values of the coefficients of variation, COV, and the correlation length L_T , or scale of fluctuation δ_v are provided.

2.1 Sources and types of uncertainty

Uncertainty in prediction of geotechnical response is a complex phenomenon resulting from many different sources, which are categorized as either random or epistemic (Lacasse et al., 1996). Uncertainties are characterized as epistemic if the modeler sees a possibility to reduce them by gathering more data or by refining models. Uncertainties are categorized as random if the modeler does not foresee the possibility of reducing them (Der Kiureghian & Ditlevsen (2009).

In geotechnical engineering, there are two types of epistemic uncertainties: measurement error, and transformation uncertainty. The first one is due to the equipment, test-operators, and the sampling error that results from the limited amount of information. This uncertainty can be minimized by considering more samples. The second one is introduced when field or laboratory measurements are transformed into design soil properties using empirical or other correlation models. This uncertainty can be reduced by considering more refined mathematical or empirical models.

On the other hand, the random uncertainty type in geotechnical engineering concerns the inherent soil variability that primarily results from the natural geologic processes which modify the in-situ soil mass. Figure 2.1 illustrates the kinds of uncertainty in geotechnical soil properties.

Only the inherent soil variability is taken into consideration in this thesis.

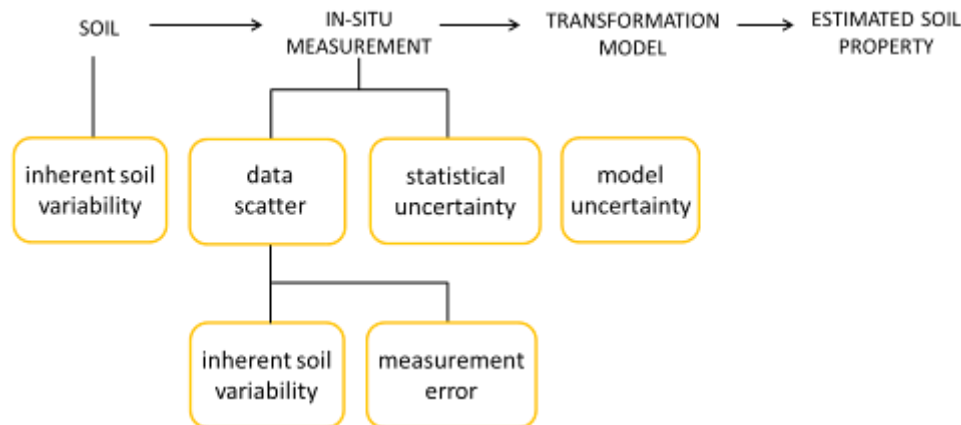


Figure 2.1 Sources and types of uncertainty (Adapted Phoon and Kulhawy, (1999a)).

2.2 Random field model for inherent soil variability

The spatial variation of the soils properties is usually separated into a spatial trend, $t(z)$, and fluctuations around this trend $w(z)$, which describes the inherent variability of the process (Figure 2.2). Therefore, a given in-situ soil property ε can be computed as:

$$\varepsilon(z) = t(z) + w(z) \quad (2.1)$$

where ε = in-situ soil property and z = the depth. If $w(z)$ is statistically homogeneous, the mean and variance of $w(z)$ are independent of depth, and the correlation of $w(z)$ signals at two different depths is a function of their spatial separation rather than their absolute locations (Vanmarcke, 1983). The standard deviation of inherent soil variability, (S_w), for a statistically homogeneous variability function $w(z)$ is defined for n data points as:

$$S_w = \sqrt{\frac{1}{n-1} \sum_{i=1}^n [w(z_i)]^2} \quad (2.2)$$

where n = number of data points and $w(z_i)$ = fluctuation at depth z_i . A useful dimensionless ratio, the coefficient of variation of inherent variability, can be calculated by normalizing (S_w) with respect to the trend function $t(z)$:

$$COV_w = S_w / t \quad (2.3)$$

On the other hand, the vertical scale of fluctuation δ_v , or correlation length L_T , is the distance within which a soil property shows a strong correlation and is essential for modeling spatial variability. Vanmarcke (1977) introduced the following approximation to estimate δ_v :

$$\delta_v \approx 0.8d \quad (2.4)$$

where d = average distance between the points where the fluctuating soil property and its trend function have equal values along the soil profile.

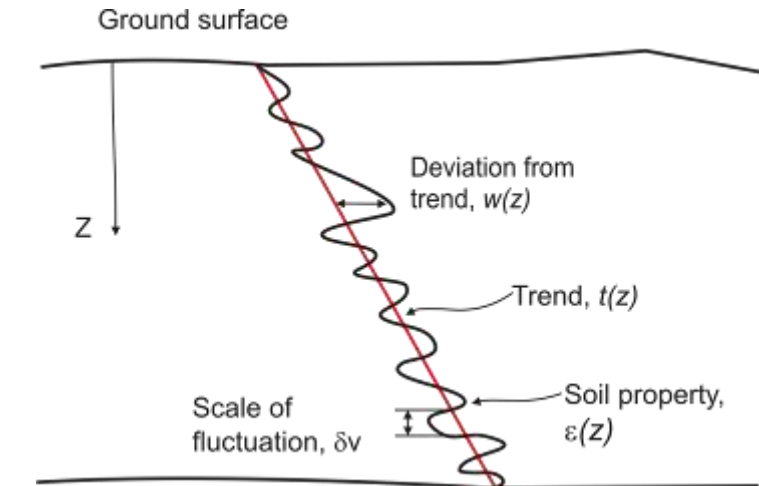


Figure 2.2 Inherent soil variability (Adapted Phoon and Kulhaw, (1999)).

2.3 Values of the statistical parameters of index laboratory properties

2.3.1 Coefficient of variation of index parameters

After extensive research, Phoon and Kulhaw (1999a, b) proposed generic guidelines for ranges of uncertainty in geotechnical properties. They used a homogeneous random field to represent the inherent soil variability, and evaluated coefficients of variations, *COV*, due to the inherent variability, and due to measurement errors. For the laboratory index parameters they found: (i) for natural water content, W_n , the typical range of *COV* is between 8 and 30%, (ii) for the liquid limit, W_L , and plastic limit, W_p , the usual range of *COV* is between 6 and 30% for both index parameters, which is comparable to that for W_n , (iii) for the plasticity, PI , the typical range of *COV* is between 9 and 50%.

Akbas and Kulhaw (2010) characterized and estimated the geotechnical property variability for Ankara Clay, which is an inorganic preconsolidated clay. They used the framework proposed by Phoon and Kulhaw (1999a, b), and found that the ranges of the *COV* of inherent variability for W_L , and W_p , are between 9 and 22%, and 6 and 19%, respectively. Regarding PI the range of *COV* is between 13 and 28%. Table 2.1 presents the values of the coefficient of variation of index parameters.

It is important to point out that the amount of information on the *COV* of inherent soil variability of the index properties is relatively limited in comparison to the shear strength parameters (shear strength c , angle of internal friction ϕ). One reason is that the index parameters are not used as soil parameters for design.

Table 2.1 Values of the coefficient of variation of index parameters.

Property ^a	Soil type	Property COV(%) Range	Mean	Author
W _n (%)	Fine grained	7 - 46	18	Phoon & Kulhawy (1999a)
W _L (%)	Fine grained	7 - 39	18	
W _P (%)	Fine grained	6 - 34	16	
PI (%)	Fine grained	9 - 57	29	
LI	Clay, silt	60 - 88	74	
γ (kN/m ³)	Fine grained	3 - 20	9	
W _n (%)	Ankara clay	12 - 22	14	Akbas & Kulhawy (2010)
W _L (%)	Ankara clay	9 - 22	14	
W _P (%)	Ankara clay	6 - 19	12	
PI (%)	Ankara clay	13 - 28	19	

^aW_n, natural water content; W_L, liquid limit; W_P, plastic limit; PI, plasticity index; LI, liquidity index; γ, total unit weight.

2.3.2 Scale of fluctuation of index parameters

Although there is some information about the statistical variation of the index parameters in a soil deposit, the amount of information on its geometrical fluctuation is relatively limited. An overview of the scale of fluctuation values of different soil types and different soil properties was published by Phoon & Kulhawy (1999a); Jones et al. (2002); El-Ramly (2003); Uzielli et al. (2005); however, these published results are mainly useful for reference purposes as they are mostly generic (due to the widely-sourced data). On the other hand, Jacksa et al., (2000); Akbas & Kulhawy (2010); Stuedlein et al., (2012) and Onyejekwe and Ge (2013) estimated the scale of fluctuation of different soil properties based on in situ and laboratory test.

Only the studies made by Phoon and Kulhawy (1999a), Akbas and Kulhawy (2010), Onyejekwe and Ge (2013) present values for the scale of fluctuation of the index parameter. The authors concluded that the horizontal scale of fluctuation, δ_h is more than one order of magnitude larger than the vertical scale of fluctuation, δ_v with a typical range of between 40–60 m. Likewise, Phoon and Kulhawy (1999a) stated that δ_v values for index parameters are the largest. Also, index parameters are less variable in both vertical and horizontal directions, in comparison with other soil parameters. Table 2.2 presents a summary of the scale of fluctuation of some index parameters.

Table 2.2 Summary of the scale of fluctuation of some index parameter.

Property ^a	Soil type ^b	Scale of fluctuation (m)		Author
		Range	Mean	
Vertical fluctuation				
W_n	Clay, loam	1.6 - 12.7	5.7	Phoon & Kulhawy (1999a)
W_L	Clay, loam	1.6 - 8.7	5.2	
γ^* (kN/m ³)	Clay	-	1.6	
γ (kN/m ³)	Clay, loam	2.4 - 7.9	5.2	
W_n	Ankara clay	2.5 - 5.5	5.2	Akbas & Kulhawy (2010)
W_L	Ankara clay	4.0 - 6.2	5.1	
γ_b (psf)		3.41 - 13.6	6.92	Onyejekwe & Ge (2013)
W_L	CH	4.69 - 5.76	5.06	
W_P		3.17 - 5.36	4.42	
W_n		3.20 - 11.91	7.1	
γ_b (psf)		0.58 - 0.7	0.64	
W_L	CL	0.91 - 0.98	0.94	
W_P		0.55 - 0.58	0.58	
W_n		0.70 - 1.31	1.01	
Horizontal fluctuation				
W_n	Clay, loam	-	170	Phoon & Kulhawy (1999a)

^a W_n , natural water content; W_L , liquid limit; W_P , plastic limit; γ^* , effective unit weight; γ , total unit weight; γ_b , bulk unit weight. ^b CH, clay of high plasticity, fat clay; CL, clay of low plasticity, lean clay.

2.4 Conclusion

Soil variability is difficult to assess and estimate due mainly to: (1) inherent soil variability, (2) measurement error, and (3) transformation uncertainty (Phoon & Kulhawy, 1999a).

A complete probabilistic characterization of a geotechnical property involved the knowing of the variance and the scale of fluctuation. While the mean and variance can be easily determined by using conventional statistical analysis, determination of the scale of fluctuation is a little more complicated. For this purpose, the random field theory can be used to estimate the autocorrelation structure of a soil property.

Although most of the studies have made a great effort to estimate the variability of soil properties, the values for the variability of the index properties is relatively limited in comparison with others soil properties.

3 EFFECTS OF SOIL VARIABILITY ON BEARING CAPACITY OF SHALLOW FOUNDATION

This section aims at providing a literature review of the impact of soil spatial variability on bearing capacity of a shallow foundation. The overview is made chronologically from 2000 until now.

3.1 Literate review

Griffiths & Fenton (2001) performed a study on bearing capacity of a smooth rigid strip footing placed on at undrained clay with a shear strength, C_u , using random fields to define the spatial variability. They developed a program that merges non-linear elastoplastic finite element analysis with random field theory in conjunction with Monte Carlo method. The finite element model had a mesh consisting of 1000 elements, with 50 columns and 20 rows, and the strip footing had a width of 10 elements. The results were given regarding the dimensionless bearing capacity factor, N_c , and were compared with the Prandtl solution value given for a homogeneous soil, i.e., 5.14.

The variability of the undrained shear strength was assumed to be characterized by a log-normal distribution with three parameters: mean, μ_{c_u} , standard deviation, σ_{c_u} , and spatial correlation length, $\theta_{m_{c_u}}$. The mean was held constant at 100 kN/m², while the standard deviation and spatial correlation length were varied. A general conclusion of this study is that the bearing capacity of a heterogeneous soil will on average be less than the Prandtl solution predicted by homogeneous soil with its strength given by the mean value. For instance, for a coefficient of variation, COV of 50% the N_c value is closer to 4, corresponding to a reduction of 20% on the Prandtl solution. In Figure 3.1 it can see the estimated mean bearing capacity factor, mN_c , as a function of the statistical parameter of the undrained shear strength, the coefficient of variation, COV and the spatial correlation length, θ in comparison with the results obtained by the Prandtl solution for a homogeneous soil.

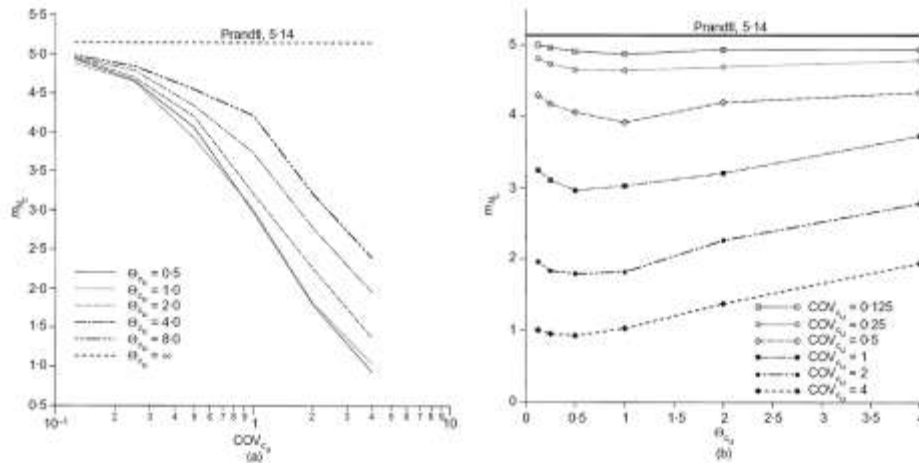


Figure 3.1 Estimated mean bearing capacity factor, mN_c , as a function of undrained shear strength statistics, COV and θ . (Taken from Griffiths & Fenton (2001)).

Griffiths et al. (2002) perform probabilistic studies of bearing capacity for a rough footing condition. Following a parametric study, the mean shear strength was held constant while the coefficient of variation and spatial correlation length of shear strength were varied systematically. The results of the probabilistic study of the rough footing were compared with the previous results obtained for the smooth footing. As a result of the probabilistic study, they concluded that there is a 50% of probability that the bearing capacity of a rough footing resting on a soil with spatially random shear strength is less than the deterministic bearing capacity calculated the mean value of the shear strength. Furthermore, they found that as the variance of the shear strength of a spatially variable soil increases, the symmetry of the failure mechanism disappears and goes one way or to the other. This behavior can be seen in Figure 3.2. Also, they found that the influence of the coefficient of variation and the correlation length of the shear strength on the mean bearing capacity is similar for rough and the smooth foundations.

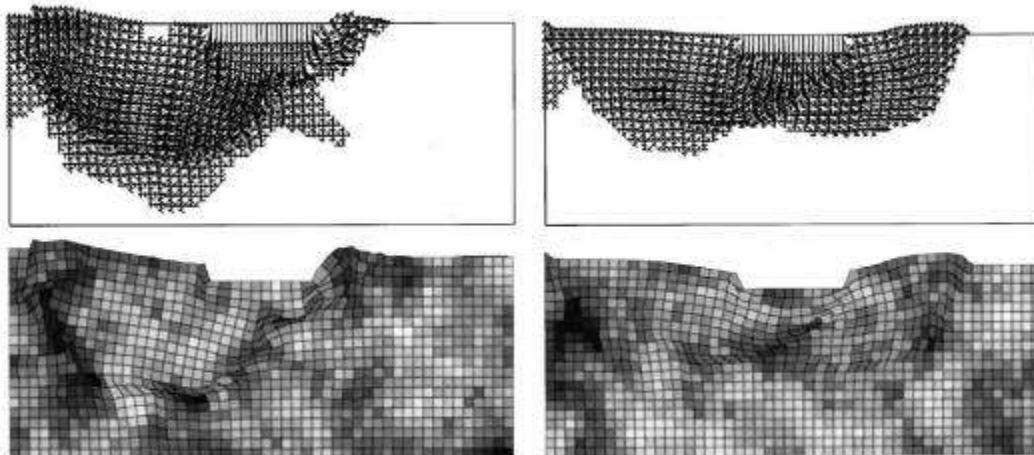


Figure 3.2 Typical deformed meshes and a corresponding plot of displacement vectors for two realizations (rough footing). (Taken from Griffiths & Fenton (2002)).

Fenton & Griffiths (2003) extend their studies to evaluate the amount to which spatial variability and cross-correlation of the soil properties (shear strength, c and friction angle, ϕ) affect the bearing capacity. They used a two-dimensional numerical model to simulate a strip foundation; the spatial variability of the soil was modeled using random field theory and elastoplastic finite element analysis. They found that a geometric average of the soil shear strength under the foundation within a domain with plastic deformations may be used as a characteristic value of soil shear strength, this domain has a depth of B and length of $5B$, B as the foundation width. Also, they found that using a correlation length equal to B results in the lowest value of the bearing capacity. Therefore, when sufficient data are not available, it can be used as a conservative value in calculations.

Popescu et al., (2005) studied the effects of random heterogeneity of soil properties on bearing capacity and differential settlements of a rigid strip foundation placed at ground level on an over-consolidated clay layer. They used a Monte Carlo Simulation approach followed by a finite element analysis for each simulated sample function. The undrained shear strength of soil, C_u , and the elastic modulus, E were considered variable (modeled as homogeneous random fields). Poisson's ratio was assumed constant and equal to 0.49. The deformation modulus E was supposed to be perfectly correlated with the undrained shear strength via the relationship $E = \alpha C_u$ with α between 300 and 1500. The parameters of the undrained shear strength of soil were: coefficient of variation, COV ranges between 0.1 and 0.4; horizontal correlation length, L_h varies between 4 and 16 m, and vertical correlation length, L_v held constant with a value of 1 m; probability distribution function, PDF used Gamma (positively skewed) and Beta (symmetrical). The finite element analysis was performed using ABAQUS/Standard code assuming perfectly plastic behavior of the soil material with Tresca's yield criterion; an increasing vertical displacement was applied at the center of the foundation; a semi-rough contact was assumed at the soil-foundation interface, and free rotations were allowed for the foundation.

The most important conclusion of this work is that the inherent spatial variability of soil properties can modify the basic form of the failure mechanisms and it changes from one realization to another; as a consequence, there is no typical failure mechanism. This modification of the failure mechanisms not only affects the value of the ultimate bearing capacity, reducing substantially compared to the corresponding deterministic (homogeneous soil) case, but also it can change the footing rotations (differential settlements). Figure 3.3 shows an example of the effects of the spatial variability of the soil property on the value of the bearing capacity and the rotation generated in the footing.

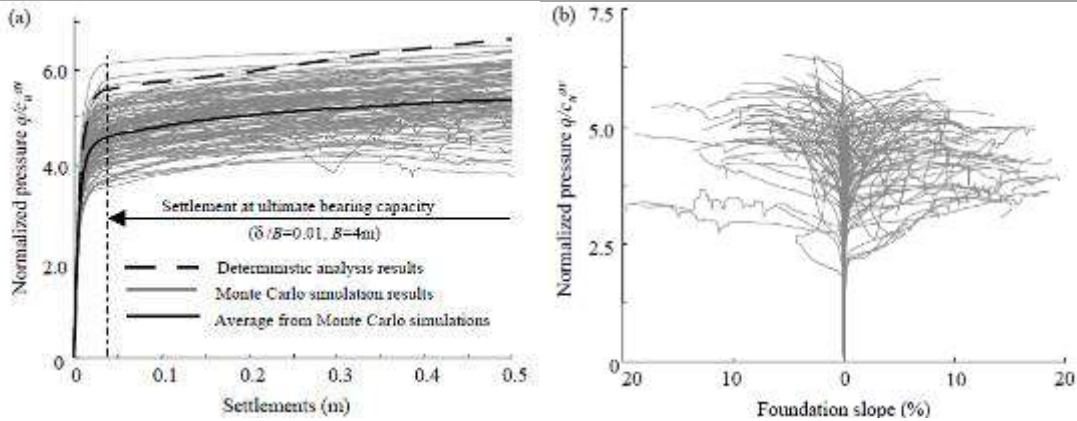


Figure 3.3 Monte Carlo simulation results involving 100 sample functions for the case COV = 40%, $L_x = 5$ m: a) normalized bearing pressures vs. settlements, b) normalized bearing pressures vs. footing rotations. (Taken from Popescu et al. (2005)).

Soubra et al., (2008) performed a study to evaluate the effect of the spatial variability of the soil properties on the ultimate bearing capacity of a vertically loaded shallow strip footing. They merge Monte Carlo Simulation approach with a numerical simulation using the Lagrangian explicit finite difference code FLAC^{3D}. In their study, the shear strength and the angle of internal friction were modeled as non-normal anisotropic random fields and were considered independent. A conventional elastic-perfectly plastic model based on the Mohr-Coulomb failure criterion was used to represent the soil. The shallow strip has a width $B=2$ m and the mesh soil domain of $15B$ in width and $2.5B$ in depth. Again, the main finding made by the authors was that the inherent spatial variability of the soil shear strength parameters modified the basic form of the failure mechanisms drastically (Figure 3.4); furthermore, differential settlements appear in the spatially varying soil leading to a rotation of the footing. In the same way, the average bearing capacity of the spatially random soil is lower than the deterministic value obtained for a homogeneous soil, and a critical case occurred when the correlation length is equal to the footing width. Finally, they found that the average value of the ultimate footing load capacity is more sensitive to the variation of the horizontal correlation length than the vertical one.



Figure 3.4 Deformed mesh corresponding to a realization of the random soil (Taken from Soubra et al. (2008)).

Cho & Park (2010) also integrate a commercial finite difference method and random field theory into a probabilistic analysis to study the effect of spatial variability of cross-correlated shear strength parameters (c , ϕ) on the bearing capacity of a strip footing. An exponential autocorrelation function that considers different correlation lengths in the vertical and horizontal directions

was used to describe the spatial variability of the soil. They conclude that the cross-correlation between shear strength and friction angle and the vertical correlation length significantly affects the behavior of the bearing capacity.

Kasama & Whittle (2011) implement a midpoint method for representing the inherent spatial variability of undrained shear strength in Monte Carlo simulations of bearing capacity strip footing on clay using numerical limit analyses. Like Griffiths et al. (2002), the mean shear strength was held constant while the coefficient of variation and spatial correlation length were varied systematically. The statistical assumptions on clay were held identical to the values used by Griffiths et al. (2002) to compare both results. They also conclude that the spatial variability reduces the bearing capacity of the footing in comparison to a deterministic calculation based on the mean undrained shear strength.

Al-Bittar & Soubra (2012) proposed a probabilistic model to calculate the probability density function (PDF) of the ultimate bearing capacity of a strip footing resting on a spatially varying (c, ϕ) weightless soil. The shear strength and friction angle were considered as two anisotropic non-Gaussian cross-correlated random fields. The significant contribution of this study is that they used the sparse polynomial chaos expansion (SPCE) methodology against the classical Monte Carlo Simulation (MCS) method to determine the PDF of the system response. It significantly reduces the simulation time. They found that the variability of the ultimate bearing capacity increases with the increase in the coefficients of variation of the random fields. Furthermore, a narrow PDF of the ultimate bearing capacity was obtained when the correlation length (L_v or L_h or $L_h = L_v$) decrease. The ultimate bearing capacity presents a lower value when the autocorrelation length is nearly equal to the footing width.

3.2 Conclusion

The effect of the spatial variability of soil properties on the response of the bearing capacity of a shallow foundation has received considerable attention in recent years. Some studies have considered the variability of only one strength parameters (shear strength, c), and others have examined the variability of both parameters (shear strength, c and friction angle, ϕ) as cross-correlated. The principal conclusions of these studies are: (i) the inherent spatial variability of the soil shear strength parameters modified the basic form of the failure mechanisms drastically; (ii) the average bearing capacity of the spatially random soil is lower than the deterministic value obtained for a homogeneous soil; (iii) a critical bearing capacity value occurred when the correlation length is equal to the footing width; (iv) differential settlements appear in the spatially varying soil leading to the rotation of the footing; (v) the average value of the ultimate footing load capacity is more sensitive to the variation of the horizontal correlation length than the vertical one.

4 CENTRIFUGE MODELING

In this section, an overview of the centrifuge modeling is presented as well as an example and a summary of the basic scaling laws. Then, it is present a description of the different types of material used for centrifuge modeling. Next, the methodologies used to consolidate are explained briefly. Finally, the mini-geotechnical centrifuge of Universidad de los Andes, where the experimental task of this thesis is undertaken is described.

4.1 Principles of centrifuge modeling

Geotechnical centrifuge modeling is a technique used to reproduce and study several geotechnical problems such as the strength, stiffness and capacity of shallow and deep foundations, stability of slopes, earth retaining structures, tunnel stability and seawalls, settlement of embankments among others. Geotechnical materials such as soil have nonlinear mechanical properties that depend on the effective confining stress and stress history. To study the behavior of a geotechnical problems is necessary to produce identical self-weight stresses in the model (reduced scale) and prototype (full-scale). It can be done by placing the model in a centrifuge that applies an increased "gravitational" acceleration to the physical model (Taylor, 1995). Centrifuge model tests provide data to improve our understanding of basic mechanisms of deformation and failure; furthermore, it can give useful benchmark to verify numerical models.

4.2 Basic scaling laws

The scaling laws are used to establish the relationships existing between the model and the prototype. In a geotechnical centrifuge test, the fundamental scaling laws are derived guarantying the stress similarity between the model and the corresponding prototype. For instance, if a model is subjected to an inertial acceleration field of N times Earth's gravity the vertical stress at depth h_m will be identical to that in the corresponding prototype at depth h_p were $h_p = Nh_m$; this is the basic scaling law for centrifuge modeling (Taylor, 1995). A summary of the main scaling laws used in geotechnical centrifuge is presented in Table 4.1. The scaling law for time, $1/n^2$, applies for diffusion problems, but if the problem involves wave propagation, earthquakes, for instance, the scaling law for time is $1/n$.

Table 4.1 Some common scaling laws for centrifuge test.

Parameter	Scaling factor	Parameter	Scaling factor
Linear dimension	$1/n$	Gravity	n
Area dimension	$1/n^2$	Force	$1/n^2$
Volume dimension	$1/n^3$	Time (diffusion)	$1/n^2$
Stress	1	Mass	$1/n^3$
Strain	1	Unit weight	n
Density	1	Velocity	n

4.3 Soil samples materials

Soil samples for centrifuge model can be made by undisturbed soils; however, working with these kinds of samples can be problematic since they can be contaminated with elements such as roots, rock fragments, fissures; furthermore, drain potential trajectories that could appear in the natural soil, which remain outside the scale of the model and hence increase the uncertainty of the analysis. These undesirable characteristics, present in undisturbed soils, are removed by the useful process performed in the laboratory mixing the soil at a water content of twice the liquid limit and then consolidating the soil at the field stress. These resulting samples are called remolded re-constituted samples.

On the other hand, the use of commercially available bulk materials like kaoline and bentonite have been used extensively to create clay centrifuge models due to their well-known properties and his similarity behavior to natural clay. For instance, Mair (1979) used Spestone and Speswhite kaolin supplied by English China Clays Ltd. in his Ph.D. research; Almeida and Parry (1985) used Speswhite kaolin to test in centrifuge a small vane and a cone penetrometer; Andersen et al., (2005) also used Speswhite kaolin to study the penetration of suction anchors performing centrifuge tests; more recently, Zhang et al., (2013) used kaolin to test a combined CHM loading apparatus for a geotechnical drum centrifuge. Nowadays, is common to use mixes of kaoline and bentonite especially if the research requires simulating a broad range of plasticity clays, which is the case for this work.

4.4 Preparation of soil

Various procedures have been used to prepare normal consolidated artificial soft soils samples. These procedures involve two major phases: one is the slurry preparation, and the other is the consolidation process. The slurry preparation is made up by mixing powder bulk material once or twice times the liquid limit of the material. This procedure can be done under vacuum for about two hours to de-air the slurry and create a smooth slurry, which latter is subjected to the consolidation process. The purpose of the consolidation process is to generate the targeted profile of pre-compression stress with depth; this process can be carried out using different techniques.

These techniques can be classified according to the stress profile achieved either uniform consolidation with depth or linear variation with depth.

4.4.1 One dimensional compression or oedometric consolidation

This technique is performed under normal gravity of $1g$, and the procedure is equivalent to the standard consolidation, in which the load is applied in steps increasing the load when reaching the required compression stress. The process is easily monitored by measuring the vertical settlement of the consolidometer piston or by measuring the amount of pore fluid expelled from the sample. This consolidation technique is useful to create a uniform consolidation pressure with depth.

4.4.2 Centrifuge consolidation technique

Another possibility is using the centrifuge to consolidate the soil. A linear variation of vertical stress with depth can be achieved spinning the slurry at the required centrifuge acceleration until reaching the primary consolidation. However, this procedure required long periods of continuous centrifugation which can present operation difficulties and expensive cost (Kimura et al., 1984; Schofield, 1995; Robinson et al., 2003; Ilyas et al., 2004).

4.4.3 Seepage consolidation technique

Seepage consolidation technique also creates a linear variation of the vertical stress with depth. It is achieved by applying a downward hydraulic gradient to the sample (Zelikson, 1969; Schofield, 1995). In the conventional form of this method, the seepage stresses are generated by applying high water pressure to the top of the clay layer, while the water at the bottom remains close to the atmospheric pressure (Zelikson, 1969; Imai, 1979).

However, the method often fails because of hydraulic fracturing of the clay along the corners, when rectangular containers are used. Robinson et al. (2003) proposed a method of achieving hydraulic consolidation by the application of negative pore water pressure (suction) at the bottom of the clay layer, which avoids the hydraulic fracturing problem. Furthermore, to reduce the time they recommended two-stage procedure for the preparation of normally consolidation clay. For the first stage, the sample is subjected to seepage consolidation under normal gravity condition; then, in the second stage, the specimen is transferred to the centrifuge to undergo the final consolidation.

In this work, consolidation is achieved in two stages: the first stage, the samples are subjected to one-dimensional compression or oedometric consolidation, in the second stage, the samples are transferred to the geotechnical centrifuge until reach total consolidation.

4.5 Mini geotechnical centrifuge of Universidad de los Andes

4.5.1 Mini geotechnical centrifuge

This small size centrifuge is housed in a circular chamber of 1.7 m in diameter by 0.7 m in height. The mini bean centrifuge has a nominal radius of 56.5 cm and is capable of accelerating a 4 kg model package to 400 g. The container has a depth of 7 cm, a width of 14 cm and a height of 12 cm. The hydraulic rotary joint provides four hydraulic or pneumatic slip rings to the test package. A wireless data acquisition system located at the rotation center of the centrifuge send the measured data, at specified time intervals, to an external computer. Also, a camera with LED lighting provides in-flight monitoring (Figure 4.1).

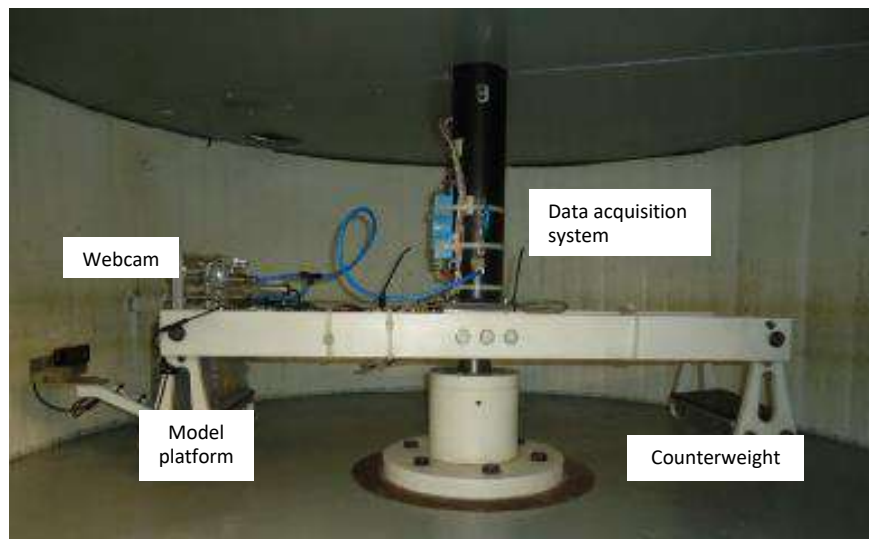


Figure 4.1 Mini geotechnical centrifuge of Universidad de los Andes.

4.5.2 Pneumatic consolidometer

This device includes the container box; a loading piston; a linear displacement transducer (LVDT); and a load cell. The load and displacement were measured and stored systematically at fixed time intervals. The consolidation process is monitored by using the Asaoka (1978) method for the prediction of consolidation time.

The Asaoka's method is performed drawing the settlements in equal intervals of time as shown in Figure 4.2. In this figure, each point of the plot is represented by the coordinates $(\rho_{k-1}; \rho_k)$; where ρ_k is the current settlement and ρ_{k-1} is the previous settlement. The primary consolidation, at a constant external load, is reached when the settlement's plot (continue line) intercepts the reference line (dotted line), which had a 45° slope. The crossing of both lines means that the difference between the current settlement and the previous settlement is negligible; consequently, the primary consolidation is reached. Figure 4.3 shows the mini-pneumatic consolidometer of Universidad de los Andes.

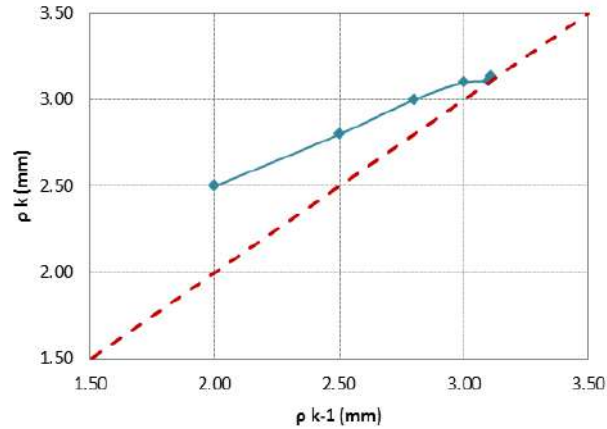


Figure 4.2 Graphical method of settlement prediction (Adapted Asaoka (1978)).

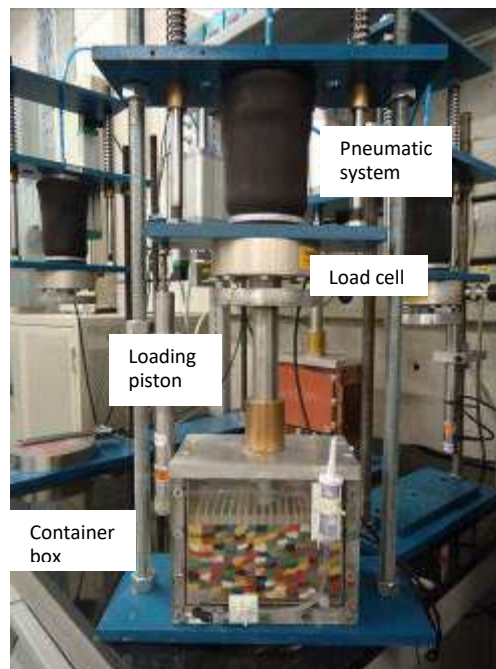


Figure 4.3 Mini-pneumatic consolidometer of Universidad de los Andes.

4.1 Conclusion

Geotechnical centrifuge modelling is an advanced physical modelling technique for simulating and studying geotechnical problems. Particularly, mini geotechnical centrifuge, i.e. centrifuges that have less than 60 cm of radius, enables to model complex geotechnical problems which requires the realization of a considered number of tests. Kaoline and bentonite have proven to be the most recommended materials for building soft soils models, and the mixture of the two allows modeling a wide variety of clays regarding its Atterberg properties. The combinations of oedometric and centrifuge consolidation techniques is the most efficient since it creates a uniform consolidation pressure with depth in a short period of time allowing the creation of a large numbers of models.

5 PHYSICAL MODELING OF SOIL VARIABILITY

This section aims to present the new technique to prepare scaled soil models with controlled variability by using the geotechnical centrifuge. The development of the new technique took a lot of time and here is going to present a summary of this development. In a first stage, the models were built in two layer, and in the final stage the models were built in one layer. From here on, these two stages will be referred to as two-layers stage and one-layer stage to better explain the development of the new technique. In two-layers stage, three isotropic heterogeneous samples were constructed, and indirect measurements of the undrained shear strength were performed. In one-layer stage, six homogeneous models and three heterogeneous models were built, direct and indirect measures of the undrained shear strength were analyzed. In this section, the construction methodology is explained, and the modeling results of the two stages are discuss.

5.1 Introduction

The behavior of fine soils can be characterized by:

- (i) the soil intrinsic characteristics, which depend on the mineralogy (usually captured by the Atterberg limits), and
- (ii) the soil state properties (i.e., void ratio, water content, strength, compressibility, etc.) that result from combining the intrinsic soil characteristics with the stress history.

The major benefit of centrifuge modeling is the possibility of reproducing stress fields that are similar to those in the field. For this reason, to reproduce soil variability that approaches field variability in a geotechnical centrifuge, the following steps are necessary:

- (i) reproducing the variability in mineralogy; for example, reproducing the variability in the liquid limit, and then
- (ii) reproducing the history of field stresses using either an oedometer or a geotechnical centrifuge or combining both methods.

In this work, a physical 2-D soil model (120 mm x 80 mm) that incorporates a previously defined random field in Section 2.2 will be constructed. The variability will be defined regarding the liquid limit. Thus, the soil will be described by a mesh of equally sized elements for which a liquid limit, P , is assigned randomly according to the properties of the random field with correlation length, L_T . In addition to the correlation length, a random field is also characterized by the mean and standard deviation of the liquid limit.

5.2 Random field generation

In this work, the random field generation method proposed by El-Kadi and Williams (2000) was used to reproduce the variability of the liquid limit of artificial samples of soil. This method applies the covariance matrix decomposition technique to generate 2-D autocorrelated distributions of

the parameter, P ; and it is based on two main assumptions: (1) the parameter P has a normal or lognormal distribution within the space of interest, and (2) P is characterized by an exponential autocorrelation function. The first assumption defines the process of determining probable values of P for each element of the space, whereas the second explains how the values of P at different locations are correlated. For this study, we assume that the random variables conform to the normal distribution function (Lumb, 1966).

For a mesh divided into m cells of the same size, the vector of liquid limit \mathbf{W}_L is estimated as follows:

$$\mathbf{W}_{L_n} = \mathbf{S} \cdot \boldsymbol{\varepsilon} + \boldsymbol{\mu}_n \quad (5.1)$$

where \mathbf{W}_L = a $[m \times 1]$ vector containing the liquid limit of each cell, \mathbf{S} is the $[m \times m]$ autocorrelation matrix, $\boldsymbol{\varepsilon}$ is a $[m \times 1]$ vector containing standard normally distributed values (i.e., with mean 0 and standard deviation 1), $\boldsymbol{\mu}$ is a $[m \times 1]$ vector containing the mean values of liquid limit, and the subscript n refers to the results for the n -th realization of the random field. The autocorrelation matrix, \mathbf{S} , can be found from:

$$\mathbf{C} = \mathbf{S}\mathbf{S}^T \quad (5.2)$$

where \mathbf{C} = the covariance matrix of the field, which has to be positive definite. The matrix \mathbf{S} can be determined from \mathbf{C} by using the Cholesky decomposition matrix technique, which decomposes a symmetric and positive definite matrix, such as \mathbf{C} , into a lower triangular matrix. The covariance matrix \mathbf{C} is defined as:

$$C_{i,j} = \sigma^2 \rho_{i,j} \quad (5.3)$$

where $C_{i,j}$ = the correlation function between the spatial points i and j , σ is the standard deviation of the liquid limit in the field, and $\rho_{i,j}$ = the autocorrelation function between points i and j . In this work an exponential form of the correlation function proposed by Vanmarcke (1977) was selected:

$$\rho_{i,j} = \exp \left[- \sqrt{ \left(\frac{d_{i,j}^x}{L_x} \right)^2 + \left(\frac{d_{i,j}^z}{L_z} \right)^2 } \right] \quad (5.4)$$

where $d_{i,j}^x$ and $d_{i,j}^z$ = are the horizontal and vertical components of the distance between the points i and j , and L_x and L_z are the correlation lengths in the x (i.e., horizontal) and z (vertical) directions, respectively.

In summary, once the input parameters of the field are known (μ , σ , L_x and L_z) the matrix of auto-correlation can be found $\rho_{i,j}$ (Eq. 5.4), and from it the matrix covariance $\mathbf{C}_{i,j}$ (Eq. 5.3). Applying the Cholesky decomposition, matrix \mathbf{S} can be defined from matrix \mathbf{C} . Finally; the matrix \mathbf{S} can be used in Equation 5.1 to determine the values of liquid limits within the random field (matrix \mathbf{W}_L).

5.3 Parameters of the random field

Plasticity is an essential characteristic for soil classification and to evaluate the soil mechanical behavior. In this study, the mean, the standard deviation and the scale of fluctuation of the liquid limit were estimated based on data of the Seismic Microzonation of Bogota, Colombia (1997). In the seismic micro-zonation, 23 boreholes were performed at depths of 20 m to 250 m. However, for this work, we considered only the highest plasticity zone, which is located in the north part of the city. In this zone, six bore-holes were analyzed, and the mean and the COV of the limit liquid were 168% and 28%, respectively. Table 5.1 compares these results with some values reported in the literature. Note that the mean and the COV values for clay in Bogota are consistently larger than the values reported by others authors. On the other hand, Bogota’s clay is ranked as one of the soils with the highest plasticity in the world.

Table 5.1 Inherent variability of liquid limit W_L .

Soil type	N° of studies	Property value		Property COV (%)	
		Range	Mean	Range	Mean
Clay, loam ^a	38	27 - 89	51	7 – 39	18
Ankara clay ^b	25	50 - 79	64	9 - 22	14
Bogota clay	6	155 - 184	168	18 - 40	28

^a Phoon and Kulhawy, 1999a ^b Akbas & Kulhawy, 2010

The vertical scale of fluctuation, δ_v , was estimated using the methodology described by Jones et al. (2002), which uses the behavior of the normalized variance under successive local averaging. The vertical scale of fluctuation estimated was 2.2 m. Note that again the results obtained for Bogota (Table 5.2) show that the scale of fluctuation is significantly narrower than the ranges reported by others authors.

Table 5.2 Vertical scale of fluctuation values of liquid limit W_L

Soil type	N° of studies	Scale of fluctuation m	
		Range	Mean
Clay, loam ^a	2	1.6 – 8.7	5.2
Ankara clay ^b	2	4.0 – 6.2	5.1
Bogota clay	6	1.3 – 3.2	2.2

^a Phoon and Kulhawy, 1999a ^b Akbas & Kulhawy, 2010

In this work, as mentioned above, three isotropic heterogeneous models were constructed to validate the repeatability and accuracy of the technique. The parameters chosen for the generation of the random field of the three models were: the vertical and horizontal scale of fluctuation (δ_v, δ_h) was 1.5 m; the standard deviation (σ) was 47%; the mean (μ) was 168%. It should be mentioned that the value chose for the vertical scale of fluctuation is not the estimated for Bogota clay (2.2 m) as the others parameters are. The selection of 1.5 m was due to a constructive reason that would be explained later in the bearing capacity test section.

Based on this information, the matrix decomposition technique was implemented in Matlab®, and three analytical random fields were generated. The model field space had a dimension of 14 cm in length and 8 cm in height and was divided into square elements of 1 cm. An example of a typical realization of the liquid limit random field within m=112 divisions is illustrated in Figure 5.1.

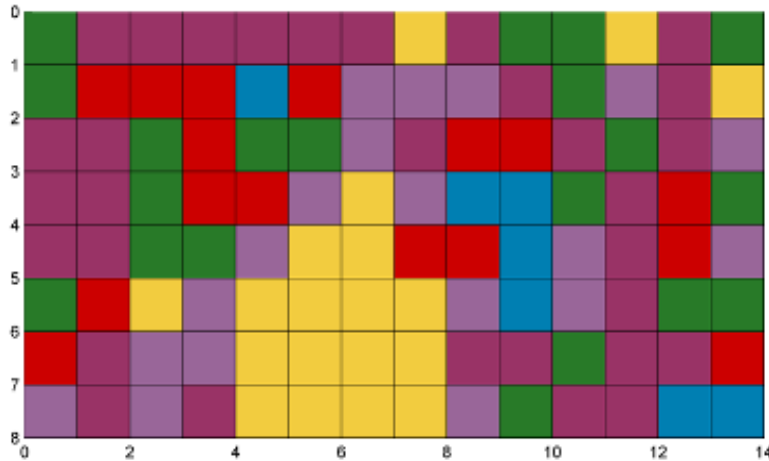


Figure 5.1 Example of a random field generation.

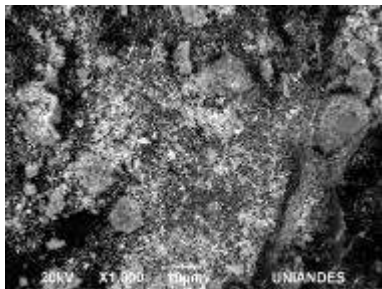
5.4 Properties analysis of homogenous mixed soils

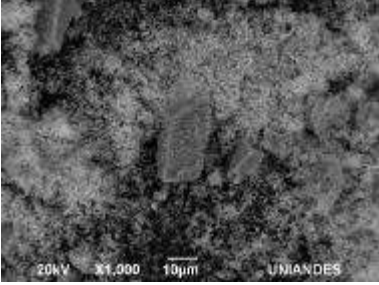
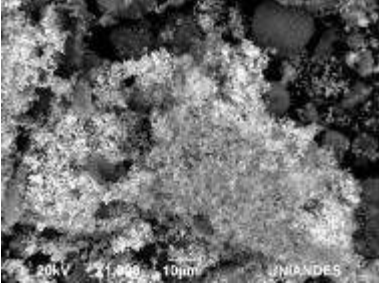
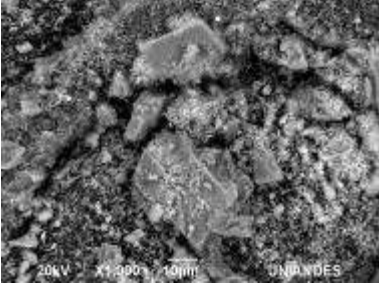
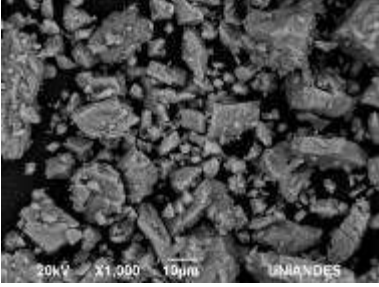
5.4.1 Basic properties of mixed soils

To capture the intrinsic soil variability, we prepared eight reconstituted homogeneous soils with a mixture of different percentages of kaolin and bentonite, with a water content of about 1.5 times the liquid limit. To differentiate the eight mixtures, we added an amount of colorants to each mixture. The composition of each colorant was studied by using a Scanning Electron Microscope, SEM. These results show that blue color has a different composition than the other colors, which are based mainly on iron oxides. Also, the iron proportion in green color is less than in red, yellow and black colors. Table 5.3 summarizes the compositions of the five colorants used in this work.

Table 5.3 Composition and Specific Gravity of the colorants.

	Composition %							
	Fe	O	Ca	Al	C	Si	S	Gs
Red	45	43	12					3.60
Yellow								



	40	51	9					3.39
Black	<hr/>							
	Fe	O	Ca	Al	C	Si	S	Gs
	43	28		2	22	4	1	2.88
Green	<hr/>							
	Fe	O	Ca	Al	C	Si	S	Gs
	18	44	17		21			3.04
Blue	<hr/>							
	Fe	O	Ca	Al	C	Si	S	Gs
		59	41					2.65

The eight mixtures were characterized in the laboratory. The Atterberg limits of the mixtures were measured using the Casagrande method. Figure 5.2 (a) and (b) show the measured Atterberg limits, and they change with bentonite percentage. According to the experimental results, there is a linear relationship between the liquid limit WL and the plasticity index PI, except for soil S6 (blue) for which a difference appears between the line and the experimental data; this disruption appears because of the colorant. This linear trend implies that mixing soils with constant intervals of bentonite content will produce soils having constant intervals of liquid limit. Figure 5.2 (c) presents the values of plasticity index PI at given liquid limit WL in the Casagrande Plasticity chart. As observed in the figure, the mixtures are classified as inorganic clays of high plasticity;

moreover, as the percentage of bentonite increases the relation between W_L and PI of the mixtures converges to the U- line.

Also, the mechanical properties of every mixture, which depend not only on the properties of the original soil but also on their state, were studied by performing triaxial and oedometer tests. All the tests were performed using the colored soils to include the effect of the colorant. Table 4 summarized the index and mechanical properties of the eight mixtures.

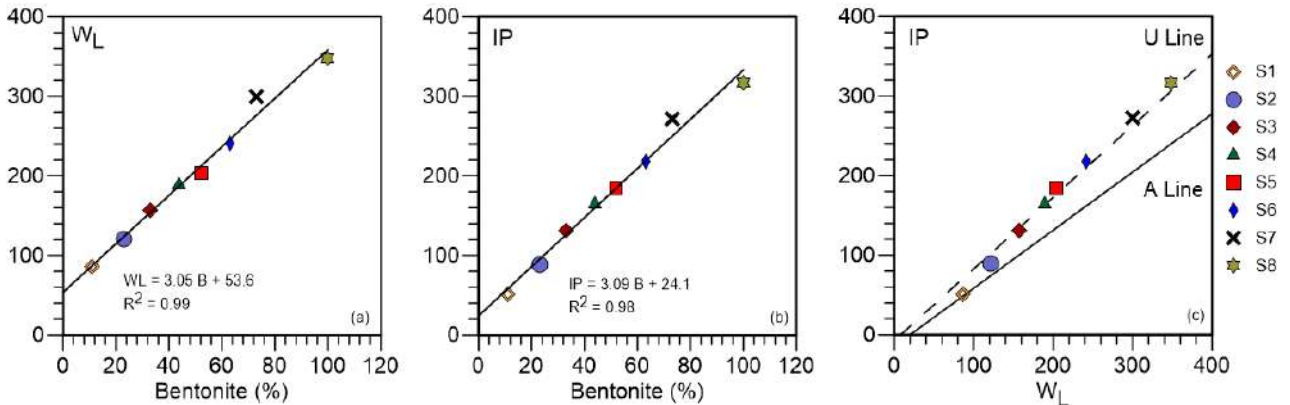


Figure 5.2 Basic relationship of homogeneous soils: (a) liquid limit and bentonite fraction (b) plasticity index and bentonite fraction (c) plasticity chart of the clay mixtures.

Figure 5.3 (a) presents the results of plastic and liquid limit of the eight mixtures, in this case, two trends appear, for liquid limits below 200 the plastic limit decrease as the liquid limit increase although for values of liquid limit above 200 an opposite trend is observed. To understand this behavior, it is essential to identify the effect of the colorant by performing tests on the mixtures without colorant. Figure 5.3 (b) shows the results of the specific gravity, G_s , for each mixture; it can see a decreasing trend as the limit liquid increase except for soil S5 (green), it could be explained by the colorant effect.

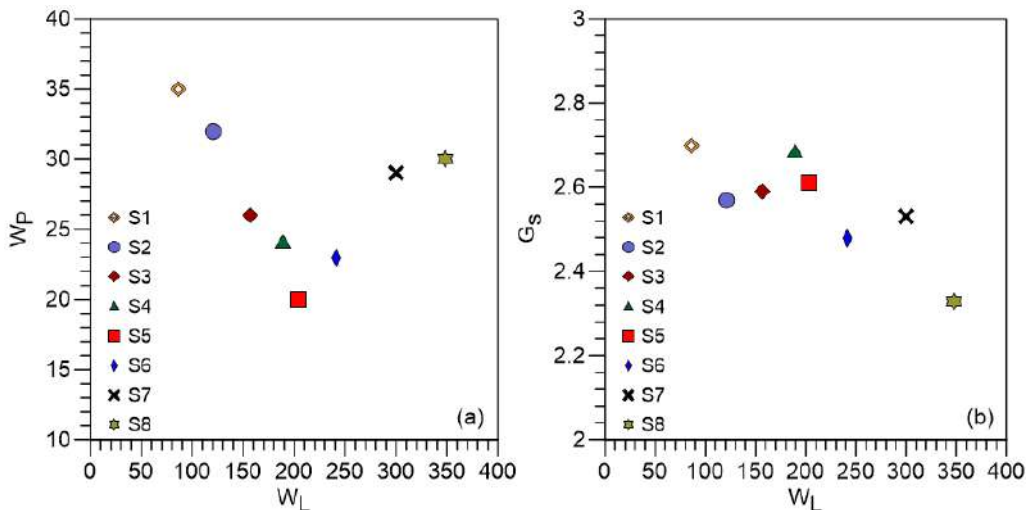


Figure 5.3 Basic relationships of soil properties: (a) relationship between liquid limit and plastic limit, (b) relationship between liquid limit and specific gravity.

5.4.2 Compressibility behavior of mixed soils

The oedometer test of the eight mixtures was performed at an initial water content of 1.5 times the liquid limit. The test was conducted following the standard procedure D2435/D2435M – 11. As specified by this standard, the initial effective vertical stress for oedometer tests should be six kPa; however, soils which are at initial water content higher than the liquid limit are often not stiff enough to support such an initial effective vertical stress, and consequently, soil squeezing occurs. For this reason, in this study, the first vertical stress applied was 0.7 kPa then gradually double load increased to 12.5 kPa. Appendix A shows the compression curves of the soil mixtures.

Figure 5.4 shows the compression curves of the eight soils; it can be seen that the compression curves can be grouped in three compressibility ranges as high (S8 and S7), medium (S6, S5 and S4) and low (S3, S2 and S1). Figure 5.5 indicates the relationship between the compression index, C_c and the liquid limit and the empirical relationship (Equation 5.5) obtained for this study with a correlation coefficient $R^2 = 0.9695$. Also, the well-known correlation for remolded soils presented by Skempton (1944) (Equation 5.6) is drawn in the figure; it can be see that kaolin-bentonite mixtures of this study show a high compressibility characteristic in comparison with the Skempton correlation, especially for soils S4 to S8.

$$C_c = 0.0105(W_L - 43) \tag{5.5}$$

$$C_c = 0.007(W_L - 10) \tag{5.6}$$

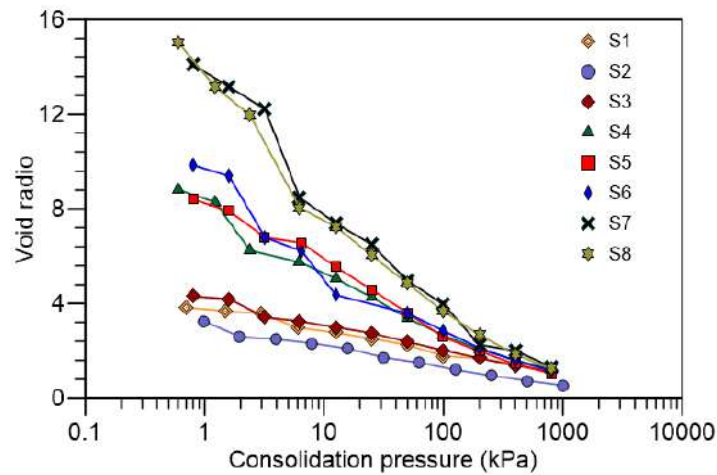


Figure 5.4 Oedometric test results: compression curves.

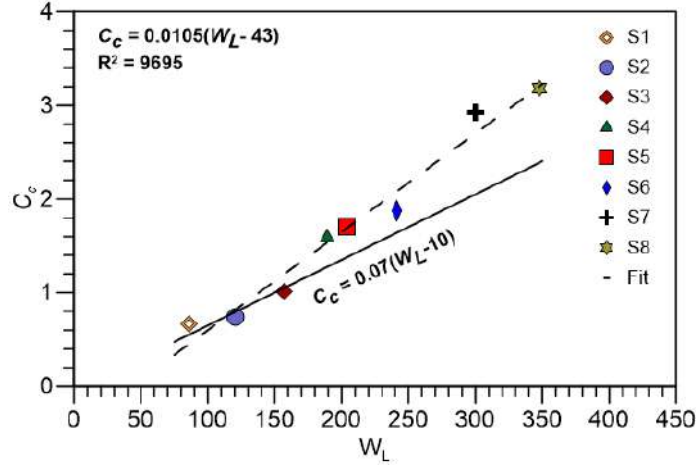


Figure 5.5 Oedometric test results: relationship between liquid limit and compression index.

The compression behavior of the eight mixtures was normalized base on the intrinsic concept proposed by Burland (1990) in which a normalizing index called the void index I_v was introduced for correlating the compression curves of various reconstituted clays with the same value at 100 kPa. The void index is defined as follows:

$$I_v = \frac{e - e_{100}^*}{C_c^*} \quad (5.7)$$

in which $C_c^* = e_{1000}^* - e_{100}^*$ is termed the intrinsic compression index, and e_{1000}^* and e_{100}^* are the voids ratios of the reconstituted clay at effective vertical stress of 100 kPa and 1000 kPa respectively. According to Burland (1990), the compression curves of reconstituted clays with an initial water content of 1.0 – 1.5 times the liquid limit can be approximated by a line, called the intrinsic compression line (ICL), characterized by the expression:

$$I_v = 2.45 - 1.285 \log \sigma_v' + 0.015(\log \sigma_v')^3 \quad (5.8)$$

It should be noted that the values of e_{1000}^* used in calculating I_v were those directly measured at a vertical stress of 100 kPa for all samples except for soil S2 which value was determined by interpolation of the compression line. On the other hand, the values of e_{100}^* were determined by extrapolation based on the compression line since the samples were subjected to a maximum effective vertical stress of 800 kPa.

Figure 5.6 compares the oedometer test results of the eight soils and the ICL (Equation 5.8). When the effective vertical stress is larger than 25 kPa, the experimental data form a line almost identical to the ICL proposed by Burland (1990). Within the range from 0.7 kPa to about 10 kPa,

the experimental results are to some degree scattered and lie a little above the ICL for soils S3 and S4, while soil S5 lie a little up the ICL. It is worth noting that soils S7 and S8 also lie up the ICL, but within the range from 0.7 kPa to about 3 kPa. Similar results about the scattered of date within this range were found by Hong et al., (2010) and Shi and Herle (2015), and it is not a surprise since Burland (1990) suggested that ICL should be used only for effective vertical stress ranging from 10 kPa to 4000 kPa.

Based on regression analysis, Burland (1990) proposed a relationship between e_L , C_c^* and e_{100}^* . Figure 5.9 and Figure 5.8 shows the relationship between e_L and the intrinsic compression parameter C_c^* and e_{100}^* respectively for the data of this study, and the two correlations proposed by Burland (1990) are also plotted. The data of the 8 soils of this study are not consisted with Burland's relationship, it can be explained since the 8 soils exhibit a high compressibility. The equations obtained for this study with a correlation coefficient $R^2 = 0.9715$ and are $R^2 = 0.9213$ are presented in Equation 5.11 and 5.12; also, they are plotted in the figures.

$$C_c^* = 0.256e_L - 0.04 \quad \text{Burland (1990)} \quad (5.9)$$

$$e_{100}^* = 0.109 + 0.67e_L - 0.089e_L^2 + 0.016e_L^3 \quad \text{Burland (1990)} \quad (5.10)$$

$$C_c^* = 0.417e_L - 0.4032 \quad (5.11)$$

$$e_{100}^* = 0.8837 + 0.2089e_L + 0.0207e_L^2 \quad (5.12)$$

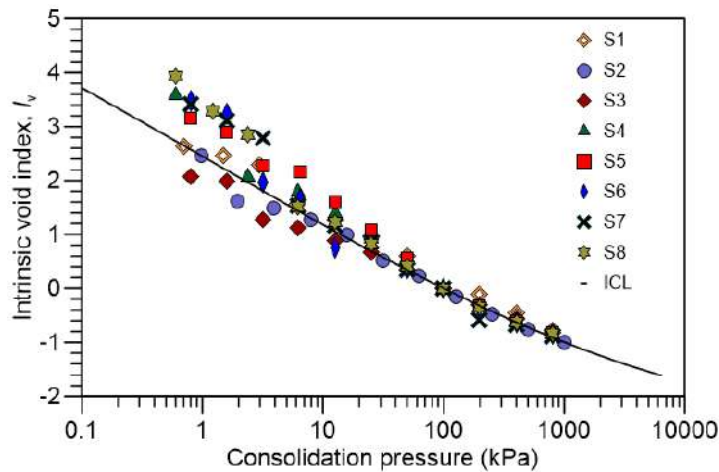


Figure 5.6 Intrinsic compression curves of the eight homogeneous soil mixtures.

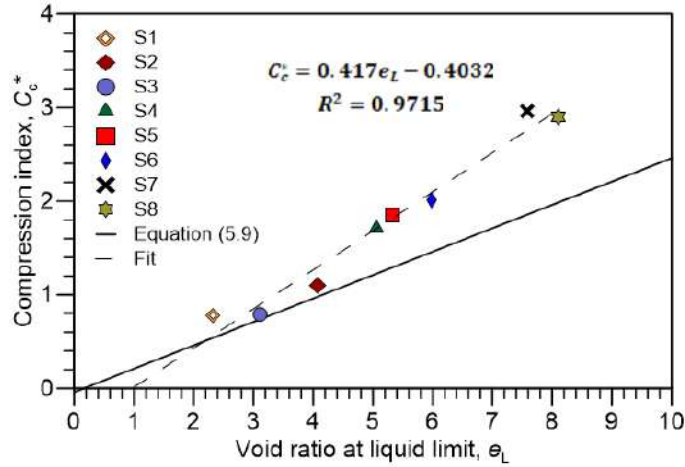


Figure 5.7 Relationship between e_L and the intrinsic compression parameter C_c^* .

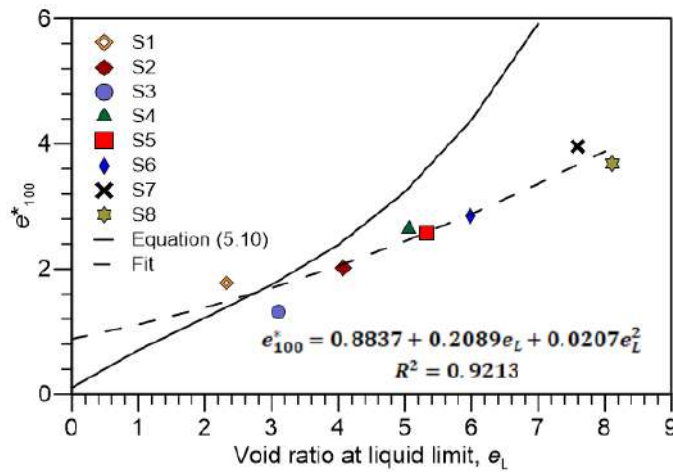


Figure 5.8 Relationship between e_L and the intrinsic compression parameter e_{100}^* .

5.4.3 Undrained shear strength behavior of mixed soil

Consolidated undrained triaxial compression tests with pore pressure measurements were performed for each mixture following the standard procedure ASTM D4767 - 11. Triaxial tests were carried out on soils prepared following the similar procedure for preparing the models; the process was as follows:

- i. First, a slurry was prepared at 1.5 times the liquid limit, then
- ii. the soil was consolidated in a tube of 75 mm diameter; this tube has lateral holes and porous plates at top and bottom to permits radial and vertical drainage simultaneously;
- iii. the soil in the container was consolidated to a vertical stress of 30 kPa; the consolidation phase was controlled using the Asaoka method;
- iv. once the soil was consolidated, it was extracted and trimmed to 50 mm to remove the soil affected by boundary friction; afterward,

- v. the soil was installed in the triaxial chamber and consolidated to reach the required confining stress; finally,
- vi. after achieving a B value of almost 0.98, the soil was tested.

Three tests with different confining stresses were performed to each mixture: 100 kPa, 200 kPa and 300 kPa, and the shear strength parameters were obtained assuming zero shear strength. Figure 5.9, Figure 5.10 and Figure 5.11 show the results of the tests. Appendix B shows consolidated undrained triaxial compression tests of the soil mixtures.

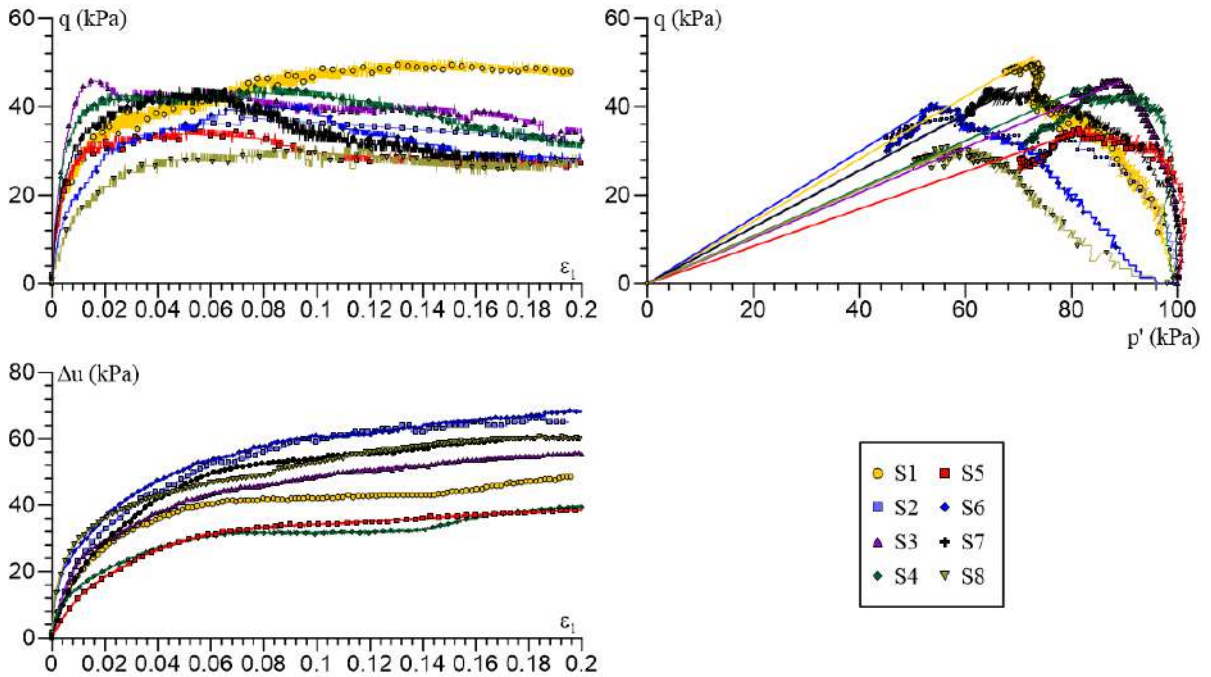


Figure 5.9 Triaxial compression tests result at 100 kPa confining stress.

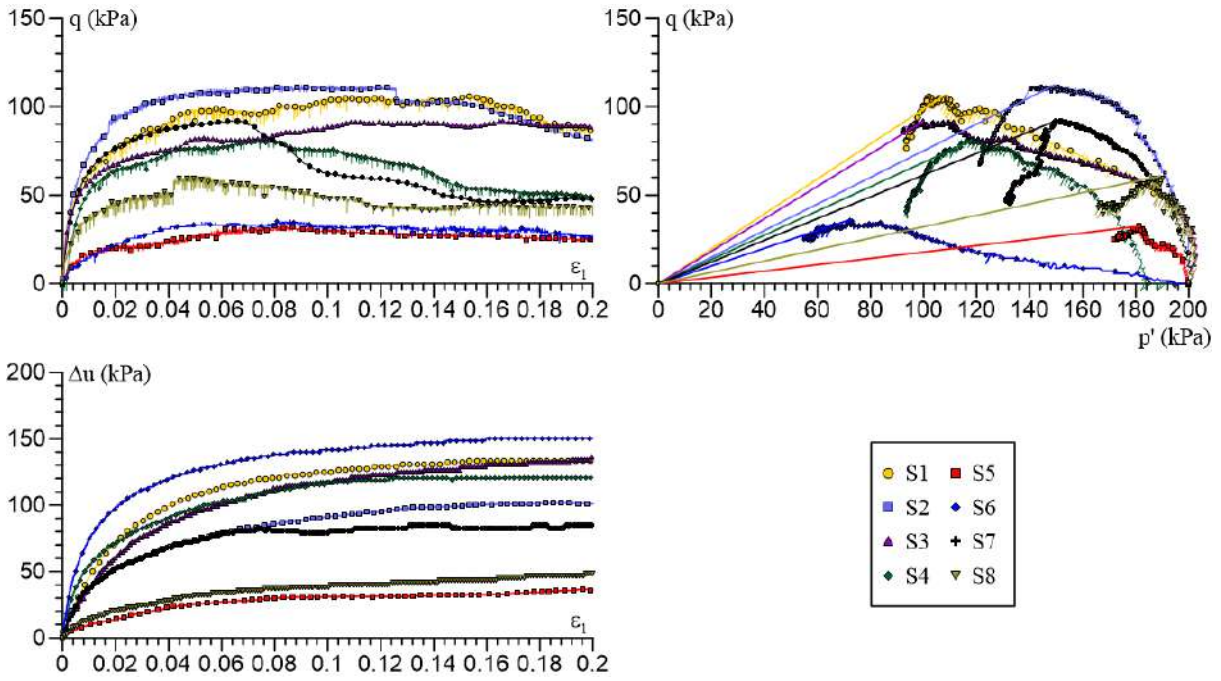


Figure 5.10 Triaxial compression tests result at 200 kPa confining stress.

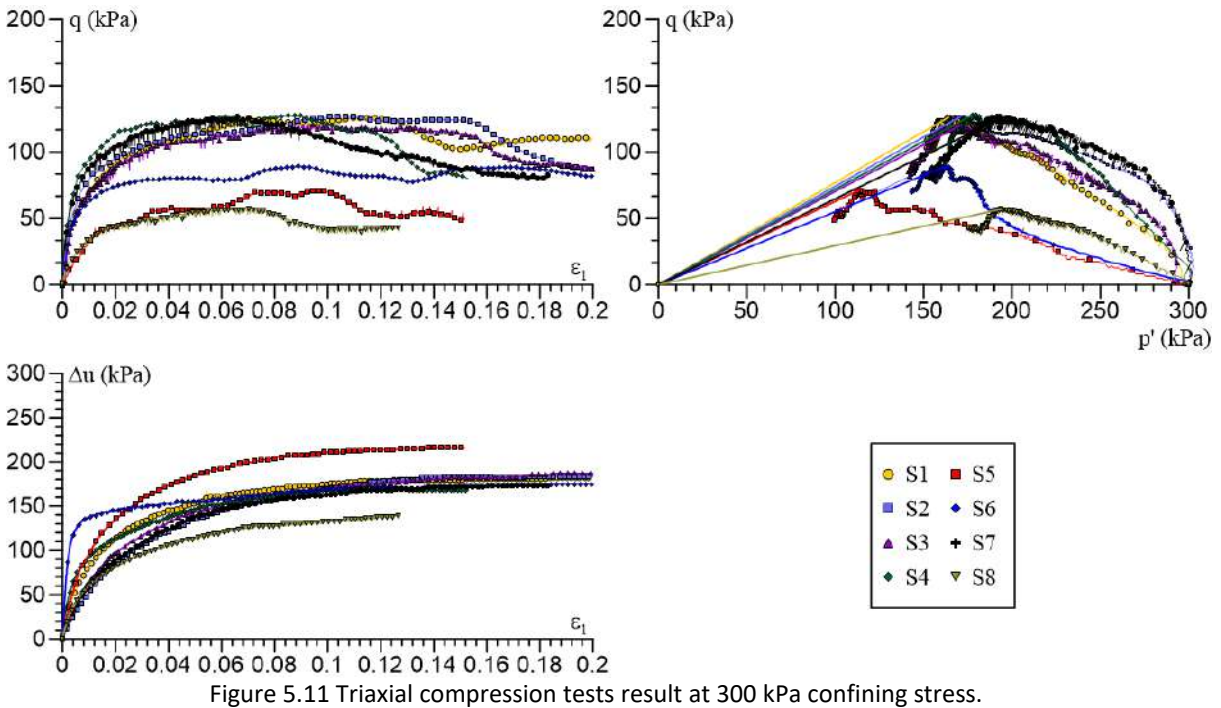


Figure 5.11 Triaxial compression tests result at 300 kPa confining stress.

Figure 5.12 shows the slope of the critical state line M for all the mixtures as well as their friction angle ϕ . Two decreasing trends are observed in these figures; however, a discontinuity is found for a value of 200 in the liquid limit. It can be explained due to the bentonite content of

mixtures since soils S6, S7 and S8 are the mixtures that have more than fifty percent bentonite content. Table 5.4 summarizes the basic and mechanical properties of the different mixture.

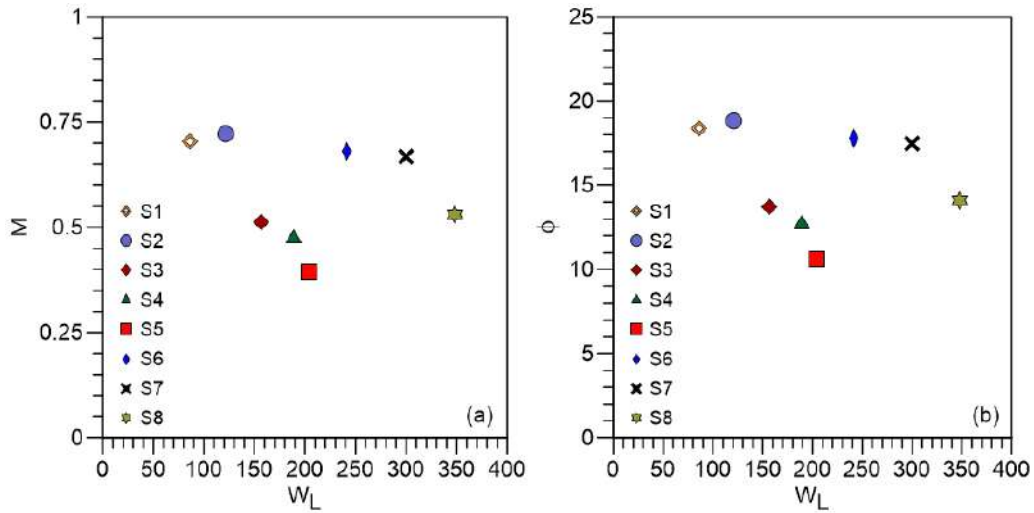


Figure 5.12 Triaxial CU results: (a) relationship between liquid limit and the critical line value, (b) relationship between liquid limit and the friction angle.

Table 5.4 Homogeneous soils properties.

Soil	Kaolin (%)	Bentonite (%)	Colorant (%)	Atterberg limits			Gs	Oedometer Test				Triaxial test (CU)		Cam Clay Parameters		
				WL (%)	WP (%)	IP		Gs	e _o ^{a,b}	C _c	C _s	C _v (cm ² /seg)	M	φ' (°)	λ	κ
S1	80	11	9 ^d	86	35	51	2.70	3.97	0.671	0.161	0.0044	0.705	18.4	0.345	0.085	0.737
S2	68	23	9 ^e	121	32	89	2.57	4.28	0.737	0.158	0.0018	0.721	18.8	0.506	0.051	0.740
S3	55	33	12 ^f	157	26	131	2.59	4.74	1.006	0.174	0.0018	0.513	13.7	0.713	0.115	1.241
S4	44	44	12 ^g	189	24	165	2.68	8.56	1.591	0.205	0.0014	0.475	12.7	0.888	0.068	1.201
S5	31	52	17 ^h	204	20	185	2.61	8.56	1.699	0.312	0.0016	0.393	10.6	1.023	0.155	1.738
S6	21	63	17 ⁱ	241	23	218	2.48	9.71	1.877	0.569	0.0016	0.680	17.8	1.093	0.174	1.896
S7	10	73	17 ^j	300	29	272	2.53	12.33	2.929	0.460	0.0013	0.667	17.5	1.260	0.116	1.793
S8	0	100	0	348	30	317	2.33	12.97	3.179	1.268	0.0011	0.530	14.1	1.475	0.119	2.024

^a Initial void ratio, ^b values are calculated from the results of oedometric test measuring the final void ratio and back calculating e at each loading stage, ^c specific volume in the critical state line at a mean effective stress value of 1 kPa, ^d yellow, ^e combinations of 2% red and 7% blue, ^f combinations of 4% red and 8% blue, ^g green, ^h red, ⁱ blue, ^j black.

Leroueil et al., (1983) proposed a correlation between undrained shear strength and the liquidity index, *IL*, based on the data collected in their study of the clay properties of eastern Canada, Equation 5.13. The correlation is given for liquidity index between 0.5 and 2.5. The relationship can be rewritten in terms of the consistency index, *IC*, Equation 5.14.

$$C_u (kPa) = \frac{1}{(IL - 0.21)^2} \quad 0.5 < IL < 2.5 \quad (5.13)$$

$$C_{ur} (kPa) = \frac{1}{(0.79 - IC)^2} \quad (5.14)$$

The liquidity index, IL is defined as follow:

$$IL = \frac{w - W_p}{W_L - W_p} \quad (5.15)$$

The consistency index, IC is defined as follow:

$$IC = \frac{W_L - w}{W_L - W_p} \quad (5.16)$$

where w = water content, W_p = plastic limit and W_L = liquid limit.

Two correlations were defined for this study base on the relationship between undrained shear strength and the consistency index, IC , given by Leroueil et al., (1983). The data uses to establish the relationships were extracted from the triaxial tests of the eight homogenous soils; Table 5.5 summarized the data. Two trends were identifying, the first trend corresponds to soils S1 to S4 whose mixes have less than 50% of bentonite, and the second trend to soils S5 to S8 whose mixes have more than 50% of bentonite. The two correlations proposed are defined in Equations 5.17 and 5.18. Figure 5.13 shows the two correlations (Equations 5.17 and 5.18), it can see a good agreement between the shear strength and the consistency index for soils S5 to S8 and moderate agreement for soils S1 to S4.

$$C_{ur} (kPa) = 4.0292e^{3.6193IC} \quad S1\ to\ S4 \quad (5.17)$$

$$C_{ur} (kPa) = 1.9505e^{4.1054IC} \quad S5\ to\ S8 \quad (5.18)$$

Table 5.5 Data used to define the relationship between undrained shear strength and the consistency index.

Soil	σ_c^1 (kPa)	C_u (kPa)	w_f^2 (%)	WL (%)	WP (%)	IC
1	100	25.7	62	86	35	0.46
	200	53.4	54	86	35	0.63
	300	63.1	55	86	35	0.61
2	100	18.8	77	121	32	0.49
	200	56.1	60	121	32	0.68
	300	63.5	55	121	32	0.74

3	100	22.9	82	157	26	0.57
	200	45.9	58	157	26	0.75
	300	60.3	53	157	26	0.79
4	100	22.4	96	189	24	0.56
	200	40.5	81	189	24	0.65
	300	64.2	69	189	24	0.73
5	100	17.7	111	204	20	0.51
	200	16.3	111	204	20	0.50
	300	36.1	82	204	20	0.66
6	100	20.5	115	241	23	0.58
	200	18.1	106	241	23	0.62
	300	44.7	80	241	23	0.74
7	100	22.2	123	300	29	0.65
	200	46.1	108	300	29	0.71
	300	63.6	87	300	29	0.78
8	100	15.7	193	348	30	0.49
	200	30.4	121	348	30	0.71
	300	28.4	117	348	30	0.73

¹ Confining stresses ² final water content

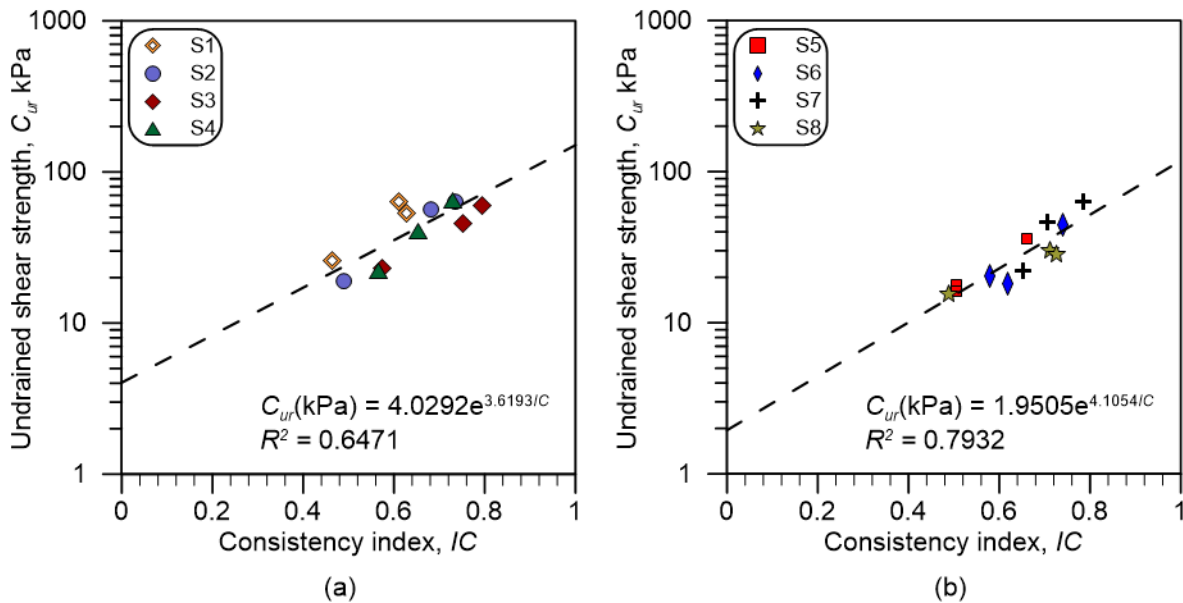


Figure 5.13 Relationship between shear strength of clay and consistency index: (a) soils S1 to S4 and (b) soils S5 to S8

An empirical approach proposed by Vardanega and Bolton (2011) for the prediction of the mobilization of the undrained shear strength, C_u , of natural clays tested from an initial isotropic state of stress is used in this study to estimated the strains and displacements that would be experienced the homogeneous mixtures at some mobilized shear stress, τ_{mob} , in relation to the

peak undrained shear strength, C_u . Vardanega and Bolton (2011) defined the shear strain, γ , and mobilized shear strength, τ_{mob} , as follow:

$$\gamma = 1.5\varepsilon \quad (5.19)$$

$$\tau_{mob} = 0.5q \quad (5.20)$$

where q is the deviator stress and ε the axial strain from the triaxial test. The ratio C_u/τ_{mob} called the mobilization factor, M_b , which is equivalent to a factor of safety on shear strength is also used by Vardanega and Bolton (2011) as border criteria of the analysis.

Figure 5.14 shows the curves of $1/M_b$ versus shear strain, γ , for the eight mixtures at the three confining stresses applied. Power laws were fitted to the data points that correspond to $1.25 \leq M_b \leq 5$ for each curve. This region is referred to by Vardanega and Bolton (2011) as the moderate-strain region, and the authors excluded low and high strain regions because of the difficulty to resolve low-strain measurements and the high degree of variability of the test curves immediately pre and post-peak.

Vardanega and Bolton (2011) used a power law model for curve-fitting the data of the tests as following

$$\frac{\tau_{mob}}{C_u} = A(\gamma)^b \quad (5.21)$$

where $\log(A)$ is the intercept of the best-fit linear through the stress-strain data plotted on log-log axes and b is the slope. The eight mixtures were fitted with power curves through the moderate-strain region, and the exponent b was determined for each test. This exponent was plotted against plasticity index, IP , limit liquid, W_L and plastic limit, W_p . The average b -value is 0.43 with a standard deviation equal to 0.10

The curves of $1/M_b$ versus shear strain, γ , were then normalized using a pivot strain taken as the strain level when $M_b = 2$, denoted as $\gamma_{M_b=2}$. This strain level was referred to by the authors as the mobilization strain. Therefore, Equation (5.21) is modified as follow

$$\frac{\tau_{mob}}{C_u} = 0.5 \left(\frac{\gamma}{\gamma_{M_b=2}} \right)^{0.43} \quad (5.22)$$

Figure 5.15 shows the measured values of plotted against those predicted using Equation 5.22. A linear regression was fit for all the data except for S1-100 kPa (confining stress); S3-200 kPa and S8-200 kPa, whose data remained as outliers. The fitted line is shown in the figure (black line) and it has a correlation coefficient $R^2 = 0.9144$. It can be seen that there is a good prediction since

the fitted line vaguely differs from the 45° line or equality line plotted red. Appendix C shows mobilization of the undrained shear strength, C_u , of the soil mixtures.

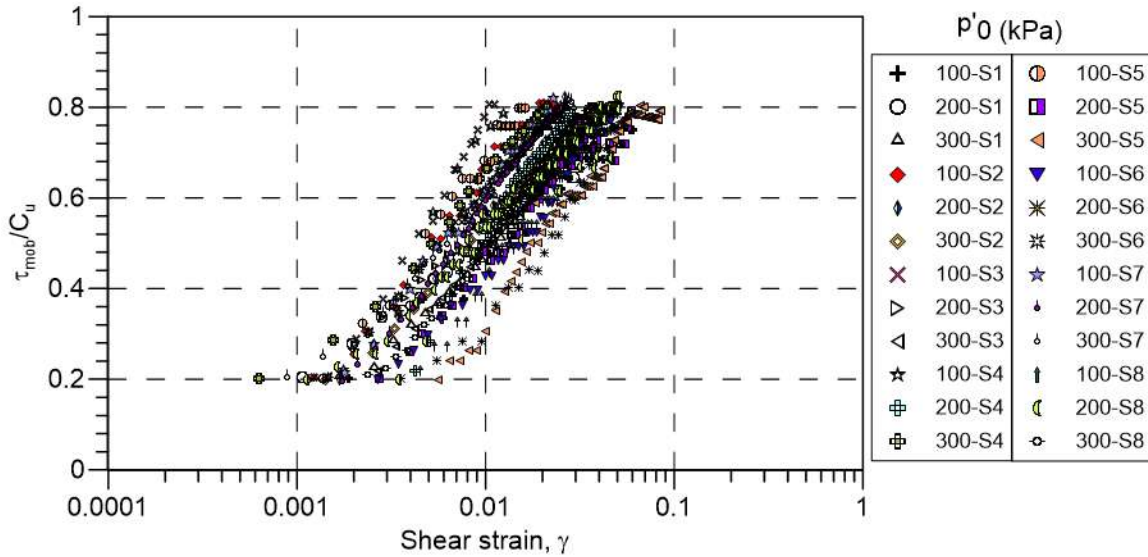


Figure 5.14 τ_{mob}/C_u versus shear strain, γ .

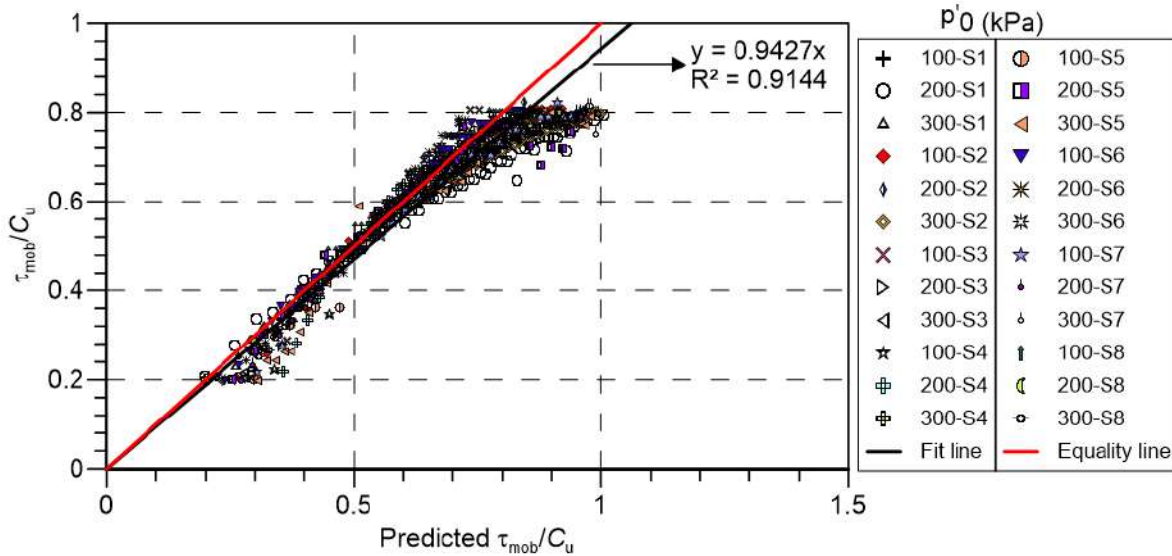


Figure 5.15 τ_{mob}/C_u versus Predicted τ_{mob}/C_u .

5.5 Development of the random soil construction technique: two-layers

In two-layers stage, three isotropic heterogeneous samples were constructed and consolidated in two layers, then indirect assessments of the undrained shear strength were performed. However, after performed some bearing capacity tests of a shallow foundation, which is explained in the

next chapter of this thesis, was necessarily modified the construction technique because a weak plane developed at the contact between the two layers undergoing consolidation.

5.5.1 Heterogeneous soil construction technique

Once the eight artificial homogeneous basic soils were prepared with a water content of about 1.5 times the liquid limit; they were placed into a container matching the realization computed following the method explained in Section 5.2. The container has a width of 14 cm, a height of 12 cm and a thickness of 7 cm. It also has removable lateral acrylic extensions of 2.5 cm of size given a total thickness of 12 cm (Figure 5.16 (a)), which were used to provide an extra depth to the model because the soil near the lateral wall is affected by boundary friction; therefore, the geometry of the cells is distorted. A porous stone was placed at the base of the container, and the acrylic lateral walls of the container were perforated to provide adequate vertical and horizontal drainage during the consolidation process, Figure 5.16 (b). The heterogeneous model was constructed by placing strings of slurries into a container using a transversal grid as a linear casing, and a manual caulking gun, Figure 5.16 (b) and (c). The 112 elements of the random configuration were placed one by one in layers starting from the bottom of the container until the top, Figure 5.16 (d). This procedure was made in two phases: in the first phase, five sublayers were constructed until reaching the top of the container; in the second phase, the remain three sublayers were created. The reason of building the model in two stages was because the height of the container (12 cm) was not enough to build the model in one time (the height of each layer was 1.2 cm). Once the heterogeneous model was constructed, it was subjected to a vacuum for 12 hours to remove voids that could be trapped during the construction.

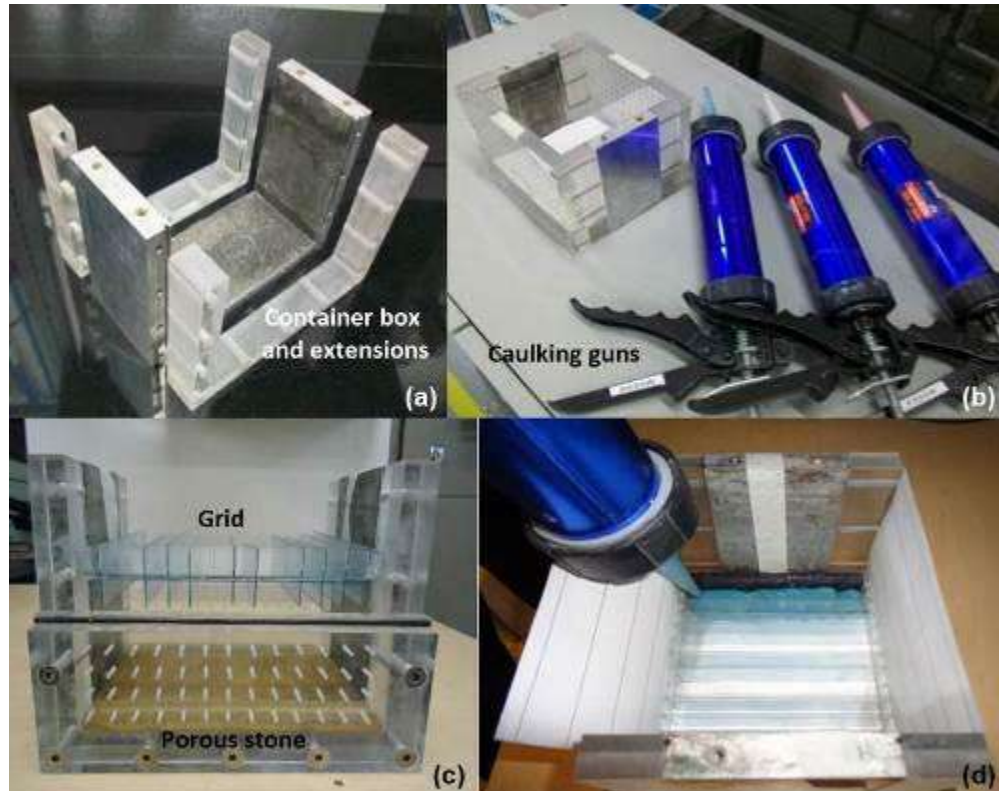


Figure 5.16 Construction of the heterogeneous model: (a) container box and acrylic extensions, (b) container box and caulking guns, (c) container box with the porous stone and the grid, (d) process of placing the strings of slurries into the container.

5.5.2 Consolidation process

The next phase of the process is to apply the consolidation stress; this process was carried out in three stages: the first vertical stress applied was 0.7 kPa then gradually double load increased to 12.5 kPa.

- i. For the first stage, the model (five sublayers) was subjected to one-dimensional compression confining the soil in the rigid container and applying a vertical stress of 30 kPa using a rigid plate. The vertical stresses were applied gradually (double load increased) starting at 3.75 kPa until reaching 30 kPa. During this stage, water drainage occurs horizontally and vertically.
- ii. For the second stage, the model (three sublayers) was also subjected to one-dimensional compression confining the soil in the rigid container and applying a vertical stress of 30 kPa using a rigid plate. During this stage, water drainage occurs horizontally and vertically. After consolidation, the lateral acrylic extensions were removed, and the slices of soil occupying the extensions were removed using a cutting wire, Figure 5.17 This procedure guarantees a better image of the square mesh avoiding the adverse effect of the walls.
- iii. For the third stage, the model was transferred to the geotechnical centrifuge and consolidated under 50g for 30 min; during this phase, water drainage occurs only vertically. To prevent

desiccation, a small film of water was left on the surface of the model. The water table was controlled by a piezometer installed on the bottom of a lateral acrylic wall. Although the 1g consolidation at 30 kPa produces higher stresses than the centrifuge, the purpose of the centrifuge is to homogenize the stress distribution during consolidation. In fact, the 1g compression stage was performed using a rigid plate that produces a heterogeneous stress distribution. Figure 5.18 shows the oedometric consolidation and the centrifuge consolidation apparatus.

The three consolidation stages were controlled by the methodology proposed by Asaoka (1978). The duration of the whole preparation process was approximately two weeks. Figure 5.19 shows the three heterogeneous models of two-layers stage.



Figure 5.17 Construction of the heterogeneous model: (a) container box and caulking guns, (b) acrylic extensions of the container box, (c) container box with the porous stone and the grid, (d) process of placing the strings of slurries into the container.



Figure 5.18 Consolidation process: (a) one-dimensional consolidation, (b) centrifuge consolidation.



Figure 5.19 Three isotropic heterogeneous models: (a) Model 1, (b) Model 2, (c) Model 3.

5.5.3 Computerized Axial Tomography (CAT Scan)

One of the concerns of the new technique was that the cells were not completely joined and that cracks were created between them. To clear this doubt, after completion of the consolidation process, one heterogeneous model was subjected to a Computerized Axial Tomography (CAT Scan) to verify the presence of cracks. Figure 5.20 shows the CAT scan of the model where it can be seen that no cracks are created; however, many small void get trapped between the cells. Knowing this results, a vacuum process was adopted to remove voids; this process took place immediately after the construction of the models. The improvement of the vacuum application can be seen in Figure 5.21 that shows a CAT scan of another two heterogeneous models. Again, it can be seen that cracks are not created and the number of trapped air bubbles has been significantly reduced.

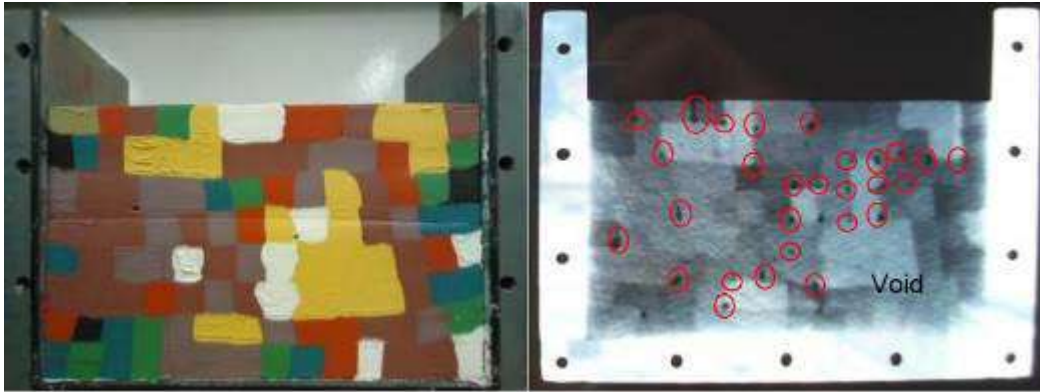


Figure 5.20 Computerized Axial Tomography of a preliminary model.

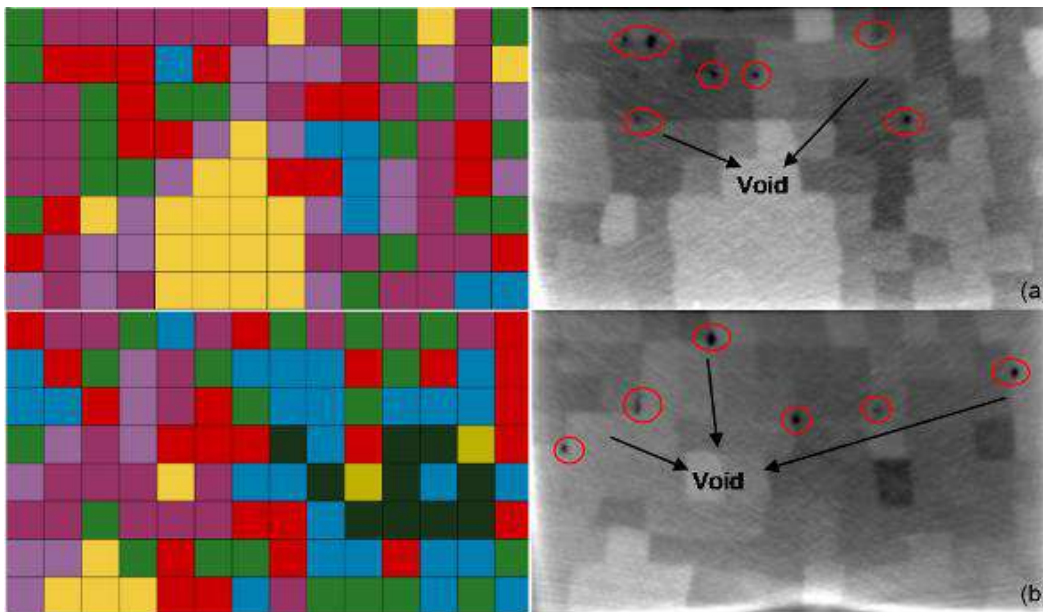


Figure 5.21 Computerized Axial Tomography: (a) Model 1, (b) Model 2.

5.5.4 Resistance (Electrical Needle Probe)

The spatial variability in depth of the models was assessed by using a novel technique proposed by Cho et al., (2004). This technique involves a needle-size probe that is pushed into the soil to measure the local electromagnetic properties of the medium along its path assessing the spatial variability of the soil. The electrical needle probe is a two-lead coaxial conductor. It is built by inserting an insulated wire (the core electrode) inside a thin metal tube (the external electrode) and filling the annular space with epoxy resin. The shaped tip of the probe is a sharp double-wedge tip. The electromagnetic properties are computed from the measured resistance, R and reactance, X , or the impedance $|Z|$ magnitude and phase angle θ . These parameters are related as follows:

$$z^* = R + j.X = |Z| \cos\theta + j|Z| \text{sen}\theta \quad (5.23)$$

The pairs $R - Z$ or $|Z| - \theta$ were determined with a 4275A Multi-Frequency LCR Meter low frequency impedance analysed.

Measurements of the resistance of the soil were made in a center plane of the model in three different locations, left, center and right (Figure 5.22 and Figure 5.23). The needle was inserted at 1 cm/min using a triaxial load frame, the needle attached to the horizontal frame, and the model was in the support base. The resistance was measured every 0.25 mm at $f = 100$ kHz.

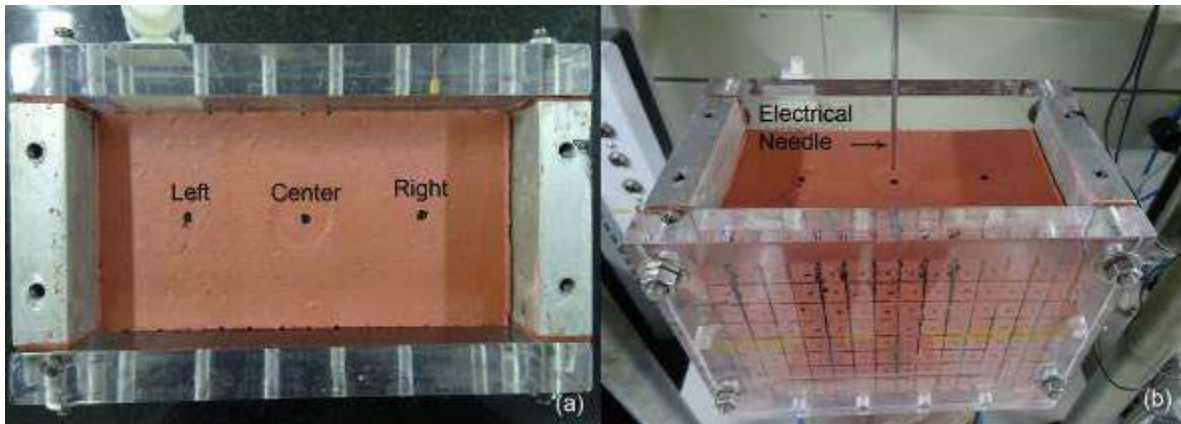


Figure 5.22 Measurement made by the electrical needle probe: (a) locations of the point measurements in the model, (b) electrical needle position.

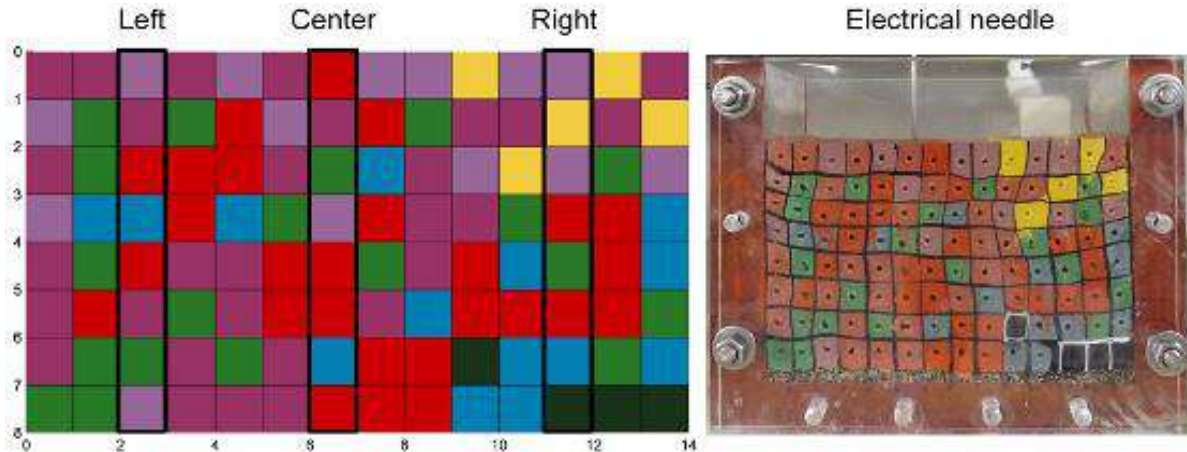


Figure 5.23 Three profiles of the heterogeneous model measurement by the electrical needle probe.

Resistance (Electrical Needle Probe) Results

Resistance profiles of the six homogeneous models are shown in Figure 5.24. Figure 5.24 (a, b, c) shows the profiles of the homogeneous models built by the traditional technique, while Figure 5.24 (d, e, f) shows the profiles of the homogeneous models built by the random technique. Also, the figures show the locations of the resistance’s measurements (left, center and right). It can be seen that the resistance profiles of five models have an average value of $3.8 \text{ k}\Omega$ and not significant variations are register. Model HR2 (Homogeneous Random 2) registers a lower resistance value

from the surface to a depth of 4 cm, after this, the register reaches the average value of 3.8 kΩ. This register can be see especially in the center and the right position. This behavior can be explained by loss the of moisture on the surface of the model.

Figure 5.25 (a, b, c) shows the resistance profiles of the three heterogeneous models (replicates) in each of the three locations of the resistance's measurements (left, center and right). It can be seen that the measured resistance profiles detect the spatial variability of the soil; furthermore, the resistance profiles of the three models repeat almost equal, which means that the new technique can be controlled and replicated in the laboratory.

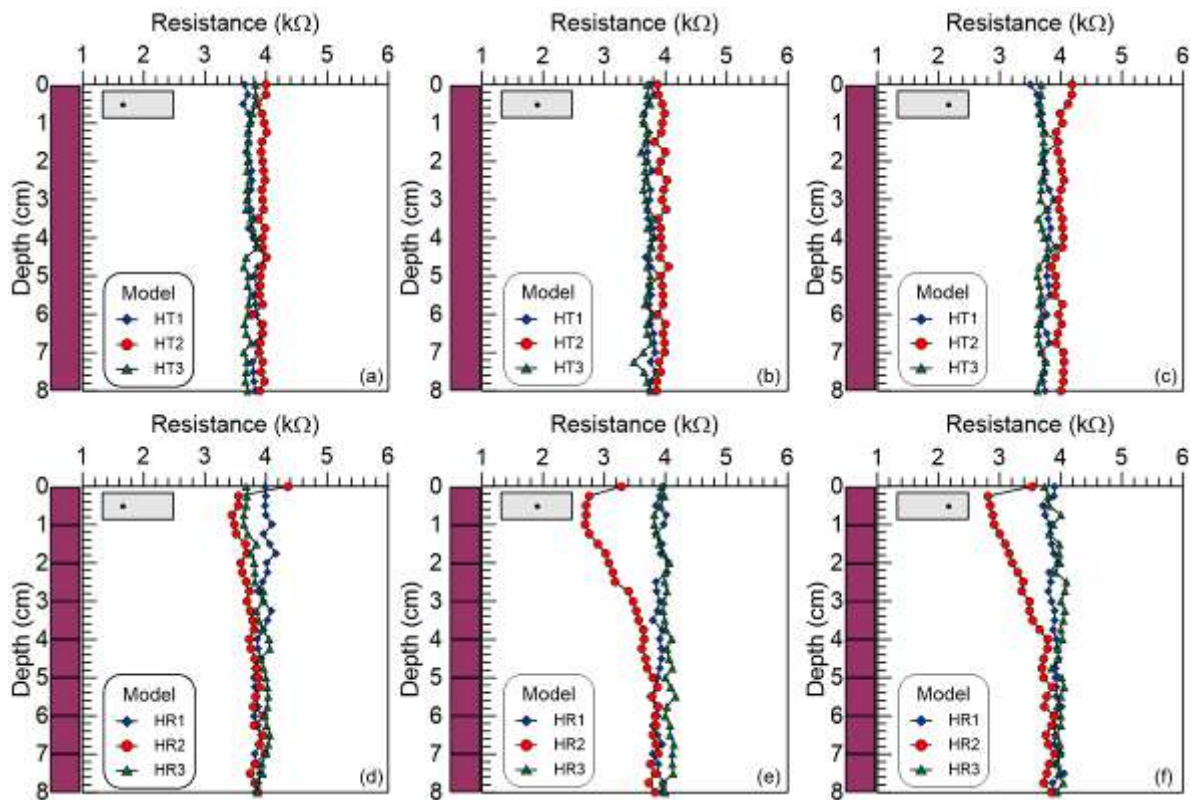


Figure 5.24 Resistance profiles of homogeneous models: (a) traditional technique left position, (b) traditional technique centre position, (c) traditional technique right position, (d) random technique left position, (e) random technique centre position and (f) random technique right position.

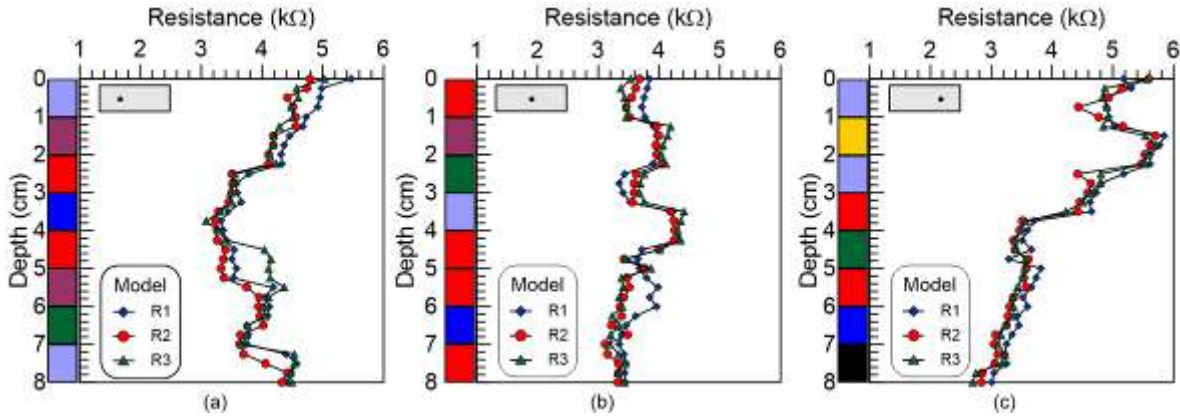


Figure 5.25 Resistance profiles of heterogeneous models: (a) left position, (b) centre position and (c) right position.

5.5.5 Undrained shear strength measurements

In two-layers stage, direct measure of the undrained shear strength of each element was not performed due to the difficult given the small size of the cells; however, the undrained shear strength was calculated indirectly using the Cam Clay theory based on the void ratio or specific volume and the effective consolidation stress (Equation 5.24).

$$C_u = \frac{M}{2} \exp\left(\frac{\Gamma - v}{\lambda}\right) \quad (5.24)$$

where C_u is the undrained shear strength, M is the slope of the critical state line, Γ is the specific volume in the critical state line at a mean effective stress value of 1 kPa, v is the specific volume and λ = virgin compression index of the soil.

To measure the final void ratio and the effective consolidation stress on each cell was necessary to measure the unit weight and the water content of each of the 112 elements. This procedure was performed by using a 0.5 cm³ syringe, which was modified to make holes and take samples from the soil (Figure 5.26). The mass of soil was found by weighing, and the water content was measured. The final void ratio was estimated by using a classical volumetric relationship:

$$e = \frac{G_s(1+w)}{\gamma_{SAT}} - 1 \quad (5.25)$$

where e is the void ratio, G_s is the specific weight, w is the water content and γ_{SAT} is the saturated unit weight. Once the void ratio was found for each of the 112 elements, the effective normal stress was estimated using the compression curves of the eight homogeneous soils.

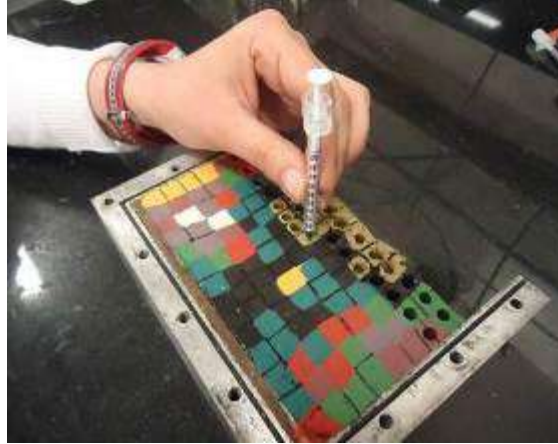


Figure 5.26 Sampling process of the 112 elements of the mode.

5.5.5.1 Effective vertical stress results

Figure 5.27 shows the random distribution of the effective vertical stress obtained using the compressions oedometric line and its histogram for the three models. The major frequencies for Model 1 (M1) are in the intervals of 5-10 kPa and 15-20 kPa, for Model 2 (M2) is in the range of 15-20 kPa, and for Model 3 (M3) in the intervals of 10-15 kPa and 25-30 kPa. Furthermore, the mean effective normal stress calculated was 22.52, 30.96 and 24.97 kPa, for M1, M2 and M3, respectively. It should be noticed that the mean value of models M1 and M3 is lower than the 30 kPa applied externally during the oedometric consolidation, and only M2 is closer (30.96 kPa). It can be said that although the construction of the three samples was well controlled and monitored, the consideration of the spatial variability of soil property leads to a different distribution of the effective normal stress from realization to realization.

On the other hand, regarding the spatial distribution of the effective normal stress, there is no clear tendency, again it changes from one to another realization of the random field. M1 exhibits an asymmetric bell curve shape, which curve's peak is given by the mean stress values of soil S1 (yellow). M2 has the highest dispersion of the effective normal stress, while M3 shows two “average” tendencies values.

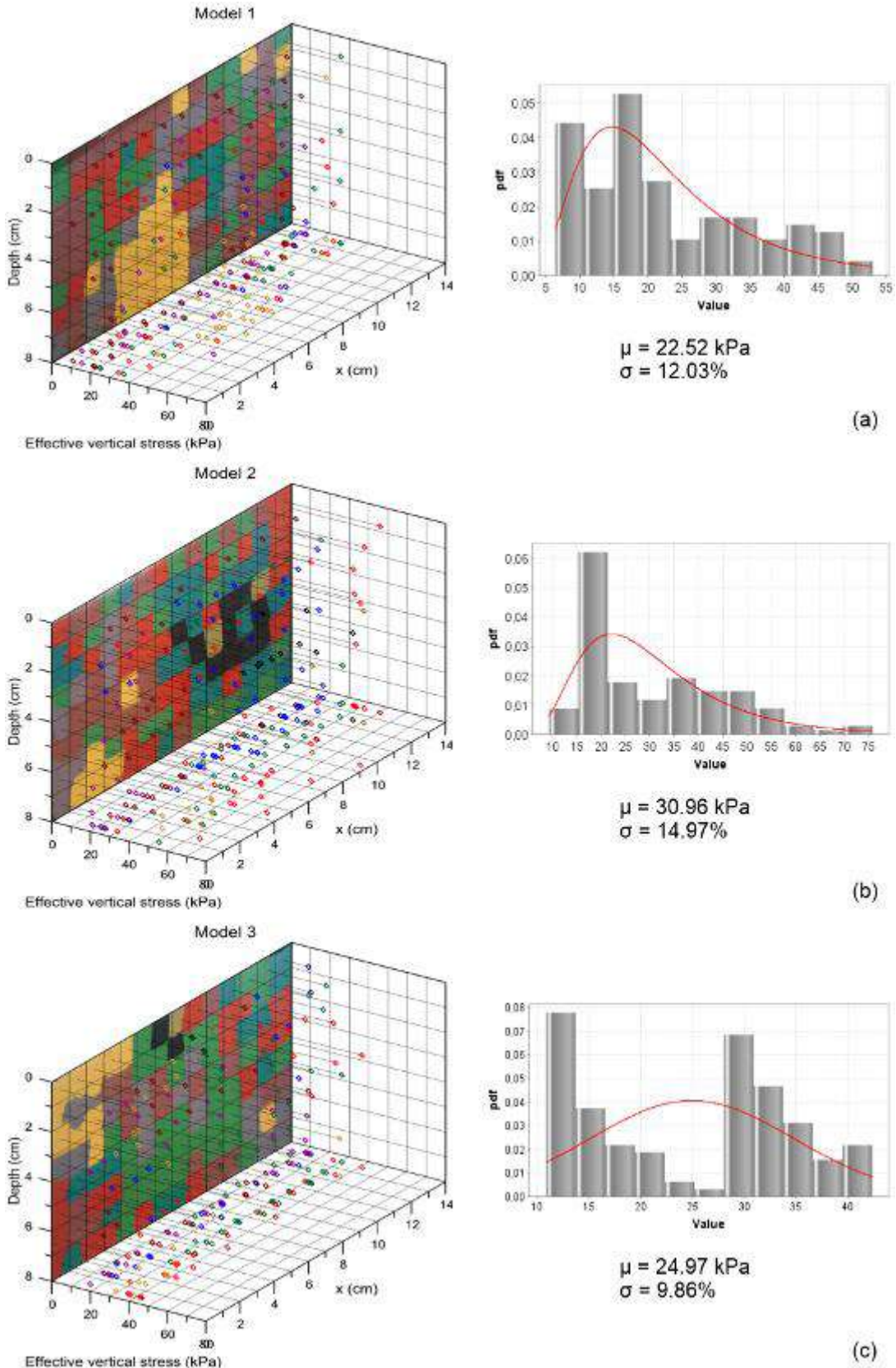


Figure 5.27 2D Random effective normal stress values and histogram in kPa: (a) Model 1, (b) Model 2, (c) Model 3.

The 2D random distributions of the effective vertical stress for the three models are shown in Figure 5.28. Analyzing the results for soil S1 (yellow) in M1, Figure 5.28(a), the mean of the effective normal stress is 41 kPa (mean of the 15 cells located on the lower middle right of the model); however, the normal stress values of the two cells S1 (located at the top and right side of the model) are 18.8 and 22.5 kPa respectively. In contrast, the value of the cell S1 (located at the top and middle of the model) is 47.7 kPa. These results show that in a heterogeneous soil the effective vertical stress depends not only on the characteristics of the soil but also on the characteristics of the neighbor soils. In fact, when the soil S1 rest on a stiff soil the vertical stress reach high values, i.e., the top cell that has 47.7 kPa, whereas cells S1 resting on a more compressible soil reach 18.8 and 25.5 kPa.

Besides in M2, Figure 5.28(b), the effective normal stress mean of S1 is 50 kPa (mean of the 4 cells located at the lower right of the model), and in M3, Figure 5.28(c) the effective normal stress mean is 33 kPa (mean of the 10 cells located at the top right of the model). Again, these results are consistent since soil S1, in M2, rests directly on the container box, whereas S1, in M3, rest on the soils that have a medium compressibility. These results show that the mechanical soil properties, which depend on the effective vertical stress, do not only depend on its intrinsic behavior, but also on the spatial distribution and its neighboring soils. Figure 5.29 shows a map of the distribution of the vertical stress for the three models where the zones of higher and lower stresses can be observed.

Figure 5.30 shows the curves of the mean value of the vertical stress calculated along each layer and the mean value plus minus one standard deviation. For model M2, the mean value of the vertical stress approaches 30 kPa that correspond to the external stress applied during consolidation. However, for models M1 and M2 this mean value is lower than 30 kPa, probably these models require more time to reach 100% of consolidation; furthermore, the first three layers of model M1 are certainly in under consolidated state since the vertical stress is far from the 30 kPa applied to the model.

20.6	9.6	8.5	7.0	8.0	9.4	10.0	47.7	10.1	21.3	21.4	18.8	10.9	30.1
21.0	26.7	17.1	20.0	19.8	19.5	9.5	10.2	9.6	8.4	20.3	9.6	9.7	22.5
6.6	7.8	19.3	17.1	18.9	20.1	9.4	10.4	19.5	17.5	9.8	18.9	9.9	9.6
18.2	17.5	30.8	35.9	46.0	14.6	41.7	14.2	16.9	16.8	19.9	17.4	29.1	29.9
17.3	17.6	36.0	33.0	16.7	40.6	46.5	42.9	41.5	17.1	11.2	17.3	32.0	11.3
33.0	37.6	32.9	14.1	40.6	40.6	46.5	35.3	14.1	16.4	13.8	17.6	25.1	29.8
30.3	17.5	14.2	53.0	36.3	52.1	30.4	40.3	18.2	16.2	31.1	17.3	14.2	26.3
11.3	17.9	15.4	17.7	45.2	38.4	34.4	45.2	43.1	25.5	6.5	18.5	15.2	12.1

(a)

29.7	17.1	16.3	44.2	25.2	18.1	50.8	37.3	16.3	37.5	16.1	37.5	15.7	50.5
21.0	63.7	48.0	16.3	17.3	42.6	19.3	18.7	19.2	75.8	21.2	32.3	26.9	42.4
23.5	27.2	46.7	9.4	19.4	35.6	14.9	17.0	31.1	16.9	26.5	18.2	16.9	36.5
51.3	21.0	30.4	12.8	52.7	42.4	11.7	47.6	28.0	12.9	16.3	30.2	50.8	37.2
22.6	23.9	20.9	18.6	42.9	20.0	18.2	17.6	31.4	50.8	44.1	18.7	45.2	18.9
23.1	26.6	56.2	21.3	21.4	18.6	42.4	47.4	19.8	15.2	15.5	16.6	17.6	37.9
16.9	21.0	55.3	53.2	71.8	38.9	37.3	67.9	21.2	21.3	44.5	19.2	18.9	31.0
16.6	44.1	48.9	52.1	54.8	59.9	21.1	21.4	35.2	37.4	37.8	25.2	38.6	20.8

(b)

38.4	35.3	37.3	33.5	23.1	31.3	15.4	17.1	32.7	16.0	13.2	31.3	31.3	13.3
38.4	16.7	16.4	13.1	12.5	31.6	30.2	12.5	34.7	30.4	29.7	29.4	29.8	14.5
29.0	31.8	23.1	13.7	12.4	11.7	11.5	21.2	13.6	29.9	32.2	14.5	12.1	26.2
15.6	14.2	38.4	30.7	16.0	15.7	13.7	14.1	12.6	33.5	12.5	32.4	36.3	41.1
42.4	18.1	21.3	19.3	30.8	10.9	30.2	30.8	12.1	30.8	30.2	32.9	17.3	30.6
41.5	16.2	36.3	34.3	30.7	31.3	30.3	28.8	31.0	31.0	30.4	12.5	11.8	13.1
35.2	13.7	11.8	20.4	34.3	34.3	32.6	30.2	12.4	30.9	30.2	12.9	38.4	12.5
36.3	20.2	42.4	42.4	34.7	42.4	19.8	21.6	40.6	16.7	17.9	30.8	14.2	11.7

(c)

Figure 5.28 2D Random effective normal stress values in kPa: (a) Model 1, (b) Model 2, (c) Model 3.

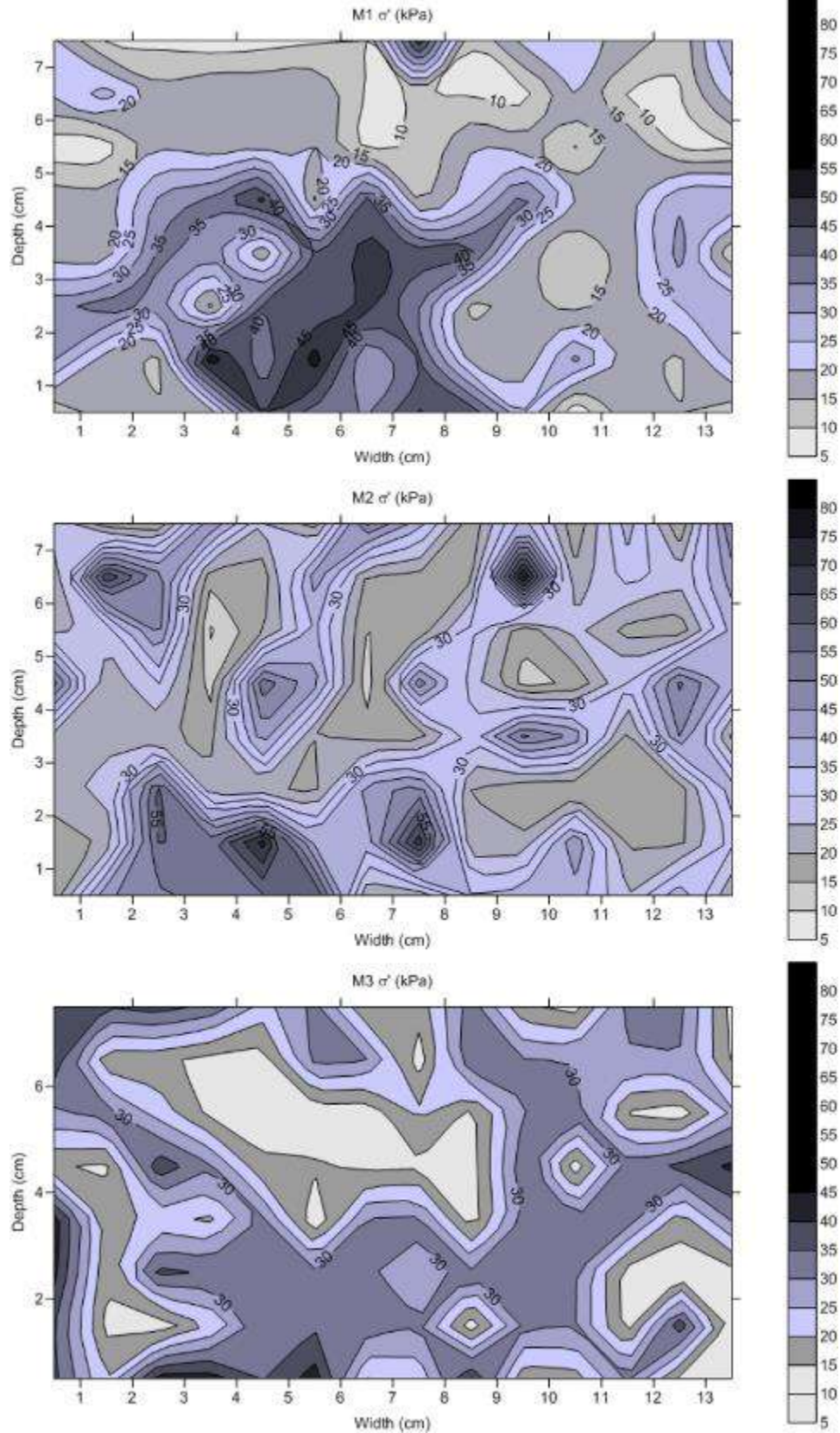


Figure 5.29 Map of the effective normal stress values in kPa for the three models.

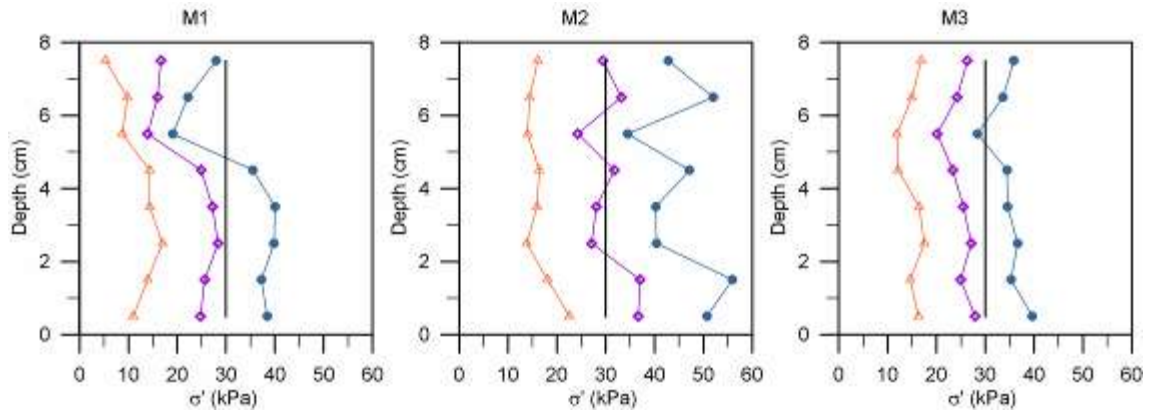


Figure 5.30 Variation with depth of the vertical stress for the three models: mean value and mean plus minus one standard deviation.

5.5.5.2 Undrained shear strength results

Figure 5.31 shows the map of undrained shear strength calculated for each model using the using the compressions oedometric line, zones of high and low cohesion are well related with low and high consolidation stresses. Figure 5.32 shows the curves of the mean value of the undrained shear strength calculated along each layer and the mean value plus minus one standard deviation of the three models.

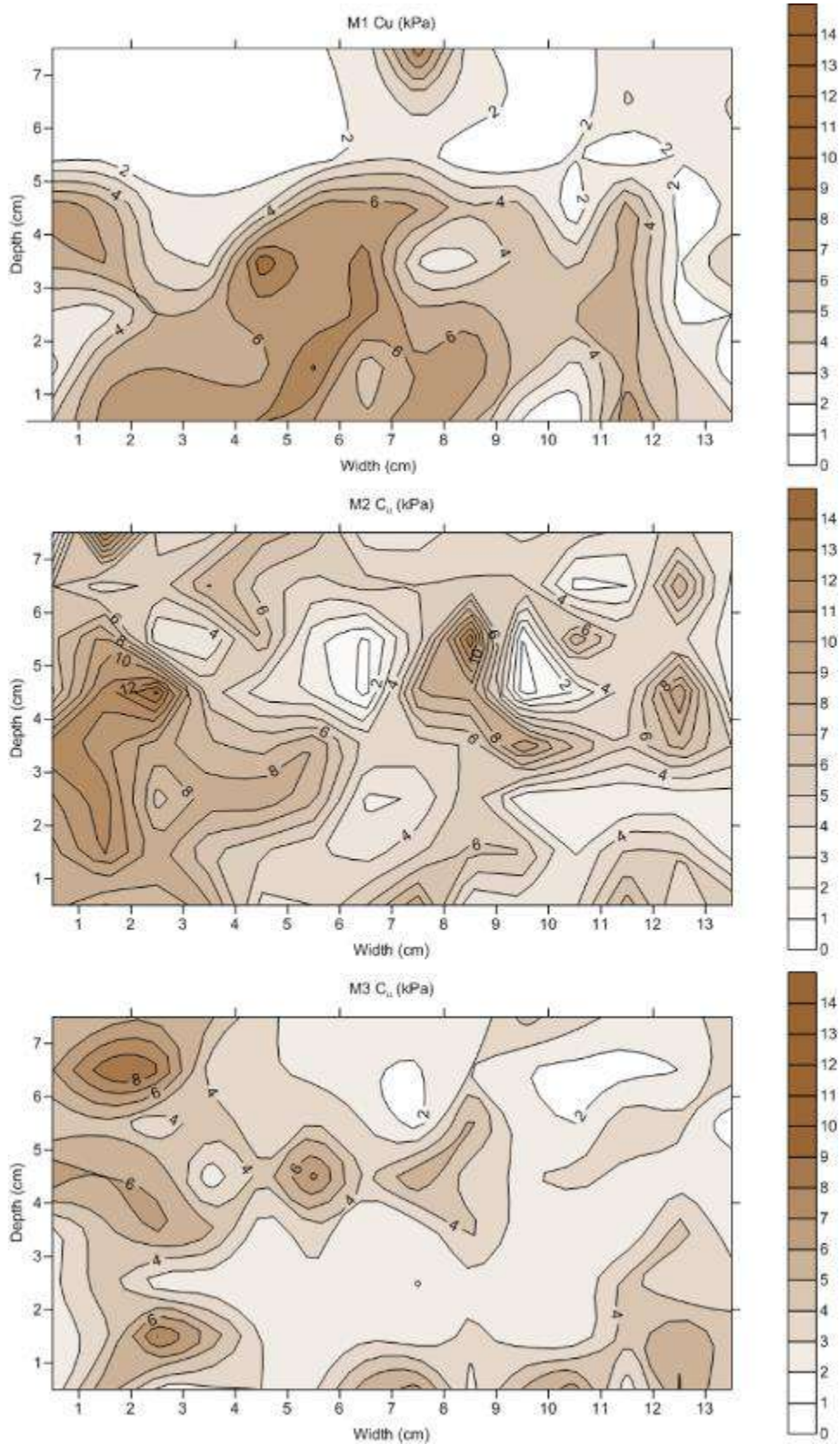


Figure 5.31 Map of the undrained shear strength values in kPa for the three models.

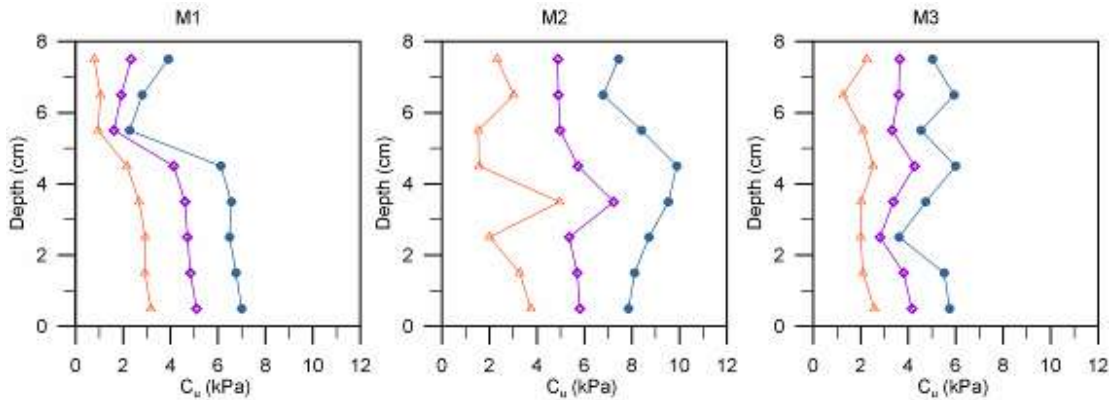


Figure 5.32 Variation with depth of the undrained shear strength for the three models: mean value and mean plus minus one standard deviation.

5.6 Development of the random soil construction technique: one-layer

In one-layer stage, six homogeneous models (HT1, HT2, HT3, HR1, HR2 and HR3) and three heterogeneous (R1, R2 and R2) models were constructed. The six homogeneous models were made with soil S3, which has a $COV_{WL} = 0\%$ or $\mu = 157\%$ and $\sigma = 0\%$, $L_x = 0$ m and $L_z = 0$ m. The three heterogeneous models (replicates) have a $COV_{WL} = 30\%$ or $\mu = 157\%$ and $\sigma = 47\%$, $L_x = 1.5$ m and $L_z = 1.5$ m, Figure 5.33.

Three homogenous models were built with the traditional technique, this is, placing the slurry in the container in a single layer, and the other three were constructed with the random technique proposed in this study, Figure 5.34 shows the traditional and the random technique. The purpose of building the homogeneous models whit the conventional and new technique was to verify that the models built with the new procedure behaved as a single unit, that is, with no signs of cracks or weak planes of failure between the joints of the layers. The objective of building three replicates was to measure the repeatability and reproducibility of the construction process.

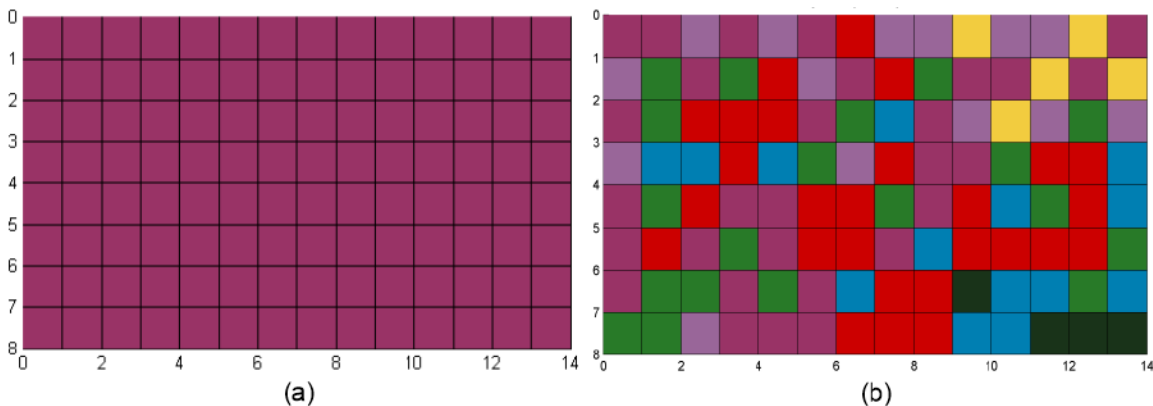


Figure 5.33 Models one-layer stage: (a) homogeneous model soil S3, (b) heterogenous models

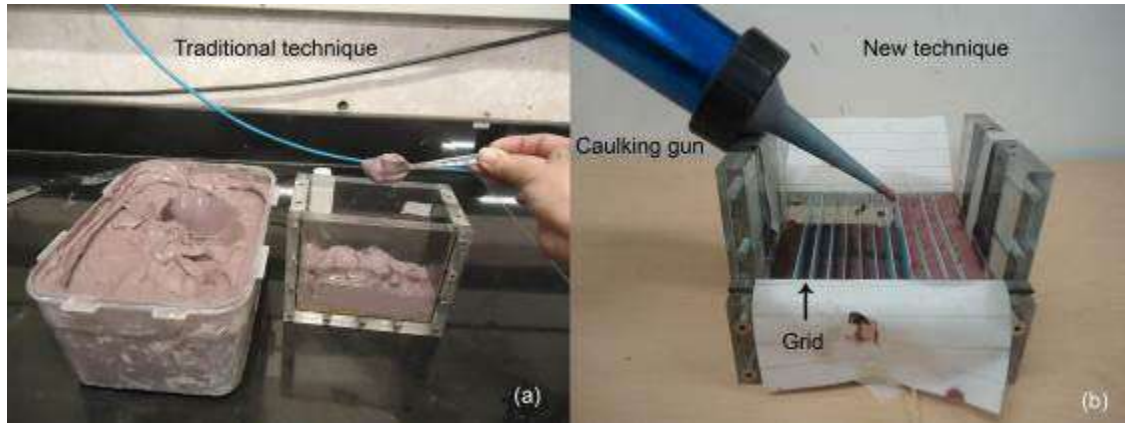


Figure 5.34 Construction of the models: (a) traditional technique, (b) random technique.

5.6.1 Modification of random soil construction technique

The random soil construction technique in one-layer stage changes with respect two-layers stage. It was necessary to modify it because a weak plane in the model was developed between rows five and six (due to the construction in two layers) affecting the bearing capacity tests of a shallow foundation, which is explained in the next chapter of this thesis. For that reason, a removable vertical acrylic extension of 7 cm of size was constructed given the container a total height of 19 cm. The vertical extension allows building the models in a single layer. The process of placing the strings of slurries was the same explained in two-layers stage, Figure 5.35 (a) shows the vertical acrylic extension, and Figure 5.35 (b and c) shows the caulking guns and the process of placing the strings of slurries into the container. The consolidation process was the same explained in Section 5.5.2.



Figure 5.35 Construction of the heterogeneous model: (a) container box with vertical extensions, (b) caulking guns, (c) process of placing the strings of slurries into the container.

5.6.2 Undrained shear strength measurements

The undrained shear strength of all nine models was estimated indirectly and directly. Direct measurements were made by using a mini ball penetrometer and a mini vane; indirect measurements were made by correlating the water content with the shear strength and the plasticity. The

ball and vane measurements were performed for each model after the centrifuge consolidation; vane measurement on one lateral side of the model and ball measurement on the other lateral side. Samples to measure the water content were taken by the side of the model the mini ball measurements were made.

5.6.2.1 Indirect measurements

The undrained shear strength was calculated indirectly by measuring the water content of the 112 cells of the models. Samples of each cells were taken with the help of a device, which was modified to make holes and take samples from the soil (Figure 5.36). Samples were taken by the side of the model where the mini ball measurements were made. The soil mass was found by weighing, and the water content determined.

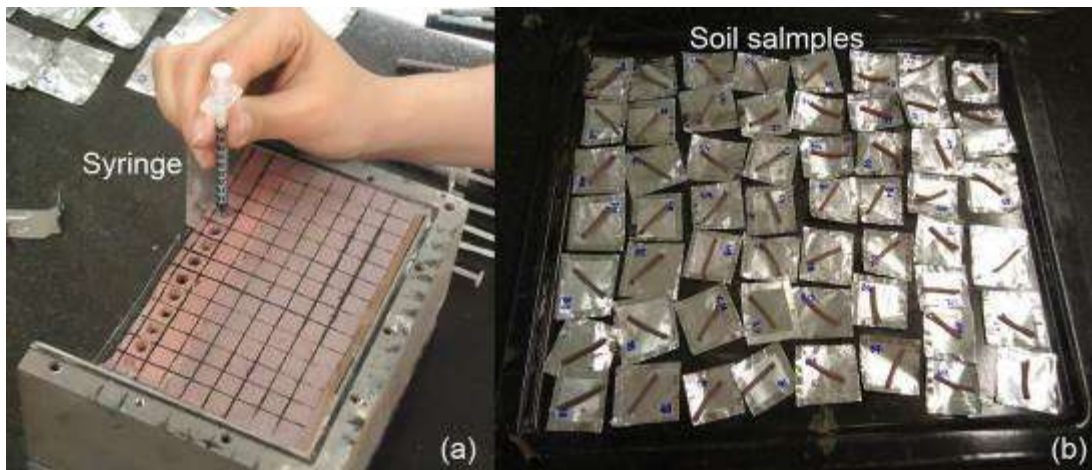


Figure 5.36 Water content measurement: (a) process of sampling with the syringe, (b) soil samples.

The undrained shear strength was then estimated by using two of the many empirical relationships with water content and Atterberg limits regarding liquidity index, IL and consistency index, IC proposed by Hong et al., (2003) and Leroueil et al., (1983). Also, it was used the relationship between the consistency index, IC computing base on the final water content measured on the triaxial tests of the eight homogenous soils, and the undrained shear strength proposed in this study (Section 5.4.3). Similarly, the undrained shear strength was estimated by using the Cam Clay theory based on the void ratio or specific volume and the effective consolidation stress explained in Section 5.5.5. To facilitate reading, a summary of the correlations to be used explained in the previous sections is presented below. The same numbering of the equations used in the previous sections is maintained; it are identified with an asterisk (*)

✓ Empirical relationships

Hong et al., (2003) compiled extensive data on undrained shear strength for various remolded soils to normalize the remolded undrained strength. The study introduces a simple index designated as normalized water content, w^* , which is the ratio of water content to the liquid limit. The relationship between the remolded undrained strength and the normalized water content was expressed by two simple equations as follow:

$$C_{ur}(kPa) = \frac{1.4}{\left(\frac{w}{W_L}\right)^{4.5}} \quad W_L \leq 150\% \quad (5.26)$$

$$C_{ur}(kPa) = \frac{23.8}{e^{2.73 \cdot \left(\frac{w}{W_L}\right)}} \quad W_L > 150\% \quad (5.27)$$

Leroueil et al., (1983) proposed a correlation between undrained shear strength and the liquidity index, IL , based on the data collected in their study of the clay properties of eastern Canada, Equation 5.28. The correlation is given for liquidity index between 0.5 and 2.5.

$$C_u(kPa) = \frac{1}{(IL - 0.21)^2} \quad 0.5 < IL < 2.5 \quad (5.13)*$$

The two correlations defined for this study base on the relationship between undrained shear strength and the consistency index, IC , given by Leroueil et al., (1983) are:

$$C_{ur}(kPa) = 4.0292e^{3.6193IC} \quad S1 \text{ to } S4 \quad (5.17)*$$

$$C_{ur}(kPa) = 1.9505e^{4.1054IC} \quad S5 \text{ to } S8 \quad (5.18)*$$

✓ **Cam Clay theory**

The undrained shear strength was estimated by using Cam Clay theory based on the void ratio or specific volume and the effective consolidation stress as followed

$$C_u = \frac{M}{2} \exp\left(\frac{\Gamma - v}{\lambda}\right) \quad (5.24)*$$

5.6.2.2 **Water content and unit weight results**

Homogeneous models

Figure 5.37, Figure 5.38 and Figure 5.39 show the result of the undrained shear strength, C_u , values estimated by the Cam Clay theory and the empirical relationships proposed by Leroueil et al., (1983), Hong et al., (2003) and the correlation defined for this study (Equation 5.17) for the 6 homogeneous models built with the traditional and random technique. There is no significant difference between the C_u values estimated for the models constructed with the traditional and the random technique. Table 5.6 summarized the results of the indirect values. It can be observed that the shear strength values estimated with the Equation 5.17 are the highest with a mean value

of 6.25 kPa and 7.27 kPa for models built with the traditional and random technique respectively. On the contrary, the results of the Hong et al., (2003) relationship has the lower values and is more homogeneous with a mean value of 2.04 kPa and 2.24 kPa for models built with the traditional and random technique respectively.

Table 5.6 Indirect values of undrained shear strength for homogeneous models.

		Indirect measurements											
		Cam Clay Theory			Leroueil et al., (1983)			Hong et al., (2003)			Equation 5.17		
		C _u (kPa)			C _u (kPa)			C _u (kPa)			C _u (kPa)		
		Mean μ	SD σ	COV	Mean μ	SD σ	COV	Mean μ	SD σ	COV	Mean μ	SD σ	COV
Traditional technique	HT1	2.91	0.66	22.64	2.30	0.33	14.44	2.08	0.22	10.43	6.45	1.08	16.81
	HT2	2.52	0.44	17.64	2.10	0.18	8.66	1.95	0.13	6.64	5.78	0.62	10.69
	HT3	2.91	0.52	17.87	2.32	0.23	9.92	2.10	0.16	7.64	6.51	0.77	11.78
	Mean	2.78	0.54	19.39	2.24	0.25	11.01	2.04	0.17	8.24	6.25	0.60	9.64
Random technique	HR1	2.18	0.46	21.08	2.38	0.35	14.92	2.13	0.23	10.69	6.70	1.13	16.86
	HR2	2.60	0.46	17.57	2.59	0.42	16.26	2.26	0.23	9.97	7.37	1.23	16.10
	HR3	2.59	0.37	14.34	2.70	0.38	14.06	2.33	0.21	8.93	7.12	1.14	14.70
	Mean	2.46	0.43	17.66	2.55	0.38	15.08	2.24	0.22	9.86	7.27	0.75	10.31



Figure 5.37 Undrained shear strength indirect measurements in kPa for homogeneous models traditional technique: (a) Cam clay theory, (b) Leroueil et al., (1983) and (c) Hong et al., (2003).



Figure 5.38 Undrained shear strength indirect measurements in kPa for homogeneous models random technique: (a) Cam clay theory, (b) Leroueil et al., (1983) and (c) Hong et al., (2003).

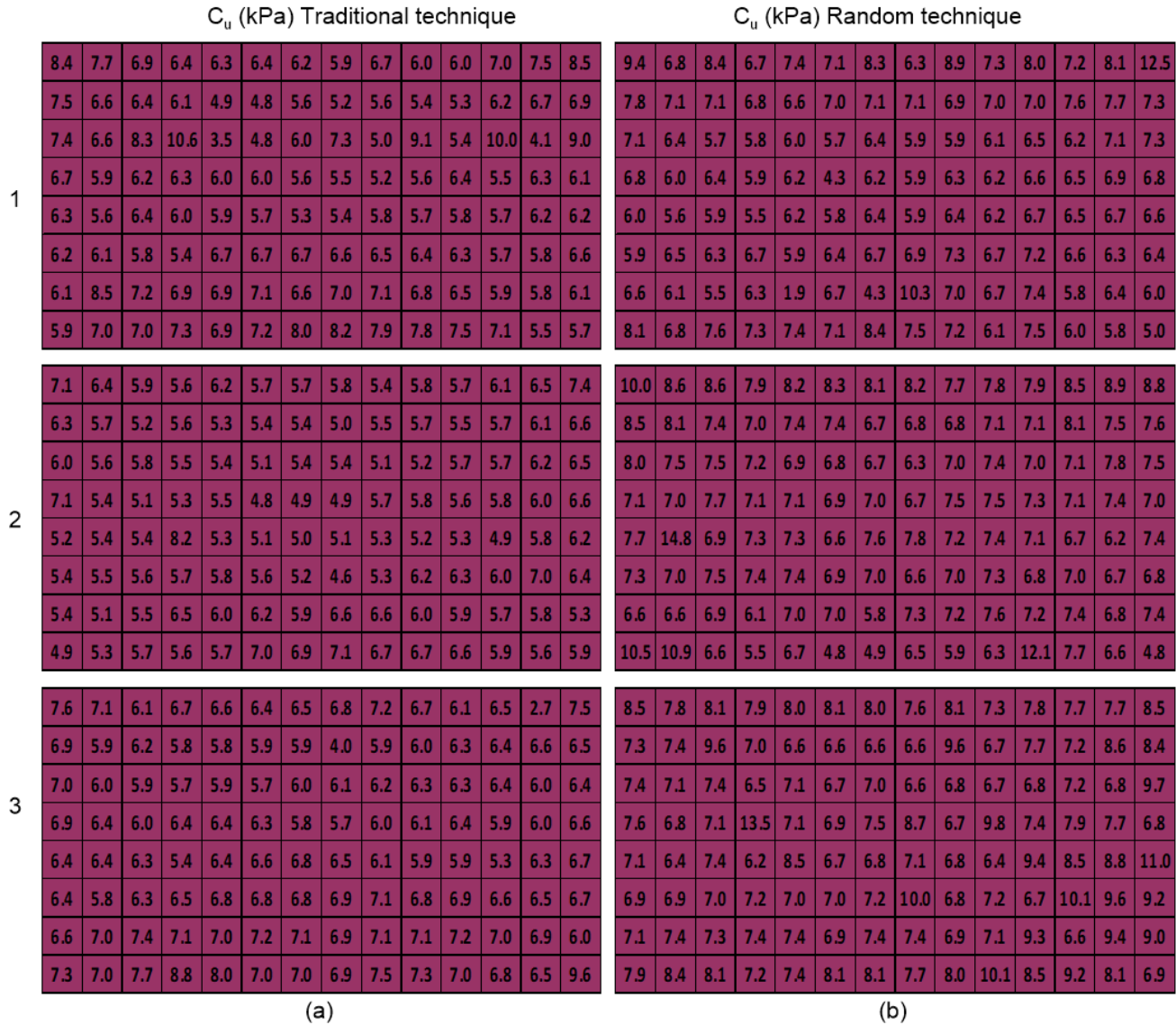


Figure 5.39 Undrained shear strength indirect measurements in kPa for homogeneous models Equation 5.17: (a) traditional technique, (b) random technique.

Heterogeneous models

Figure 5.40 shows the result of the undrained shear strength, C_u , values estimated by the Cam Clay theory, and the empirical relationships proposed by Leroueil et al., (1983) and Hong et al., (2003) and Figure 5.41 shows the result of Equations 5.17 and 5.18 for the three heterogeneous models (replicates). Table 5.7 summarizes the results of the indirect values. As observed in the homogeneous models, the values estimated with the Equations 5.17 and 5.18 has the major values of undrained shear strength (7.12 kPa), but the most variable (COV 42.02) is the values estimated by the Cam Clay theory. In contrast, the values estimated with Hong et al., (2003) relationship has the lower values (2.60 kPa) and is more homogeneous (COV 16.18).

Table 5.7 Indirect values of undrained shear strength for heterogeneous models.

		Indirect measurements											
		Cam Clay Theory			Hong et al., (2003)			Leroueil et al., (1983)			Equations 5.17 and 5.18		
		C_u (kPa)			C_u (kPa)			C_u (kPa)			C_u (kPa)		
		Mean μ	SD σ	COV	Mean μ	SD σ	COV	Mean μ	SD σ	COV	Mean μ	SD σ	COV
Heterogeneous	R1	4.08	1.75	42.81	2.64	0.52	19.84	3.16	1.35	42.79	7.31	3.47	47.45
	R2	3.79	1.54	40.64	2.54	0.37	14.50	2.90	0.64	22.09	6.86	2.82	41.12
	R3	4.06	1.73	42.61	2.63	0.37	14.21	3.02	0.54	17.85	7.19	2.74	38.17
	Mean	3.97	1.67	42.02	2.60	0.42	16.18	3.03	0.84	27.58	7.12	2.62	36.76

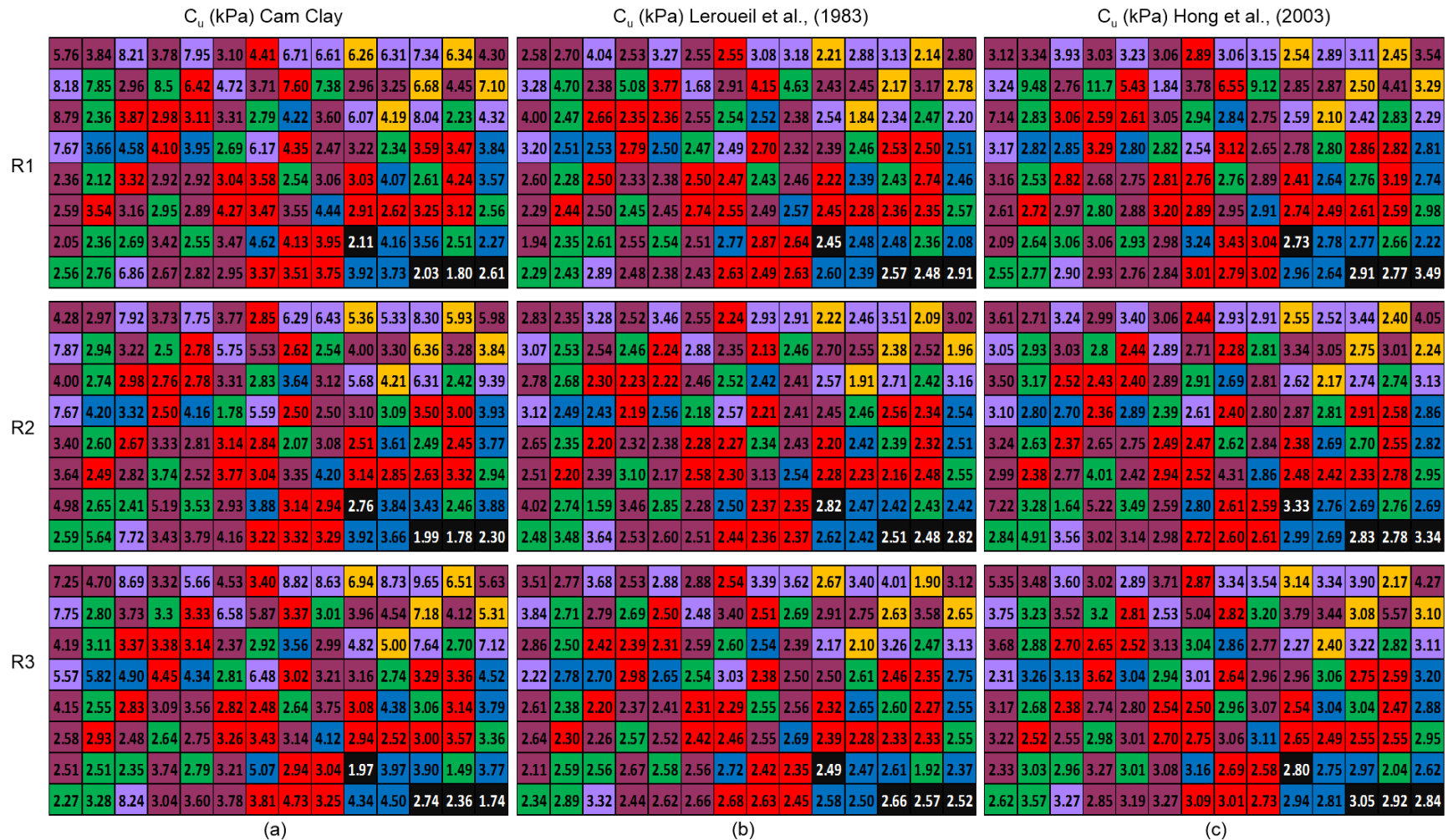


Figure 5.40 Undrained shear strength indirect measurements in kPa of heterogeneous models: (a) Cam clay theory, (b) Leroueil et al., (1983) and (c) Hong et al., (2003).

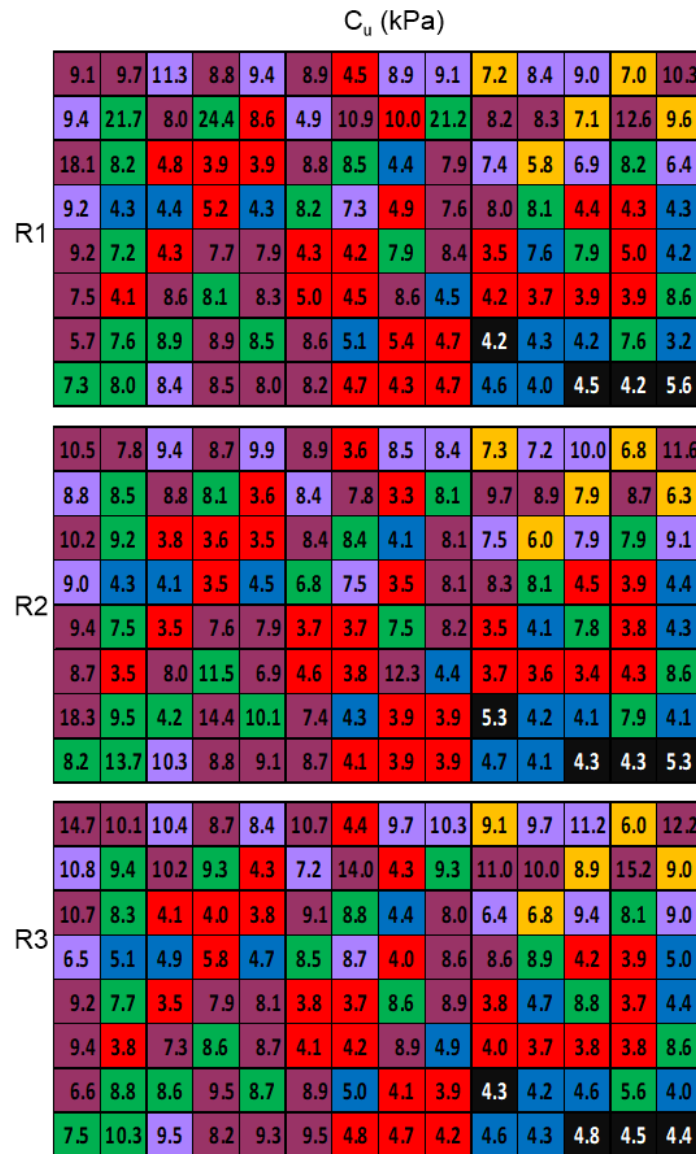


Figure 5.41 Undrained shear strength indirect measurements in kPa of heterogeneous models Equations 5.17 and 5.18.

5.6.2.3 Direct measurements

A mini ball penetrometer and a mini vane were built to measure the undrained shear strength of the 112 cells of the homogeneous and heterogeneous models. The PLA mini vane has a diameter of 8 mm and a height of 12 mm. A miniature screwdriver reaction torque sensor (100 in-oz capacity) is attached to the vane steel shaft, Figure 5.42(a). The mini ball has a steel spherical body and slender shaft; the spherical diameter is 2.94 mm. A mini compression - tension load cell (250 g capacity) is attached to the shaft, Figure 5.42(b). The ball and vane measurements were performed for each model after the centrifuge consolidation; vane measurement on one lateral side of the model and ball measurement on the other lateral side. A handheld portable digital display was used to facilitate the measurements, Figure 5.43.

From the mini ball penetrometer, the undrained shear strength can be estimated as the ratio of net penetration resistance, q_{Net} , and the strength factor, N_{ball} , Equation 5.28. Empirical N factors were calculated by Weemees et al., (2006) for soft Canadian clays as 10.3 and 11, for this study N_{ball} was taken as 10.3. Likewise, the undrained shear strength can be estimated from the mini vane using Equation 5.29, where T , is the maximum value of measured torque in N·m; d is the vane diameter in mm and h is the vane height in mm.

$$C_u = \frac{q_{Net}}{N_{ball}} \quad (5.28)$$

$$C_u = \frac{T}{\pi \left(\frac{d^2 h}{2} + \frac{d^3}{6} \right)} \quad (5.29)$$

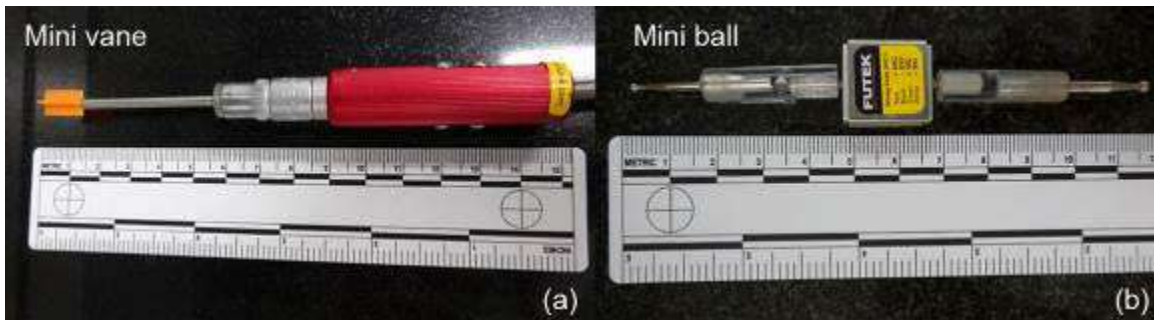


Figure 5.42 Direct measurements tools: (a) mini vane and (b) mini ball penetrometer.

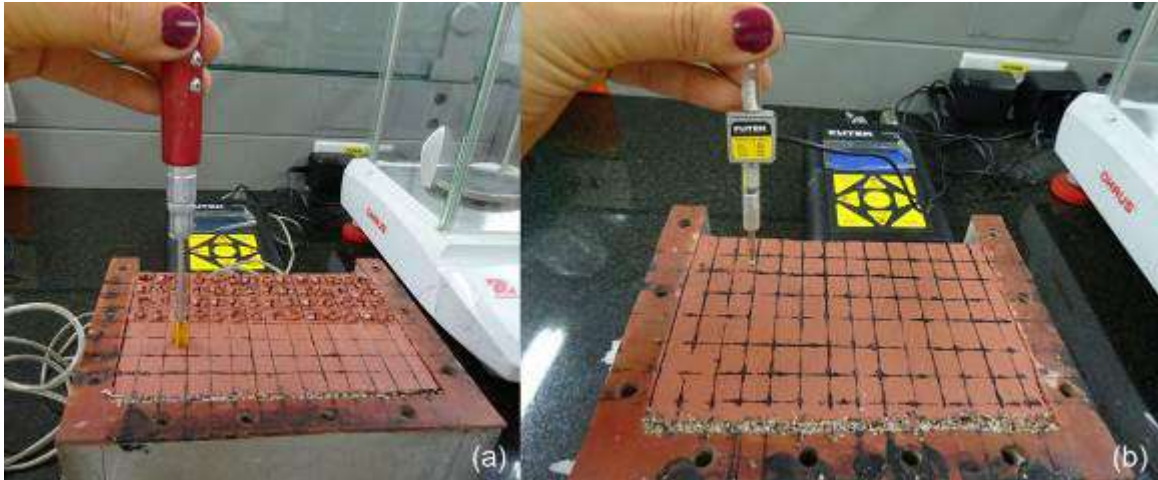


Figure 5.43 Undrained shear strength direct measurements: (a) mini vane and (b) mini ball penetrometer.

5.6.2.4 Direct measurements results

Homogeneous models

Figure 5.44 and Figure 5.45 show the result of the undrained shear strength, C_u , values measured with the mini ball penetrometer and the mini vane in the six homogeneous models built with the traditional technique as the random technique. Table 5.8 summarizes the statistical values of the undrained shear strength for the six homogeneous models measured with the mini ball and the mini vane. In addition, the table shows the values estimated with the correlation defined for this study base on the relationship between undrained shear strength and the consistency index (Equation 5.17).

The results show that the C_u values measured with the mini ball are 1.5 times greater than those measured with the mini vane for the models constructed with the traditional technique; likewise, for the models constructed with the random technique, the magnitude is 1.6 times greater. Also, there are no significant differences between the mean of the undrained shear strength of the models built with the traditional and the random technique for both measures (mini ball and mini vane). For the mini ball, values are 6.81 kPa and 6.97 kPa; for the mini vane, values are 4.64 kPa and 4.24 kPa. The standard deviation for the mini ball is the same for models built with the traditional and the random technique, and has a value of 0.45 kPa; however, for the mini vane, the standard deviation varies between 0.48 kPa and 0.52 kPa. It can be noticed that values measured with the mini ball are close to the values estimated by Equation 5.17.

Table 5.8 Direct values of undrained shear strength for homogeneous models.

		Direct measurements						Indirect measurement		
		Mini Ball			Mini Vane			Equations 5.17		
		C _u (kPa)			C _u (kPa)			C _u (kPa)		
		Mean μ	SD σ	COV	Mean μ	SD σ	COV	Mean μ	SD σ	COV
Traditional technique	HT1	6.75	0.44	6.47	4.77	0.53	11.09	6.45	1.08	16.81
	HT2	6.76	0.45	6.70	4.77	0.43	9.02	5.78	0.62	10.69
	HT3	6.92	0.46	6.67	4.38	0.49	11.17	6.51	0.77	11.78
	Mean	6.81	0.45	6.61	4.64	0.48	10.43	6.25	0.60	9.64
Random technique	HR1	7.02	0.46	6.58	4.25	0.48	11.35	6.70	1.13	16.86
	HR2	7.13	0.49	6.87	4.48	0.51	11.31	7.37	1.23	16.70
	HR3	6.77	0.39	5.79	3.98	0.57	14.35	7.12	1.14	14.70
	Mean	6.97	0.45	6.41	4.24	0.52	12.34	7.27	0.94	10.31



Figure 5.44 Undrained shear strength direct measurements in kPa of homogenous traditional technique models: (a) mini ball penetrometer and (b) mini vane.



Figure 5.45 Undrained shear strength direct measurements in kPa of homogenous random technique models: (a) mini ball penetrometer and (b) mini vane.

Heterogeneous models

Figure 5.46 shows the result of the undrained shear strength, C_u values measured with the mini ball penetrometer and the mini vane in the three heterogeneous models (replicates) built with the random technique. The values of the mini vane are presented in the figure with and without the Bjerrum's correction factor (Bjerrum, 1973). The results show that the C_u values measured with the mini ball are 3.4 and 1.9 times greater than those measured with the mini vane (with and without the Bjerrum's correction) respectively.

Table 5.9 summarizes the undrained shear strength statistical values for the three heterogeneous models. For the mini ball, the mean value is 7.31 kPa; for the mini vane, values are 3.95 kPa and 2.25 kPa without and with Bjerrum correction respectively. There is more variability in the measurements made by the mini vane that those made by the mini ball the values of the COV are 13.11 for the mini ball and 15.36 and 19.91 form mini vane. Likewise, the table shows the values estimated with the correlation defined for this study base on the relationship between undrained shear strength and the consistency index Equation 5.17 and Equation 5.18. As in the homogeneous models that values measured with the mini ball are close to the values estimated by Equations 5.17 and 5.18.

Table 5.9 Direct values of undrained shear strength for heterogeneous models.

	Direct measurements									Indirect measurement			
	Mini Ball			Mini Vane			Mini Vane Bjerrum			Equations 5.17 and 5.18			
	C_u (kPa)			C_u (kPa)			C_u (kPa)			C_u (kPa)			
	Mean μ	SD σ	COV	Mean μ	SD σ	COV	Mean μ	SD σ	COV	Mean μ	SD σ	COV	
Heterogeneous	R1	6.97	0.98	14.06	3.93	0.62	15.74	2.23	0.45	19.94	7.31	3.47	47.45
	R2	7.48	0.98	13.11	3.91	0.63	16.01	2.23	0.46	20.72	6.86	2.82	41.12
	R3	7.48	0.91	12.15	4.00	0.57	14.33	2.28	0.43	19.07	7.19	2.74	38.17
	Mean	7.31	0.96	13.11	3.95	0.61	15.36	2.25	0.45	19.91	7.12	2.62	36.76

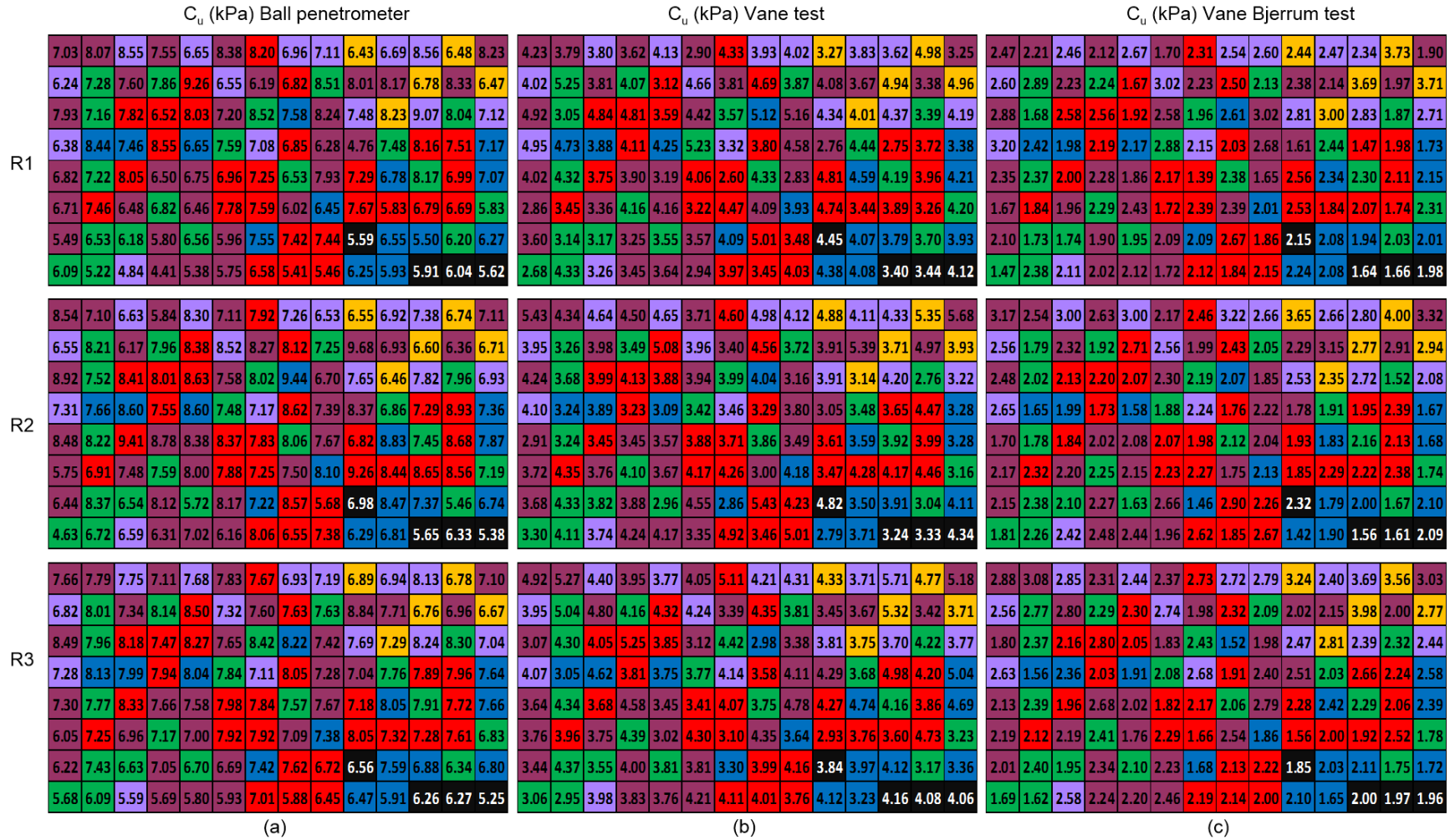


Figure 5.46 Undrained shear strength direct measurements in kPa of heterogeneous models: (a) mini ball penetrometer, (b) mini vane and (c) mini vane Bjerrum correction.

The direct measurements of the undrained shear strength were analysed versus different index properties. This analysis was made with the mean values of the three heterogeneous models for each of the instruments used in the testing.

Figure 5.47 presents the average of the undrained shear strength for the mini ball penetrometer, the mini vane (without correction) and the mini vane with the Bjerrum's correction.

Figure 5.48 shows the relationship between the undrained shear strength and the liquid limit. In Figure 5.48 (a) it can be seen a little increase in the undrained shear strength (mini ball) as the liquid limit increases. On the contrary, in Figure 5.48 (b) y (c) it can be seen that as the liquid limit increases the undrained shear strength decreases after applied the Bjerrum correction factor to the values.

Figure 5.49 shows the relationship of the undrained shear strength and the water content. The behavior of this relationship is comparable as the liquid limit; this is, for mini ball results the shear strength increase slightly as the water content increase, but for mini vane results, the shear strength decrease as the water content increase. Another common relationship made of the undrained strength is with the liquidity index, this relationship also was analyzed and the results are shown in Figure 5.50; however no correlation was found either for the values measured with the mini ball or with those measured with the mini vane. A similar analysis was made with the normalized water content, w^* , which is the ratio of water content to liquid limit. Figure 5.51 shows this relationship, but as for liquidity index no correlation was found.

After the analyses made above, it was decided to select the mini ball penetrometer as the tool to measure the undrained shear strength of the models, in which the bearing capacity tests are to be carried out, on the next section of this thesis. The reason was (i) these results were those that presented better agreement with the results estimated with the correlation between undrained shear strength and the consistency index (Equation 5.17 and Equation 5.18). The undrained shear strength values estimated by these relationships are the most reliable since the data used to establish the correlation were extracted from the triaxial tests of the eight homogeneous soils; (ii) the mini ball penetration test is much quicker than the vane shear test. In addition, vane shear test results typically show more scatter due to the varying amounts of soil disturbance and consolidation, as a result of the vane insertion, before the vane shear test is conducted (Lunne et al. 2011; Zhou and Randolph, 2009a, b; Yafrate et al. 2007).

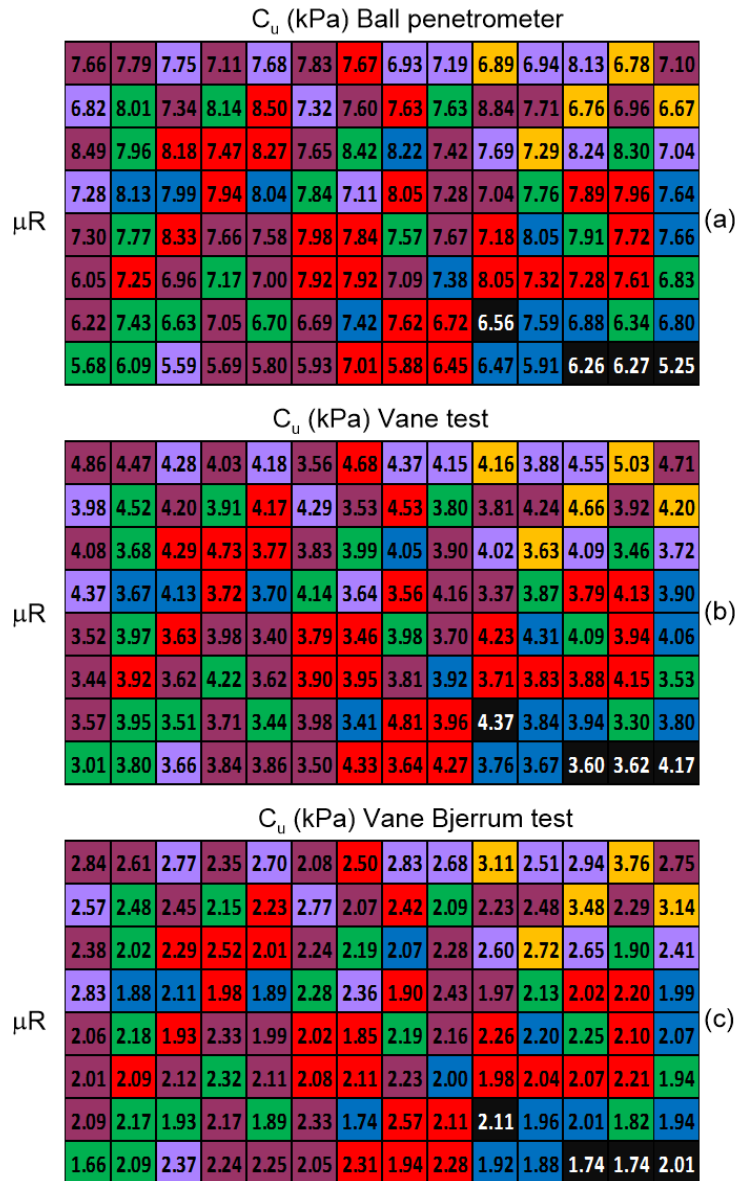


Figure 5.47 Average undrained shear strength direct measurements in kPa of heterogeneous models: (a) mini ball penetrometer, (b) mini vane and (c) mini vane Bjerrum's correction.

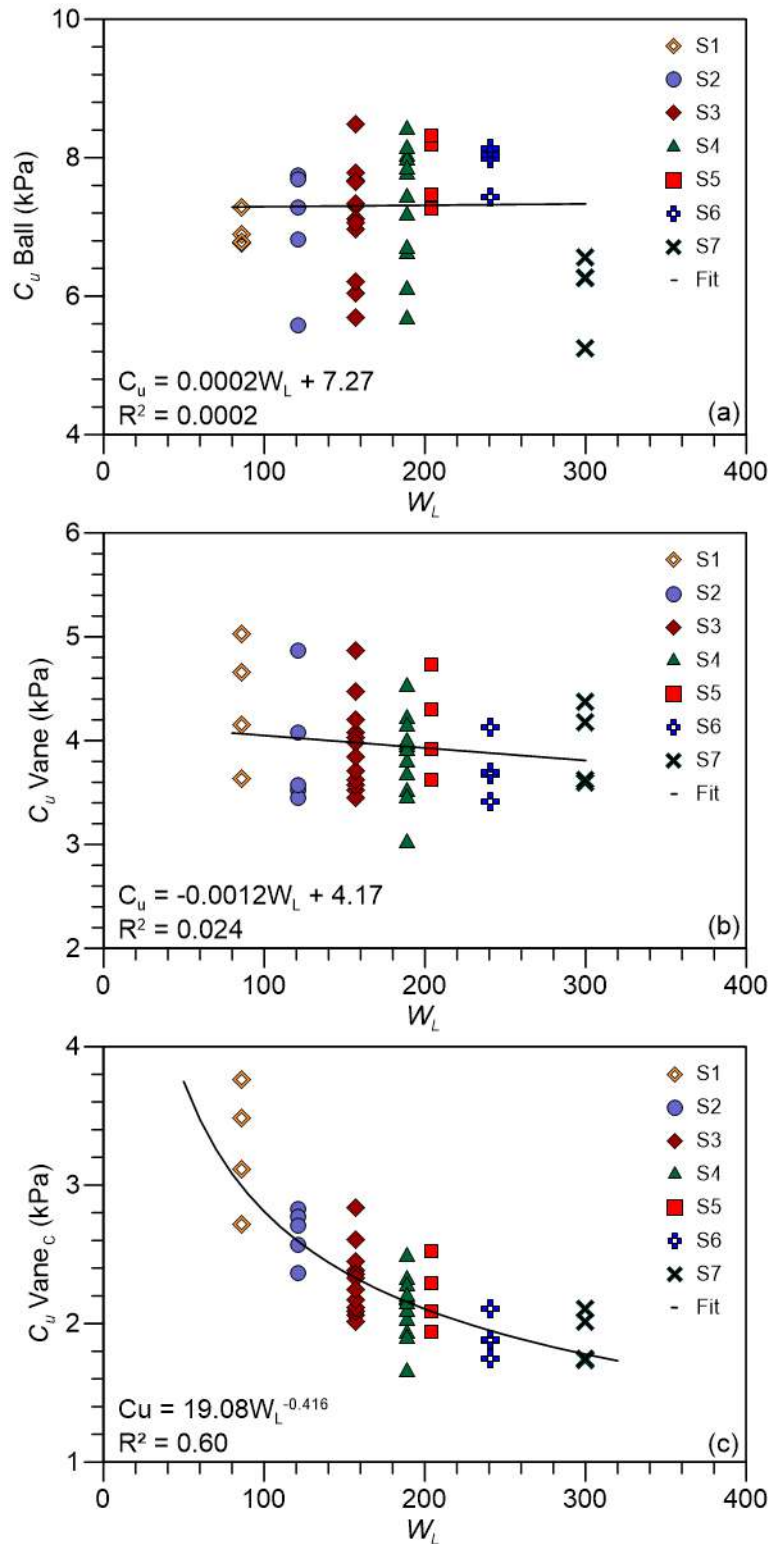


Figure 5.48 Relationship between liquid limit and direct measurements of undrained shear strength: (a) mini ball penetrometer, (b) mini vane and (c) mini vane Bjerrum's correction.

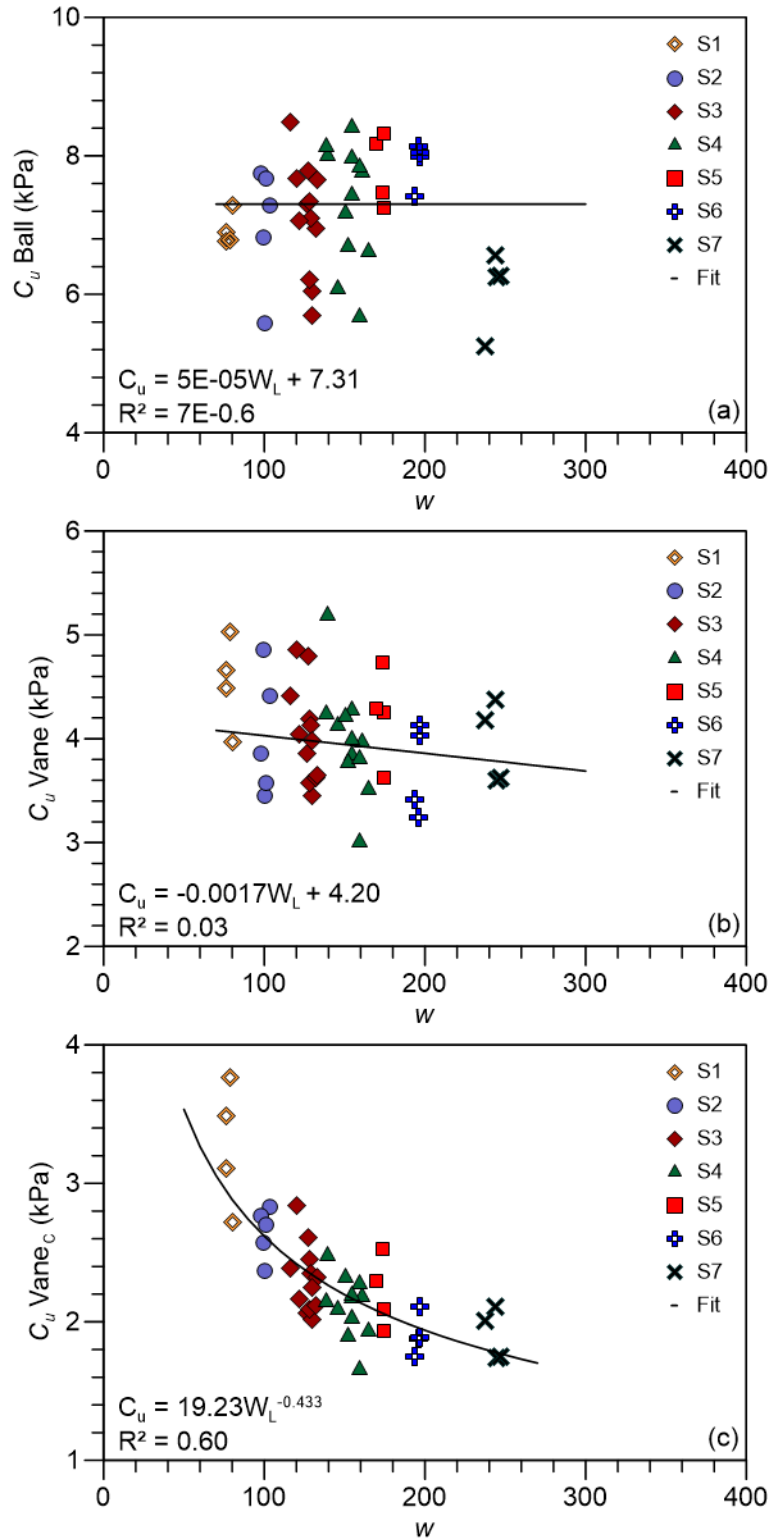


Figure 5.49 Relationship between water content and direct measurements of undrained shear strength: (a) mini ball penetrometer, (b) mini vane and (c) mini vane Bjerrum's correction.

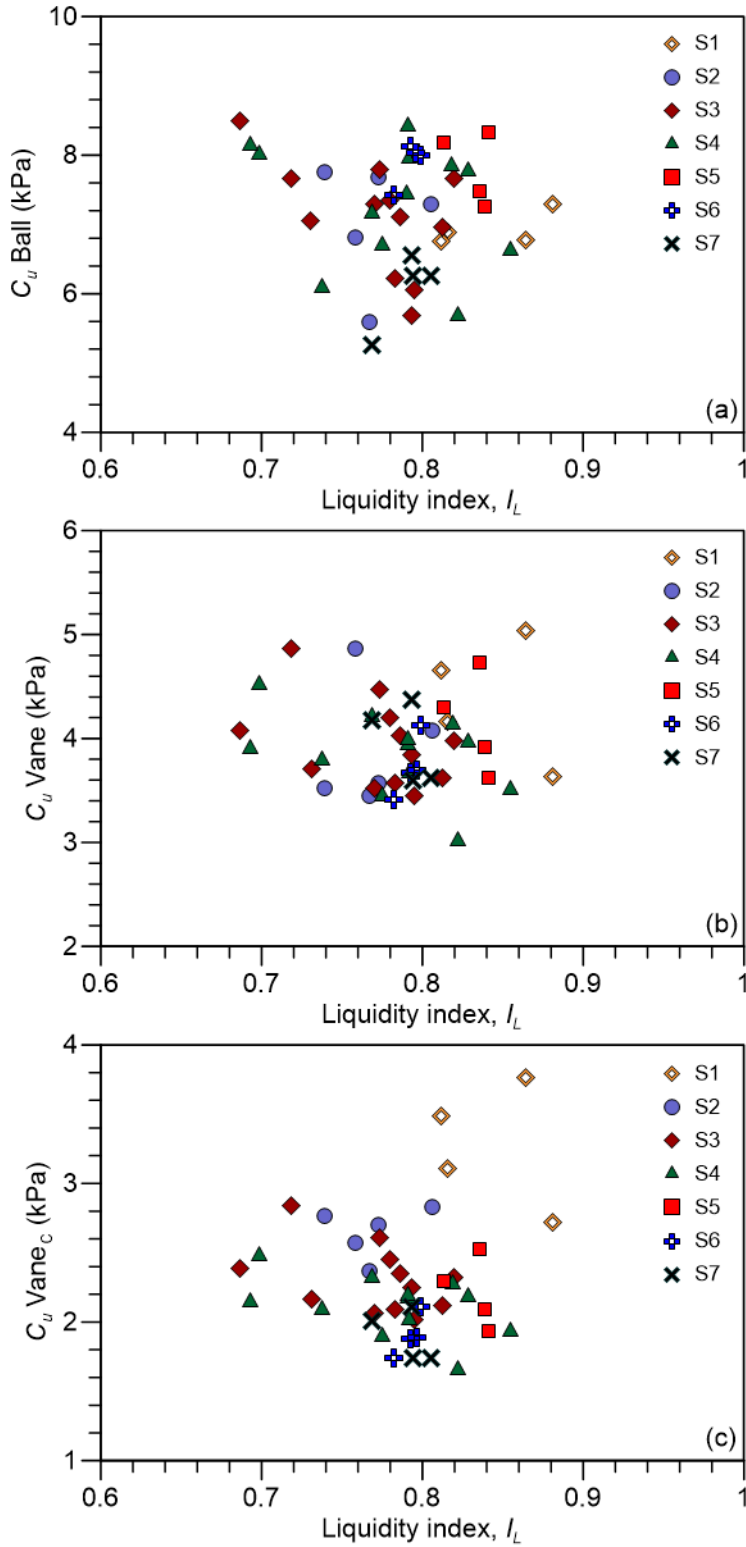


Figure 5.50 Relationship between liquidity index and direct measurements of undrained shear strength: (a) mini ball penetrometer, (b) mini vane and (c) mini vane Bjerrum's correction.

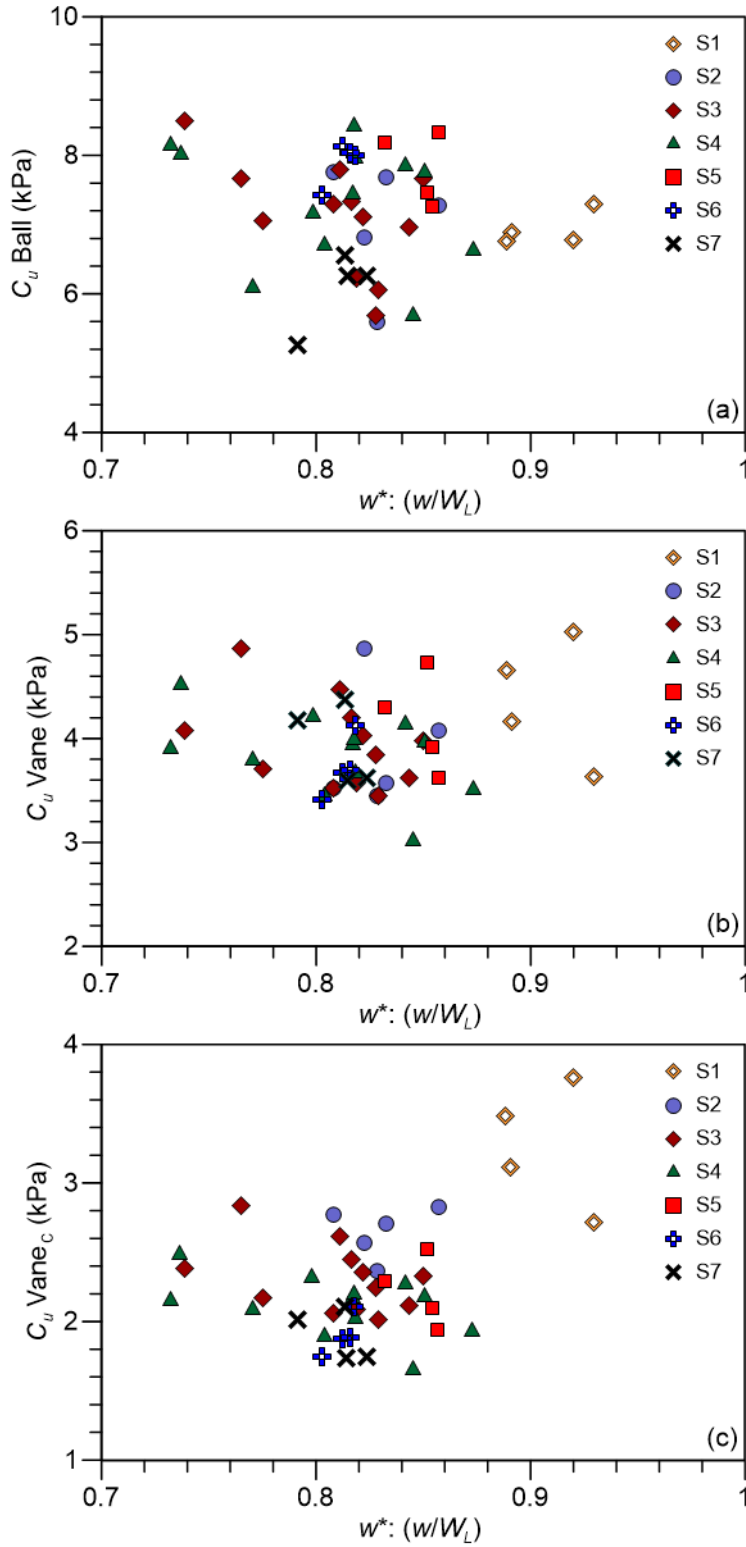


Figure 5.51 Relationship between normalized water content, w^* and direct measurements of undrained shear strength: (a) mini ball penetrometer, (b) mini vane and (c) mini vane Bjerrum's correction.

5.7 Conclusions

The effect of the uncertainty of soil properties has been widely studied using a variety of numerical models constructed from random field theory. However, to our knowledge, no effort has been made to verify these numerical results experimentally. This work presents a new technique to prepare reduced scale soils models with controlled variability. The methodology proposed combined random field theory with geotechnical centrifuge modeling. One realization from a prescribed random field is reproduced by varying the mineralogy, manifested by varying liquid limit, in each cell of the physical model. In short, this physical model consists of discrete cells where variability is controlled by a simulation realization of a random field. A physical model containing variable mechanical property (undrained shear strength) is then created by consolidating the physical model in one stage. Note that the variability of the mechanical property is not the same as the variability of the liquid limit, because the former is an output from a boundary value problem (non-uniform 1D stress applied to the top of the physical model using a rigid plate) while the latter is the input. The method proposed in this work offers new possibilities for the study of the effect of soil variability on the behavior of geotechnical structures; furthermore, this method could be a powerful tool to validate and calibrate numerical models.

- A new technique to prepare reduced scale soils models with controlled variability have been development satisfactory in the laboratory. Proof of this is that the spatial variability has been captured by the resistance measurements of the soil made by the electrical needle prove.
- The heterogeneous model built in the laboratory behave as a compact and single model since not fissures or week planes develop between the interfaces of each soil due to construction.
- The consolidation process has worked well since the stress levels imposed have been reached; moreover, there are no significant differences in the values of the undrained shear strength between the models constructed with the traditional technique and the new technique.
- The undrained shear strength has been calculated directly by the mini ball and the mini vane apparatus, and indirectly by the Cam Clay theory (measurements of water content) and two empirical correlations Leroueil et al., (1983) and Hong et al., (2003).
- Two correlations were defined for this study base on the relationship between undrained shear strength and the consistency index, IC , given by Leroueil et al., (1983). The date uses to establish the relationships were extracted from the triaxial tests of the eight homogeneous soils.

- The results show that the undrained shear strength, C_u values measured with the mini ball are 3.4 and 1.9 times greater than those measured with the mini vane (with and without the Bjerrum's correction) respectively.
- There are good agreement between the undrained shear strength, C_u estimated with the two correlations with the consistency index (Equation 5.17 and Equation 5.18) and the undrained shear strength, C_u measured with the mini ball.
- The mini ball penetrometer was selected as the tool to measure the undrained shear strength of the models, in which the bearing capacity tests are to be carried out, on the next section of this thesis.

6 PHYSICAL MODELING OF SHALLOW FOUNDATION

In this section, the effect of the spacial variability of the soil property on the behavior of a shallow foundation was studied. For that purpose, a micro loading apparatus operating under controlled displacement was designed and built. In the first part of this section, a description of this micro loading apparatus is presented. Then, the characteristics of the bearing capacity test are stated. The results of seven in-flight bearing capacity tests result of six heterogeneous models and one homogeneous model, which were constructed with the procedure followed in the two-layers stage explained in Charter 5 are presented first. Then, 55 in-flight bearing capacity tests results (50 heterogeneous and five homogeneous), which were constructed in one-layer are discussed later. The discussion started with a qualitatively analysis of the failure mechanisms of some of the 55 models. Finally, the results of the bearing capacity test performed are discussed. All the tests were performed in the mini-geotechnical centrifuge of Universidad de los Andes.

6.1 Bearing capacity test characteristic

In this work, the effect of the coefficient of variation, COV_{WL} and the horizontal scale of fluctuation, δ_h on the bearing capacity of a shallow foundation was physically validated. These parameters were selected because: (i) in the studies made by Fenton and Griffiths (2002); Fenton and Griffiths (2003); Popescu et al. (2005) and Griffiths et al., (2006) was found that the coefficient of variation is one of the most important probabilistic parameters that reduced the ultimate bearing capacity; (ii) Soubra et al. (2008) stated that the footing load capacity is more sensitive to the variation of the horizontal correlation length than the vertical one. For the coefficient of variation three cases were evaluated: COV_{WL} 51%, COV_{WL} 30% and COV_{WL} 13%, and for the horizontal scale of fluctuation three cases were considered: 1.5m, 6m and 15m in prototype scale, for each example 10 realizations of the random field were performed for a total of 50 in-flight bearing capacity tests in heterogeneous models (the 10 realizations of model with COV_{WL} 30% are the same of the model with $\delta_h=1.5m$). Also, five in-flight bearing capacity tests were conducted in homogeneous models, soil S3, which have a liquid limit corresponding to the mean of the liquid limit of the heterogeneous models.

At the beginning of the study, the value of the vertical scale of fluctuation was chosen equal to the estimated for the Bogota's clay, 2.2 m; however, this value change to 1.5 m due to the size of the model, the size of the soil elements and the width of the model foundation 1.5m in prototype scale. Furthermore, it was a convenient value for the vertical scale of fluctuation since it permits to evaluate the isotropic case studied by Fenton and Griffiths (2003) and also the statement of Soubra et al., (2008), which said that a critical case occurred when the horizontal scale of fluctuation is equal to the footing width, B .

On the other hand, the horizontal scale of fluctuation for the two anisotropic cases was chosen 30m and 60m initially. These values are one order of magnitude larger than the vertical scale and are in the range of 40m - 60m suggested values by Phoon and Kulhawy (1999). However, the ran-

dom fields generated with these horizontal autocorrelations length create layered soils as it can see in Figure 6.1. For this reason, the final horizontal scales of fluctuation chosen were 6m and 15m generating more variable fields (Figure 6.2). Table 6.1 summarized the working plan of the bearing capacity test.

Table 6.1 Bearing capacity tests plan.

Input parameters of the WL random field			
Model	Constant parameter	Variable parameter	Number of Realizations
Heterogeneous			1.5m*
	$\mu_{WL}^a = 157\%$ $COV_{WL}^b = 30\%$ $\delta_v^c = 1.5m^*$	δ_h^d	6m*
			15m*
			51%
	$\mu_{WL}^a = 157\%$ $\delta_h^d = 1.5m^*$ $\delta_v^c = 1.5m^*$	COV_{WL}^b	30%
			13%
Model	Input parameters of the WL random field		Number of Realizations
Homogeneous	$\mu_{WL}^a = 157\%$ $COV_{WL}^b = 0\%$		5
Total bearing capacity tests			55

^amean liquid limit, ^bcoefficient of variation liquid limit, ^cvertical scale of fluctuation liquid limit, ^dhorizontal scale of fluctuation liquid limit, ^ethese realizations are the same of the isotropic model $\delta_h = 1.5m$, *values are given in prototype scale.

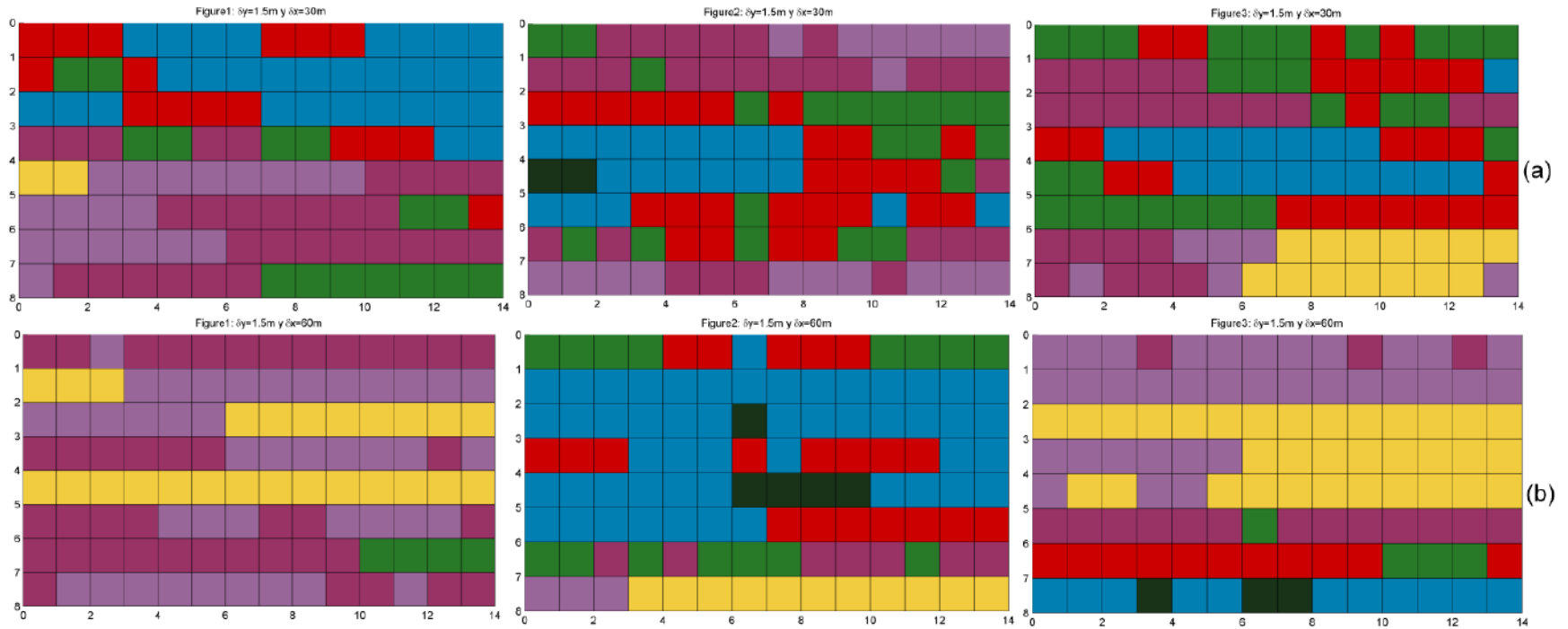
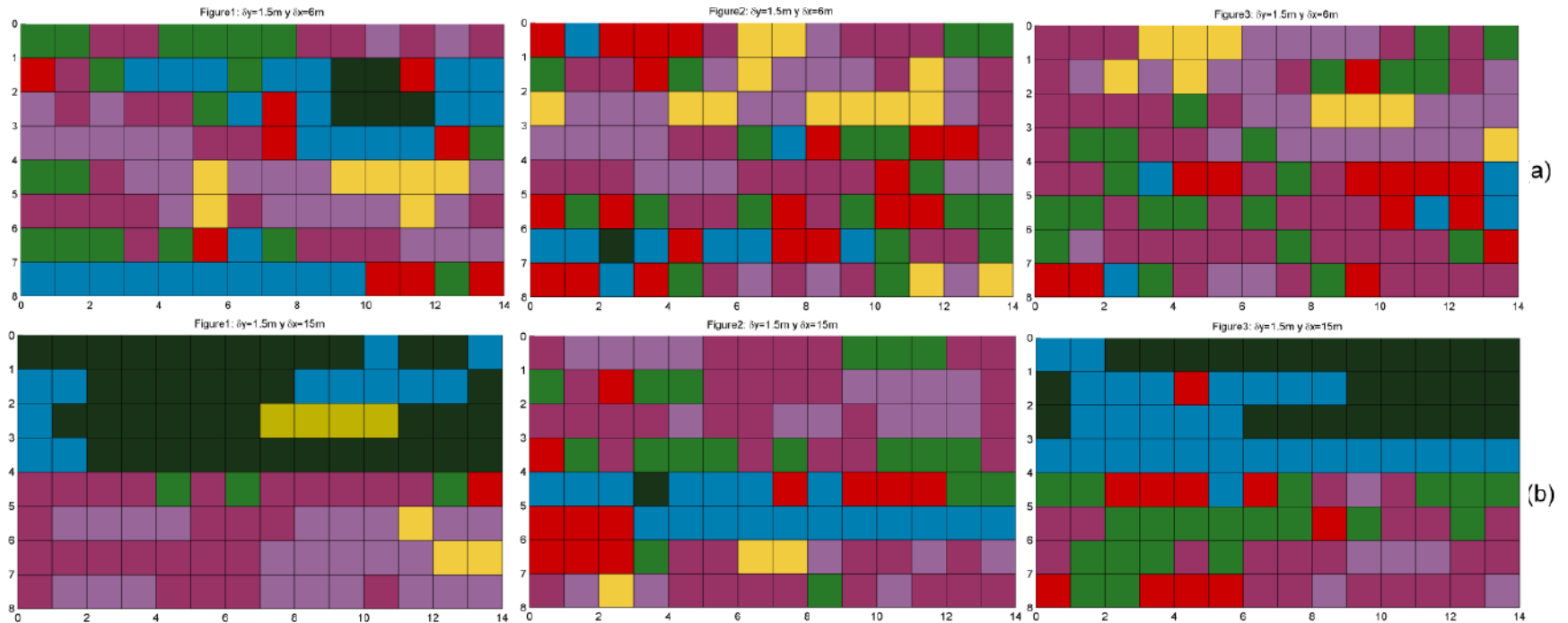


Figure 6.1 Random fields: (a) horizontal scale of fluctuation of 30m, (b) horizontal scale of fluctuation of 60m.



6.2 Micro-loading system

6.2.1 General description

The device has two major parts: (i) a fixed beam having the driving stepper motor with a linear actuator, and two guiding shafts; and (ii) a moving platform that has a secondary supporting beam, this beam has two bushings to guarantee a linear vertical displacement without any rotation, and three load cells to measure the vertical, moment and horizontal reactions over the foundation. The two parts are connected to the motor shaft, which is attached to the moving platform beam. The beams, the auxiliary components, and the footing strip are made of epoxy fiberglass 10 mm in thickness. This material was selected due to its high yield point and lightweight. The bushings and the shafts are in stainless steel. Figure 6.3 shows the two major parts of the micro-loading system. The micro-loading system can drive the footing strip at a constant rate into the clay.

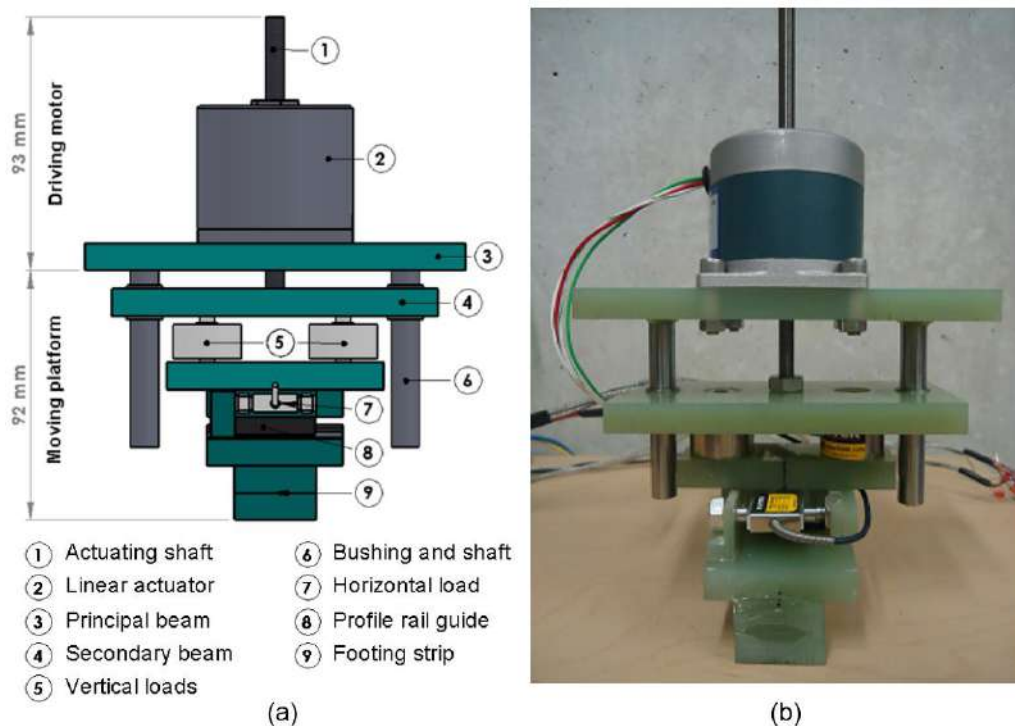


Figure 6.3 Micro-loading system: (a) scheme, (b) constructed model

6.2.2 Driving motor part

As described above, the driving motor part has a central supporting beam of 57 mm in width and 140 mm in length. On top of the beam, a linear actuator is fixed, and two stainless steel shafts of 75 mm in length are joined at the edges. The linear actuator has a body size of 57 x 57 mm and 4.3 mm in height. It has an EAD motors Size 23 hybrid stepping motor, having an internal rotating nut made of SAE 660 bearing bronze. Figure 6.4 shows the sizes of the driving motor part.

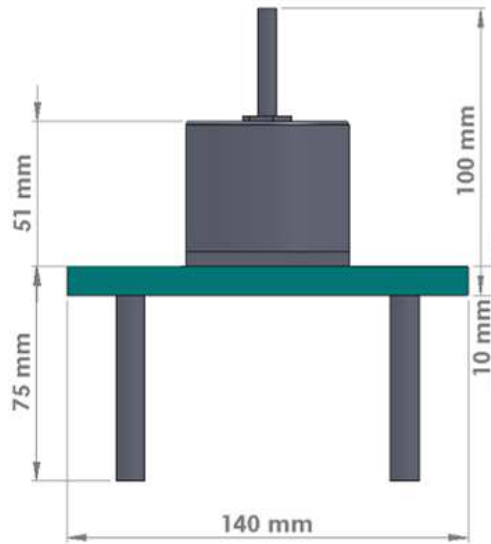


Figure 6.4 Schema of the driving motor part.

6.2.3 Moving platform part

The moving platform is the most complicated part of the device since in this part the loading system is housed. The platform has the following components: a supporting beam of 57 mm in width and 120 mm in length, which has at the edges two stainless steel bushings. Then, two mini tension-compression load cells of 222.4 N, 30.73 mm in height and 24.89 mm in diameter are fixed in the inner part of the supporting beam. Next, another supporting beam of 26 mm in width and 80 mm in length holds the base of the tension-compression load cells. Then, a miniature S beam load cell of 44.5 N is sticking to an L-shaped beam, which is fixed to a profile rail guide that is attached to another pole. Finally, the footing strip of 70 mm in width and 30 mm in length is formed by two epoxy fiberglass elements to create a footing of 20 mm in depth. Figure 6.5 shows the moving platform part.

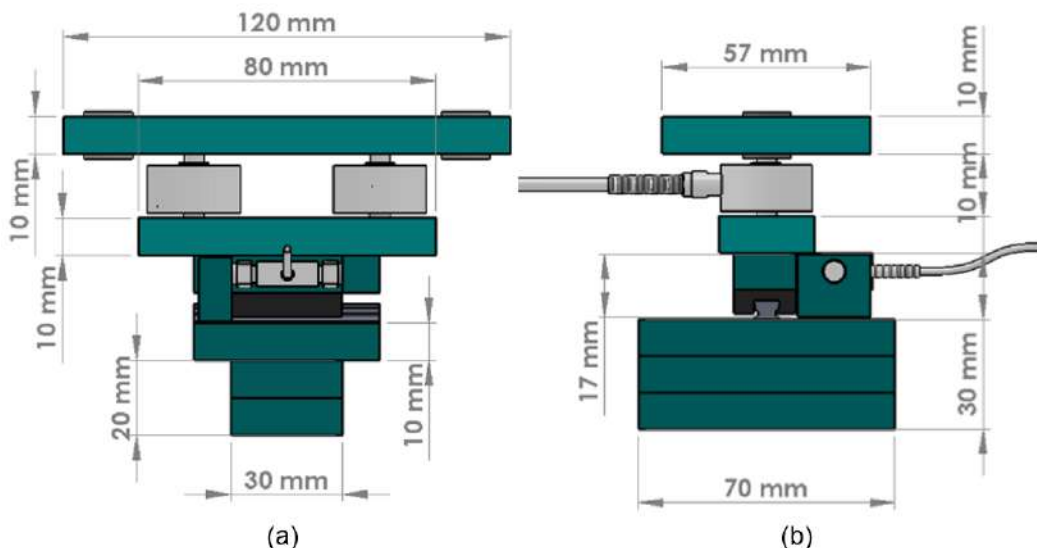


Figure 6.5 Schema of the moving platform: (a) front view, (b) lateral view.

6.2.4 Software development

The control software was developed using LabView (National Instruments Corporation, 2014). As mentioned above, the device was designed to perform tests at a constant rate of displacement; for that reason, the software allows manual control of the displacement rate. The minimum and maximum rate of displacement are 0.01 mm/min and 5 mm/min respectively. The load and displacements data are sent to an external computer through the wireless data acquisition system mounted at the rotation center of the mini centrifuge.

6.3 Step by step of the bearing capacity test

The bearing capacity test is performed immediately after the centrifuge consolidation. Before carrying out the test, the models surface is sliced to guarantee a horizontal surface, and a grid is painted at a separation of 1 cm x 1 cm to analyze the failure mechanism (Figure 6.6). The micro-loading device was fixed to the centrifuge container using two stainless steel supports. Then, the centrifuge was accelerated up to 50g. Next, the model was allowed to fly for one minute until the system got stabilized. Finally, the bearing capacity test was performed at a displacement rate of 0.05 mm/min. The test finished until reach a displacement of 20 mm. A web camera fixed to the swinging basket container captured images during the test. Figure 6.7 shows the assembly of the bearing capacity test.

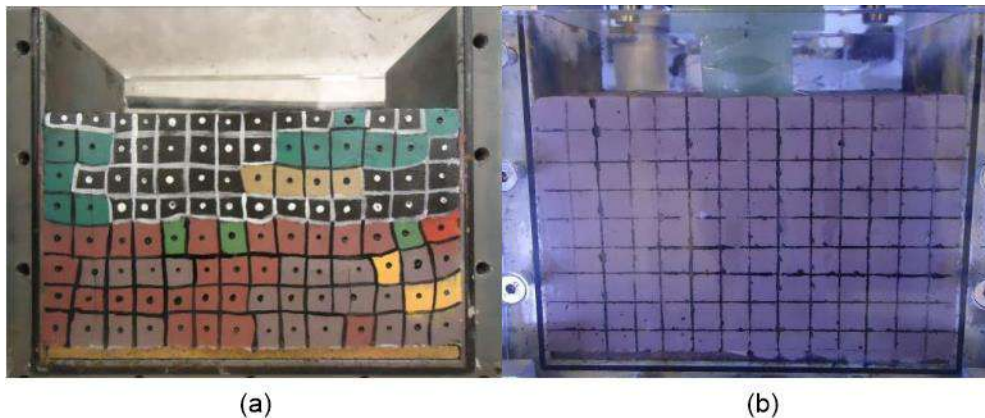


Figure 6.6 Painted grid model: (a) heterogeneous model, (b) homogeneous model.

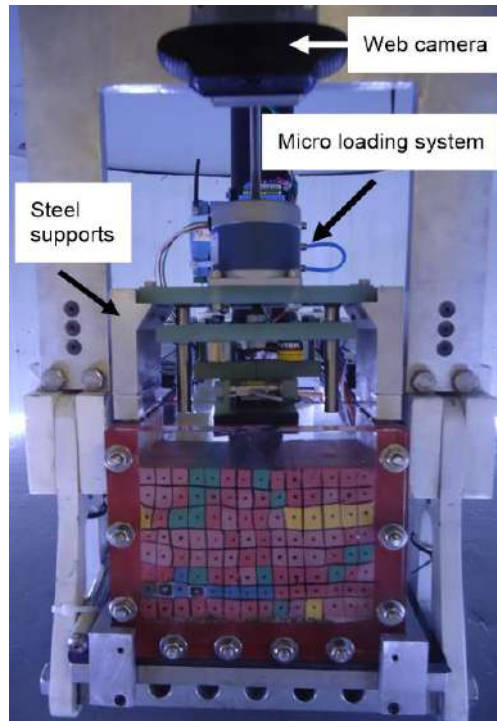


Figure 6.7 Micro-loading system installed in the mini centrifuge.

6.4 Bearing capacity test results: models built in two-layers procedure

As mentioned above, seven bearing capacity test was performed in the mini-geotechnical centrifuge of Universidad de los Andes (one homogeneous and six heterogeneous). The homogeneous case was the soil S2, and the six heterogeneous models have different horizontal scale of fluctuation: $\delta_h=1.5m$, $\delta_h=6m$ and $\delta_h=15m$ (two of each one). The models were named M1-1.5m and M2-1.5m, M1-6m and M2-6m, and M1-15m and M2-15m. It should be mentioned here that the results of the seven tests aim to demonstrate the capabilities of the micro-loading device. A detailed analysis of the effect of the soil spatial variability on the ultimate bearing capacity as well as on the failure mechanisms is described in Section 6.5.

Figure 6.8 shows the results of the bearing capacity tests of the homogeneous model, and Figure 6.9, Figure 6.10 and Figure 6.11 show the results of the bearing capacity tests of the three heterogeneous models for the different horizontal scales of fluctuation. The initial and final images of the model (before and after the test) are presented on the left side of the figures, while the load-settlement curves are show on the right side. For the homogeneous model (soil S2), it can be seen that the values of the two vertical loads (V1 and V2) are similar and therefore any moment was generated; moreover, the value of the horizontal load (H) was nearly zero. In contrast, for the three heterogeneous models the two vertical loads cells recorded different loads that correspond to a moment in the foundation, and a non-null horizontal load was measured. Also, it can be seen as the horizontal scale of fluctuation increases the response of the capacity of the soil increase.

After study the recorded images, it was detected, for all models, that the failure mechanism ongoing in the third row (counting from top to bottom). This weak plane coincides with the boundary layer of the construction technique development in two-layers explained in Section 5.5. Another consequence of building the models in two-layers was that the first five model's rows were over consolidated and the last three rows normal consolidated affecting the bearing capacity results.

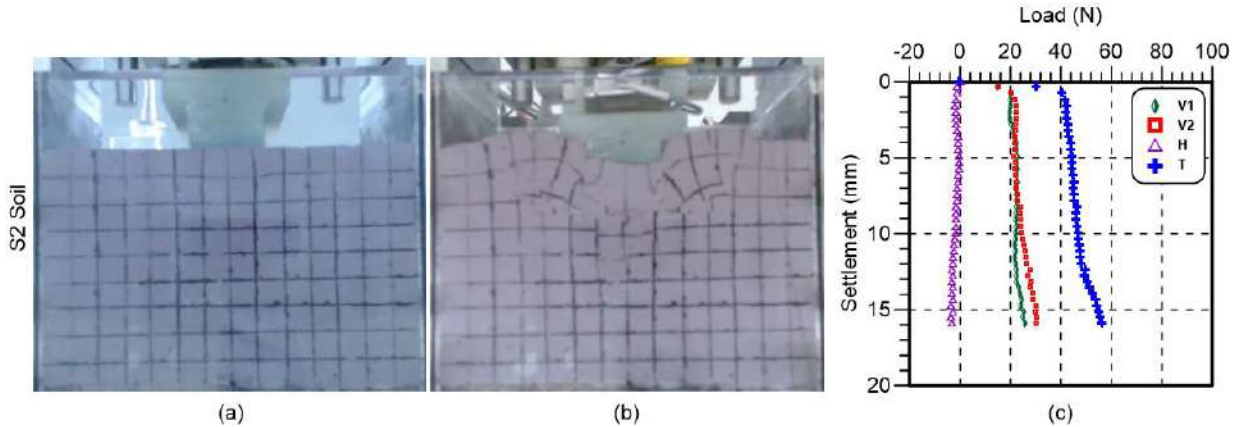


Figure 6.8 Initial and final images and settlement-load curves: homogenous model S2

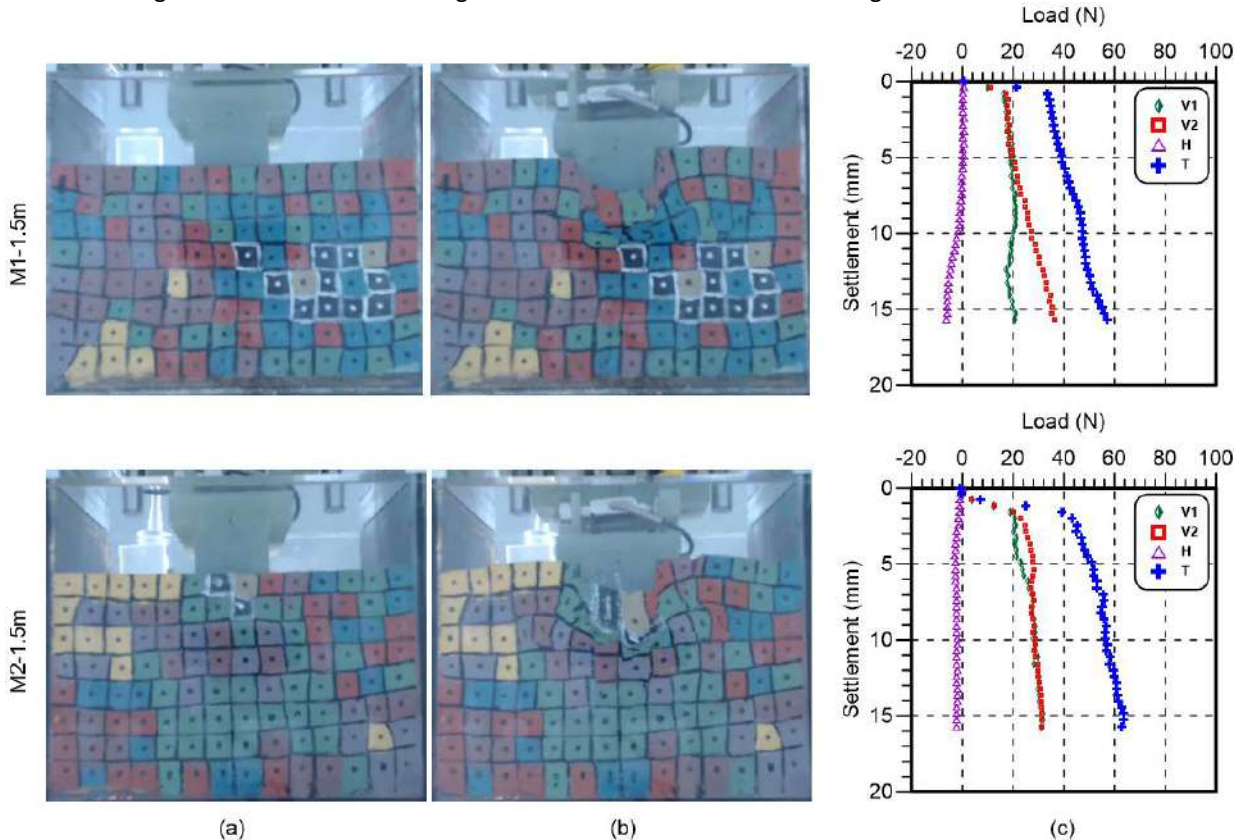


Figure 6.9 Initial and final images and settlement-load curves: models M1-1.5m and M2-1.5m

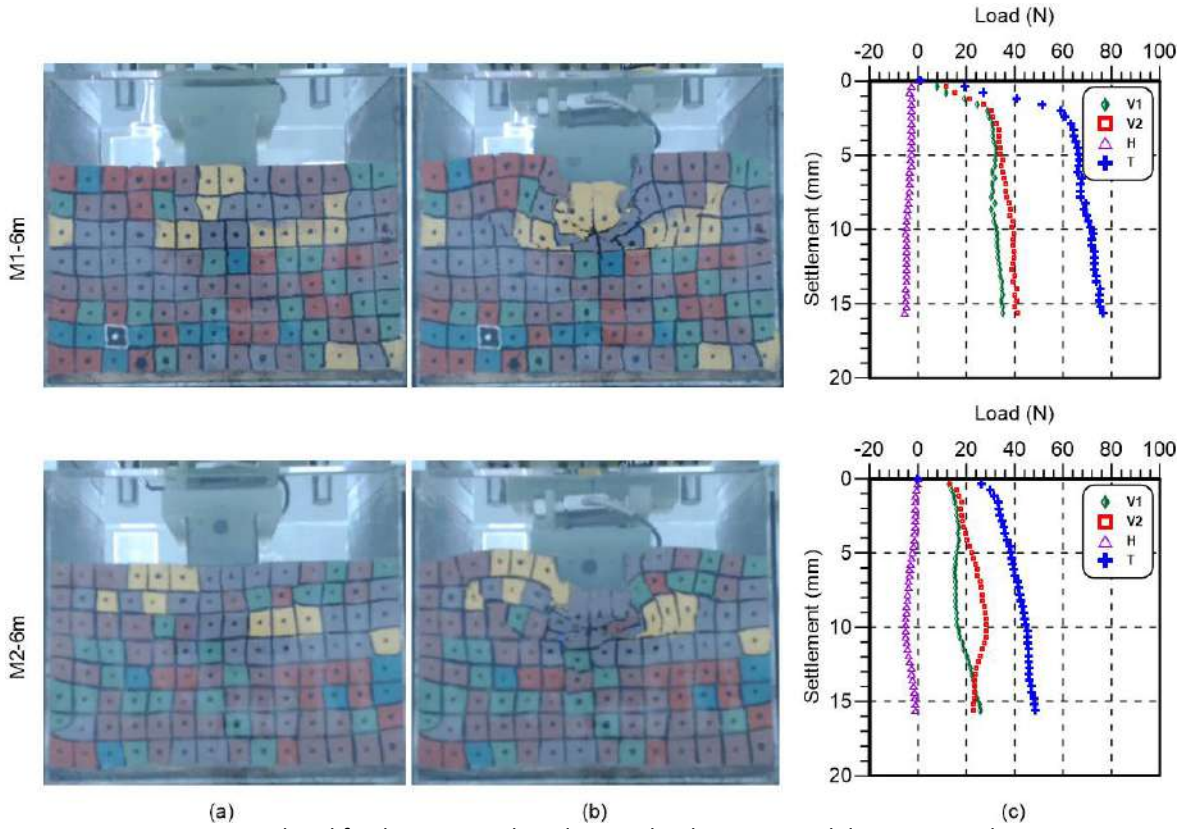


Figure 6.10 Initial and final images and settlement-load curves: models M1-6m and M2-6m

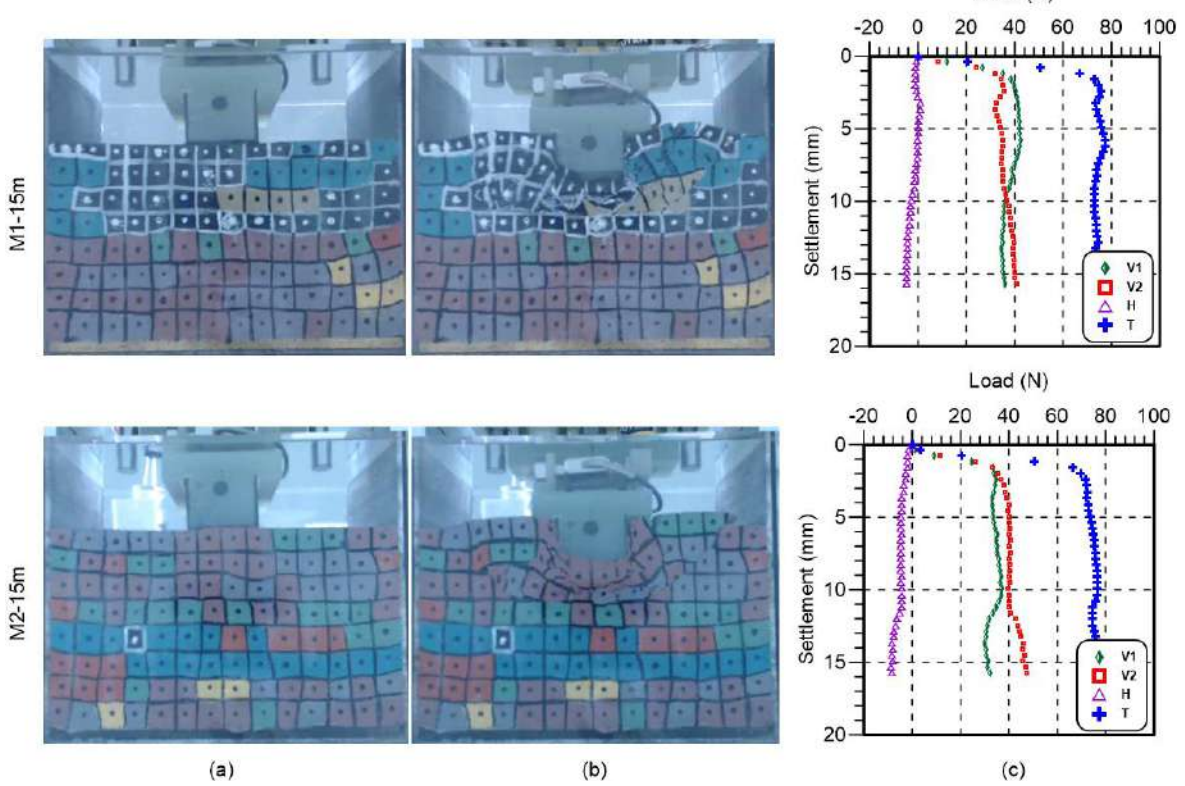


Figure 6.11 Initial and final images and settlement-load curves: models M1-6m and M2-6m

Figure 6.12 shows the effect of the horizontal scale of fluctuation on the bearing capacity. As mentioned above, the lower value corresponds to the case when the horizontal scale of fluctuation is the same than the width of the foundation.

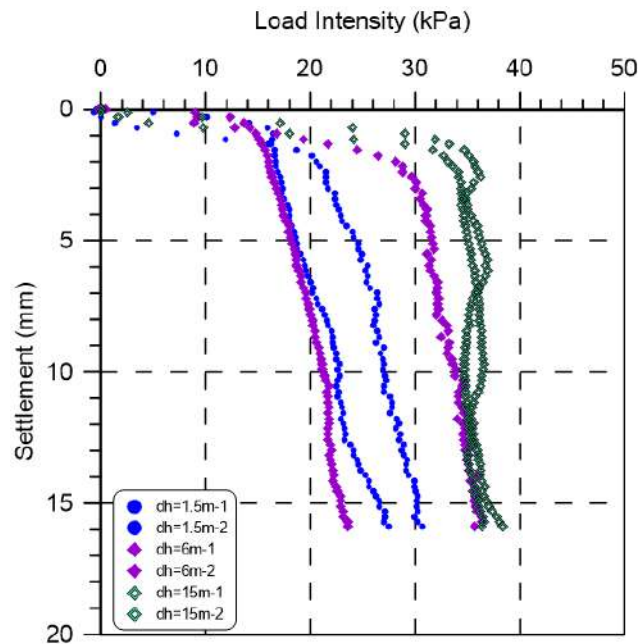


Figure 6.12 Effect of the horizontal scale of fluctuation.

6.5 Bearing capacity test results: models built in one-layer procedure

As mention above, 55 in-flight bearing capacity tests were performed, 50 for heterogeneous models and 5 for homogeneous. For evaluating the effect of the coefficient of variation, three cases were assessed COV_{WL} 51%, COV_{WL} 30% and COV_{WL} 13%, and for assessing the effect of the horizontal scale of fluctuation three cases were considered 1.5m, 6m and 15m, for each case 10 realizations of the random field were performed for a total of 50 in-flight bearing capacity tests in heterogeneous models (the 10 realizations of model with COV_{WL} 30% are the same of the model with $\delta_h=1.5m$). The models were named COV_{WL} 51% - 1 to 10 for the three cases of the coefficient of variation; the same for the three cases of horizontal scale of fluctuation $\delta_h=1.5m$ - 1 to 10. Also, five in-flight bearing capacity tests were conducted in homogeneous models, soil S3, which have a liquid limit corresponding to the mean of the liquid limit of the heterogeneous models, in this case the models were named HOMO 1 to 5. For all the test load-settlement curves were draw, and the ultimate bearing capacity were estimated using a serviceability criterion. For all models, the undrained shear strength of each of the 113 cells was measurement by using the mini ball penetrometer as described in Section 5.6.2; this procedure was made after the bearing capacity test. Furthermore, for all the models, a qualitatively analysis of the failure mechanism was made.

6.5.1 Analysis of the failure mechanism

The failure mechanics were analyzed qualitatively by compared the images in different times of the bearing capacity test. This analysis was made for all the models; however, only one model of

each case is presented in this section, one homogenous model and five heterogenous models: COV_{WL} 51%, COV_{WL} 30%, COV_{WL} 13%, $\delta_h = 6m$ and $\delta_h = 15m$ (case $\delta_h = 1.5m$ is the same case of COV_{WL} 30%). The four times selected correspond to 0mm, 3mm, 10.5mm and 18mm settlement or 0%, 10%, 35% and 60% displacement of the foundation diameter $B = 30mm$ (model scale).

Figure 6.13 shows the failure mechanism and the load - settlement curve for the homogeneous model number three Homo 3. It can be seen that a punching wedge, slightly tilted to the right, appear first followed by the development of symmetrical failure surface that travels until the surface; it can observe a boundary problem due to the size of the container that does not allow the total development of the failure surface.

Figure 6.14 shows the failure mechanism and the load - settlement curve for the heterogeneous model COV_{WL} 13% number three. It can be seen that the failure surfaces appear after settling greater than 3mm. The failure surface is development first at the right, and then progress to the left to a final symmetrical failure surface that travels until the surface. It can also be seen that a secondary failure surface appears in the upper right part of the model as a concave curve upwards.

Figure 6.15 shows the failure mechanism and the load - settlement curve for the heterogeneous model COV_{WL} 30% number three. It can be seen that the failure surface first appears as a straight line sloping to the left just below the footing. Also, it can be seen that soil S6 and soil S4, which are arranged diagonally one below the other, failed with shear failure and in this zone, the failure surface begins to develop. Finally, a non-symmetric shape of the failure mechanism that rotated to the left is formed.

Figure 6.16 shows the failure mechanism and the load - settlement curve for the heterogeneous model COV_{WL} 51% number three. Similar to the failure mechanism of the heterogeneous model explained above, the failure surface first appears as a straight line sloping to the left just below the footing. Then, another two straight failure lines appear, one sloping to the left and the other sloping to the right. Finally, these two straight failure lines form a symmetrical failure surface that travels until the surface; also in this model, the boundary problem that does not allow the development of the failure mechanics to the surface is presented.

Figure 6.17 shows the failure mechanism and the load - settlement curve for the heterogeneous model $\delta_h=6m$ number three. In this model again the failure surfaces appear first as straight line sloping to the left in this area soil S4 fail with shear failure. Then, multiples straight failures lines appear below the footing forming a non-symmetric failure shape that rotated to the right.

Figure 6.18 shows the failure mechanism and the load - settlement curve for the heterogeneous model $\delta_h=15m$ number three. Like the other models, the first failure surface that

is formed is a straight line with slope to the right. Then, a punching wedge, slightly tilted to the left, formed followed by the development of a non-symmetric failure shape that rotated to the left.

A general conclusion of the failure mechanics analysis of the 50 heterogeneous soils and the five homogeneous soils is that in the case of the homogeneous models symmetric shape failure was present, whereas in the case of the heterogeneous soils a non-symmetric shape of the failure mechanism is visible. This phenomenon is critical to understand since the inherent spatial variability of the soil properties is not only affecting the bearing capacity value of the soils, but it is also modifying the basic form of the failure.

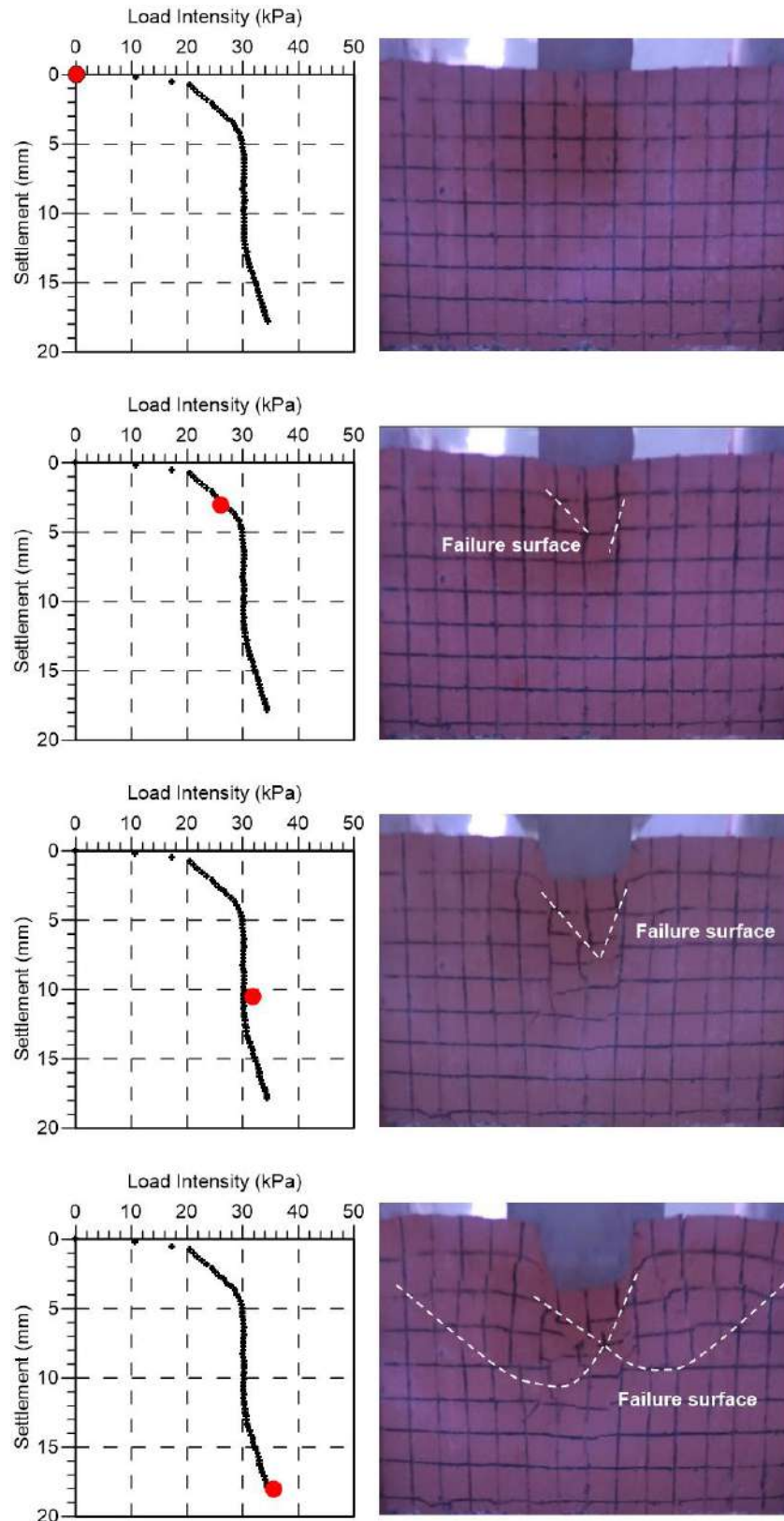


Figure 6.13 Evolution of the failure mechanism of homogeneous model Homo 3.

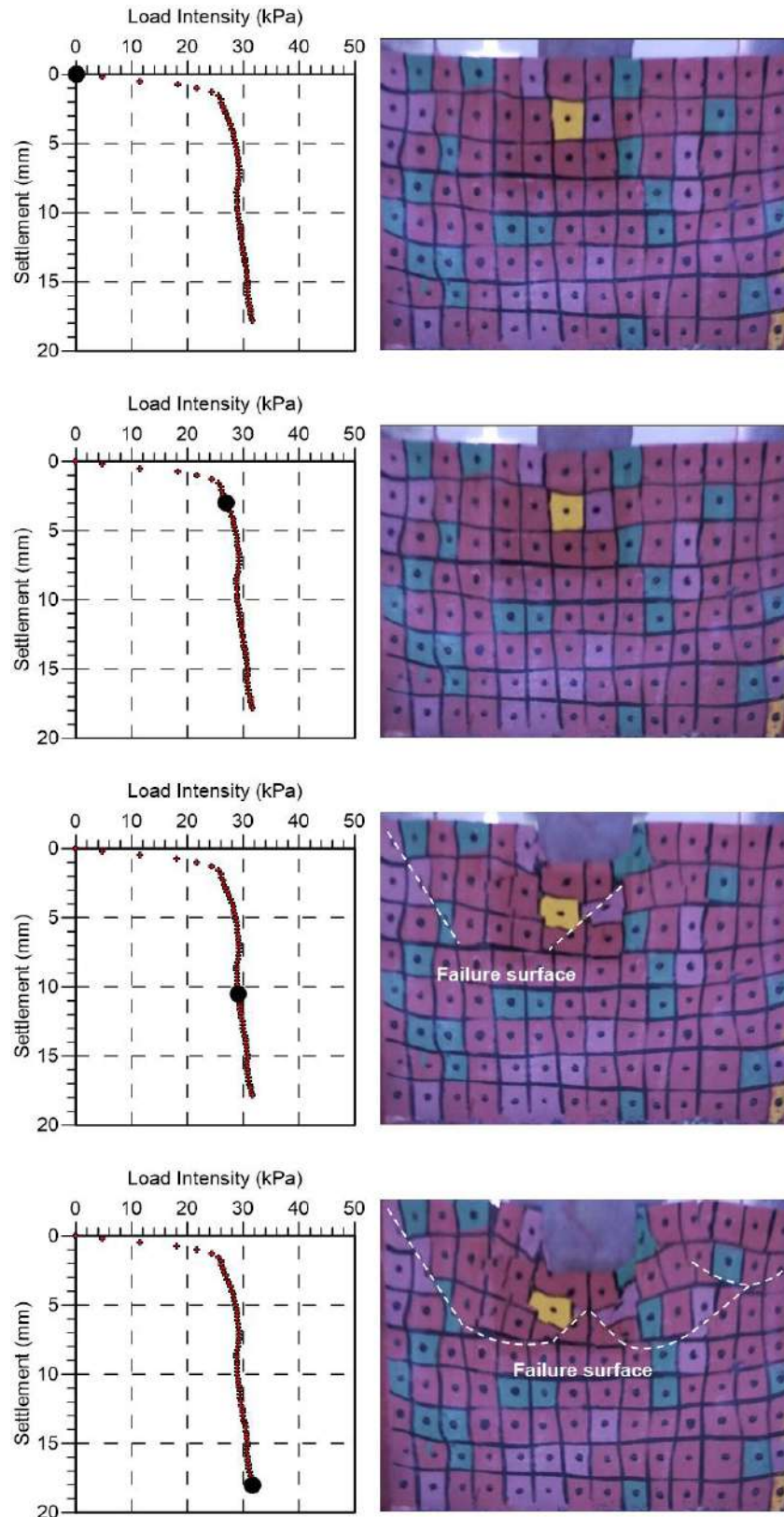


Figure 6.14 Evolution of the failure mechanism of heterogeneous model COV_{wl} 13%.

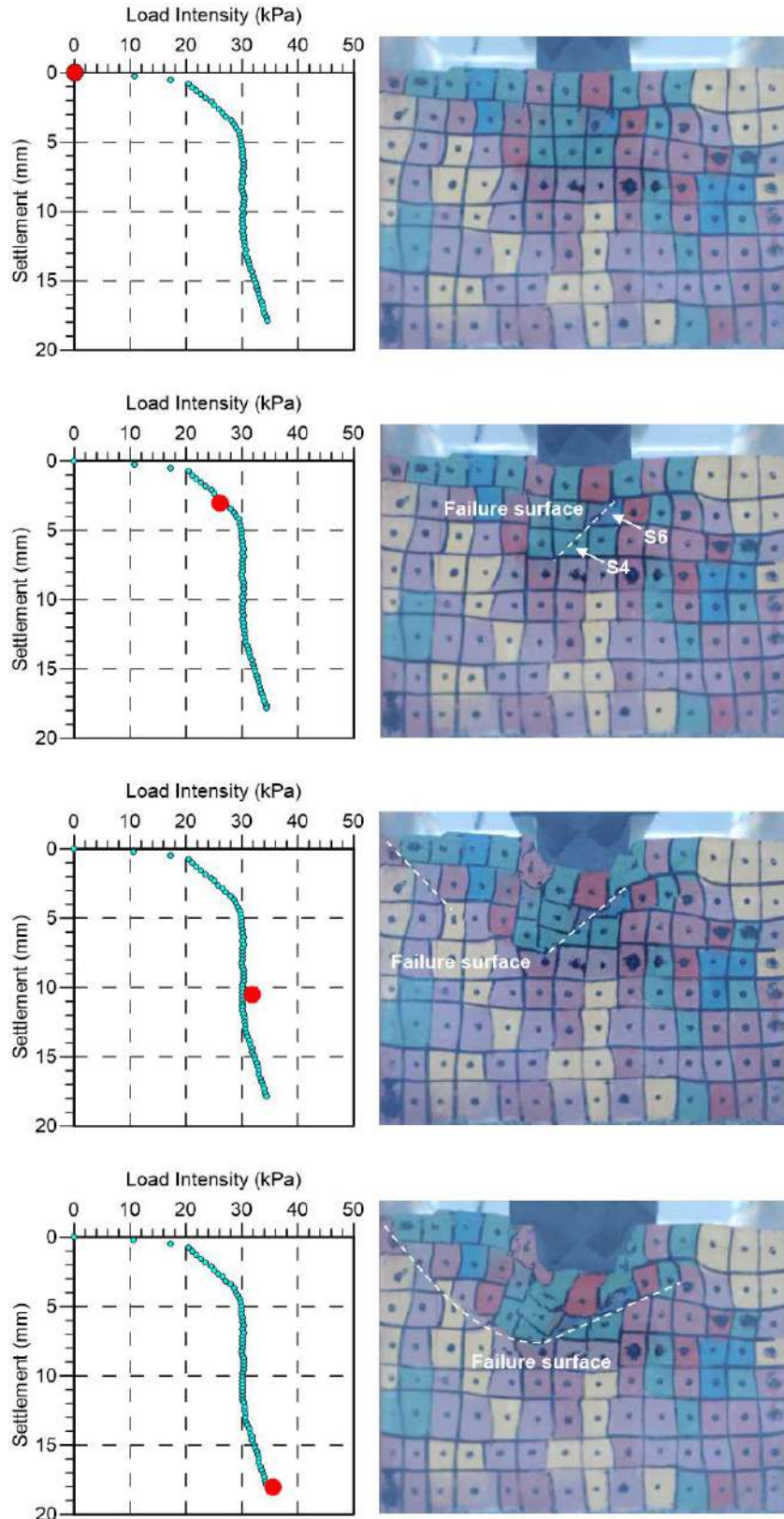


Figure 6.15 Evolution of the failure mechanism of heterogeneous model COV_{wl} 30%.

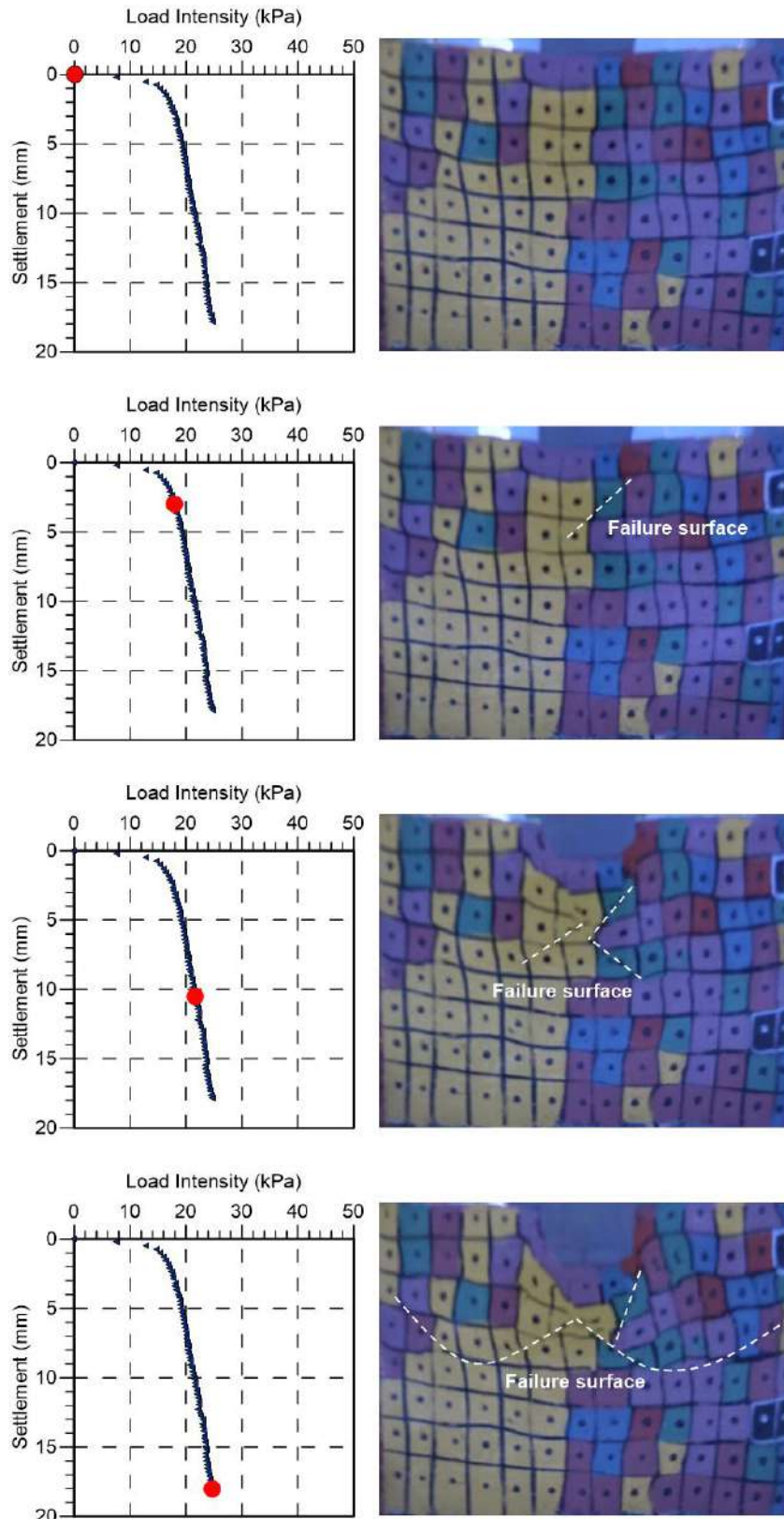


Figure 6.16 Evolution of the failure mechanism of heterogeneous model $COV_{WL} 51\%$.

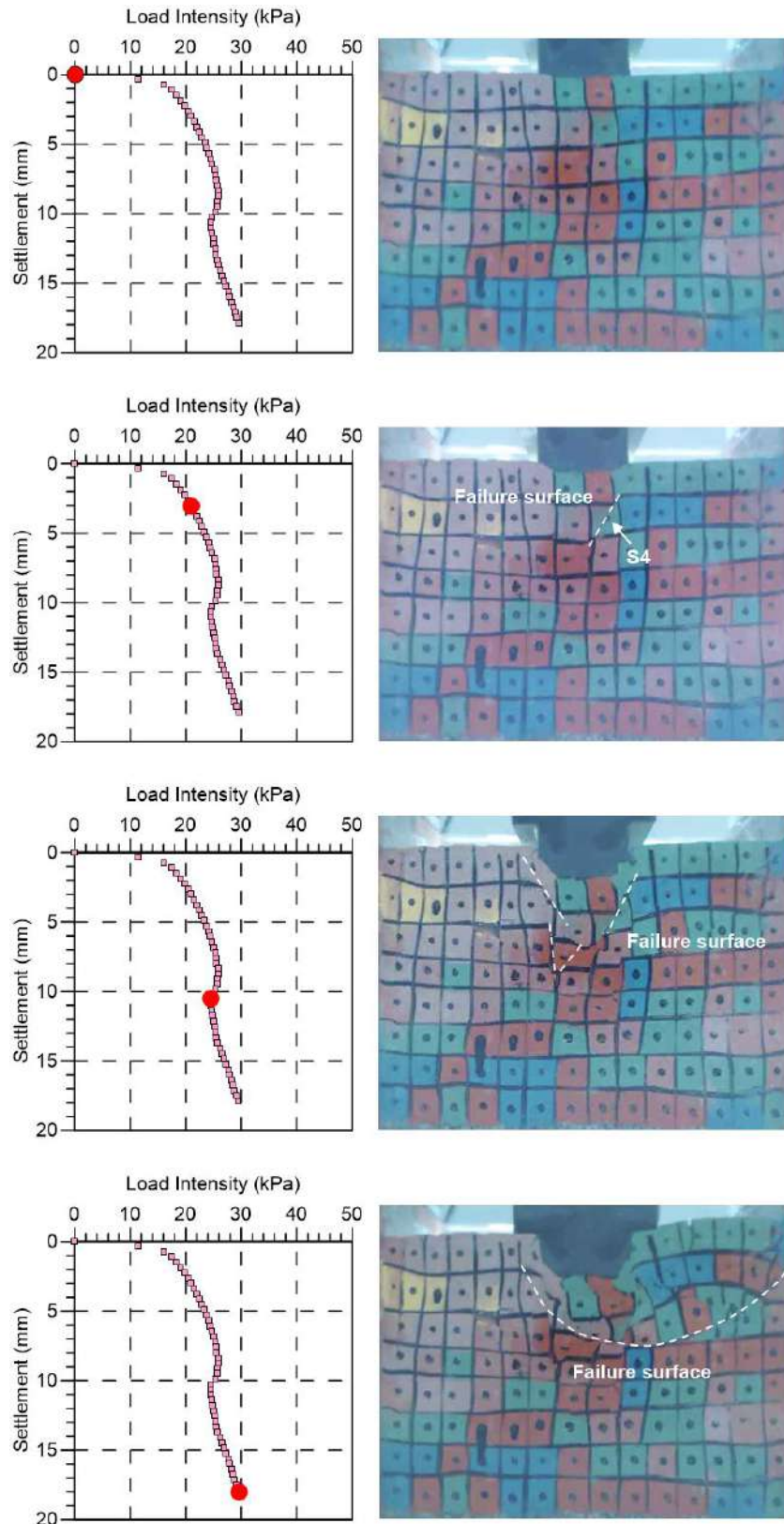


Figure 6.17 Evolution of the failure mechanism of heterogenuous model $\delta_h=6m$

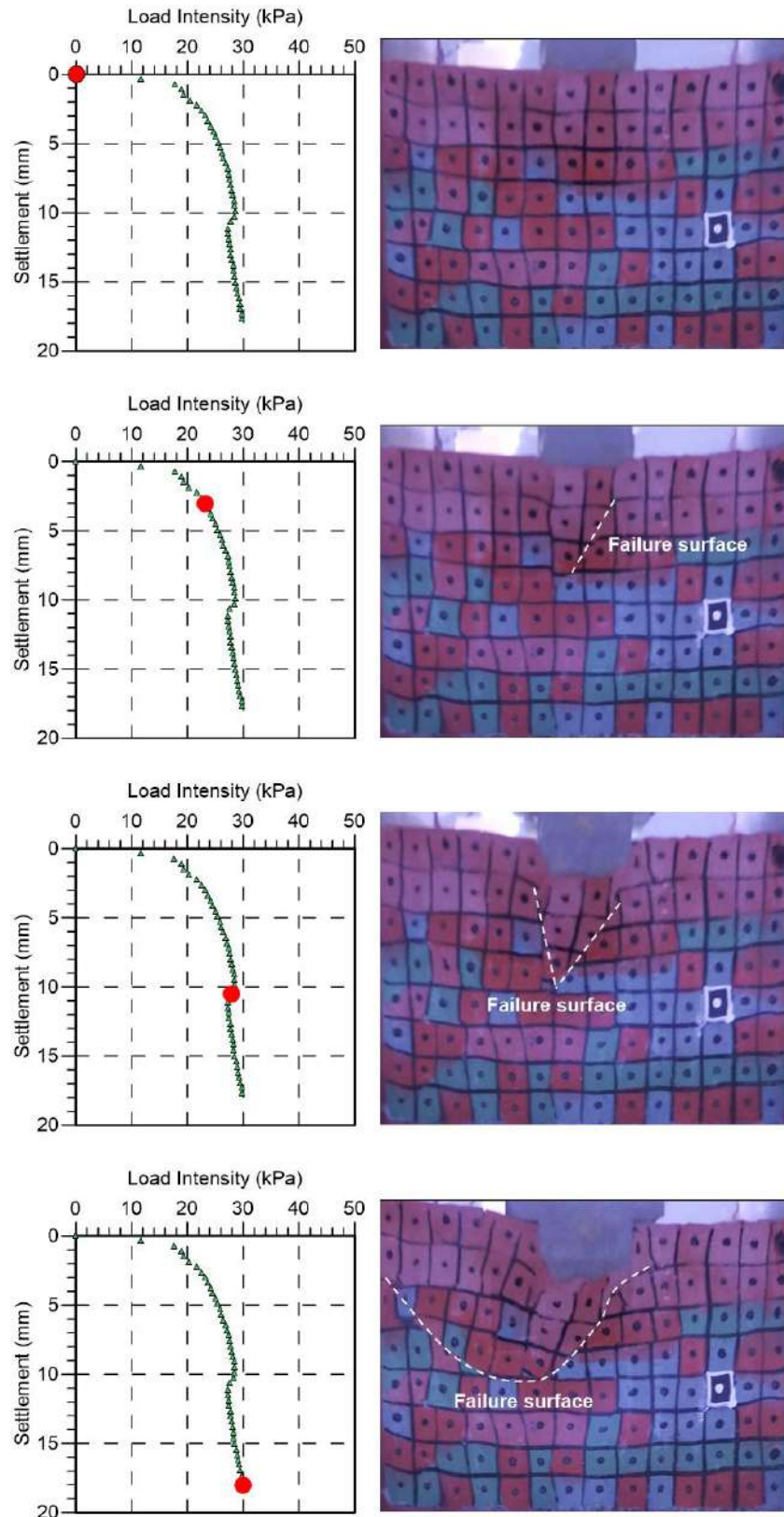


Figure 6.18 Evolution of the failure mechanism of heterogeneous model $\delta_h=15m$

6.5.2 Ultimate bearing capacity strength criteria

The ultimate bearing capacity of a rigid strip footing laying at the surface of a homogenous undrained clay with a shear strength, C_u ($\phi_u=0$) was calculated analytically by using the Terzaghi, 1943 relationship

$$q_f = N_c C_u + \bar{q} N_q + \frac{1}{2} \gamma B N_\gamma \quad (6.1)$$

where q_f is the theoretical ultimate bearing capacity, C_u is the undrained shear strength of the soil beneath the footing, \bar{q} is the overburden stress, γ is the unit soil weight, B is the footing width, and N_c , N_q and N_γ are the bearing-capacity factors. For a homogenous with a constant undrained shear strength, C_u ($\phi_u=0$) N_c is given by the Prandtl solution and equals $2+\pi$ or 5.14, N_q is equal to 1 and N_γ is equal to zero. To simplify the analysis in this study the soil is assumed to be weightless. Under this assumption, the bearing capacity equations simplifies to

$$q_f = 5.14 C_u \quad (6.2)$$

The undrained shear strength, C_u used in this equations was, for the homogeneous models, the estimated in Section 5.6.2 by using the correlation defined for this study base on the relationship between undrained shear strength and the consistency index, IC Equation 5.17. Likewise, for the isotropic heterogeneous models, which have same values of horizontal and vertical scale of fluctuation, δ_h and $\delta_v = 1.5m$, $\mu_{WL} = 157\%$ and $COV_{WL} = 30\%$ the ultimate bearing capacity was estimated by using the Equation 6.2.

The theoretical ultimate bearing capacity, q_f was then compared with the mean ultimate bearing capacity measured in the in-flight bearing capacity test, q_u . As it is a physical modeling, the bearing capacity is affected by overburden stress so the ultimate bearing capacity was corrected by the overburden stress, \bar{q} . Thereby, the corrected measured ultimate bearing capacity correspond to

$$q_u = q_{test} - \bar{q} \quad (6.3)$$

where q_{test} is the measured ultimate bearing capacity and \bar{q} is the overburden stress.

The overburden stress, \bar{q} is defined as follow:

$$\bar{q} = D_f \gamma \quad (6.4)$$

where D_f is the depth of the footing measured from the ground surface.

Figure 6.19 shows the mean of the undrained shear strength random field estimated by Equations 5.17 and 5.18 for homogeneous and isotropic heterogeneous models calculated in Section 5.6.2. Figure 6.20 shows the mean of unit soil weight in kN/m^3 random field for homogeneous and isotropic heterogeneous models.

Table 6.2 summarizes the mean of undrained shear strength and the mean of the unit soil weight estimated for the homogeneous and isotropic heterogeneous models.

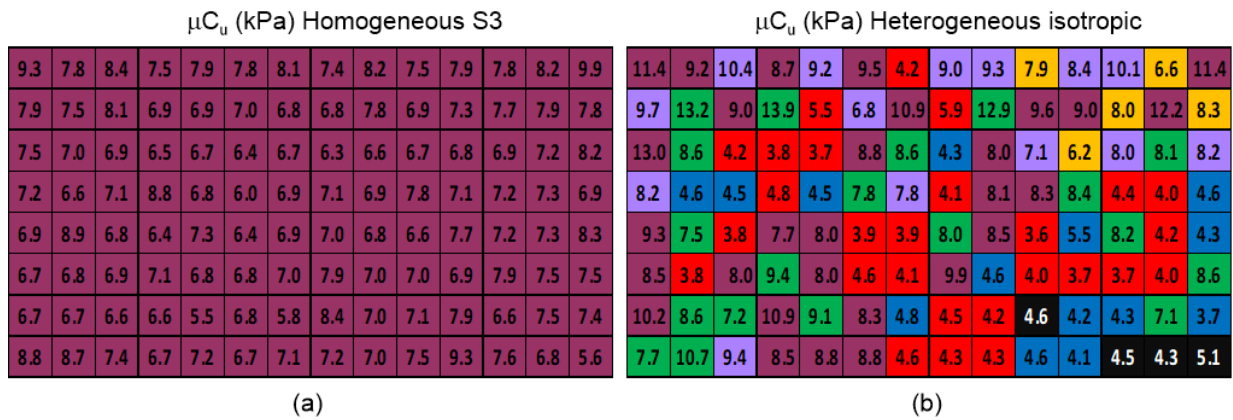


Figure 6.19 Mean of the undrained shear strength in kPa estimated by Equations 5.17 and 5.18: (a) homogeneous model, (b) isotropic heterogeneous model.

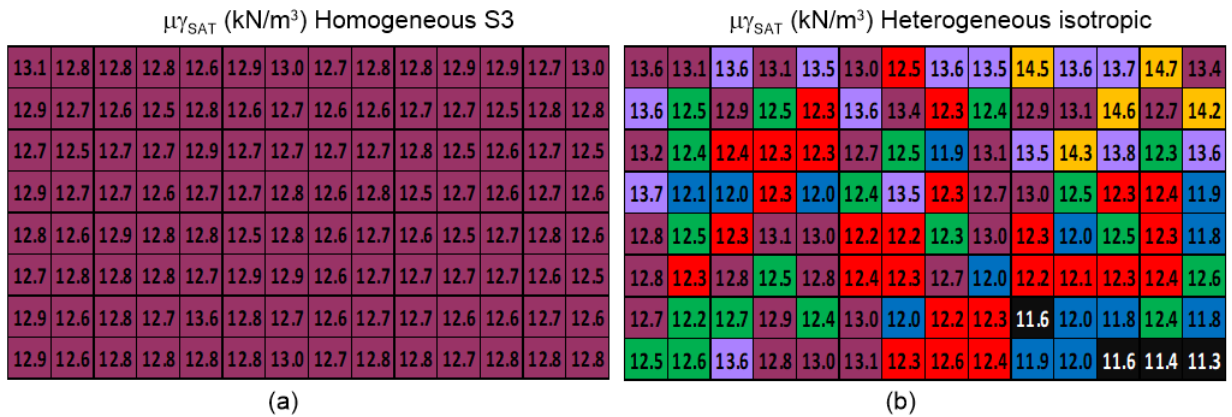


Figure 6.20 Mean of unit soil weight in kN/m³ (a) homogeneous model, (b) isotropic heterogeneous model.

Table 6.2 Undrained shear strength and unit soil weight of the homogeneous and heterogeneous models.

Models	C_u (kPa)			γ (kN/m ³)		
	Mean μ	SD σ	COV	Mean μ	SD σ	COV
Homogeneous	7.27	0.75	10.31	12.73	0.14	1.14
Heterogeneous	7.12	2.62	36.76	12.69	0.68	5.33

The mean load-settlement curve of the five homogenous models was computed, and the ultimate bearing capacity corresponds to the maximum value. The same procedure was made for the ten realizations of the isotropic heterogeneous models. Figure 6.21 shows the comparison between the theoretical ultimate bearing capacity, q_f calculated by Equations 6.2, the mean of the ultimate bearing capacity measured in the in-flight test, q_{test} and ultimate bearing capacity, q_u cor-

rected by the overburden stress, \bar{q} . Table 6.3 summarizes the values of the ultimate bearing capacity: q_f , q_{test} and q_u for the homogeneous and isotropic heterogeneous models. It can be noticed that for homogenous models the difference between the theoretical ultimate bearing capacity and the measured ultimate bearing capacity (after the correction by the overburden stress) is close to 1.5%. However, for the heterogeneous models, the difference is much greater, approaching 27.9% noticing the effect of the spatial variability of the properties on the bearing capacity.

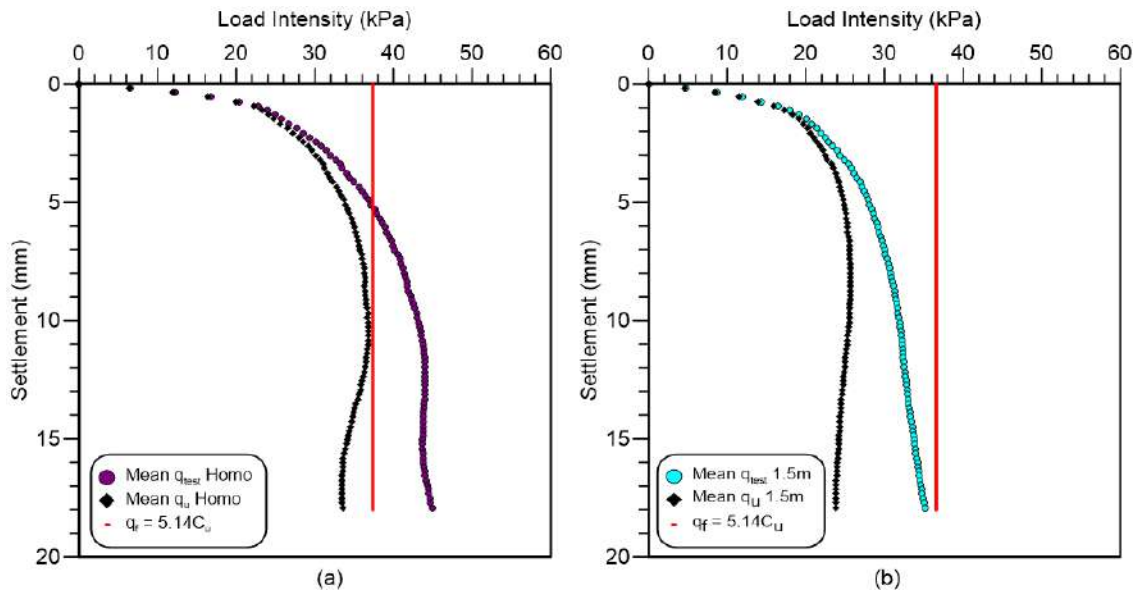


Figure 6.21 Comparison between the ultimate bearing capacity estimated by Equations 6.2 and the calculated by the in-flight test: (a) homogeneous model, (b) isotropic heterogeneous model.

Table 6.3 Mean of q_f , q_{test} and q_u in kPa for homogeneous and heterogeneous models..

Models	μq_f (kPa)	μq_{test} (kPa)	μq_u (kPa)
Homogeneous	37,37	45,09	36,80
Heterogeneous	36,60	35,30	25,71

6.5.3 Ultimate bearing capacity serviceability criteria

The ultimate bearing capacity of the tests was calculated using the serviceability criteria of 10% displacement of the foundation diameter proposed by Amar et al., (1994). This ultimate bearing capacity it will be called q_s . The load-settlement curves of all the tests were plotted as well as the mean curve.

6.5.3.1 Homogeneous models results

Figure 6.22 shows the load-settlement curves of the five homogenous models as well as in color red the mean load-settlement curve. The mean ultimate bearing capacity was 32kPa.

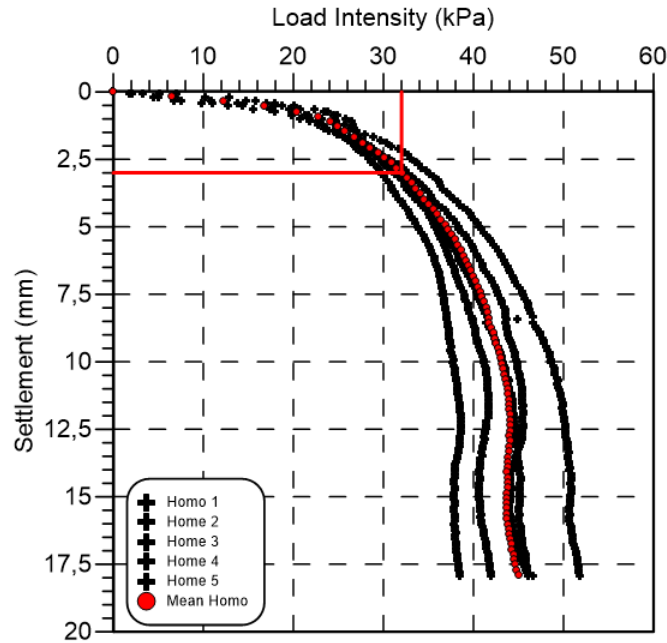


Figure 6.22 Load intensity- settlement curves homogenous models

6.5.3.2 Heterogeneous models results

Effect of the coefficient of variations COV_{WL}

Figure 6.23, Figure 6.24 and Figure 6.25 show the load-settlement curves (ten realizations) of the heterogeneous models with COV_{WL} of 51%, 30% and 13% respectively. Figure 6.26 shows the average load-settlement curve of the three heterogeneous models and the homogeneous models. Also, the mean ultimate bearing capacity, q_s were plotted for each case; the capacities were 21.3kPa, 24.3kPa and 25.2kPa for the models with COV_{WL} of 51%, 30% and 13% respectively. It can be seen that there is a reduction in the mean bearing capacity of the heterogeneous models compared with the corresponding bearing capacity of the homogeneous models that have the same mean property.

The average ultimate bearing capacity, q_s of the heterogeneous models was normalized by the average ultimate bearing capacity of the homogenous models, to distinguish, this capacity was called q_{Homo} . Figure 6.27 show COV_{WL} versus the normalized bearing capacity $\frac{\mu q_s}{\mu q_{Homo}}$. It can be seen that as the COV_{WL} decreases, the mean bearing capacity decreases approaching the value of the bearing capacity of the homogeneous soil with the same liquid limit. Table 6.4 summarizes the results of the ultimate bearing capacity; there is a reduction on the bearing capacity of 33%, 24%, and 21% for the models with COV_{WL} of 51%, 30% and 13% respectively.

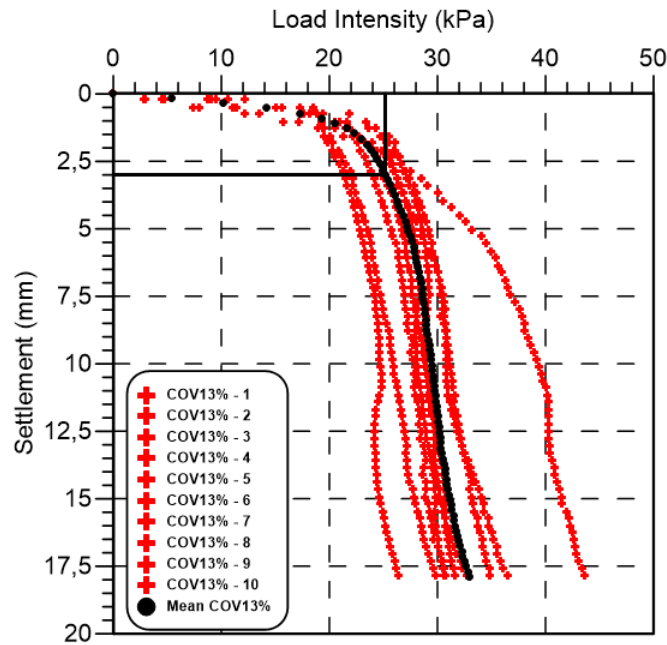


Figure 6.23 Load intensity- settlement curves heterogeneous models $COV_{wL}13\%$

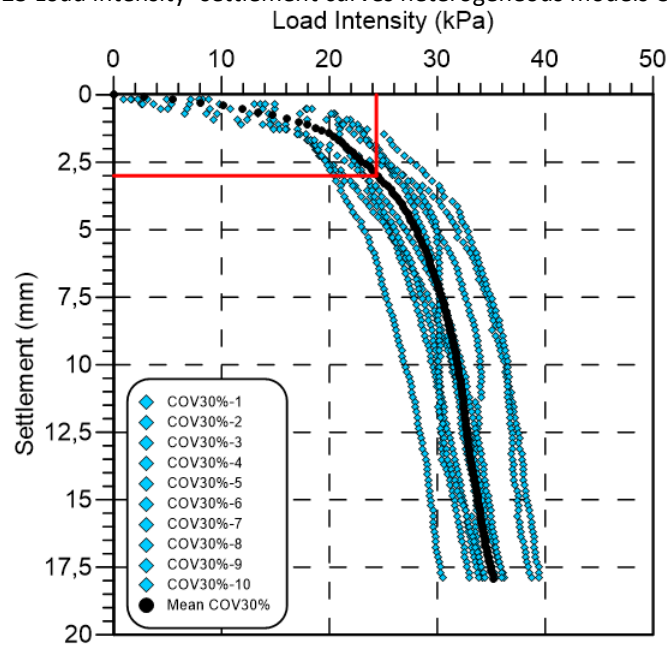


Figure 6.24 Load intensity- settlement curves heterogeneous models $COV_{wL}30\%$

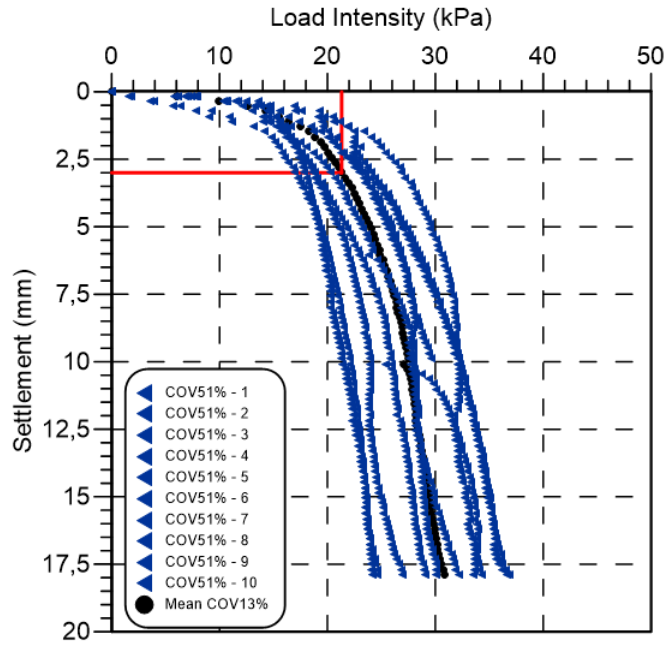


Figure 6.25 Load intensity- settlement curves heterogeneous models $COV_{WL}51\%$

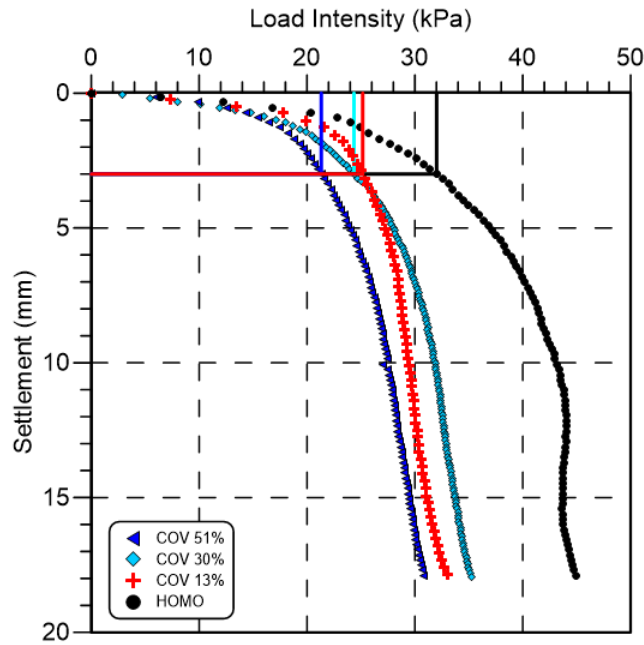


Figure 6.26 Effect of the variation of the COV_{WL} on the bearing capacity.

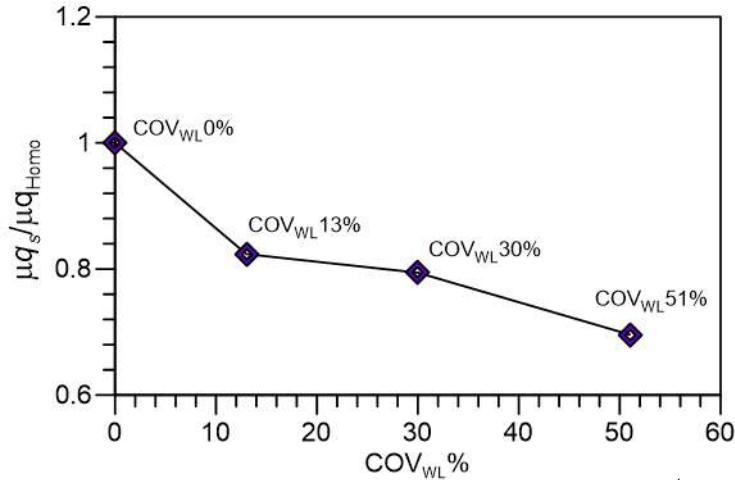


Figure 6.27 COV_{WL} versus the normalized bearing capacity $\mu q_s / \mu q_{Homo}$.

Table 6.4 Effect of the variation of the COV_{WL} on the bearing capacity.

Model	q _s * (kPa)				
	COV _{WL}	Mean μ	SD σ	COV	% Reduction
Heterogeneous	51%	21.3	3.25	15.3	33%
	30%	24.3	2.95	12.1	24%
	13%	25.2	2.20	8.7	21%
Homogeneous	0%	32.0	1.99	6.2	0%

*Ultimate bearing capacity base on serviceability

Effect of the horizontal scale of fluctuation

Figure 6.28, Figure 6.29 and Figure 6.30 show the load-settlement curves of the heterogeneous models (ten realizations) with horizontal scales of fluctuation, δ_h of 1.5m, 6m and 15m respectively. Figure 6.31 shows the average load-settlement curve of the three heterogeneous models and the homogeneous models. Also, the mean ultimate bearing capacity, q_s were plotted for each case; the capacities were 24.3kPa, 24.3kPa and 25.6kPa for the models with δ_h of 1.5m, 6m and 15m respectively. It can be seen that also there is a reduction in the mean bearing capacity of the heterogeneous models compared with the corresponding bearing capacity of the homogeneous models that have the same mean property.

Like the previous analysis of the effect of the COV_{WL}, the average ultimate bearing capacity, q_s of the heterogeneous models was normalized by the average ultimate bearing capacity of the homogenous models, q_{Homo}. Figure 6.32 show δ_{hWL} versus the normalized bearing capacity $\mu q_s / \mu q_{Homo}$. It can be seen that at lower value of horizontal scales of fluctuation lower value of the bearing capacity. However, it can not be affirmed that as the horizontal scales of fluctuation increases the mean bearing capacity increases approaching the value of the bearing capacity of the homogeneous soil with the same liquid limit. It is evidenced because the ultimate bearing capacity

values for horizontal scales of fluctuation of 1.5m and 6m has the same value of 24.3kPa. Neither was found the critical case when the horizontal scale of fluctuation is equal to the footing width, B .

Table 6.5 summarizes the results of the ultimate bearing capacity. There is a reduction on the bearing capacity of 24%, 24%, and 20% for the models horizontal scales of fluctuation, δ_h of 1.5m, 6m and 15m respectively.

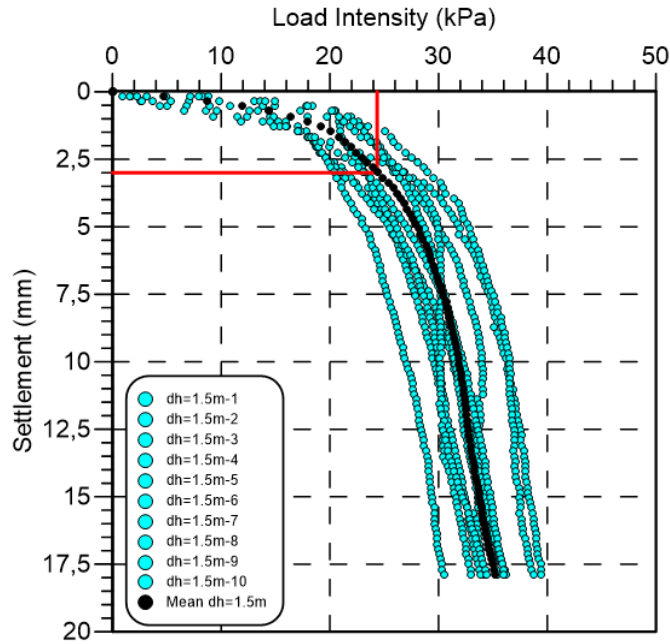


Figure 6.28 Load intensity- settlement curves heterogeneous models $\delta_h=1.5m$

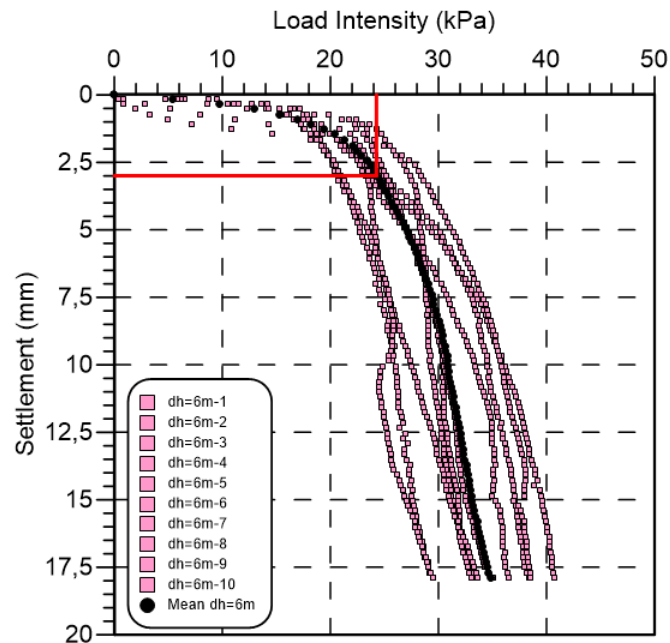


Figure 6.29 Load intensity- settlement curves heterogeneous models $\delta_h=6m$

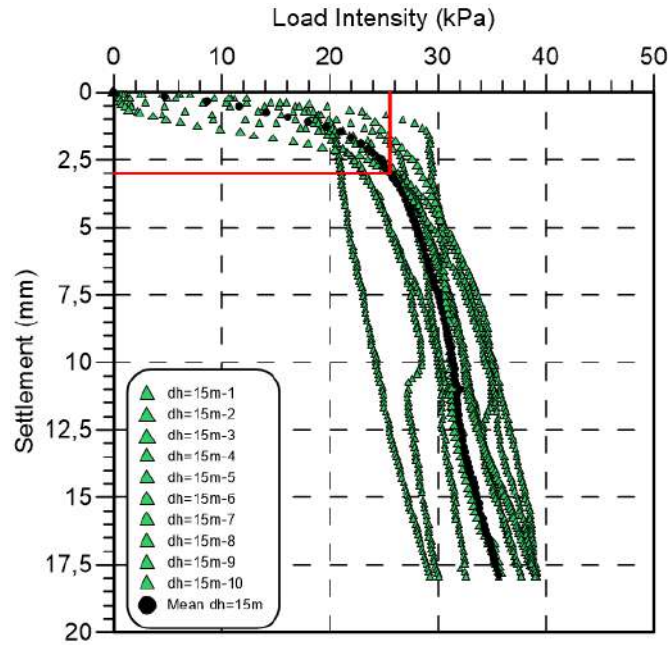


Figure 6.30 Load intensity- settlement curves heterogeneous models $\delta_h=15m$

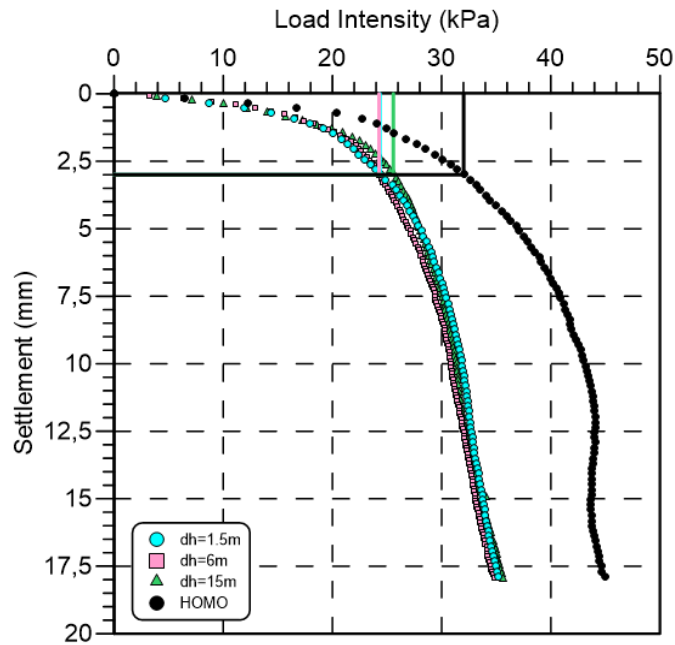


Figure 6.31 Effect of the horizontal scale of fluctuation, δ_{hWL} on the bearing capacity.

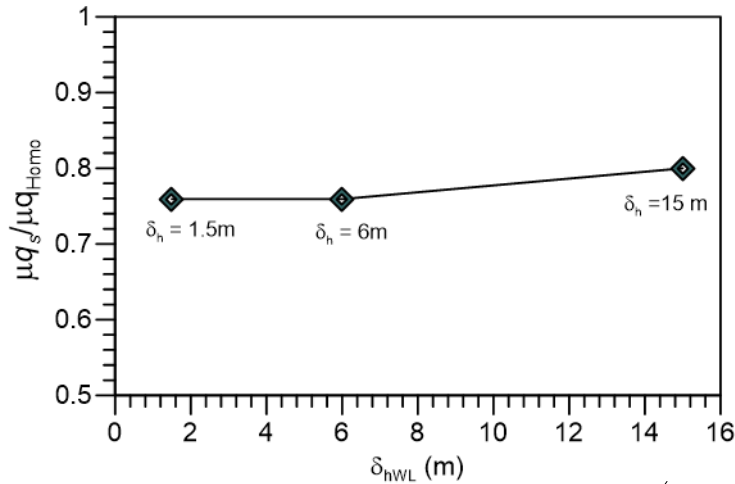


Figure 6.32 δ_{hWL} versus the normalized bearing capacity $\frac{\mu q_s}{\mu q_{Homo}}$.

Table 6.5 Effect of the horizontal scale of fluctuation, δ_h on the bearing capacity.

Model	δ_{hWL} (m)	q_s^* (kPa)			
		Mean μ	SD σ	COV	% Reduction
Heterogeneous	1.5	24.3	2.95	12.1	24%
	6	24.3	2.41	9.9	24%
	15	25.6	2.54	9.9	20%
Homogeneous	0%	32.0	1.99	6.2	0%

*Ultimate bearing capacity base on serviceability

6.5.4 Undrained shear strength measurements

The undrained shear strength of all the models was measured by using the mini ball penetrometer; the measures were made immediately after the bearing capacity test. Table 6.6 summarizes the statistical parameters of the undrained shear strength measured for all the models. It can be seen that the higher the variation of the liquid limit, the lower the value of the undrained shear strength. The average undrained shear strength for models with COV_{WL} of 51%, 30% and 13% are 6.2kPa, 6.5kPa and 6.8kPa respectively. Likewise, the average undrained shear strength for models with horizontal scales of fluctuation, δ_{hWL} of 1.5m, 6m and 15m are 6.5kPa, 6.3kPa and 6.5kPa respectively. The average undrained shear strength for models homogenous models was 7.1kPa similar to 7.21kPa, the average of the homogeneous models that were built when the random construction technique was being developed.

Regarding the variations of the undrained shear strength, it can be seen that the coefficient COV_{Cu} for the heterogeneous models with COV_{WL} vary between 13.4 and 16.3; and for the heterogeneous models with horizontal scales of fluctuation, δ_{hWL} vary between 13.7 and 14.9. Figure 6.33 shows the range of the values of coefficient of variation of the undrained shear strength,

COV_{Cu} for various procedures of testing (in situ or laboratory soil tests) recommended by Phoon and Kulhaway (1999a) along with the range of the mini ball penetrometer finding for this study. It can be noticed that the range of the mini ball penetrometer test is far below of the others tests. However, due to the lack of statistical data in the literature on full-flow penetrometers challenging to make an accurate conclusion about the measures assessed in this study.

Table 6.6 Statistical parameters of the undrained shear strength.

	C_u (kPa)			
	Model	Mean μ	SD σ	COV
COV_{WL}	51%	6.2	1.01	16.3
	30%	6.5	0.97	14.9
	13%	6.8	0.91	13.4
δ_{hWL}	1.5m	6.5	0.97	14.9
	6m	6.3	0.91	14.4
	15m	6.5	0.89	13.7
Homogeneous	S3	7.1	0.94	13.2

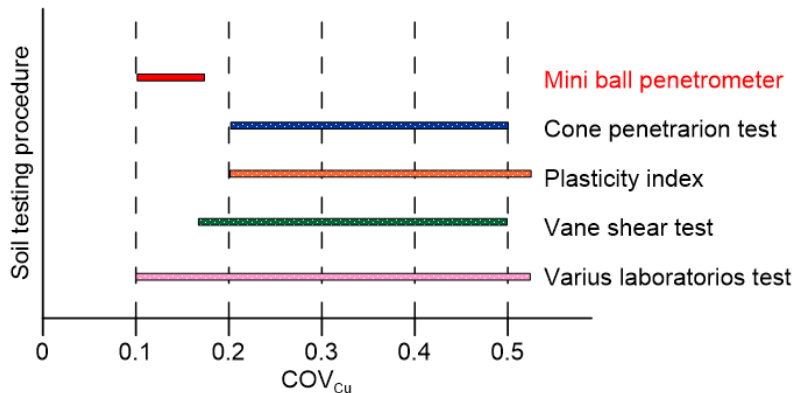


Figure 6.33 Range of values of coefficient of variation of the undrained shear strength, COV_{Cu} for various tests (Adapted Popescu et al. (2005)).

6.6 Conclusions

The effects of soil heterogeneity on the bearing capacity of a shallow foundation have been widely studied numerically using random field theory to model the heterogeneity, and finite elements to compute the bearing capacity response, in conjunction with Monte Carlo Simulation approach. The results obtained from numerical stochastic geotechnical models are difficult to verify experimentally, mainly due to the difficulty to model the inherent spatial variability. This work constitutes the first attempt to ascertain the effect of the variability of soil properties on the behavior of shallow foundation experimentally.

- ✓ A micro loading apparatus for a mini geotechnical centrifuge that is operating under controlled displacement was designed and built.
- ✓ A total of 55 in-flight bearing capacity tests were performed in a mini geotechnical centrifuge: 50 heterogeneous models and five homogeneous models.
- ✓ The effect of the coefficient of variation, COV_{WL} was physically validated. Three cases of ten realizations each one was evaluated for COV_{WL} equal to 13%, 30% and 51%. It was found that there is a reduction in the mean bearing capacity of the heterogeneous models compared with the corresponding bearing capacity of the homogeneous models that have the same mean property. Also, as the COV_{WL} decreases, the mean bearing capacity decreases approaching the value of the bearing capacity of the homogeneous soil with the same liquid limit properties.
- ✓ The effect of the horizontal scale of fluctuation, δh on the bearing capacity of a shallow foundation was physically validated. Three cases were considered $\delta h = 1.5m, 6m$ and $15m$. Like in the case of the effect COV_{WL} there is a reduction in the mean bearing capacity of the heterogeneous models compared with the corresponding bearing capacity of the homogeneous models that have the same mean property. However, it can not be affirmed that as the horizontal scales of fluctuation increases the mean bearing capacity increases approaching the value of the bearing capacity of the homogeneous soil with the same liquid limit. Neither was found the critical case when the horizontal scale of fluctuation is equal to the footing width, B .
- ✓ The analysis of the images has shown that the inherent spatial variability of the soil can modify the basic form of the failure mechanics drastically. This conclusion, also found in the numerical studies, becomes vital since the analytical solutions for the ultimate bearing capacity of shallow foundations are made based on supposing symmetrical failure mechanism.
- ✓ The results obtained emphasize the importance of study the effect of the inherent variability of the soil experimentally and numerically studies since the observed phenomenon like non-symmetrical failure mechanisms cannot be observed if the studies are carried out considering the soil as homogeneous.

7 GENERAL CONCLUSIONS AND RECOMMENDATIONS

This thesis presents the first attempt to validate experimentally the ultimate bearing capacity of a rigid strip footing resting on a spatially varying soil. The physical modeling was developed in two parts: (i) preparation of reduced scale soils models with controlled spatial variability, and (ii) perform bearing capacity tests of a single rigid strip foundation.

In the first part, a new technique to prepare reduced scale soil models with controlled variability for centrifuge modeling was proposed. In this methodology, the spatial variability of the soils is controlled in the sense that each heterogeneous soil model is a physical representation of a random field realization. With this technique, it is possible to build heterogeneous soils by reproducing the variability in mineralogy, i.e. liquid limit and reproducing the history of field stresses by using an oedometric compression and then reproducing the field stresses in a geotechnical centrifuge. The heterogeneous model constructed, with a variable liquid limit, will result in a model having variable mechanical soil properties, e.g. undrained shear strength.

The undrained shear strength of the random field was measured directly by the mini ball and the mini vane apparatus, and indirectly by an empirical correlation base on the relationship between undrained shear strength and the consistency index, IC , given by Leroueil et al., (1983). Although the mini ball penetrometer was selected to measure the undrained shear strength of the models after performing the bearing capacity test, it is recommended to find new ways to measure the undrained cohesion in each cell of the random field of the model. The above, with the aim of, having a reliable random field of the mechanical properties.

Since coupling numerical and physical models, as well as numerical and analytical models, are robust methodologies to assess the behavior of geotechnical works, another recommendation arising from this work is to model numerically the procedure proposed here to model the spatial variability of the soil properties. To model numerically this technique will allow to evaluated from a different perspective than the one evaluated so far by the numerical studies, i.e. vary the mechanical soil properties. This thesis leaves an extensive database to compare the results of numerical modeling.

The method presented in this thesis offers new possibilities for studying the effect of soil variability on the behavior of geotechnical structures using geotechnical centrifuges. This work laid the foundations for a new development that is currently carried out in the Universidad de los Andes, i.e. the design and construction of a soft soil 3D printer machine that will allow building models in 3D with spatial variability of soil properties.

In the second part, 55 in-flight bearing capacity tests are performed in the mini-geotechnical centrifuge of Universidad de los Andes. A micro loading device was designed and constructed for

that purpose; this device can carry out bearing capacity test at a constant rate of strain allowing a reliable recording of the bearing capacity. Likewise, the device can measure vertical and horizontal forces as well as moments. The effect of the coefficient of variation, COV_{WL} and the horizontal scale of fluctuation, δ_h on the bearing capacity of a shallow foundation was physically validated. For evaluating the effect of the coefficient of variation, three cases were assessed COV_{WL} 51%, COV_{WL} 30% and COV_{WL} 13%, and for evaluating the effect of the horizontal scale of fluctuation three cases were considered 1.5m, 6m and 15m, for each case 10 realizations of the random field were performed.

Regarding the effect of the coefficient of variation, COV_{WL} ; it was found that there is a reduction in the mean bearing capacity of the heterogeneous models compared with the corresponding bearing capacity of the homogeneous models that have the same mean property. Also, as the COV_{WL} decreases, the mean bearing capacity decreases approaching the value of the bearing capacity of the homogeneous soil with the same liquid limit properties.

Regarding the effect of the horizontal scale of fluctuation, δ_h there is a reduction in the mean bearing capacity of the heterogeneous models compared with the corresponding bearing capacity of the homogeneous models that have the same mean property. However, it cannot be affirmed that as the horizontal scales of fluctuation increases the mean bearing capacity increases approaching the value of the bearing capacity of the homogeneous soil with the same liquid limit. Neither was found the critical case when the horizontal scale of fluctuation is equal to the footing width, B .

A general conclusion of the qualitative analysis of the failure mechanics it is for the heterogeneous models a non-symmetric shape was developed. As this phenomenon is critical to understand since the inherent spatial variability of the soil properties is not only affecting the bearing capacity value of the soils, but it is also modifying the basic form of the failure mechanics. This thesis leaves a recorded images database of the bearing capacity tests that can be used to assess the strip footing displacement and the failure mechanism by using optical flow methods.

REFERENCES

- Akbas, S.O. and Kulhawy, F.H. (2010). Characterization and Estimation of Geotechnical Variability in Ankara Clay: A Case History. *Geotechnical Geological Engineering*, 28, 619–631.
- Al-Bittar, T. and Soubra A.H. (2012). Bearing capacity of strip footings on spatially random soils using sparse polynomial chaos expansion. *International Journal for Numerical and Analytical Methods in Geomechanics*.
- Almeida, M. and Parry, R. (1985). Small cone penetrometer tests and piezocone tests in laboratory consolidated clays. *Geotechnical Testing Journal*. ASCE, 8, (1), 14-24.
- Andersen, K.H., Jeanjean, P., Luger, D., Jostad, H.P. (2005). Centrifuge tests on installation of suction anchors in soft clay. *Ocean Engineering*, 32, 845–863.
- Asaoka, A. (1978). Observational procedure of settlement prediction. *Soils and Foundations*, Japanese Society of Soil Mechanics and Foundation Engineering, 18, (4).
- Burland, J.B. (1990). On the compressibility and shear strength of natural clays. *Geotechnique*, 40, (3) 329-378.
- Chakraborty, P. and Popescu, R. (2012). Numerical simulation of centrifuge tests on homogeneous and heterogeneous soil models. *Computers and Geotechnics*, 41, 95–105.
- Chen, J-F. and Yu, S-B. (2011). Centrifugal and Numerical Modeling of a Reinforced Lime-Stabilized Soil Embankment on Soft Clay with Wick Drains. *International Journal of Geomechanics*, 11, (3), 167-173.
- Ching, J. and Phoon, K.K. (2013a). Mobilized shear strength of spatially variable soils under simple stress states, *Structural Safety*, 41, 20-28.
- Ching, J. and Phoon, K.K. (2013b). Probability distribution for mobilized shear strengths of spatially variable soils under uniform stress states, *Georisk*, 7(3), 209-224.
- Ching, J., Phoon, K.K., and Kao, P.H. (2014a). Mean and variance of the mobilized shear strengths for spatially variable soils under uniform stress states, *ASCE Journal of Engineering Mechanics*, 140(3), 487-501.
- Ching, J. and Phoon, K. K. (2014b). Transformations and correlations among some parameters of clays – the database. *Canadian Geotechnical Journal*, 51(6), 663-685.
- Ching, J. and Phoon, K. K. (2014c). Correlations among some clay parameters – the multivariate distribution. *Canadian Geotechnical Journal*, 51(6), 686-704.
- Ching, J., Hu, Y.G., and Phoon, K.K. (2016a). On characterizing spatially variable soil shear strength using spatial average, *Probabilistic Engineering Mechanics* (in press), 45, 31-43.
- Ching, J., Lee, S.W., and Phoon, K.K. (2016b). Undrained strength for a 3D spatially variable clay column subjected to compression or shear, *Probabilistic Engineering Mechanics*, 45, 127–139.
- Ching, J., Tong, X.W., and Hu, Y.G. (2016c). Effective Young’s modulus for a spatially variable elementary soil mass subjected to a simple stress state, *Georisk*, 10(1), 11-26
- Cho, G., Lee, J., and Santamarina, J. (2004). Spatial Variability in Soils: High Resolution Assessment with Electrical Needle Probe. *Journal of Geotechnical and Geoenvironmental Engineering*, 130, (8) 843-850.

- Cho, S.E., and Park, H.C. (2010). Effect of spatial variability of cross-correlated soil properties on bearing capacity of strip footing. *International Journal for Numerical and Analytical Methods in Geomechanics*, 34, 1–26.
- Der Kiureghian, A. and Ditlevsen, O. (2009). Aleatory or epistemic? Does it matter? *Structural Safety*, 31,(2), 105-112.
- El-Kadi, A.I. and Williams, S. A. (2000). Generating Two-Dimensional Fields of Autocorrelated, Normally Distributed Parameters by the Matrix Decomposition Technique. *Ground Water*, 38, (4), 523-532.
- El-Ramly, H., Morgenstern, N.R. and Cruden, D.M. (2003). Probabilistic stability analysis of a tailings dyke on presheared clay-shale. *Canadian Geotechnical Journal*, 40, 192-208.
- Fan, H., Huang, Q. and Liang, R. (2014). Reliability analysis of piles in spatially varying soils considering multiple failure modes. *Computers and Geotechnics*, 57, (Apr), 97–104.
- Fenton, G.A. and Griffiths, D.V. (2002). Probabilistic Foundation Settlement on a Spatially Random Soil. *Journal of Geotechnical and Geoenvironmental Engineering*, 128, (5), 381-390.
- Fenton, G.A. and Griffiths, D.V. (2003). Bearing capacity prediction of spatially random $c-\phi$ soils. *Canadian Geotechnical Journal*, 40, (1), 54-65.
- Garzón, L.X., Caicedo, B., Sánchez-Silva, M. and Phoon, K.K. (2015). Physical modeling of soil uncertainty. *International Journal of Physical Modelling in Geotechnics*, 15, (1) 19 -34.
- Griffiths, D.V. and Fenton, G.A. (2001). Bearing capacity of spatially random soil: the undrained clay Prandtl problem revisited. *Geotechnique*, 51, (4), 351-359.
- Griffiths, D.V. Fenton, G.A. and Manoharan, N. (2002). Bearing capacity of rough rigid strip footing on cohesive soil: Probabilistic study. *Journal of Geotechnical and Geoenvironmental Engineering*, 128, (9), 743-755.
- Griffiths, D.V. Fenton, G.A. and Manoharan, N. (2006). Undrained Bearing Capacity of Two-Strip Footings on Spatially Random Soil. *International Journal of Geomechanics*, 6, (6), 421- 427.
- Griffiths, D.V., Huang, J. and Fenton, G.A. (2009). Influence of Spatial Variability on Slope Reliability Using 2-D Random Fields. *Journal of Geotechnical and Geoenvironmental Engineering*, 135, (10), 1367-1378.
- Haldar, S. and Babu, S. (2008). Effect of soil spatial variability on the response of laterally loaded pile in undrained clay. *Computers and Geotechnics*, 35, 537–547.
- Hicks, M.A. and Spencer, W.A. (2010). Influence of heterogeneity on the reliability and failure of a long 3D slope. *Computers and Geotechnics*, 37, 948–955.
- Hong, S. and Helin, F. (2011). Spatial Variability and Slope Reliability Analysis. *The Electronic Journal of Geotechnical Engineering*, 16, 1261-1276.
- Hong, Z. and Liu, H. (2003). Remolded undrained shear strength of soils. *China Ocean Engineering*, 17, (1) 133-142
- Hong, Z. (2007). Void ratio-suction behavior of remolded Ariake clay. *Geotechnical Testing Journal*, 30, (3) 234-239.
- Honjo, Y. and Otake, Y. (2013). A Simple Method to Assess the Effects of Soil Spatial Variability on the Performance of a Shallow Foundation. *Foundation Engineering in the Face of Uncertainty*, 385-404.
- Huber, M., Hicks, M.A., Vermeer, P.A. and Moormann, C. (2010). Probabilistic calculation of differential settlement due to tunneling. *Proceedings of the 8th International Probabilistic Workshop*, 1-13.

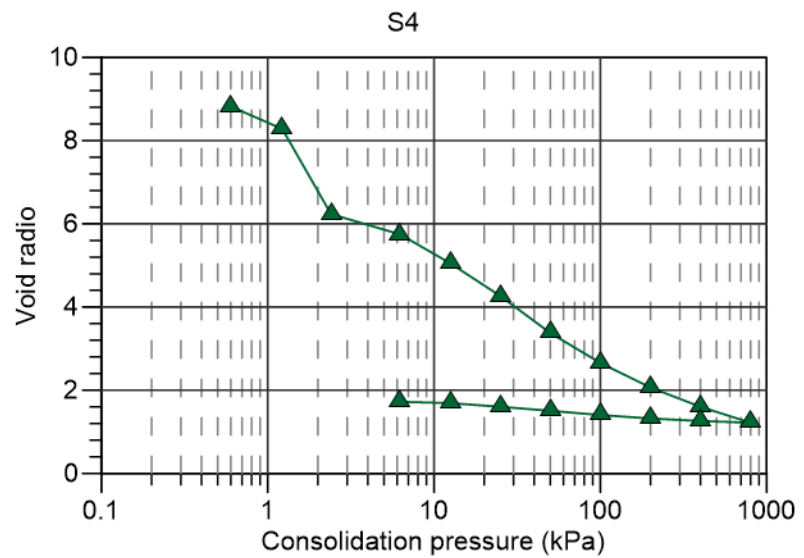
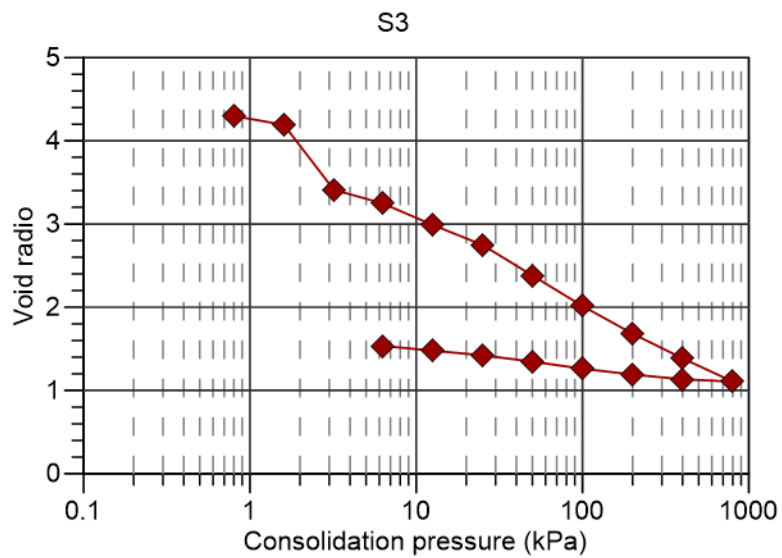
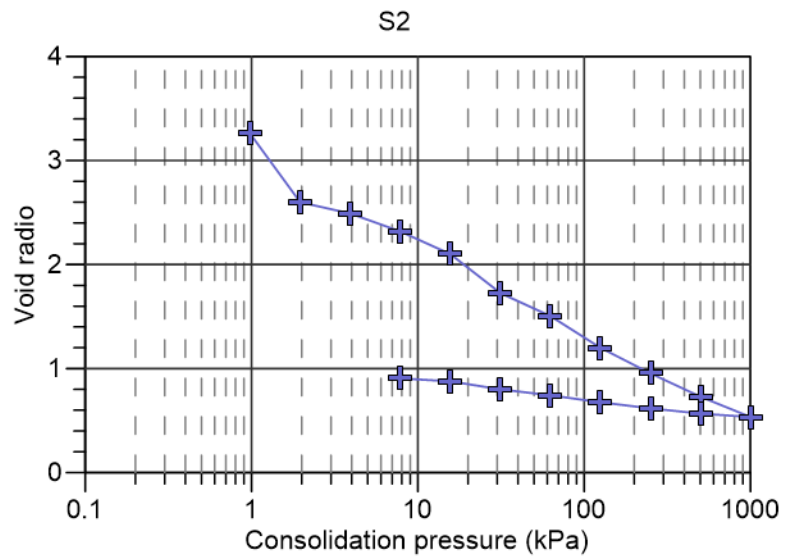
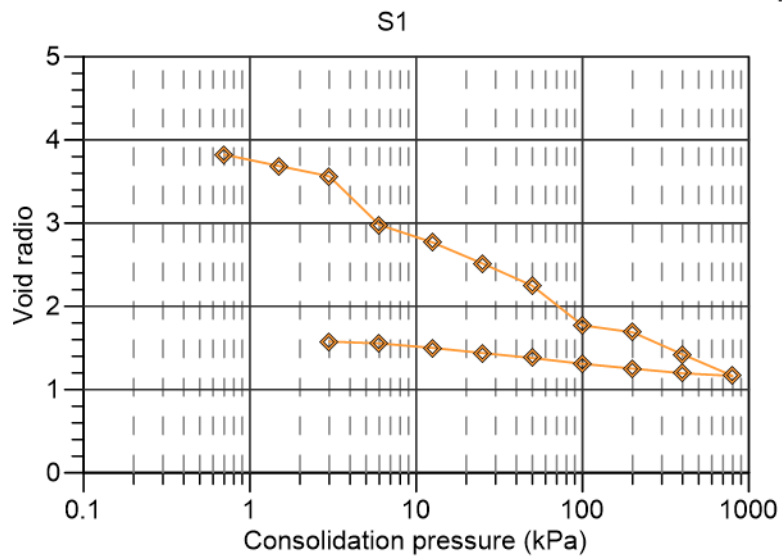
- Imai, G., 1979, Development of a New Consolidation Test Procedure Using Seepage Force. *Soils and Foundations*, 19, (3), 45–60.
- Jacksa, M.B., Kaggwa, W.S. and Brooker, P.I. (2000). Experimental evaluation of the scale of fluctuation of a stiff clay. 8th International Conference on Application of Statistics and Probability, Rotterdam, Netherlands, 415–422.
- Jones, A.L., Kramer. S.L. and Arduino, P. (2002). Estimation of uncertainty in geotechnical properties for performance-based earthquake engineering, PEER report 2002/16.
- Kasama, K. and Whittle, J. (2011). Bearing Capacity of Spatially Random Cohesive Soil Using Numerical Limit Analyses. *Journal of Geotechnical and Geoenvironmental Engineering*. ASCE,137,(11) 691 – 698.
- Kasama, K. and Zen, K. (2011). Effects of Spatial Variability of Soil Property on Slope Stability. *Vulnerability, uncertainty, and risk analysis, modeling and management*. ASCE, 691 – 698.
- Kimura, T., Kusakabe, O., Takemura, J. and Saitoh, K. (1984). Preparation of Normally Consolidated Clay Stratum in a Centrifuge. *Soils and Foundations*, 24, (4), 71-83.
- Lacasse, S. and Nadim, F. (1996). Uncertainties in characterizing soil properties. *Uncertainty in the Geologic Environment, From Theory to Practice, Proceeding of Uncertainty 96*. Geotechnical Special Publication No. 58. 49-75.
- Leroueil, S., Tavenas, F. and Leblond, J. P. (1983). Propriétés Caractéristiques des Argiles de l'est du Canada. *Canadian Geotechnical Journal*, 20, (4) 681-705.
- Li, Y. J., Hicks, M. A., and Nuttall, J. D. (2015). Comparative analyses of slope reliability in 3D. *Engineering Geology*, 196, 12-23.
- Li, Y. J., Hicks, M. A., and Vardon, P. J. (2016). Uncertainty reduction and sampling efficiency in slope designs using 3D conditional random fields. *Computers and Geotechnics*, 79, 159-172.
- Lumb, P. (1966). The Variability of Natural Soils. *Canadian Geotechnical Journal*, 3, (2), 74-97.
- Microzonificación Sísmica de Santa Fe de Bogotá. (1997). Convenio Administrativo 01-93. INGEOMINAS, UPES and DNPAD.
- Mitchell, R. J. (1998). The eleventh annual R. M. Hardy keynote address, 1997: Centrifugation in geoenvironmental practice and education. *Canadian Geotechnical Journal*, 35, (4), 630-640.
- Onyejekwe, S. and Ge, L. (2013). Scale of Fluctuation of Geotechnical Parameters Estimated from CPTu and Laboratory Test Data. *Foundation Engineering in the Face of Uncertainty*, 434-443.
- Phoon, K.K. and Kulhawy, F.H. (1999a). Characterization of geotechnical variability. *Canadian Geotechnical Journal*, 36, 612-624.
- Phoon, K.K. and Kulhawy, F.H. (1999b). Evaluation of geotechnical property variability. *Canadian Geotechnical Journal*, 36, 625–639.
- Popescu. R., Deodatis. G. and Nobahar. A. (2005). Effects of random heterogeneity of soil properties on bearing capacity. *Probabilistic Engineering Mechanics*, 20, 324–341.
- Rajesh, S. and Viswanadham, B.V.S. (2012). Centrifuge and Numerical Study on the Behavior of Clay-Based Landfill Covers Subjected to Differential Settlements. *Journal of Hazardous, Toxic, and Radioactive Waste*, 16 (4), 284-297.

- Randolph, M.F. and House, A.R. (2001). The complementary roles of physical and computational modelling. *International Journal of Physical Modelling in Geotechnis*, 1, 1-8.
- Robinson, R. G., Tan, T. S., and Lee, F. H. (2003). A comparative study of suction-induced seepage consolidation versus centrifuge consolidation. *Geotechnical Testing Journal*, 26, (1) 1-10.
- Salgado, R. and Kim, D. (2014). Reliability analysis of load and resistance factor design of slopes. *Journal of Geotechnical and Geoenvironmental Engineering*, 140, (1), 57–73.
- Schofield, A.N. (1980). Cambridge Geotechnical Centrifuge Operations. *Geotechnique*, 30, (3), 227-268.
- Schofield, A., 1995, Geotechnical Centrifuge Technology, R. N. Taylor, Ed., Blackie Academic and Professional, Glasgow.
- Skempton, A.W. (1944). Notes on compressibility of clays. *Quarterly Journal of the Geological Society*, London, 100, (2), 119–135.
- Soubra, A.H., Youssef Abdel Massih D.S. and Kalfa, M. (2008). Bearing capacity of foundations resting on a spatially random soil. *GeoCongress 2008: Geosustainability and Geohazard Mitigation*, ASCE, GSP 178, 66–73.
- Stuedlein, A.W., Kramer, S.L., Arduino, A. and Holtz, R.D. (2012). Geotechnical Characterization and Random Field Modeling of Desiccated Clay. *Journal of Geotechnical and Geoenvironmental Engineering*, 138, (11), 1301-1313.
- Taylor, D. W. (1948). *Fundamentals of Soil Mechanics*, John Wiley and Sons Inc., New York, pp. 238-242.
- Taylor, R. N. (1995). *Geotechnical Centrifuge Technology*, Ed., Blackie Academic and Professional, Glasgow.
- Uzielli, M., Vannucchi, G., and Phoon, K.K. (2005). Random field characterization of stress-normalised cone penetration testing parameters. *Geotechnique*, 55, (1), 3-20.
- Vanmarcke, E.H. (1977). Probabilistic modeling of soil profiles. *Journal Geotechnical Engineering Division*. ASCE, 103, 1227-1246.
- Vanmarcke, E.H. (1983). *Random fields: analysis and synthesis*. MIT Press, Cambridge.
- Vardanega, P.J. and Bolton, M.D. (2011). Strength mobilization in clays and silts. *Canadian Geotechnical Journal*, 48, 1485-1503.
- Weemee, L., Howie, J., Woeller, D., Sharp, J., Cargill, E., and Greig, J. (2006). Improved techniques for the in-situ determination of undrained shear strength of soft clays. *Sea to sky géotechnique*, Canadian Geotechnical Society, Richmond, Canada, 89-95.
- Yafrate, N.J., DeJong, J.T., and DeGroot, D.J. (2007). The influence of full-flow penetrometer area ratio on penetration resistance and undrained and remoulded shear strength. *In Proceedings of the 6th International Offshore Site Investigation and Geotechnics Conference: Confronting New Challenges and Sharing Knowledge*. London, 11–13 September 2007. Society for Underwater Technology, London. pp. 461–468.
- Yang, K-H., Kniss, K.T., Zornberg, J.G. and Wright, S.G. (2008). Finite Element Analyses for Centrifuge Modeling of Narrow MSE Walls. The First Pan American Geosynthetics Conference & Exhibition, Cancun, Mexico.
- Zelikson, A. (1969). Geotechnical models using the hydraulic gradient similarity method. *Geotechnique*, 19, (4), 495-508.
- Zhang, Y., Cassidy, M.J. and Bienen, B. (2013). Development of a combined VHM loading apparatus for a geotechnical drum centrifuge. *International Journal of Physical Modelling in Geotechnics*, 13, (1), 13–30.

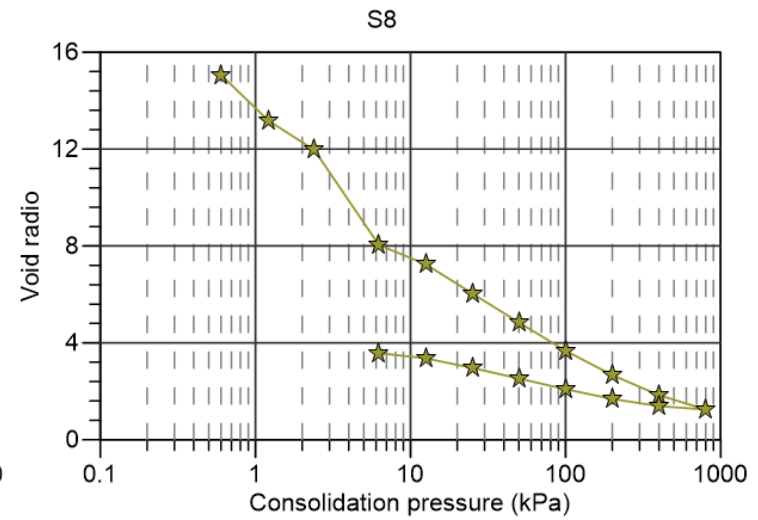
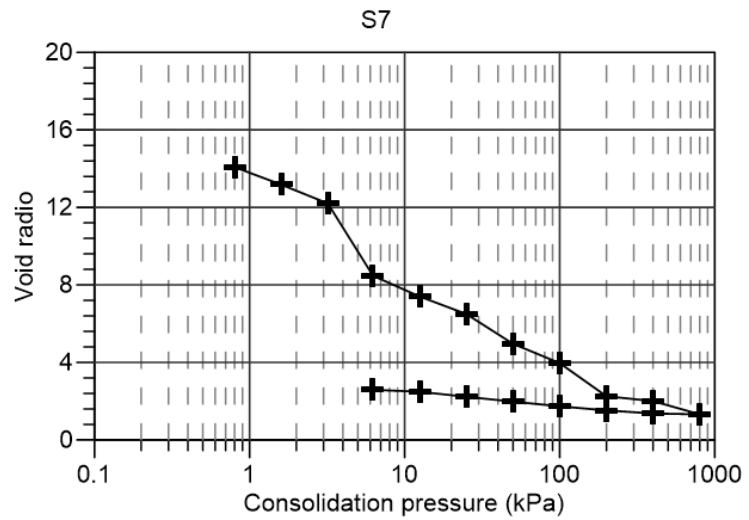
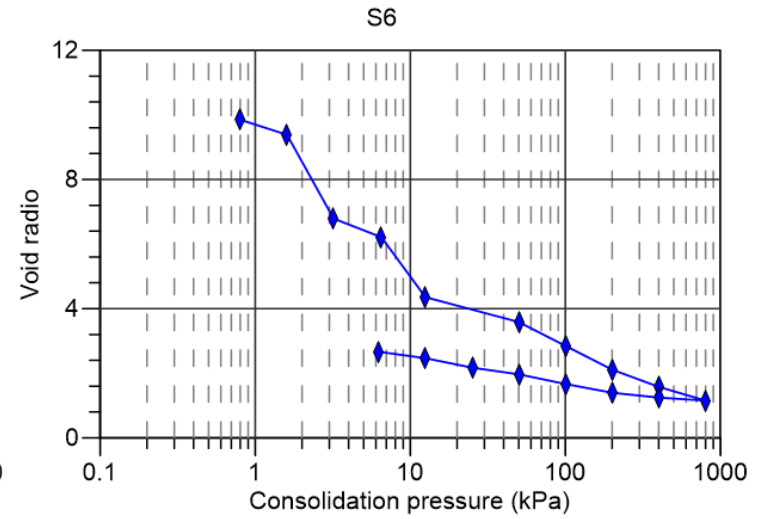
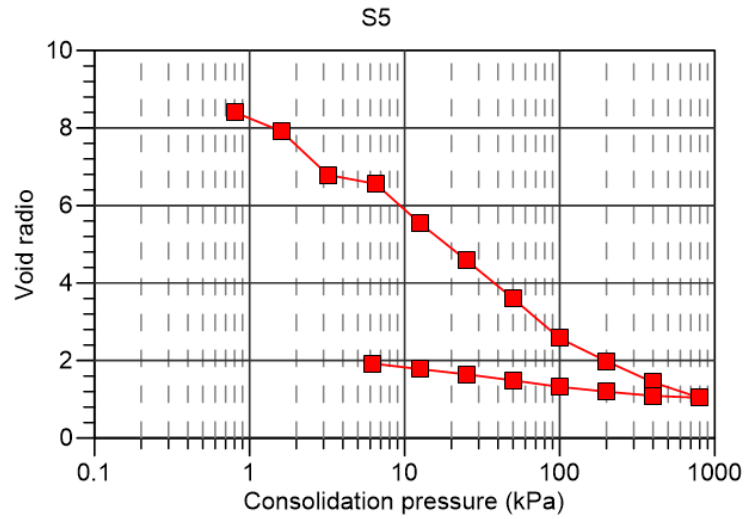
- Zhou, H., and Randolph, M.F. (2009a). Resistance of full-flow penetrometers in rate-dependent and strain-softening clay. *Géotechnique*, 59, (2) 79–86.
- Zhou, H., and Randolph, M.F. (2009b). Numerical investigation into cycling of full-flow penetrometers in soft clay. *Géotechnique*, 59, (10) 801–812.

APPENDIX A

Oedometer test standard procedure D2435/D2435M – 11

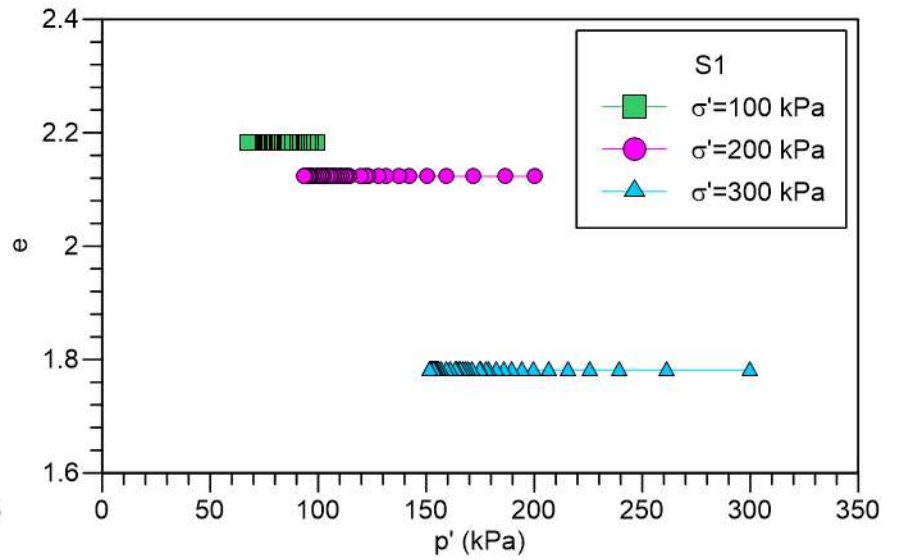
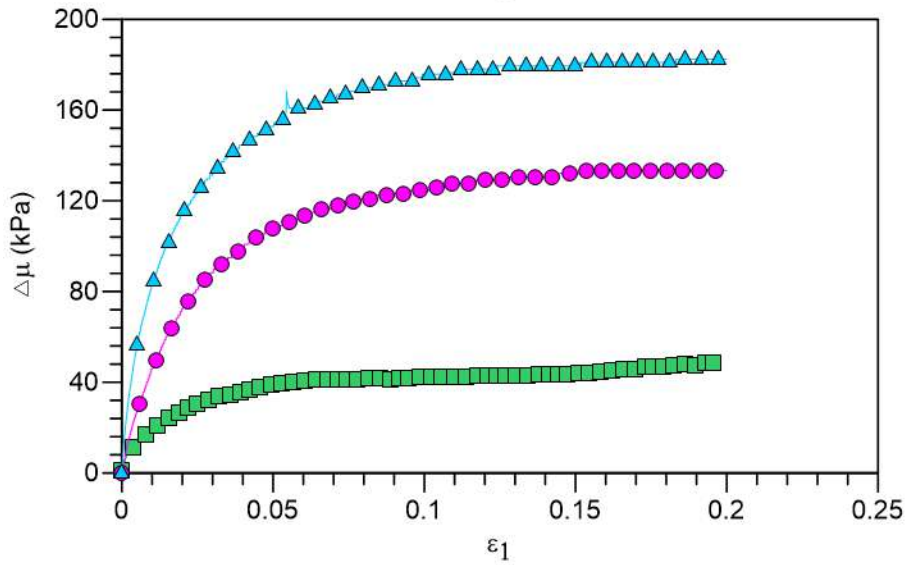
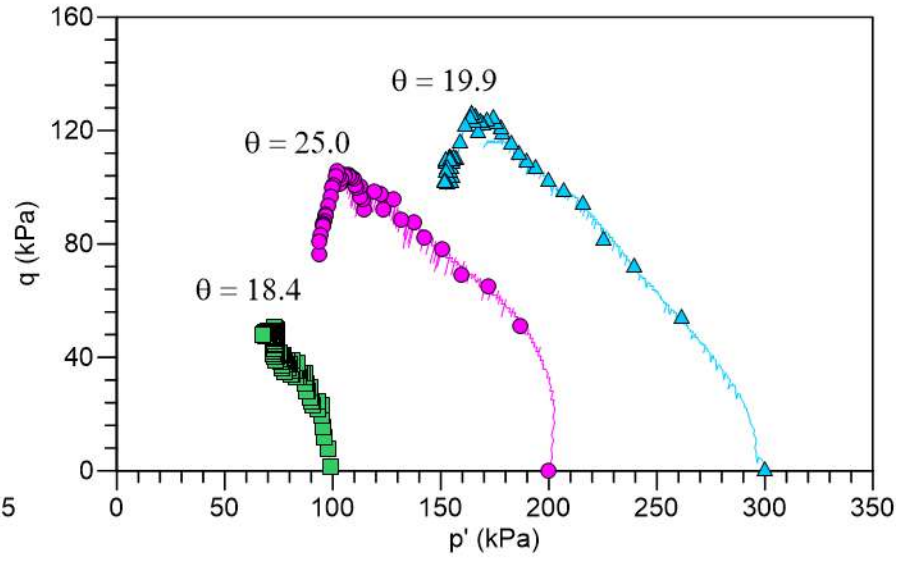
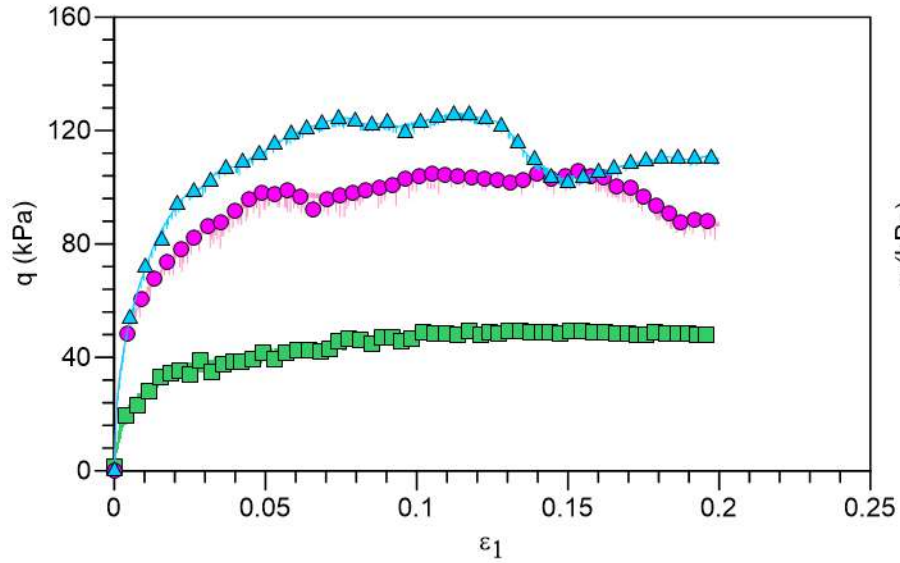


Oedometer test standard procedure D2435/D2435M – 11

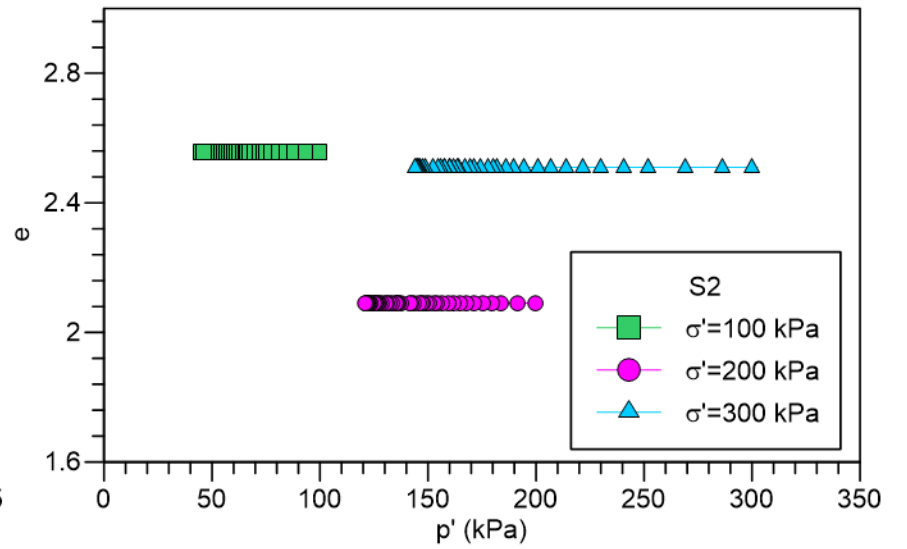
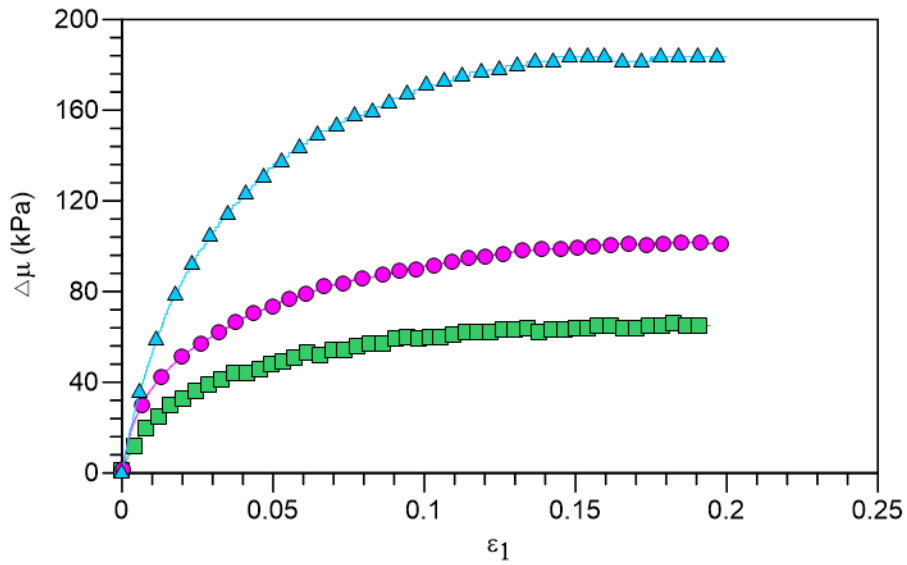
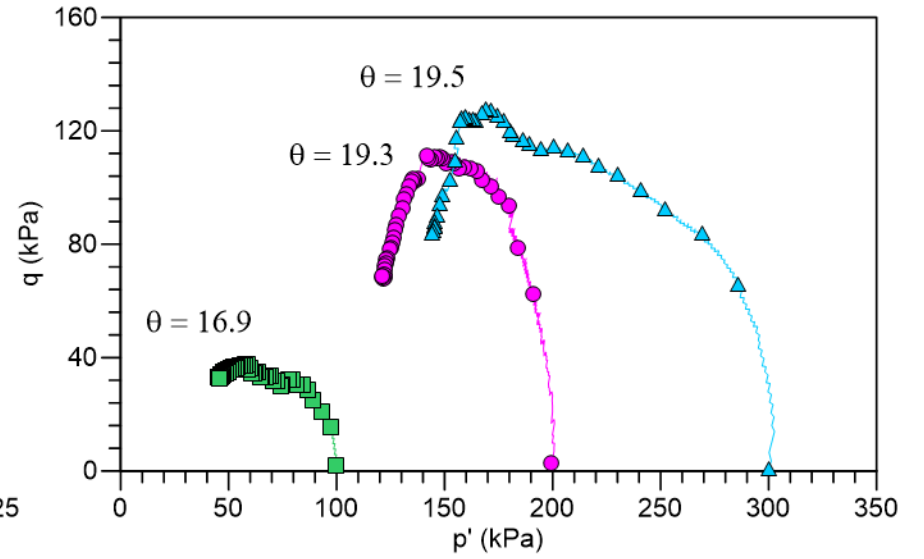
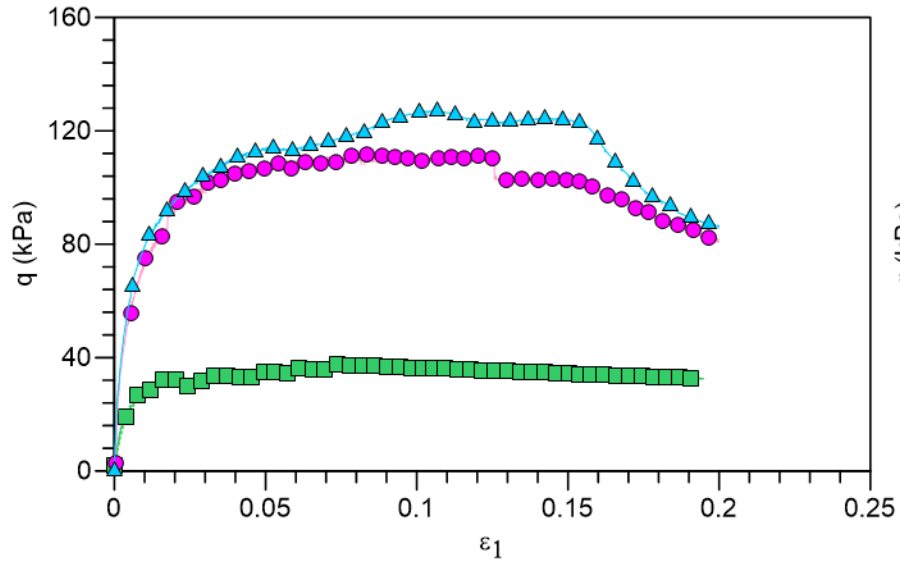


APPENDIX B

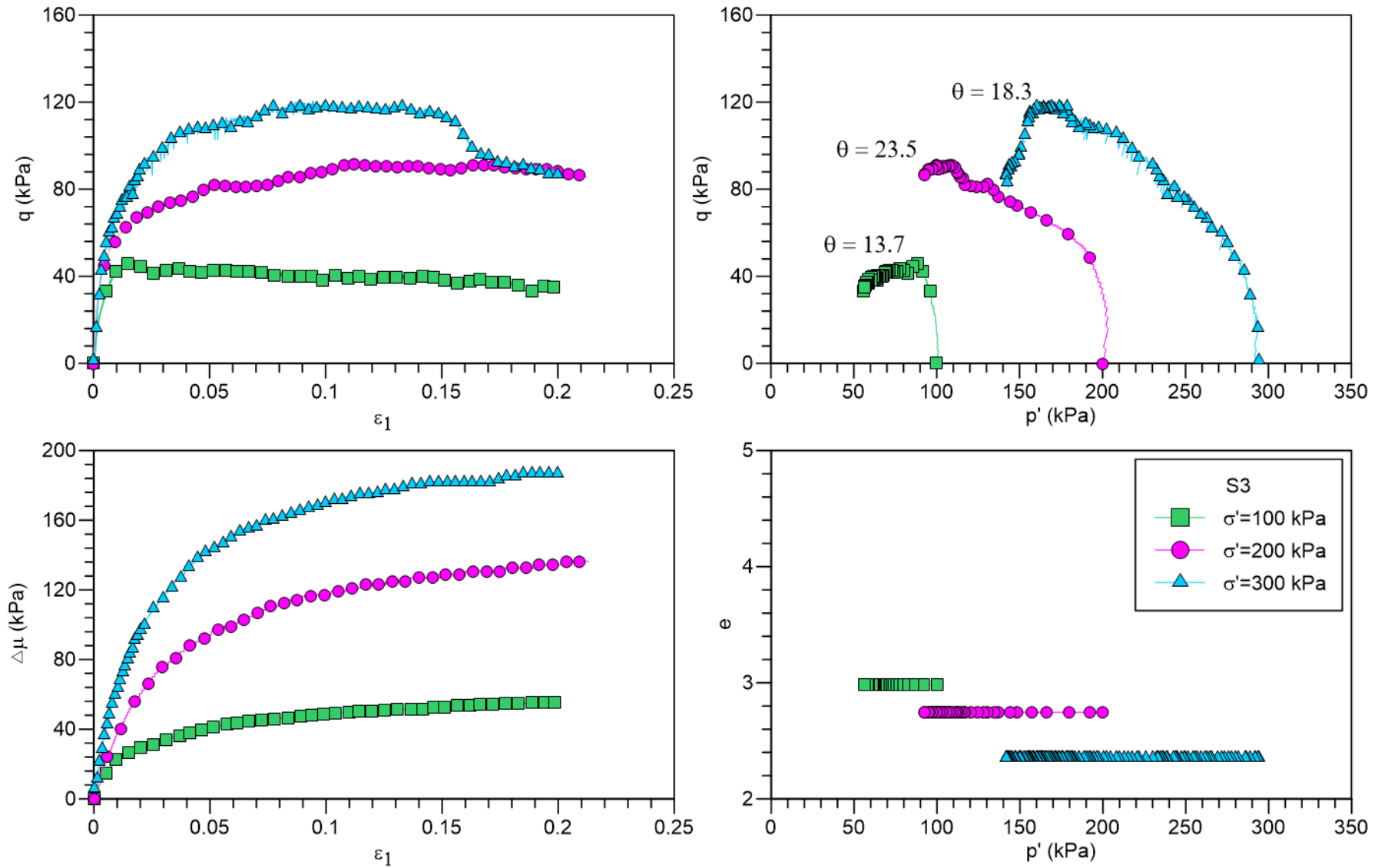
Consolidated undrained triaxial compression tests S1



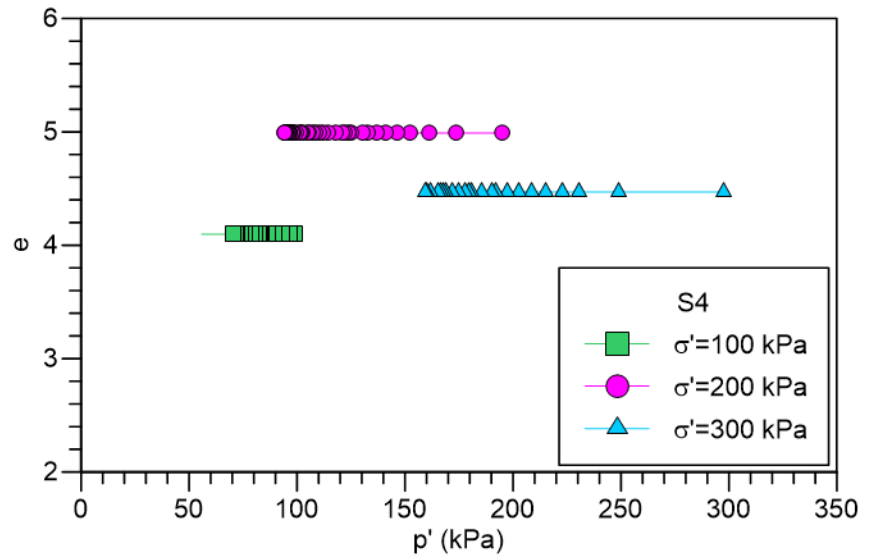
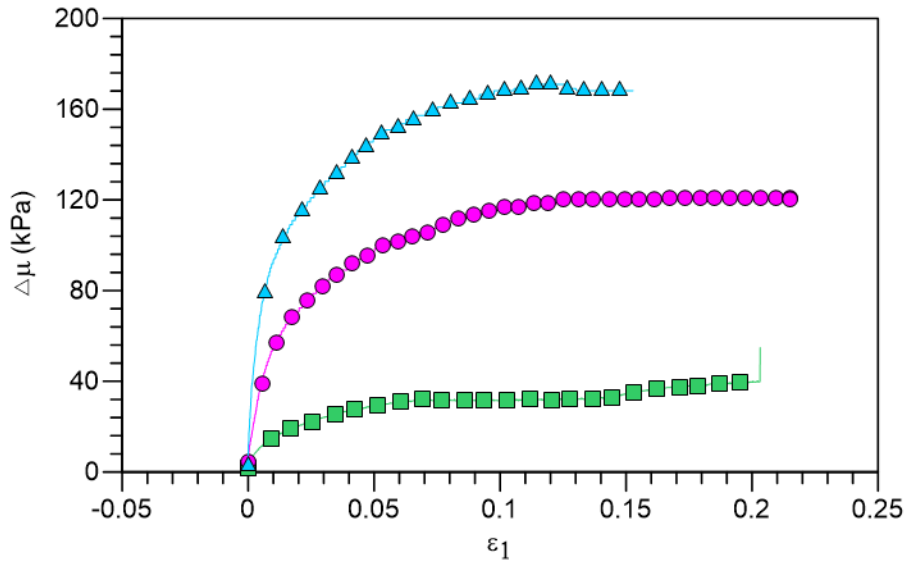
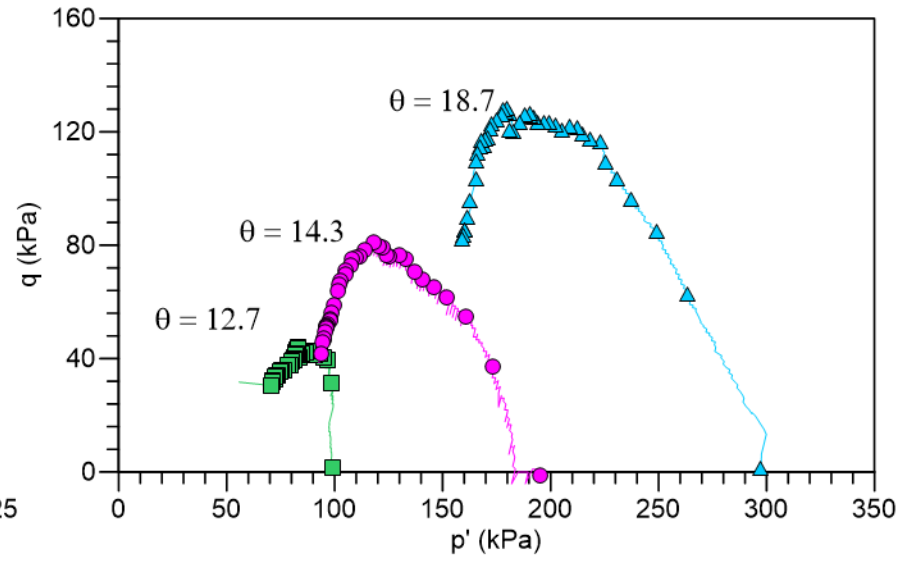
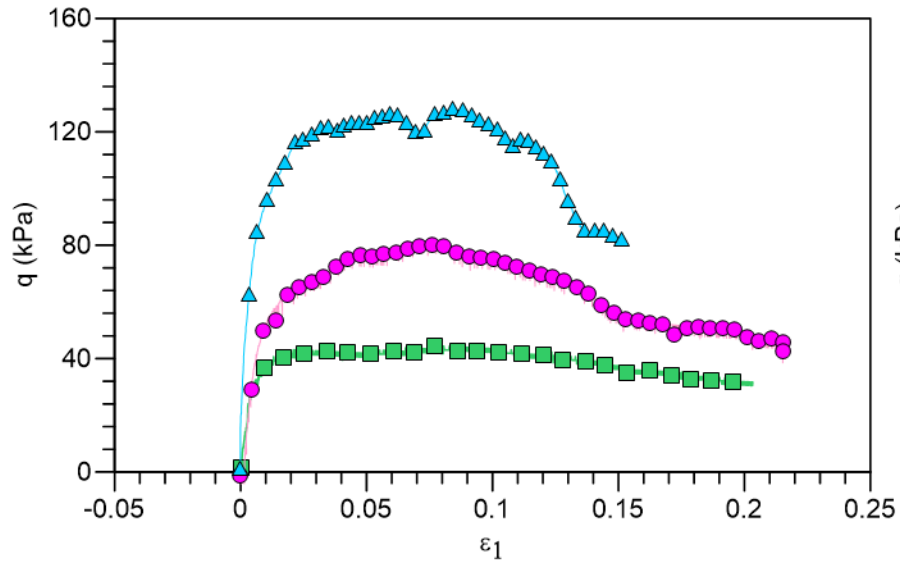
Consolidated undrained triaxial compression tests S2



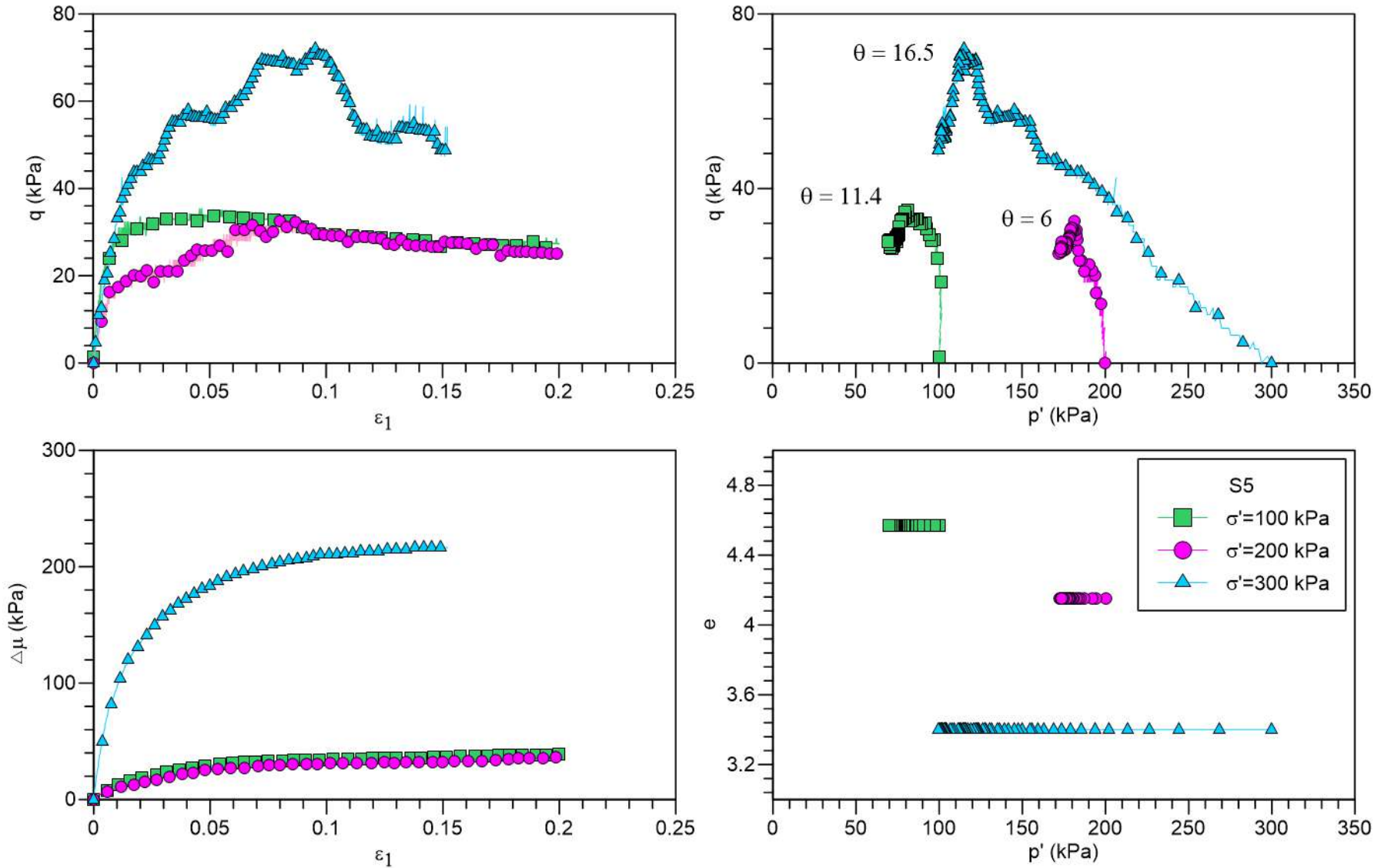
Consolidated undrained triaxial compression tests S3



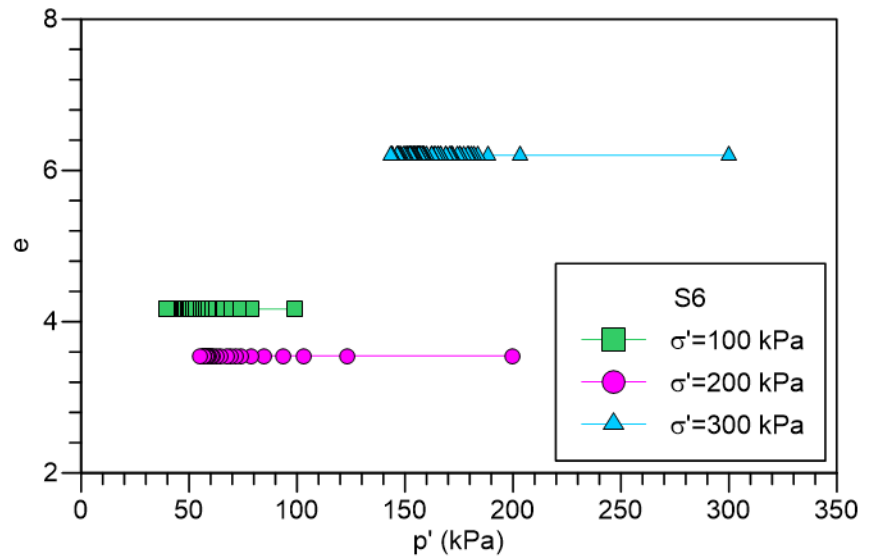
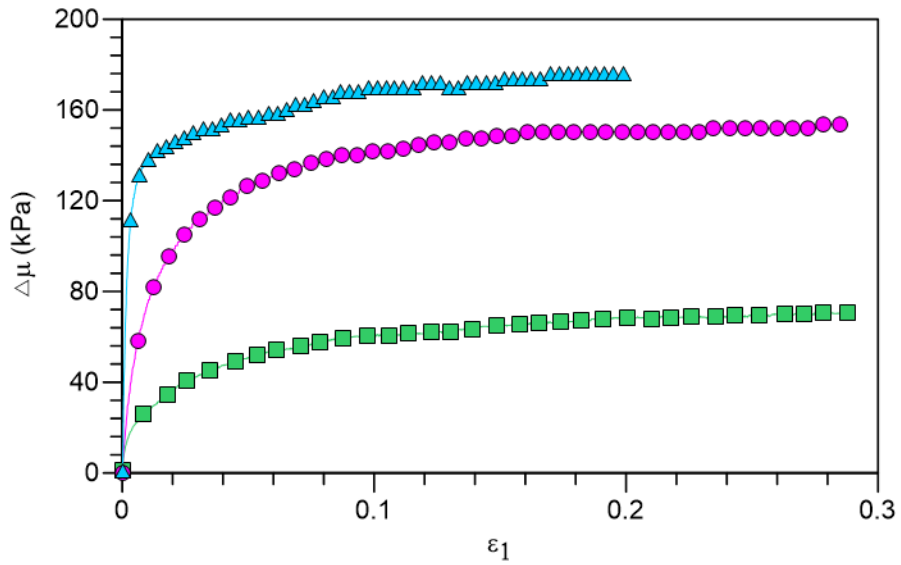
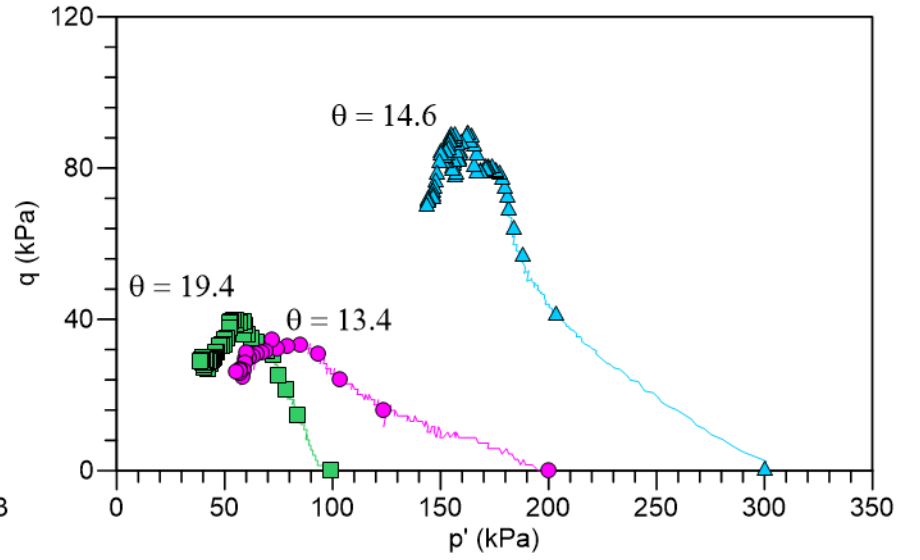
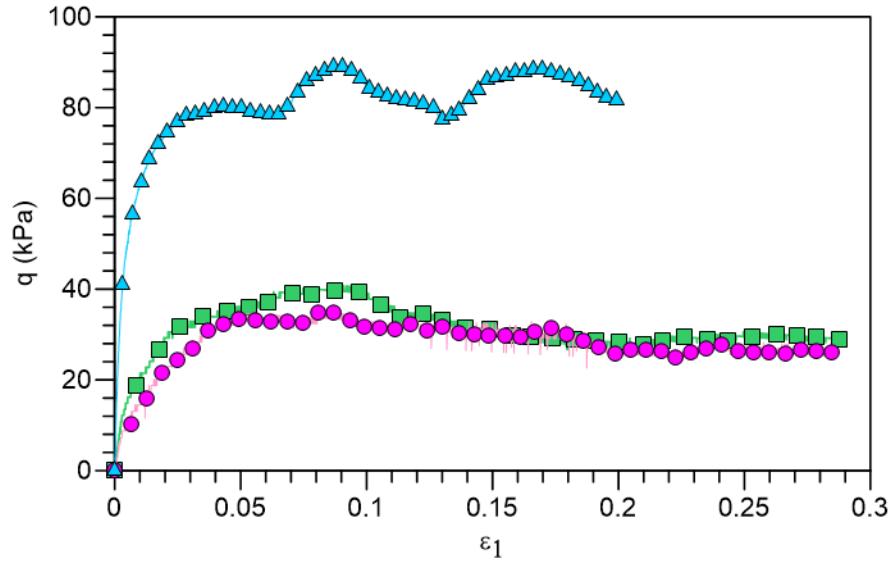
Consolidated undrained triaxial compression tests S4



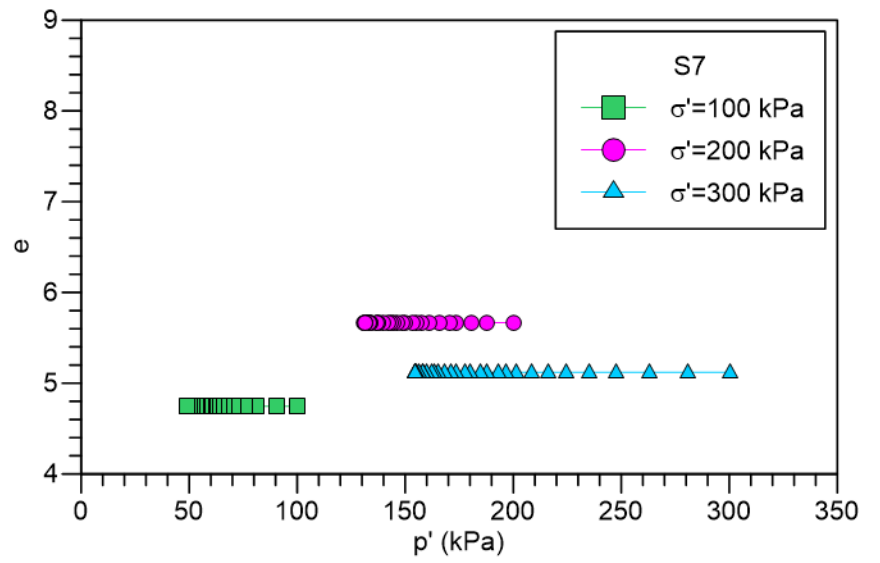
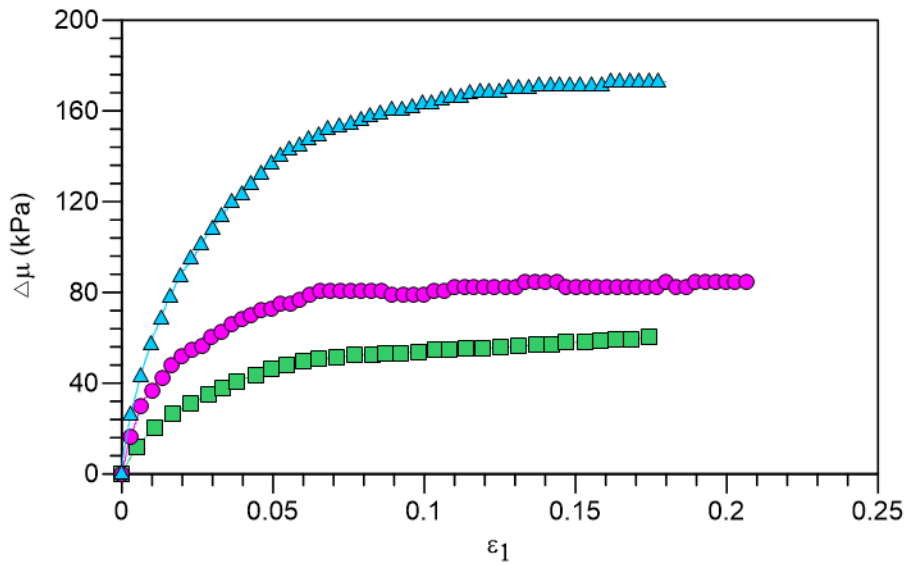
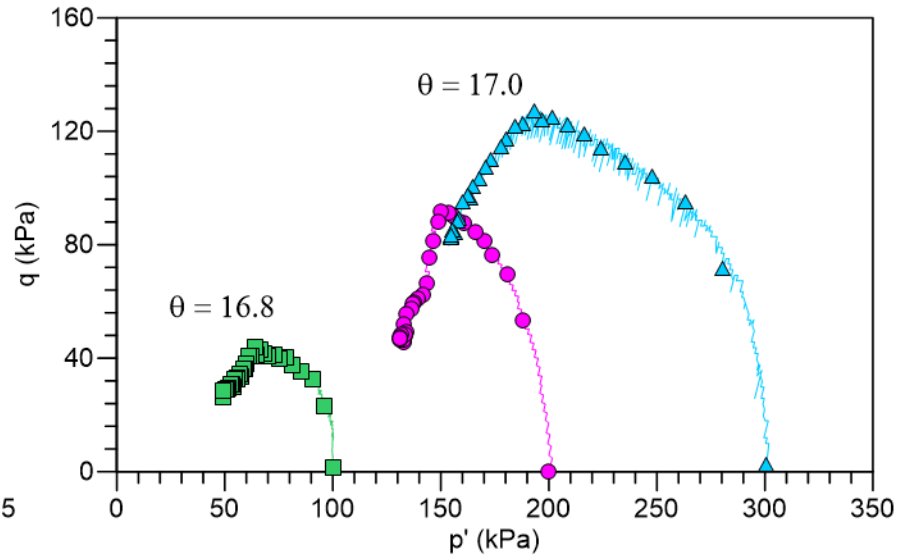
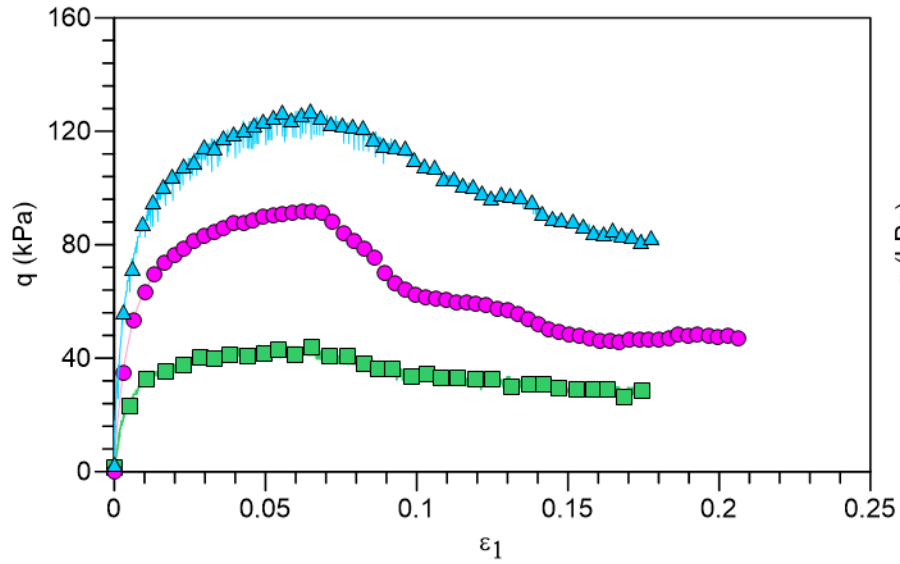
Consolidated undrained triaxial compression tests S5



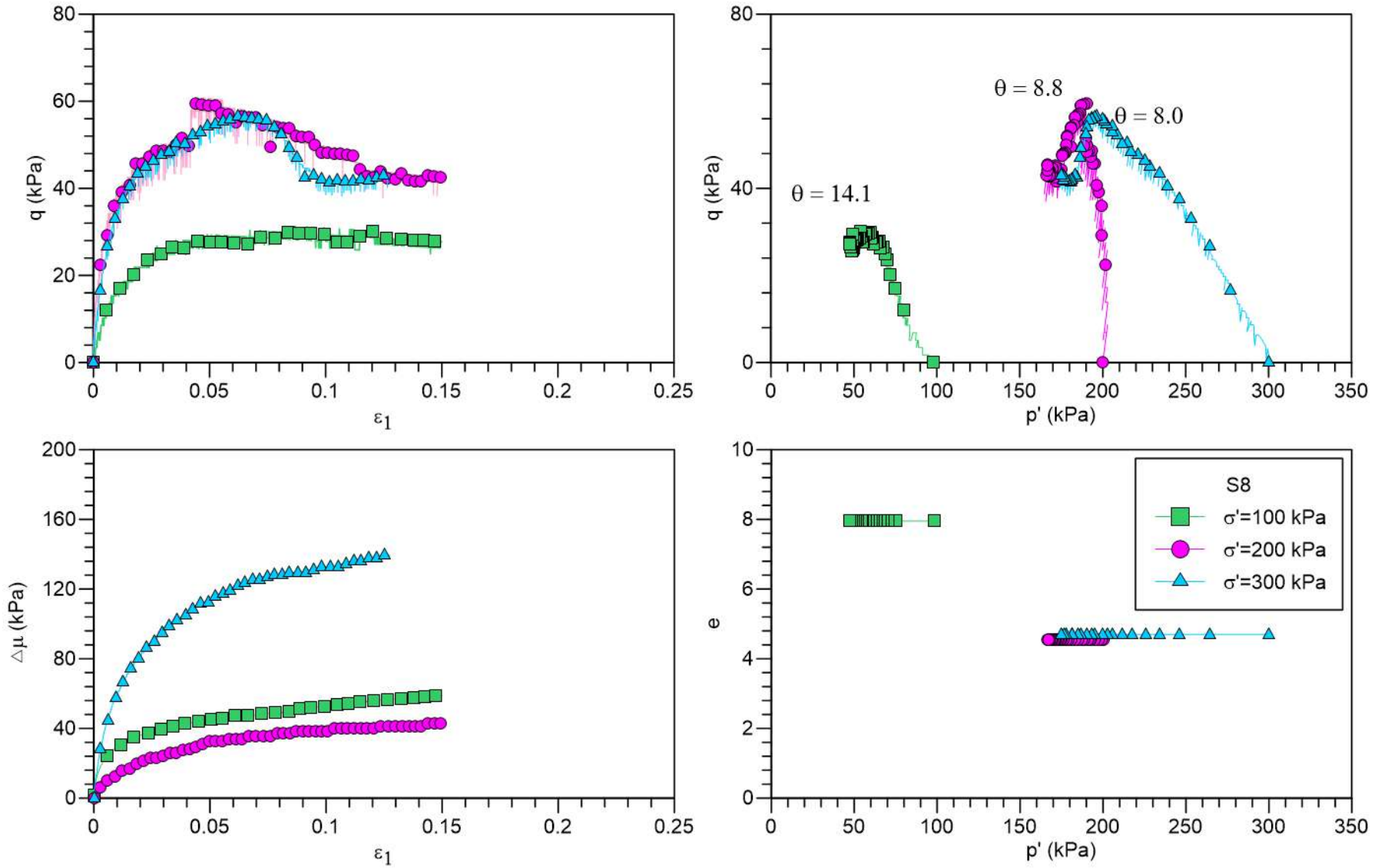
Consolidated undrained triaxial compression tests S6



Consolidated undrained triaxial compression tests S7

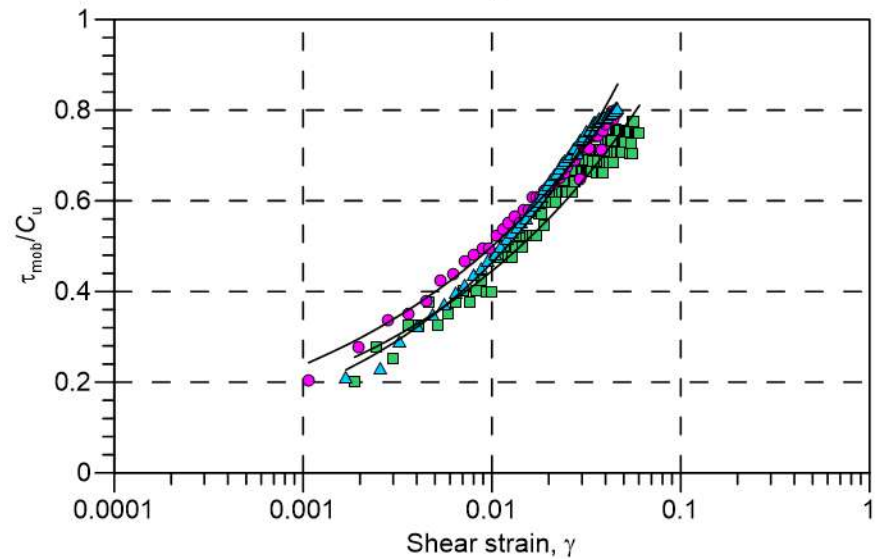
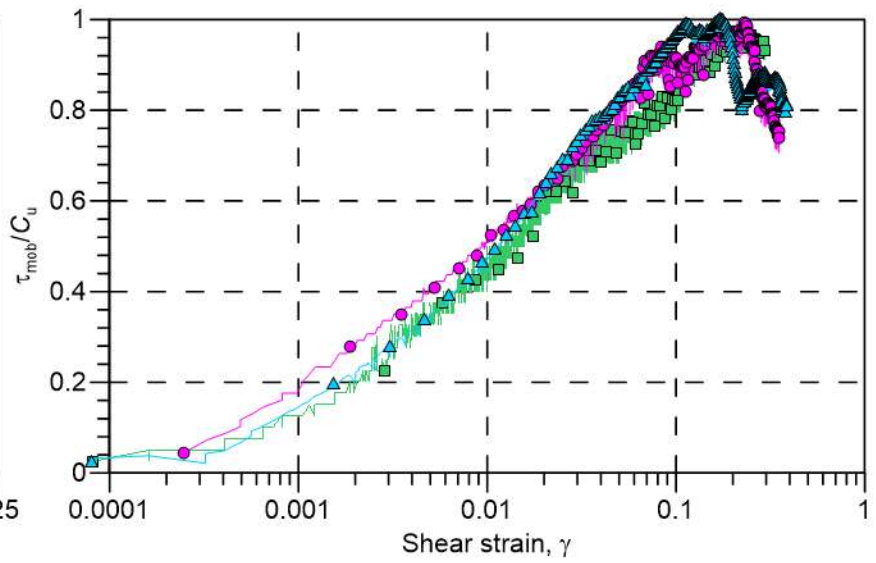
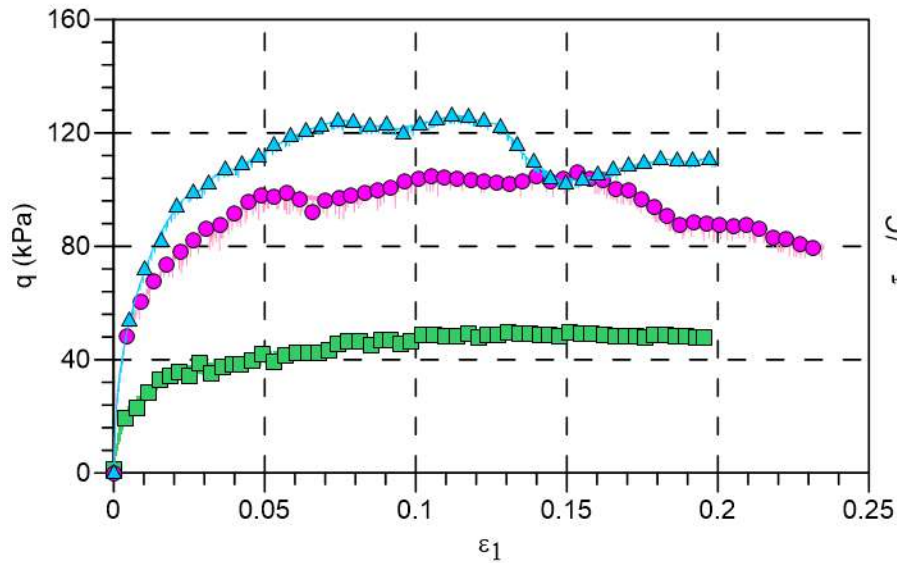


Consolidated undrained triaxial compression tests S8



APPENDIX C

Power law model by Vardanega and Bolton (2011)



$$\tau_{mob}/C_u = 2.06\gamma^{0.33}$$

$$R^2 = 0.94$$

■ $\sigma' = 100$ kPa

$$\tau_{mob}/C_u = 2.20\gamma^{0.32}$$

$$R^2 = 0.99$$

▲ $\sigma' = 300$ kPa

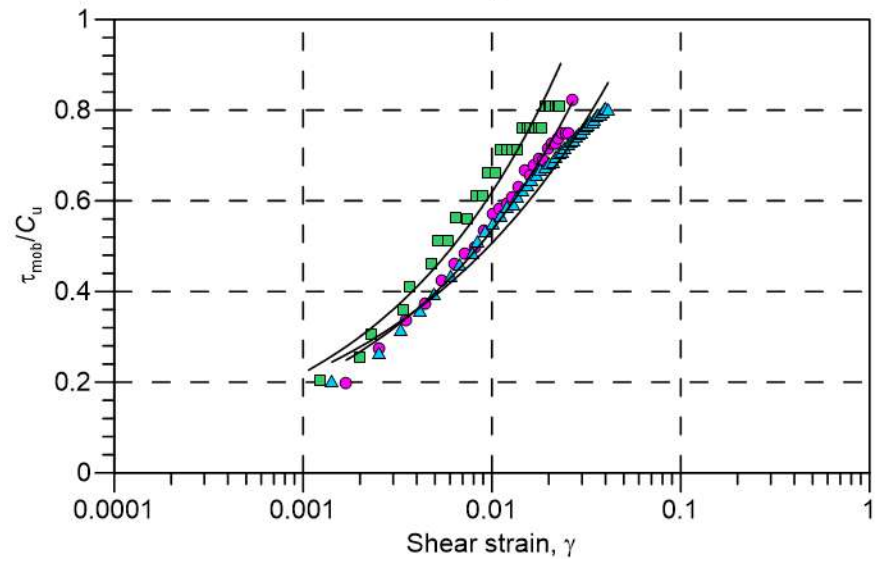
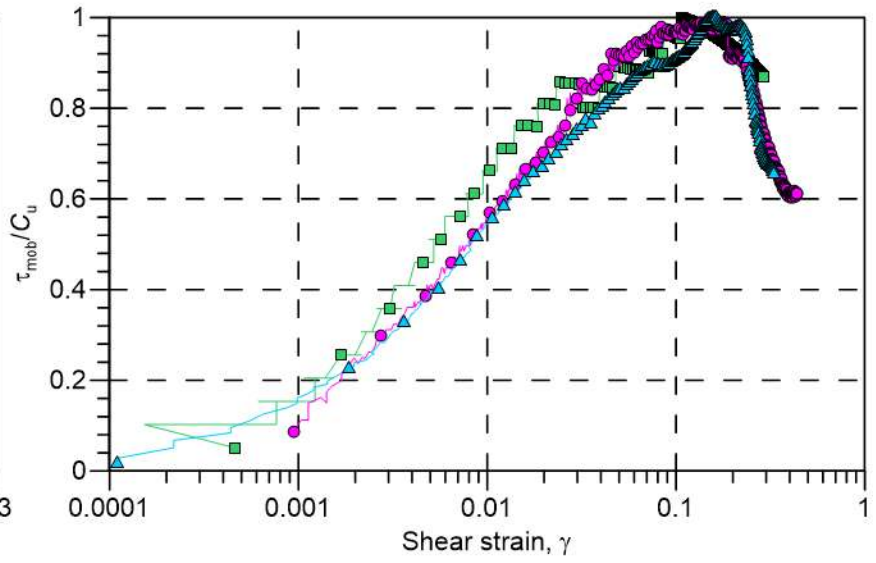
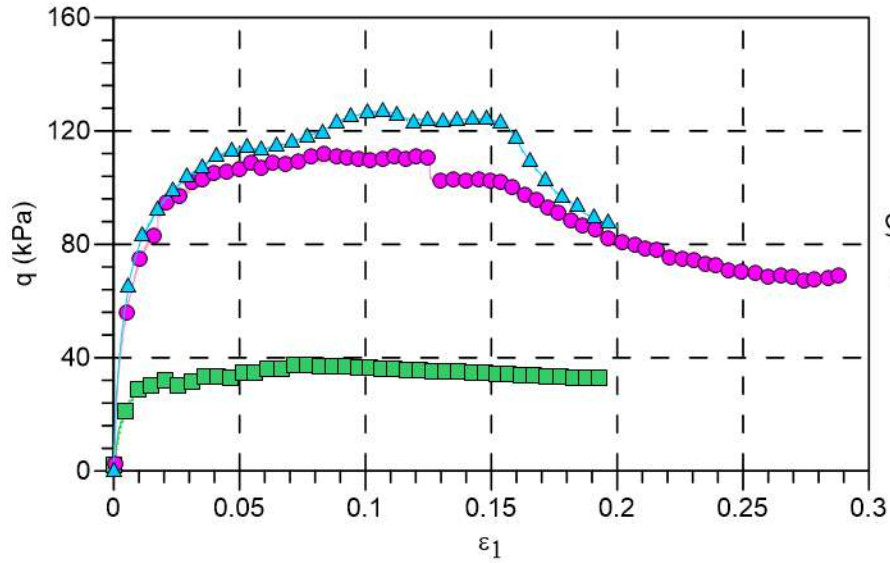
$$\tau_{mob}/C_u = 2.94\gamma^{0.40}$$

$$R^2 = 0.99$$

● $\sigma' = 200$ kPa

S1

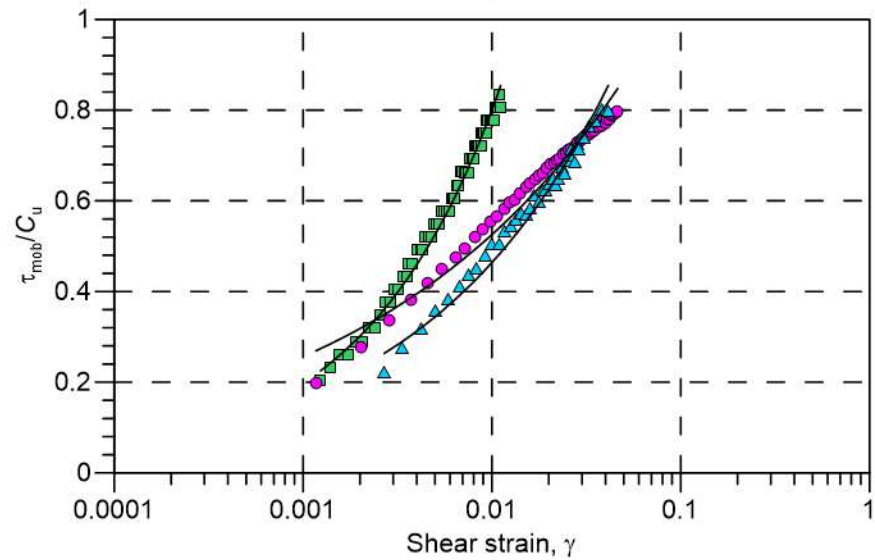
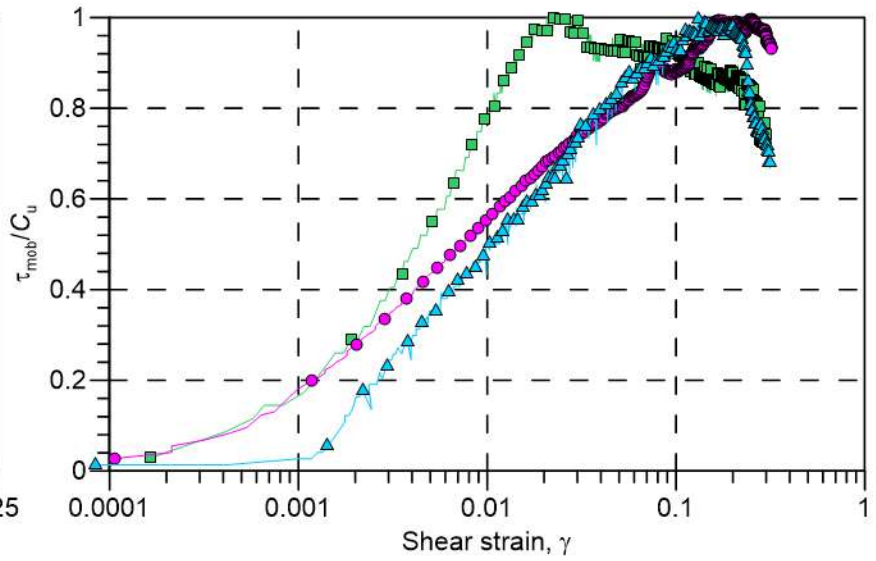
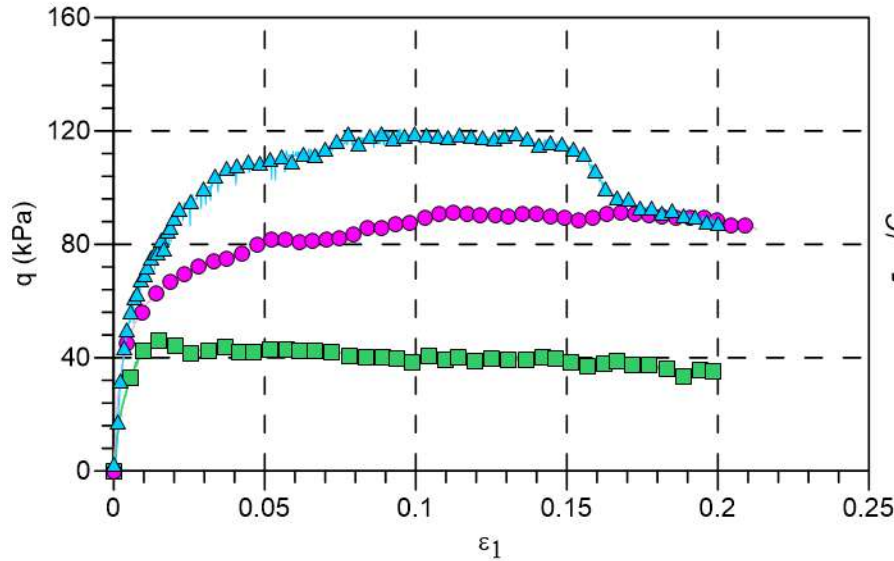
Power law model by Vardanega and Bolton (2011)



S2

$\tau_{mob}/C_u = 4.90\gamma^{0.45}$ $R^2 = 0.95$	■ $\sigma' = 100$ kPa
$\tau_{mob}/C_u = 3.90\gamma^{0.43}$ $R^2 = 0.98$	▲ $\sigma' = 300$ kPa
$\tau_{mob}/C_u = 2.83\gamma^{0.37}$ $R^2 = 0.97$	● $\sigma' = 200$ kPa

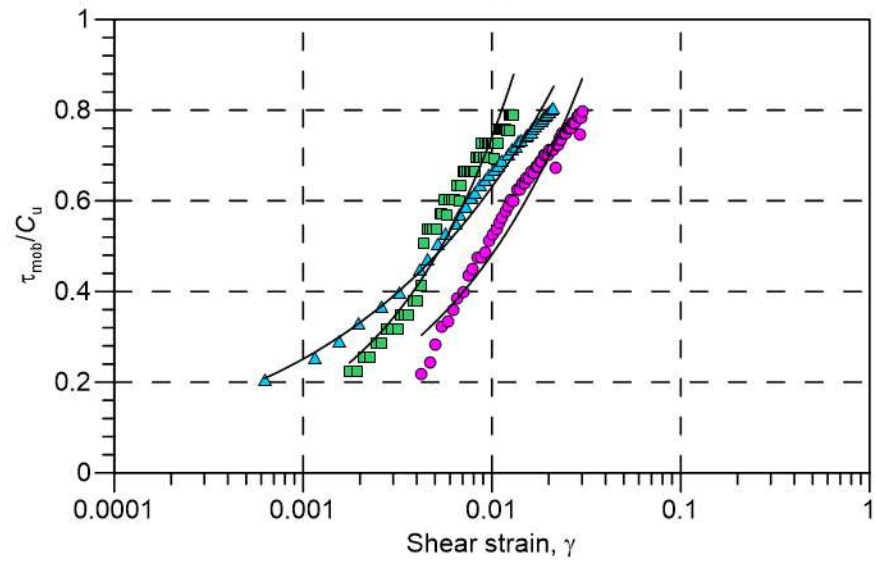
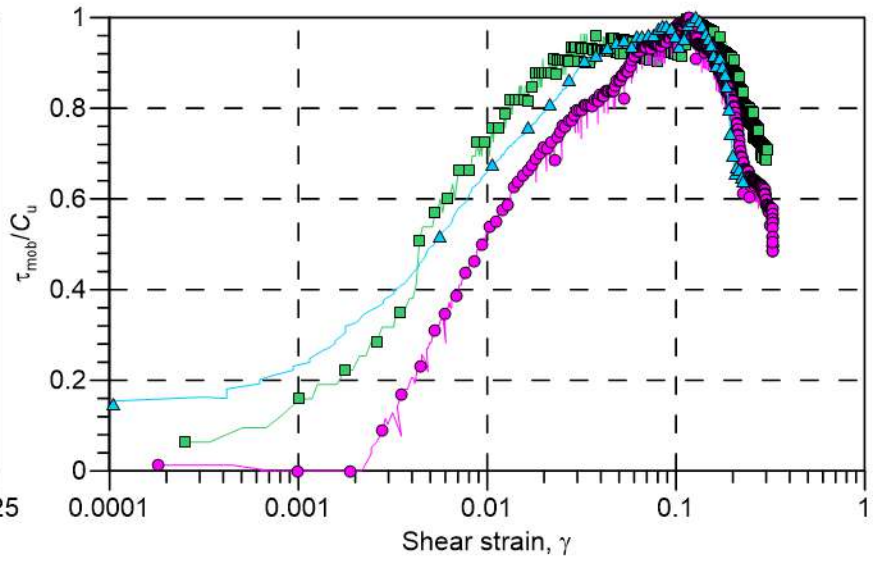
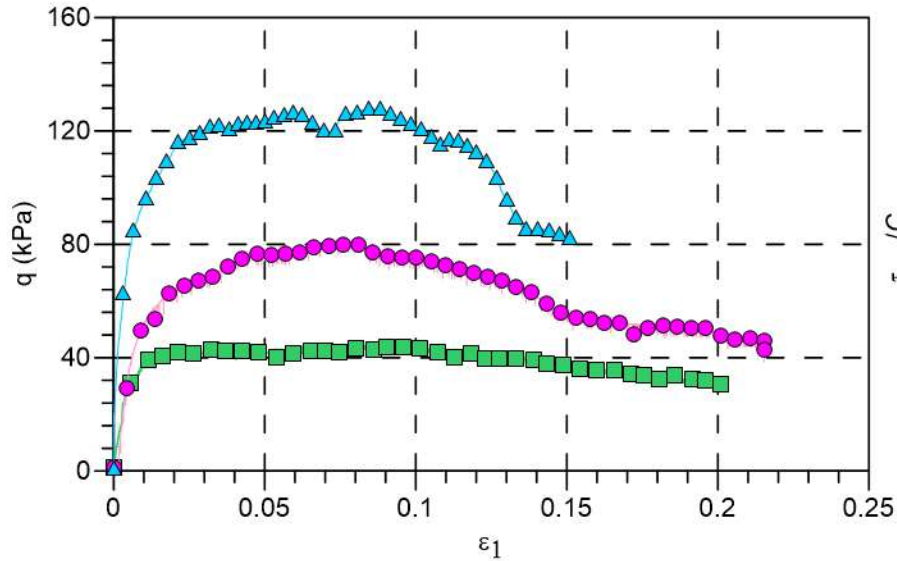
Power law model by Vardanega and Bolton (2011)



S3

$\tau_{mob}/C_u = 13.07\gamma^{0.61}$ $R^2 = 0.99$	■ $\sigma' = 100$ kPa
$\tau_{mob}/C_u = 2.21\gamma^{0.31}$ $R^2 = 0.96$	▲ $\sigma' = 300$ kPa
$\tau_{mob}/C_u = 3.37\gamma^{0.43}$ $R^2 = 0.97$	● $\sigma' = 200$ kPa

Power law model by Vardanega and Bolton (2011)



S4

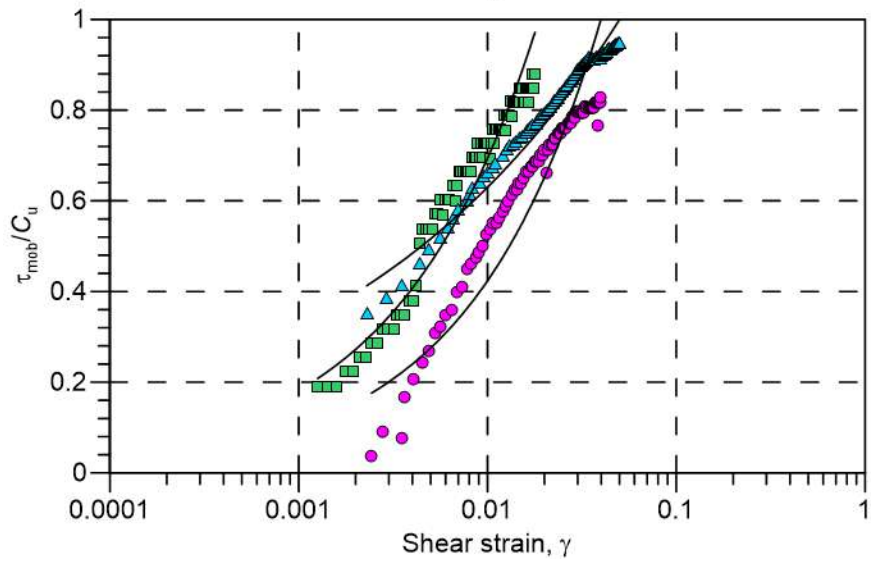
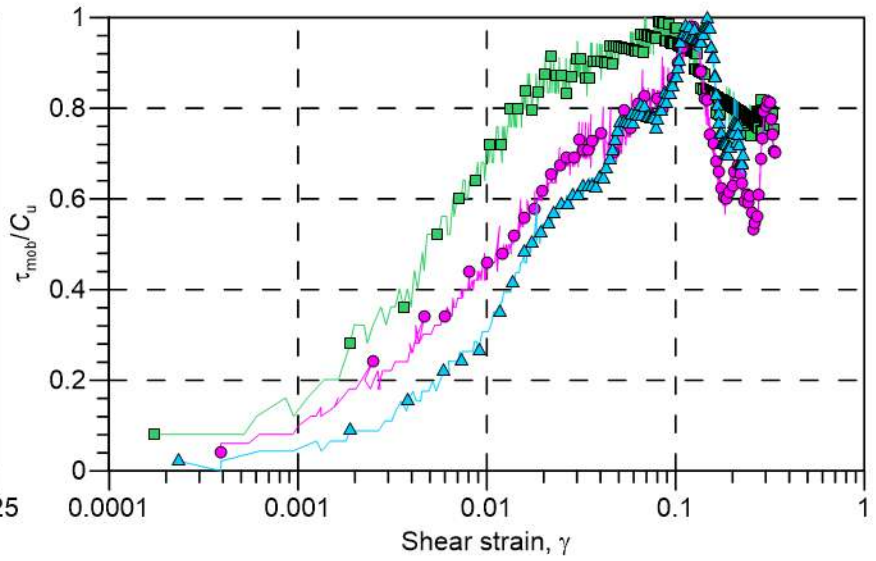
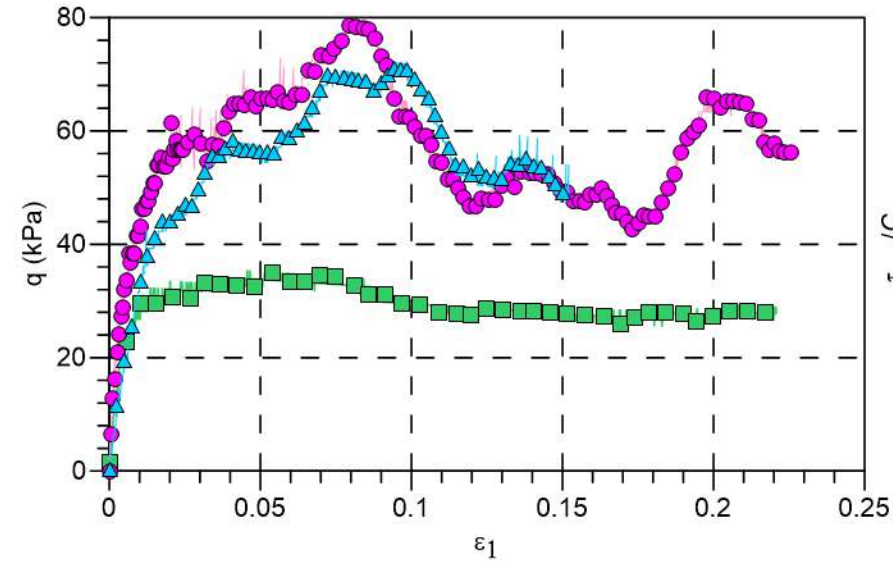
$\tau_{mob}/C_u = 14.27\gamma^{0.64}$
 $R^2 = 0.94$

$\tau_{mob}/C_u = 5.69\gamma^{0.54}$
 $R^2 = 0.93$

$\tau_{mob}/C_u = 3.97\gamma^{0.40}$
 $R^2 = 0.98$

■ $\sigma' = 100$ kPa
▲ $\sigma' = 300$ kPa
● $\sigma' = 200$ kPa

Power law model by Vardanega and Bolton (2011)



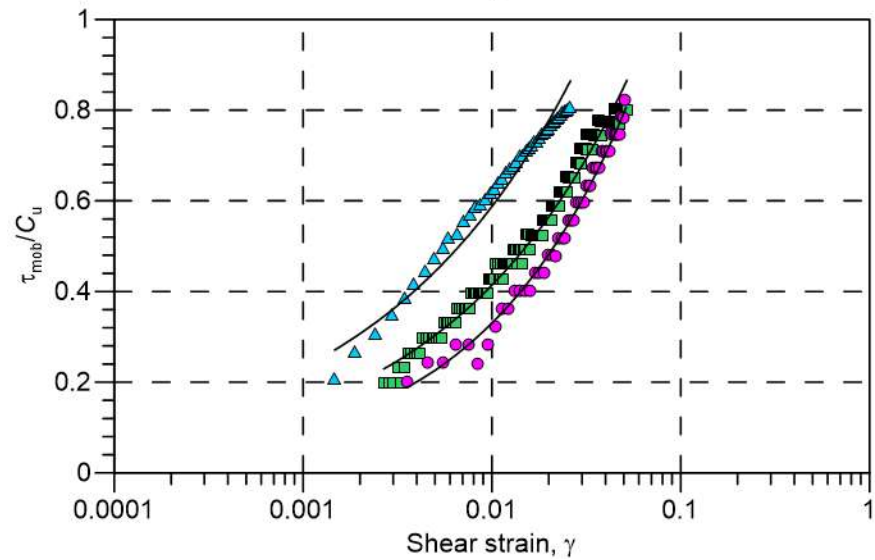
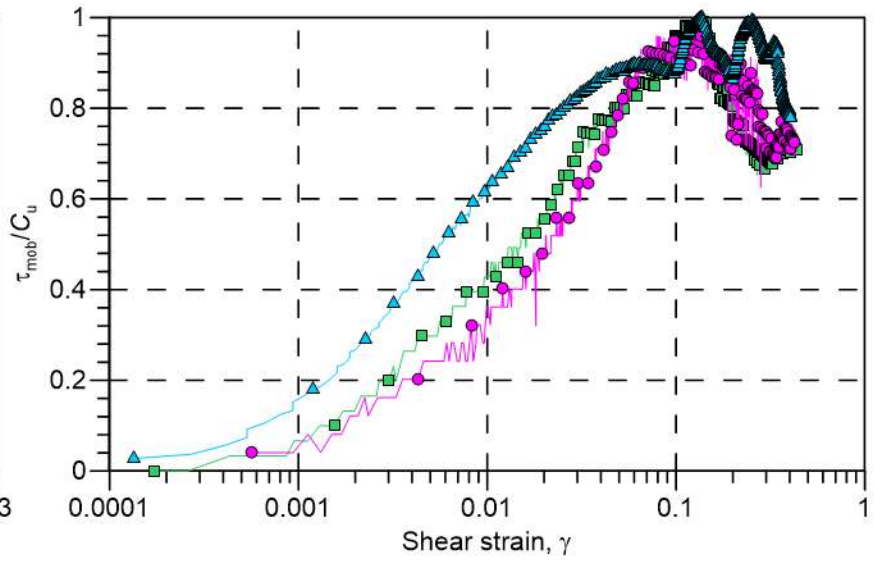
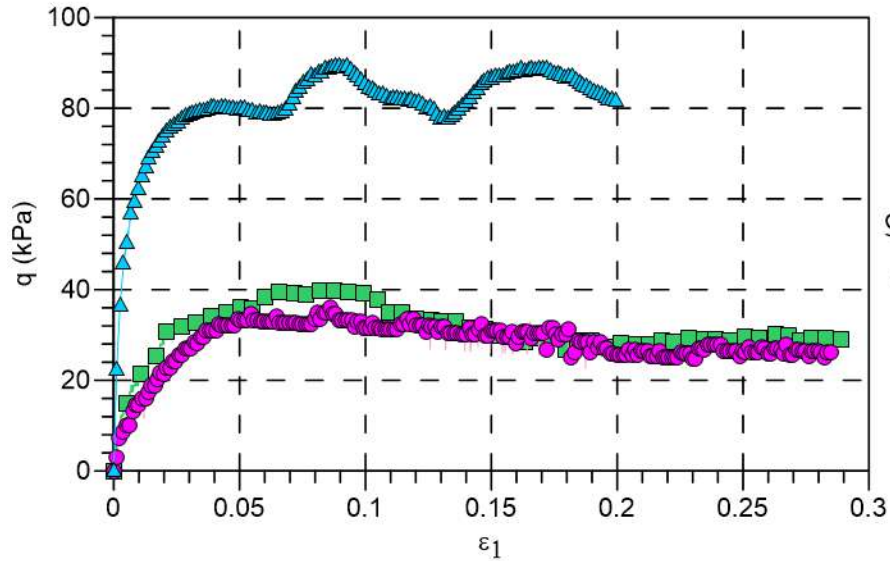
S5

$\tau_{mob}/C_u = 10.96\gamma^{0.58}$
 $R^2 = 0.95$
■ $\sigma' = 100$ kPa

$\tau_{mob}/C_u = 7.39\gamma^{0.62}$
 $R^2 = 0.82$
▲ $\sigma' = 300$ kPa

$\tau_{mob}/C_u = 2.36\gamma^{0.29}$
 $R^2 = 0.96$
● $\sigma' = 200$ kPa

Power law model by Vardanega and Bolton (2011)



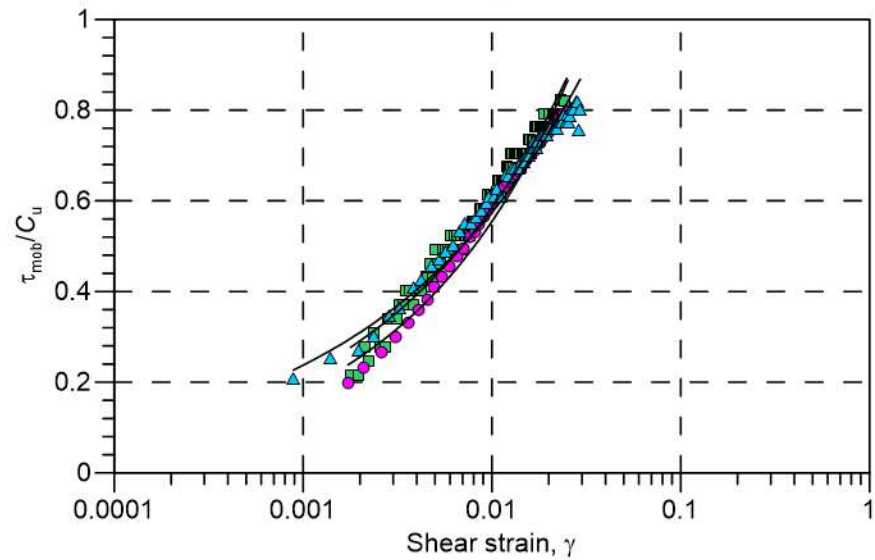
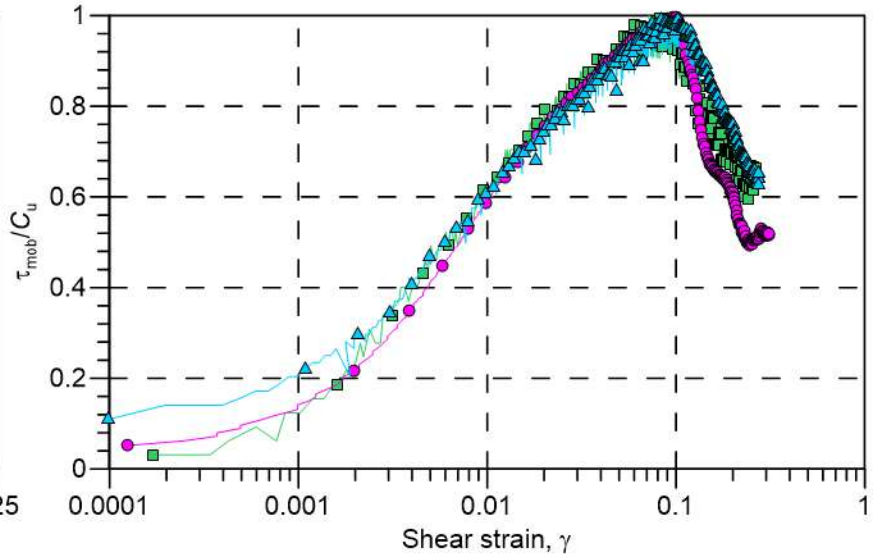
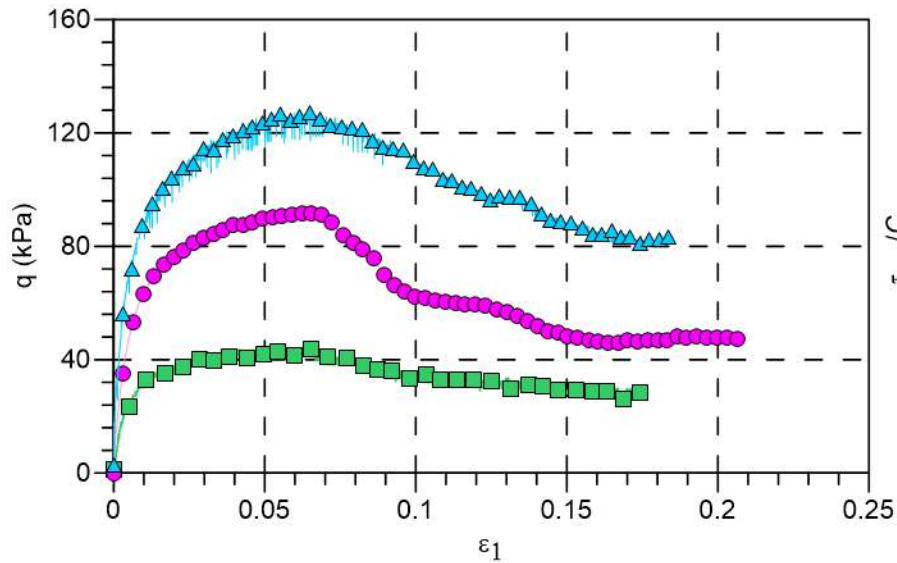
S6

$\tau_{mob}/C_u = 3.26\gamma^{0.45}$
 $R^2 = 0.98$
■ $\sigma' = 100$ kPa

$\tau_{mob}/C_u = 4.06\gamma^{0.54}$
 $R^2 = 0.98$
▲ $\sigma' = 300$ kPa

$\tau_{mob}/C_u = 3.76\gamma^{0.40}$
 $R^2 = 0.96$
● $\sigma' = 200$ kPa

Power law model by Vardanega and Bolton (2011)



$$\tau_{mob}/C_u = 4.32\gamma^{0.43}$$

$$R^2 = 0.95$$

S7
■ $\sigma' = 100$ kPa

$$\tau_{mob}/C_u = 5.09\gamma^{0.48}$$

$$R^2 = 0.97$$

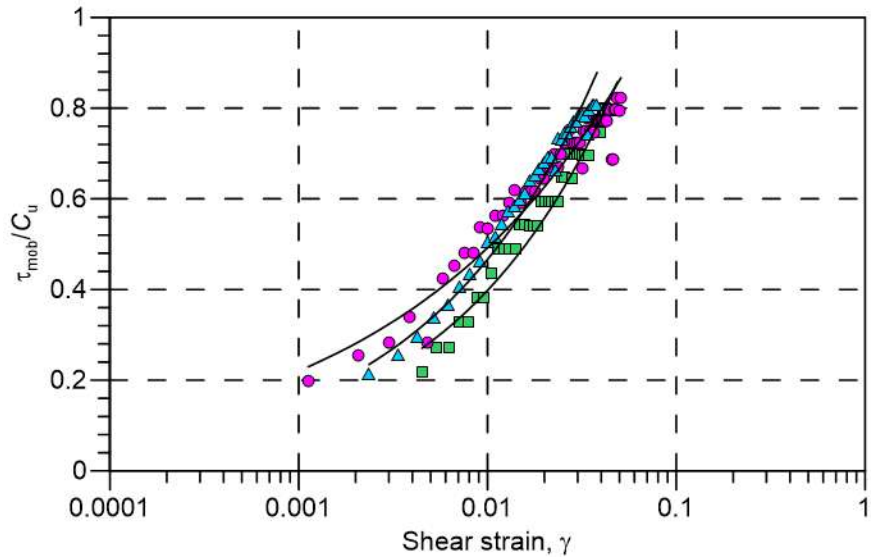
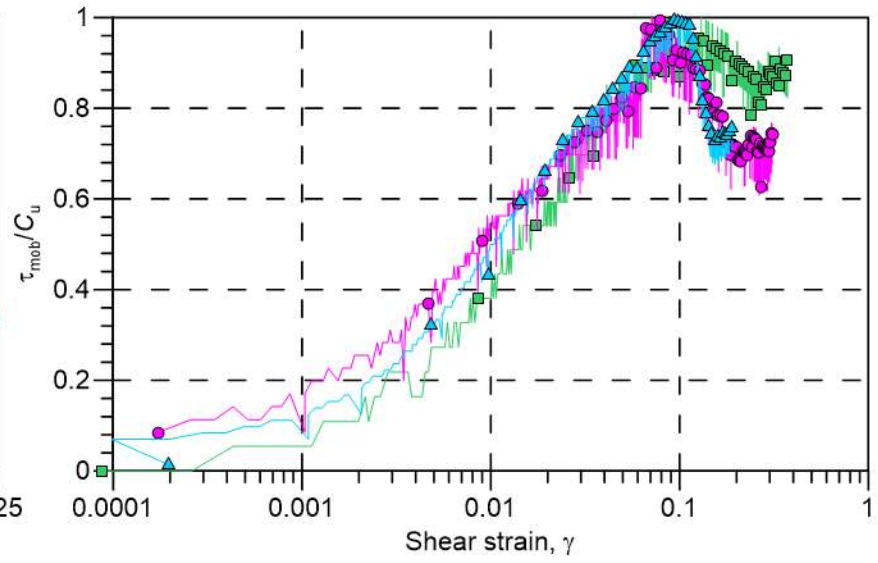
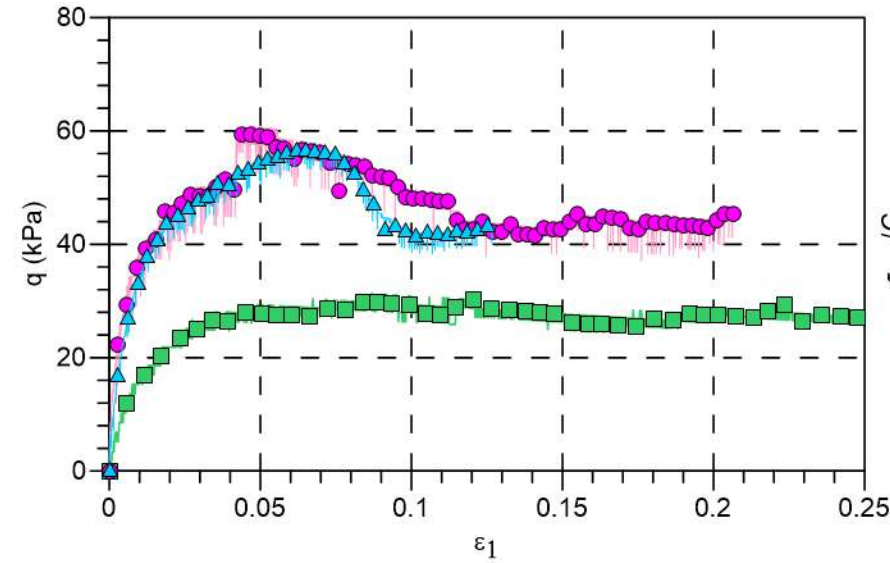
▲ $\sigma' = 300$ kPa

$$\tau_{mob}/C_u = 3.36\gamma^{0.38}$$

$$R^2 = 0.97$$

● $\sigma' = 200$ kPa

Power law model by Vardanega and Bolton (2011)



$$\tau_{mob}/C_u = 3.71\gamma^{0.48}$$

$$R^2 = 0.97$$

$$\tau_{mob}/C_u = 2.45\gamma^{0.35}$$

$$R^2 = 0.94$$

$$\tau_{mob}/C_u = 4.20\gamma^{0.48}$$

$$R^2 = 0.97$$

S8

■ $\sigma' = 100$ kPa

▲ $\sigma' = 300$ kPa

● $\sigma' = 200$ kPa